University of Southampton

University of Southampton Research Repository

University of Southampton

Faculty of Engineering and Physical Sciences

Institute of Sound and Vibration Research

Prediction of airborne noise inside railway vehicles

by

Hui LI

Thesis for the degree of Doctor of Philosophy

May 2020

University of Southampton

<u>Abstract</u>

Faculty of Engineering and Physical Sciences

Institute of Sound and Vibration Research

<u>Doctor of Philosophy</u>

Prediction of airborne noise inside railway vehicles

by Hui LI

Railway vehicles are important means of transportation and vital to the public. However, the noise within railway vehicles is an important aspect that can affect the passengers' and train crew's comfort. High interior noise can be attributed to strong external noise sources and insufficient sound insulation by the train wall structures. To predict the interior noise is challenging. Existing approaches such as the finite and boundary element (FE/BE) method or statistic energy analysis (SEA) are not suitable for a wide frequency spectrum solution and are either of high computational cost or of low accuracy. The aim of this thesis is to develop a comprehensive modelling approach to predict the interior airborne noise of modern railway vehicles, taking into account different noise sources and transmission paths as well as the complexity of the car body structure.

An approach is presented for modelling the noise propagation beneath the train floor and this is applied to rolling noise sources by assuming that the sound incident on the train floor is made up of a direct and a reverberant component. An equivalent source model is used to represent the direct component, and SEA model is used for the reverberant part. The sound power of the rolling noise is obtained by using the TWINS model. A wavenumber-domain boundary element (2.5D BE) approach is adopted to predict the propagation of rolling noise to the train external surfaces. Comparisons are made with measurements showing good agreement. Noise propagation from the pantograph to the train external surfaces is studied considering the influence of flow on the sound propagation. The total sound power from the pantograph is calculated based on the component-based approach and a database of factors of influence created by previous researchers. The 2.5D BE method is again employed to calculate the relevant sound propagation. The influence of flow on the sound propagation is modelled either by a uniform mean flow or by allowing for the variation of velocity through the turbulent boundary layer. Laboratory experiments and the ray tracing approach verified the 2.5D models for predicting the pantograph noise propagation. To calculate the noise transmission through extruded train wall structures, use is made of a 2.5D FE/BE model and an SEA model. The 2.5D FE model is used to study the bending waves in the extruded panel to calibrate the input parameters for the SEA model. With the aid of such a calibration using the 2.5D FE model, the SEA model can give good quality predictions of the sound transmission loss and radiation efficiency of the extruded panel in comparison with the measurements.

Finally, an overall framework is provided to predict the airborne noise inside railway vehicles, in which another SEA model is created for the interior space of the train. The power input to the interior SEA model is determined from the incident sound power on the train external surfaces. The framework of interior noise prediction is verified against measurements on a metro train. It is found that the predictions agree reasonably well with the measurements in terms of sound spectra and overall sound pressure levels.

Contents

Table of Contents

List of Figures

List of Figures

List of Figures

List of Figures

List of Tables

Research Thesis: Declaration of Authorship

Print name: Hui Li

Title of thesis: Prediction of airborne noise inside railway vehicles

I declare that this thesis and the work presented in it are my own and has been generated by me as the result of my own original research.

I confirm that:

1. This work was done wholly or mainly while in candidature for a research degree at this University;

2. Where any part of this thesis has previously been submitted for a degree or any other qualification at this University or any other institution, this has been clearly stated;

3. Where I have consulted the published work of others, this is always clearly attributed;

4. Where I have quoted from the work of others, the source is always given. With the exception of such quotations, this thesis is entirely my own work;

5. I have acknowledged all main sources of help;

6. Where the thesis is based on work done by myself jointly with others, I have made clear exactly what was done by others and what I have contributed myself;

Parts of this work have been published as:

- H. Li, D. Thompson, G. Squicciarini, Using the waveguide boundary element and SEA method to determine the sound incident on a train external surface. The Fourth International Conference on Railway Technology: Research, Development and Maintenance, Sitges, Barcelona, Spain, 3-7 September 2018.

Declaration of Authorship

- H. Li, D. Thompson, G. Squicciarini, X. Liu, M. Rissmann, F.D. Denia, J. Giner-Navarro, Using a 2.5D boundary element model to predict the sound distribution on train external surfaces. The 13th International Workshop on Railway Noise, Ghent, Belgium, 16-20 September 2019.

Signature: Date:

Acknowledgements

Completing a PhD is challenging and exhausting; without the help and support from many I would not have been able to finish this journey. I would like to acknowledge those who have helped me.

I am extremely grateful to my first supervisor Prof. David Thompson and my second supervisor Dr. Giacomo Squicciarini for their tireless supervision, support, insight, advice, motivation and patience. They really are qualified and experienced supervisors. We had supervisory meetings nearly every week from September 2016 to December 2019. So many new ideas that have been presented in this thesis came out in those meetings. Performing research one often faces valleys that can be frustrating. My supervisors' attitude towards research inspired and motivated me. They were always helpful every time when I was struggling and gave me constructive suggestions.

I want to thank Prof. Jungsoo Ryue, Dr. Hongseok Jeong, and Dr. Yumei Zhang, who kindly helped me with understanding the 2.5D theory and use of the WANDS software. I want to thank Dr. Xiaowan Liu for her help with using the OpenFoam platform for CFD simulations and with the use of the component-based approach. I want to thank Prof. Alec Wilson in ISVR, who kindly helped me with the ray tracing method. I appreciate the help of Dr. Xiaowan Liu, Dr. Hongseok Jeong, Mr. Phil Oxborrow and other technicians in the laboratory measurements at ISVR in February 2018. Also, many thanks to Dr. Xianying Zhang for sharing her measured data on scale ballast. I am also grateful to the RUN2RAIL project of the Shift2Rail Joint Undertaking under the European Union's Horizon 2020 research and innovation programme (grant agreement no. 777564) who gave me the chance to access some field experimental data to validate some of the models in this thesis.

I would like to thank my family, especially my wife, Ren Xing and my little son, for their love and support. Without their support I would not be able to finish the thesis. I wish to thank my colleagues in the Dynamics Group within ISVR, especially my office colleagues, including the ones who finished before me: Hongsoek, Ding, Kola, etc. and the ones who will finish after me: Boniface, Palm, Rahma, Milene, Davide, etc. We have had great and valuable time together.

Acknowledgements

List of symbols and abbreviations

A	Area
a	Length of strips
B	Bending stiffness
b	Width of strips
$\mathbf{C_a}, \mathbf{C_b}, \mathbf{C_c}$	Coefficients when assigning the boundary conditions
$C_{l,rms}$	rms fluctuating lift coefficient
c_0	Speed of sound
c_{eq}	Equivalent speed of sound
c_B	Phase velocity of bending waves
D	Doppler factor
D_{rad}	Directivity factor of the noise
d	Diameter
E	Young's modulus
E_g	Stored energy of the global subsystems
E_l	Stored energy of the local subsystems
$\mathbf{F}$	Vector of forces in the spatial domain
$\tilde{\mathbf{F}}$	Vector of forces in the wavenumber domain
f	Frequency
f_c	Critical frequency
f_1	First natural frequency
G	Shear modulus
$\mathbf{G}$	Matrices of Green's functions
$\mathbf{H}$	Matrices of Green's functions
H, h	Thickness
$I, \bar{I}$	Sound intensity
I_i	Second moment of area
i	$\sqrt{-1}$
$\mathbf{K}$	Stiffness matrices
K_H	Linearized contact stiffness
k_0	Acoustic wavenumber
k_x	Wavenumbers in the x direction
k_r	Structural wavenumbers, propagating part

List of symbols and abbreviations

k_0'	Equivalent acoustic wavenumber
L, l	Length
L_p	Sound pressure level
L_W	Sound power level
$\mathbf{M}$	Mass matrix
M	Mach number
M''	Material density of extrusion
m_s	Sleeper mass per unit length
m_g	Mass per unit area of global modes
m_l	Mass per unit area of local modes
m''	Material density of strip
$\mathbf{n}$	Unit vector normal to the surface
n_g	Modal density of global modes
n_l	Modal density of local modes
P_in	Input power
p	Sound pressure in the spatial domain
$\tilde{p}$	Sound pressure in the wavenumber domain
Q	Volume velocity amplitude
R	Sound transmission loss
Re	Reynolds number
r	Distance
r	Roughness amplitude
S	Surface area
St	Strouhal number
S_q	Source
s	Second
s_p	Pad stiffness per unit length
s_b	Ballast stiffness per unit length
T_{60}	Reverberation time
t	Receiving time
$\mathbf{u}_0$	Flow velocity
u_1, u_2	Rail receptance components
$\overline{u_{eq}}$	Equivalent speed of fluid
V	Volume

$\mathbf{v}_s$	Velocity at the source
v	Particle velocity in the spatial domain
$\tilde{v}$	Particle velocity in the wavenumber domain
v_r, v_w, v_c	Vibrational velocity amplitude (of rail, wheel and contact)
W	Sound power
X, x	Cartesian coordinate
Y, y	Cartesian coordinate
Y	Mobility in the spatial domain
$\tilde{Y}$	Mobility in the wavenumber domain
Y_r, Y_w, Y_c	The mobility of the rail (of rail, wheel and contact)
Z, z	Cartesian coordinate
z_n	Surface normal impedance
α	Angle
α	Absorption coefficient
β	Angle
β	Structural wavenumbers, evanescent part
Γ	The perimeter of acoustic domain boundary
γ_i	Scaling factor
Δt	Time step
δ	Thickness of the boundary layer
η_i	Dissipation loss factor
η_{ij}	Coupling loss factors
θ	Angle
μ	Fluid viscosity
v	Poisson's ratio
ρ_0, ρ	Air density
σ	Radiation efficiency
σ_e	Equivalent flow resistivity
τ	Emission time
τ, τ_d	Transmission coefficient
$\mathbf{\Phi}$	Nodal displacement vector in the spatial domain
$\tilde{\mathbf{\Phi}}$	Nodal displacement vector in the wavenumber domain
φ	Angle
ω	Angular frequency

List of symbols and abbreviations

2D	Two dimensional
2.5D FE	Wavenumber domain finite element method
2.5D BE	Wavenumber domain boundary element method
2.5D FE/BE	Wavenumber domain coupled finite element and boundary element method
3D	Three dimensional
CFD	Computational fluid dynamics
dB	Decibel
ISVR	Institute of Sound and Vibration Research
SEA	Statistical energy analysis
SPL	Sound pressure level
STL	Sound transmission loss
TWINS	Track-Wheel Interaction Noise Software
WANDS	Wave Number Domain Software

Chapter 1   Introduction

1.1   Background and motivation

Railway noise, both inside and outside the train, is troubling for the railway industry and slowing the development of railways. External noise sources, such as rolling noise and aerodynamic noise will cause environmental impact, and also, the noise around the outside area of the train will be transmitted to the interior of the coach. The interior noise plays an important role for the comfort of passengers and train crew. It is often a contractual requirement to keep the interior noise below a certain level although there is no universal standard that specifies the acceptable noise levels. Moreover, there is a tendency to require the same interior noise limits even for trains that will run at higher speeds.

Train manufacturers dedicate much attention to the development of quieter vehicles, but the interior noise of trains is still a significant problem [1]. There are various reasons for high levels of interior noise in railway vehicles. Apart from the acoustical design of the interior area, there are at least two other main reasons:

(1).There are strong noise sources

There are quite a few noise sources associated with railway vehicles, such as rolling noise, caused by wheel/rail interaction [2], and aerodynamic noise, caused by flow/structure interaction [3], as seen in Figure 1.1. Rollling noise is important in a wide range of speeds. At high speeds, aerodynamic noise is also a significant noise source. Besides, noise from motors and electrical equipment should also be considered, although they are usually less imporant than rolling noise or aerodynamic noise at high speeds. Moreover, there are other noise sources which can also contribute significantly to the train interior acoustic environment, for example, duct noise from train heating/cooling system. The ducts of the ventilation system usually open directly into the train cabin. Hence although the source may have lower levels than rolling noise, it has a higher contribution to the interior noise as it transmitted directly to the interior volume. Other noise sources include curve squeal, bridge noise, traction noise from diesel engines and so on. The noise transmission from these sources is not studied further in the current work.
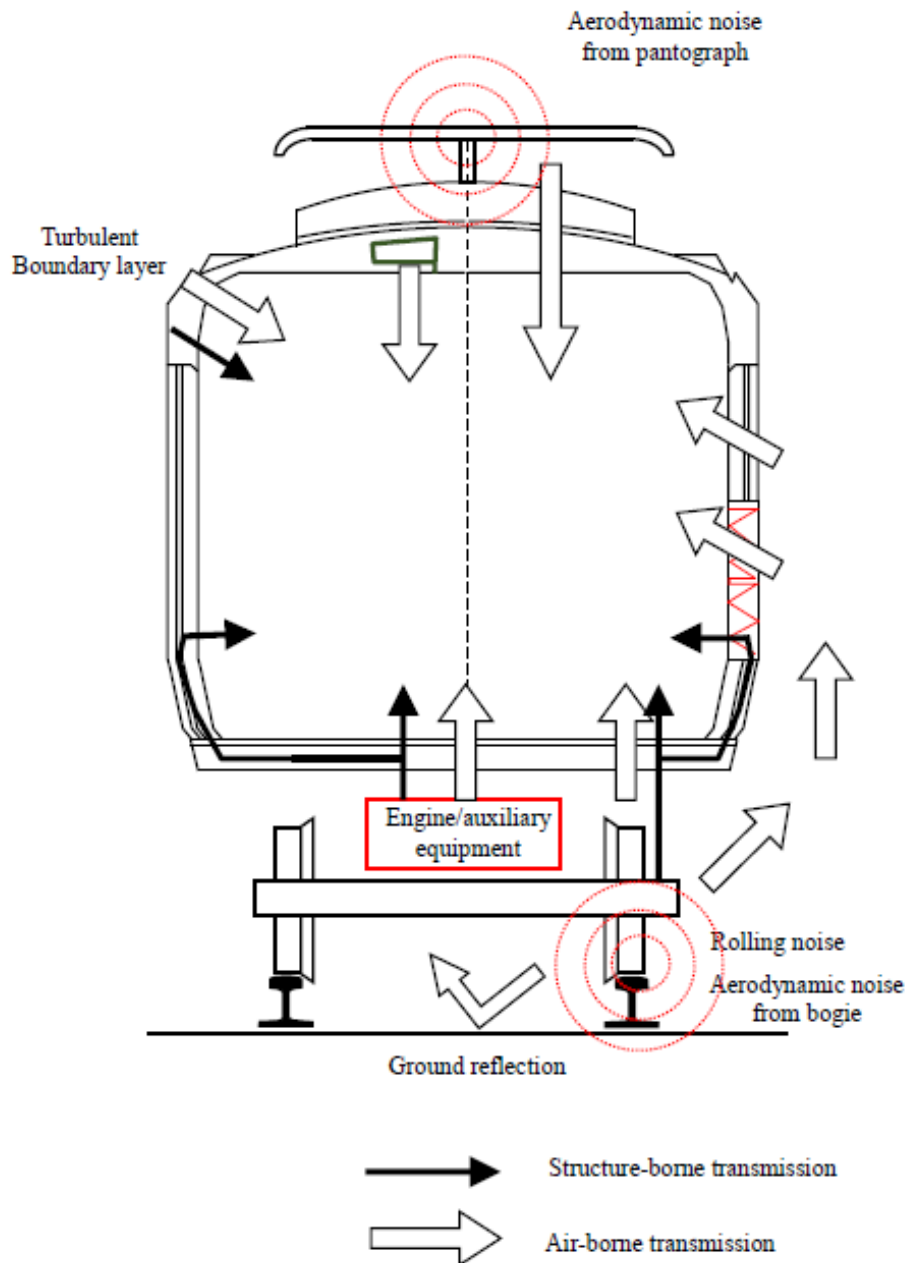
Figure 1.1. Noise source and transmission paths. Adapted from [2].

(2).The sound insulation of the train wall structures may not be sufficient

To achieve a light-weight and high strength train body, the use of extruded aluminium panels for train walls and floors leads to poor sound insulation. An example of an extruded panel used in railway vehicles is shown in Figure 1.2. For noise transmission through panels, including the train wall structures, the paths can be briefly classified into two categories; one is airborne noise and the other is structure-borne noise [4]. For airborne paths, the sound from the exterior noise sources is incident on the train external surfaces, like walls, floors,

etc., and then it is transmitted from the outside to the inside. For structure-borne paths, the mechanical vibration caused by the wheel/rail contact is transmitted through the suspensions and the bogie to the car body, inducing it to vibrate and eventually radiate sound to the internal cabin.

Figure 1.2. Examples of extruded aluminium panels for railway vehicles [5].

To improve the interior acoustic environment, a better understanding of the mechanisms of railway noise sources and the noise transmission paths is required. The motivation of this work is to provide a deeper understanding of the mechanism of the exterior noise sources, the transmission through extruded panels and the interior noise, which will benefit the manufacturer and as well the passengers.

1.2 Research aims and objectives

The aim of this thesis is to develop a comprehensive modelling approach to predict the interior airborne noise of modern railway vehicles, taking into account different noise sources and different transmission paths. Also, it will be necessary to take account of the complexity of the car body structure, the distribution of sound around the outside of the vehicle as well as the interior acoustics of the vehicle. The research objectives are listed as follows:

- To modify / extend an existing 2.5D boundary element (2.5D BE) model to calculate the rolling noise and the sound incident on the train sides and roof due to rolling noise. Rolling noise is generated underneath the train floor and mostly covered by fairing at the train bottom. There is no direct sound incident on the train sides. The 2.5D BE method will be used to calcuate the sound diffraction and scattering.

- To investigate the acoustic environment below the train floor.

- To model the aerodynamic noise from the pantograph using the Computational Fluid Dynamics (CFD) method and to calculate its transmission to the train external surfaces using the 2.5D BE model.

- To develop a relatively efficient and accurate model to predict the sound transmission through the train wall structures. The statistical energy analysis (SEA) method is of high efficiency and the 2.5D coupled finite and boundary element (2.5D FE/BE) method is of high accuracy. Making the use of the 2.5D FE approach to determine the essential parmeters for the SEA model will combine the advantages of the two methods.

- To develop an SEA model to predict noise inside a railway vehicle and to apply the overall framework to a real case for validation.

1.3   Original contributions

The original contributions of this thesis are
- The acoustic environment beneath a railway vehicle is thoroughly investigated. The direct and reverberant sound beneath the train floor and their relative contributions to the total sound power incident on the train floor are quantified.

- An existing 2.5D BE model is applied to a scattering case, in which the ground effect is considered, to model the sound from sources beneath the vehicle incident on the train sidewalls where there is no direct sound impinging.

- Fundamental monopole and dipole sources are implemented in a 2.5D BE model. They are used to model sound from the wheel and the pantograph.

- The influence of flow on the sound transmission is modelled in the 2.5D BE model when investigating the pantograph noise transmission. At low frequency it is modelled by using a uniform mean flow and the results are compared with analytical

results, while at high frequency it is modelled by using an equivalent acoustic wavenumber obtained from the ray tracing model.

- The sound transmission loss of the train wall structures and as well the radiation efficiency are studied by the 2.5D FE/BE approach and also studied by the SEA method with parameters determined by the 2.5D FE models.

- The radiation efficiency of an extruded panel is studied for mechanical excitation at different locations on the panel. The vibrational properties of the extrusion are used to explain the differences in their radiated sound power and radiation efficiencies.

- An interpolation method is developed in the 2.5D BE model. Specifically, the results are calculated in 2D as a function of frequency, and they are mapped and interpolated to the wavenumber domain based on the consistency of wavenumber in the transverse plane.

- Comparisons are made with measurements of noise on the train external surfaces to quantify the relative contributions of the wheel, the rail and the sleeper to the total sound.

1.4 Structure of the thesis

The layout of the thesis is as follows. After the introduction in this chapter, a review of existing research of railway noise, noise transmission through panels and interior noise is first presented in Chapter 2. Chapter 3 explains the noise generation and propagation beneath the train floor. Chapter 4 presents the method to work out the sound distribution on the train side and roof surfaces. Chapter 5 focuses on the noise radiated from the train pantograph and its propagation to the train external surfaces, considering the influence of flow. In Chapter 6 the 2.5D FE/BE method is used to study the noise radiation and transmission through an extruded aluminium panel which is typical of those widely used in railway vehicles. Chapter 7 considers the use of the SEA method for the noise radiation and transmission loss of the same panel, but with essential parameters determined from the 2.5D FE model. Chapter 8 provides a framework to predict the airborne noise inside a railway vehicle using the sound pressure on the train external surfaces calculated from the previous chapters. Chapter 9 gives the main conclusions of this work and recommendations for further work. The TWINS model used to calculate the sound power of rolling noise is presented in the **Appendix A.**

Chapter 1

The field measurements used for validation carried out by Vibratec and Polytechnic University of Valencia (UPV) in the RUN2Rail project are described in the **Appendix B.1** (rolling noise validation) and **Appendix B.2~B.6** (exterior and interior noise measurements).

Chapter 2   Literature review

In order to mitigate and control the interior noise of a railway vehicle, it is first necessary to understand and study the various sources that are generating noise and understand the various noise transmission paths. For train applications wayside noise measurements are sometimes carried out with devices such as a microphone array. It is found that rolling noise is usually the main noise source associated with a railway vehcle [2] and aerodynamic noise can also be important when the speed is high [6, 7], see Figure 2.1. Another aspect that has to be considered in predicting the interior noise is the noise transmission through the train wall structures.

(a)

(b)

(c)
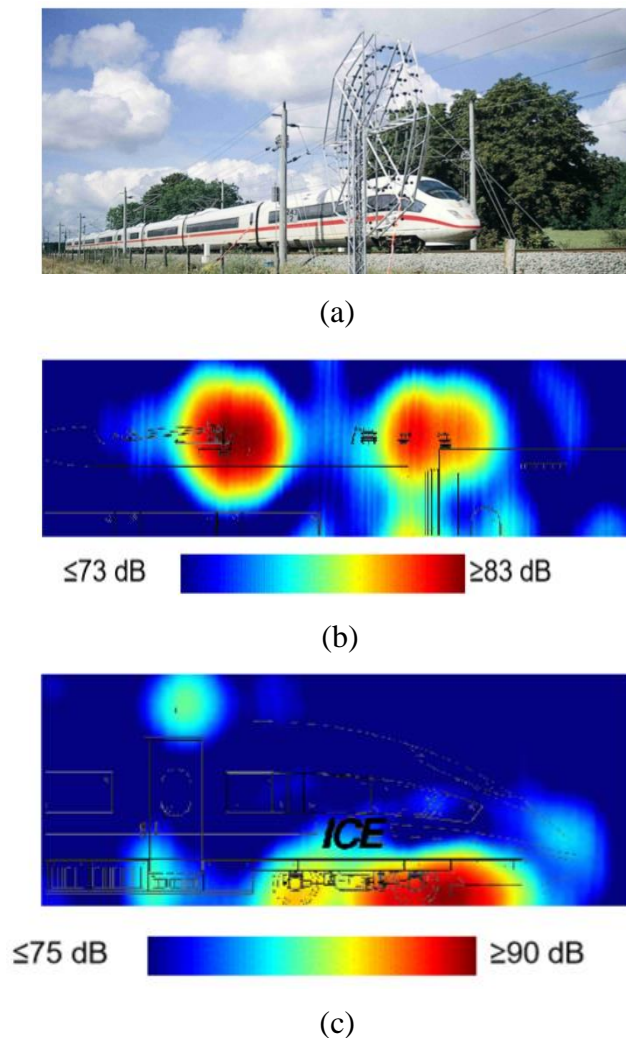
Figure 2.1. Acoustic map obtained during a pass-by measurement of an ICE 3 at a speed of 350 km/h [6]. (a) Acoustic array, (b) noise around the pantograph, (c) noise around the bogie.

Chapter 2

In general, to study the noise sources and the noise diffraction/transmission associated with a railway vehicle, and go further to predict the interior noise, the candidate approaches must comply with three main criteria for successful application in the industrial design process. (1) Accuracy: the candidate methods should be able to predict interior noise for various excitation types, including structural, acoustical, and turbulent boundary layer forces; besides, the prediction should be produced with at least one-third octave band resolution; (2) Computational cost: prediction results should be available in an acceptable amount of time to allow different design solutions to be assessed and compared; (3) Frequency range: potential methods should be functional in a wide frequency range, roughly from 100 Hz to 5 kHz for railway noise.

The above requirements make many traditional approaches unsuitable for application to railway noise, at least not suitable for a wide frequency spectrum solution. For example, the application of traditional FE/BE methods to railway vehicles would be a great challenge because of the frequency range of interest (generally up to 5 kHz) and also because of the typical dimensions of a railway vehicle (roughly $3 \times 3 \times 20$ m^3). An attractive way to deal with noise radiation and transmission through the structure of a railway vehicle at higher frequencies is to use statistical energy analysis (SEA) methods [8] and the waveguide approach [9]. They have many advantages but they also have their own limitations.

In this literature review existing methods, approaches and studies that have been done on the modelling of noise sources (including the rolling noise and the aerodynamic noise), noise transmission and interior noise are reviewed. At the end, by analyzing these different methods, those considered further in this thesis are introduced.

2.1 Review of studies on noise sources

2.1.1 Rolling noise

Rolling noise, including the interaction between the wheel and the track, has been well studied by Thompson in recent decades and validated models exist, such as TWINS [10] in which, the wheel/rail system is excited by the combined roughness of the wheel and rail through a contact spring [2]. Thompson studied the dynamic behaviour based on both theoretical and experimental methods, finding for example that the dynamic behaviour of a railway track in the frequency region 100-5000 Hz is of great importance in relation to the generation of noise by moving trains. The high frequency dynamics of the track at the

excitation point plays an important role in the wheel-rail interaction. The sleeper is the dominant source of noise at low frequency, the rail is dominant between about 500 and 1600 Hz, and at higher frequencies the wheel becomes predominant [2, 11]. One example of the relative sound contributions due to the vibration of the wheels, the rails and the sleepers to the total noise generated in the railway system obtained using the Track-Wheel Interaction Noise Software, TWINS [10, 12] (also in **Appendix A**) is shown in Figure 2.2.
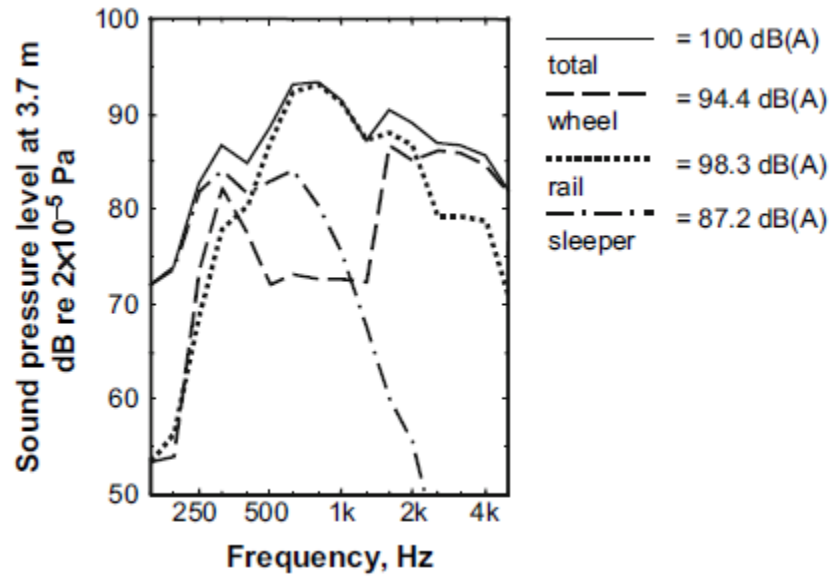
Figure 2.2. Prediction of contribution of rail, sleeper and wheel noise to total noise using the TWINS model [10, 12].

When the rail is excited, various structural waves propagate along it [13]. The noise performance of the track is closely linked to the rate of decay of structural waves along the rail, since it controls the effective radiating length of the rail. Jones et al. [14] pointed out that decay rates could be used as an indicator of the acoustic performance of the track. Jones and his colleagues also proposed a direct and automated method for calculating the decay rates from measurement data.

To investigate sound radiation from waves in rails, two-dimensional models of the rail cross-section are often employed. In [15], Thompson suggested that a two-dimensional model gives satisfactory results for sound radiation for most practical cases, whereas three-dimensional effects need only be considered for frequencies below about 250 Hz. Kitagawa and Thompson [16] modelled the rail vibration as a Timoshenko beam and used an equivalent source model, based on [15], to study the sound radiation from it. Their results

show the direction of sound radiation is determined by the ratio of the wavenumbers in the rail and in air. However, the presence of the vehicle was not considered in any of the studies mentioned here.

In an alternative approach, Nilsson et al. [17] developed a coupled waveguide finite element and boundary element approach (also called a 2.5D FE/BE approach) to predict the noise from railway and tram rails in a two-dimensional (2D) geometrical domain. In that work, the vibration of the rail and the related sound radiation were determined using a 2D model of the cross-section with a spectrum of wavenumber in the third dimension (along the track). The 2.5D method allows a number of the simplifying assumptions in the established methods to be avoided. For example, the deformation of the cross-section of the rail can be considered in the 2.5D model. It also takes advantage of the 2D geometry of a rail to provide an efficient numerical approach but nevertheless takes into account the three-dimensional nature of the vibration and sound field and the infinite extent of the rail. Nilsson et al.[17] used this method to calculate the radiated power of the normal railway rails and the embedded tram rails. The 2.5D method achieved reasonable accuracy. Ryue et al. [18] used the 2.5D FE/BE model to investigate the sound radiation efficiency and directivity of the rail in the presence of a reflective ground. An absorptive ground was modelled by applying impedance boundary conditions at the ground surface to investigate the influence of the ground on the rail noise. For rails attached to a rigid ground or located at a certain distance above it, the influence of the ground was examined in terms of the radiation ratio and longitudinal directivity. It was found out that the presence of the ground and its impedance condition have considerable effects on the level and directivity patterns of the noise radiated from the rail. However, one limitation of the 2.5D method in this case is that the rail is considered to be on a continuous support, whereas it is discretely supported on sleepers in reality. This might cause non-negligible errors when the stiffness of the rail pad is high.

More recent research on railway rolling noise has led to improved models for the track vibration [19] and rail radiation [20]. Zhang et al. [19] recently proposed a model of the vibration of a discretely supported track by using the 2.5D FE method. In their work, the rail was coupled to a finite number of sleepers, by means of an array of springs representing each rail pad, using a receptance coupling method. The sleepers were represented by flexible beams, supported on an elastic foundation. Their results were presented in terms of the point mobility and track decay rate and these were compared with the corresponding field measurements for two tracks, one with soft rail pads and one with stiff rail pads. Very good

agreement was found between the predictions and the measurement results, but this model has not been extended to the noise radiation. Zhang et al. [20] have also extended the sound radiation models used for the railway track to take account of the proximity of the ground by using the boundary element method in 2D. Allowance is made for the effect of wave propagation along the rail by applying a correction in the 2D modelling. It is shown that a correction to the 2D model is necessary at low frequency, for both vertical and lateral motion of an unsupported rail, especially in the vicinity of the corresponding critical frequency. However, for a supported rail no correction is needed to the 2D result for vertical motion while for lateral motion the corresponding correction would depend on the pad stiffness.

Of interest is also the effect of slab track [21, 22] and the influence of the rail fastener stiffness [23]. A Fourier transform-based method has been formulated in reference [21] for calculating the response of a slab track subject to a moving harmonic load. Zhang et al. [22] investigated the differences in the noise radiation characteristics of ballasted and slab tracks. They found that differences were included in the sound radiation of the rails and sleepers due to the presence of absorptive or reflective ground. Li et al. [23] experimentally studied the influence of the fastener stiffness on the rail radiation and its effect on the interior noise inside a railway vehicle.

The acoustic environment beneath the train floor is complicated. When rolling noise is generated, some of this noise is absorbed by the ballast, some propagates away from the vehicle through gaps at the sides, and the rest is incident on the floor. The sound reaching the floor is mostly reflected back beneath the train. The equipment under the train adds additional reflections and scattering and a reverberant sound field can develop beneath the vehicle [24]. This can also be enhanced by the presence of fairings along the sides, which cause further reflections into the region beneath the train. Understanding and improving the acoustic environment beneath the vehicle can help in controlling the airborne component of interior noise that would be transmitted through the train floor as well as the exterior noise.

However, research on the acoustic environment beneath a vehicle is limited. One of the few studies was carried out by Jones et al. [24]. They developed numerical modelling methods to study the acoustical behaviour beneath a railway vehicle with acoustic shields mounted on the train and the track using a combination of SEA and the BE method. As the focus of their work was mainly on the performance of the shields in reducing exterior noise, the distribution of sound incident on the train floor was not studied. Some other researchers have

studied the airborne noise transmission of rolling noise to the vehicle interior, but they did not specifically study the acoustic environment below the vehicle. To obtain the sound pressure incident on the train floor for interior noise prediction, they mainly employed commercial software or measurements [1, 25-27].

2.1.2   Pantograph noise

Although rolling noise is the dominant source over a wide speed range, it is found that the aerodynamic noise associated with trains becomes dominant above a certain speed, which is called the transition speed. Many studies have shown that the transition speed occurs at approximately 300 km/h [3, 28], although it depends on the specific design of train. Modern trains allow operational speeds up to 350 km/h so in such a situation, aerodynamic noise is no doubt significant. The main aerodynamic noise sources identified from different studies on various high-speed trains [29-31] are classified as two groups. One is the noise generated by flow over structural elements like the pantograph and the bogie, etc. [6]. This type of aerodynamic noise source is associated with the surfaces of the structure and cavity flows and the noise has a dipole-like property [32]. The other group of noise sources is generated by turbulent flow, including aerodynamic noise from the nose and rear of the train. The second type of aerodynamic noise source has a quadrupole-like property [32]. Based on the scaling law [33, 34] the sound power of the dipole-like aeroacoustic sources is proportional to the 6th power of the Mach number while for the quadrupole-like sources it is proportional to the 8th power. The Mach number corresponding to the train speed is much smaller than 1 (for instance, the Mach number of a 300 km/h train is 0.24). Besides, the aerodynamic noise from turbulence in railway engineering is mainly broadband while that from the train pantographs and bogies has tonal components with high pitch (depending on the dimensions). Therefore in general the aerodynamic noise from turbulent flow is not as significant as that from the first group in railway engineering.

Aerodynamic noise of the dipole type is generated by unsteady airflows induced by the various structural components, generating both aeolian tone noise and broadband noise [35, 36]. Both the bogies and the pantograph belong in this group and they are strong aerodynamic noise sources. An example of the tonal noise and broadband noise from a Japanese pantograph is shown in Figure 2.3. However, it is difficult to separate the aerodynamic noise of the bogies from the rolling noise. The presence of the ground and other auxiliary equipment around the bogie affects the flow behaviour beneath the train and increases the difficulty to study the aerodynamic noise from the bogie. On the other hand,

pantographs are mounted in cavities on the train roof, which might introduce flow and cavity interaction. Unlike the aerodynamic noise of the bogies, the noise barriers cannot shield the sound from the pantograph. The pantograph will no doubt causes more considerable effect to the environment.

(a)   (b)
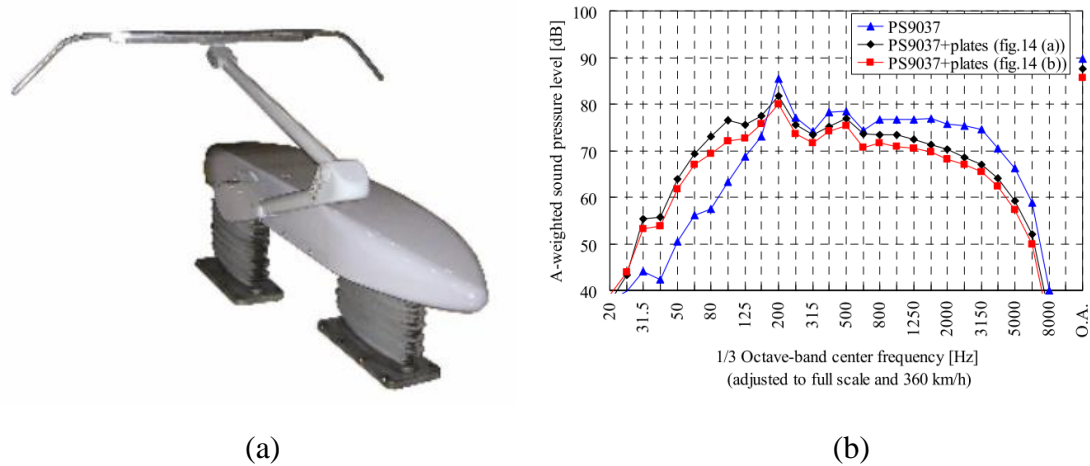
Figure 2.3. (a) Pantograph PS9037, (b) investigation of aero-acoustic noise from pantograph PS9037 with noise control strategies. [36].

In Japan the importance of pantograph noise was noticed in the development of the Shinkansen bullet trains [30]. Many experimental studies and efforts have been made to reduce the pantograph noise of high-speed trains since then, including optimisation of the pantograph to achieve low noise radiation [30, 35, 36] and adding more effective shape of noise insulation plates on the roof [36]. A multi-segment slider was attached to the low-noise pantographs to collect current, in turn contributing to the reduction of the pantograph peak noise levels [36]. Besides, porous materials [37] and flow control technology [38] for the reduction of pantograph noise were studied. To identify the relative contributions of each part to the whole pantograph in terms of sound power, Grosche and Meier [39] measured the noise from a full-scale DSA pantograph using acoustic mirrors in a wind tunnel. They found that the panhead, the knee joint and the foot region are significant noise sources.

Latorre et al. [40] experimentally studied the noise from a single component of a pantograph. In order to gain a better understanding of the aeroacoustic characteristics of the pantograph arms which are inclined to the airflow, Latorre et al. assessed the dependence of the noise on the yaw angle, flow speed, cross-sectional shape, angle of attack and radiation angle (directivity). They found that the amplitude and frequency of the vortex shedding noise decrease with increasing yaw angle. The relative bandwidth of the vortex shedding peak was

13

found to increase with the yaw angle for all the cylinder cross-sections considered except for the elliptical cylinders. They also noticed that the cross-sectional shape of the cylinder affects the frequency, amplitude and speed dependence of the vortex shedding noise. A square cylinder was found to be the noisiest and elliptical cylinders the quietest.

Explaining the mechanism of the aerodynamic noise from the pantograph becomes possible after Curle [32] extended Lighthill's acoustical analogy [33] to noise generation in the flow with the presence of stationary solid boundaries. This was later extended to moving surfaces by Ffowcs Williams and Hawkings [41], who showed the existence of monopole and dipole-like noise sources on the structure surfaces. In company with the development of computer science and advanced turbulence models such as the large eddy simulation (LES) [42] and detached eddy simulation (DES) [43], computational aeroacoustics (CAA) became possible, but due to the complexity of the geometry and the flow, it is extremely time consuming to perform a detailed aerodynamic noise simulation for a full-scale pantograph. Even though Lei, et al. [44] for example have numerically studied a full pantograph in considerable detail, the CFD techniques they used to obtain the noise sources are based on the Reynolds Averaged Navier-Stokes (RANS) model, which is not sufficient to capture the small turbulent structures that are expected to be important for aerodynamic noise.

Liu et al. [45] numerically studied the noise from individual cylinders representing pantograph components. They proposed the idea that by adding spanwise waviness to square bars, the aerodynamic noise can be dramatically reduced, see Figure 2.4. They showed that a straight square bar in cross-flow produces strong tonal noise associated with the vortex shedding. When they introduced waviness along the bar span they found that when the wave amplitude is nearly half the bar width, a large noise reduction of as much as 30 dB is achieved from both numerical simulations and measurements, including a 10 dB reduction in the broadband level. Through analysis of the flow features, they explained the reasons that had led to the reduction of the noise. With increased wave amplitudes along the bar, the spanwise flow becomes significant and strong crossflow vortices develop in the near wake which effectively suppress the primary vortex shedding. This reduces the noise level significantly, especially the tonal noise associated with the vortex shedding.
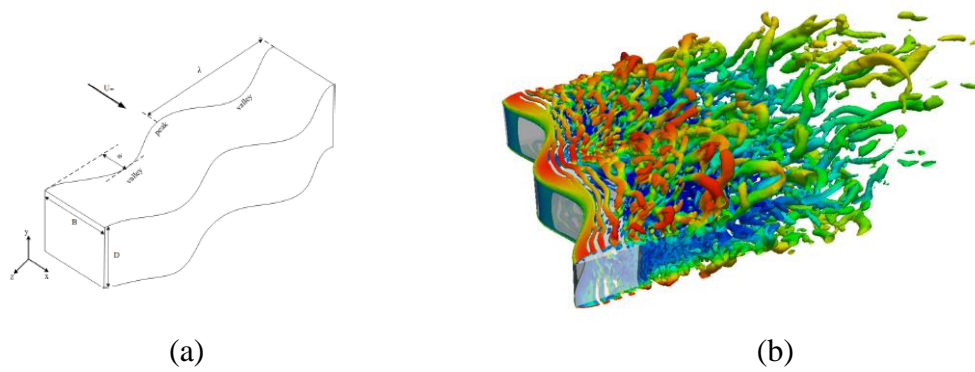
Figure 2.4. (a) Definition of wavy bar geometry, (b) the vortex behind the wavy bar [45].

To predict noise from complex structures, a semi-empirical approach has been proposed, which is called the component-based approach. The component-based approach was first derived particularly for predicting aircraft landing gear noise [46]. Because it has been found effective in practical applications, later it was employed to predict the train pantograph noise by Behr, et al. [47]. Latorre et al. [48] used this approach to predict the aerodynamic noise of a high-speed train pantograph. They initially used empirical constants obtained from existing noise measurements from full-scale pantographs to calibrate the spectral shape and amplitude for each group of components. A good agreement between the experimental results and the predictions was obtained in terms of overall noise level but the measured spectral shape was governed by individual peaks that were not reproduced by the model. Latorre et al. [49] and Liu et al. [50] then developed a more detailed model where each strut of the pantograph was modelled using existing experimental data for various aerodynamic parameters of cylinders with different cross-sections in an air flow, such as the Strouhal number, fluctuating lift coefficient and correlation length. Besides, the spectral shape, the effect of the inclination of each of the struts (the yaw angle), and the influence from cross-section and the incoming flow turbulence intensity, etc were used to adjust the results for different situations. Now the component-based approach has a good agreement with the measurement in terms of sound pressure prediction from a pantograph. However, one drawback of this approach is it needs to be calibrated by using a database of experimental or numerical results and the prediction is limited to the range of that database. Moreover, flow interactions are neglected which can be important in some situations.

From these above contributions, the sound pressure from a pantograph can be predicted well using the existing models. To study how the pantograph noise contributes to the train interior noise and affects train crew and passengers' comfort, there is a lack of study of the transmission of sound from the pantograph to the train external surfaces. Previously, the

boundary element method has been adopted to investigate the sound field around a pantograph using a commercial software [44], but in this approach it is difficult to handle high frequencies and large structures. Moreover, the influence of flow on sound propagation was not considered. An efficient and reliable method for predicting noise propagation from the pantograph to the train external surfaces is therefore required.

2.2   Review of studies on extruded panel

Noise transmission through panels has been studied for many years, particularly in the field of building acoustics. For a single homogeneous panel, the sound transmission loss (STL) can be theorectically expressed and described by the mass law region, the damping-controlled region and the stiffness-controlled region [51]. If the properties of the panel are known, the sound transmission loss can be obtained straightforwardly. Unfortunately, the principle for noise transmission through a single homogeneous panel can only be applied to train wall structures (an example is shown at Figure 1.2) at low frequencies where there are no local modes of the wall structure because in that frequency region, the train wall structures can be considered as a uniform single panel [5].

There are many studies on sound transmission and insulation of double panels. Different existing models are avaliable. Hongisto et. al [52] listed seventeen existing prediction models for double panels and gave a qualitative and quantitative comparison of them. In his work, a quantitative comparison betweens models was made in four groups and compared with measurement data containing altogether 52 laboratory tests for double walls. They pointed out that those models work for particular cases and the most accurate model should be selected according to the type of the double wall. The models for double walls can be used for the train windows because they are often made of two layers of glass. Zhang et al. [53] investigated the noise transmission through a high speed train window by using a double layer panel model. The theoretical results agreed well with the measurements.

However, the train wall structures are more complicated than double walls. They are often made of extruded aluminium panels with stiffners in the middle and beams on the two sides. Theoretical study of the transmission loss of these extruded panels will be difficult. Various strategies have been presented for noise transmission through train wall structures such as the SEA method [54] and the 2.5D FE/BE approach [55, 56]. The SEA method can give understanding of how the energy flows through the complex wall structure of a train with high efficiency, which is beneficial at the design stage. The 2.5D FE/BE approach is more

accurate and gives a deeper understanding of the mechanism of noise transmission through complex walls. Both approaches can be used for both the airborne and the structure-borne paths.

An example of applying SEA methods for modelling structures made from extruded panels was presented by Geissler and Neumann [57]. In their study, the profiles were modelled as either sandwich or orthotropic panels. Commercial software Auto-SEA was used in their research and not many details were given. Later, Brühl et al. [58] applied both a sandwich representation and a more detailed model for their analysis in the Auto-SEA software. The authors used SEA without any comparison with measurements. Xie et al. [55] used the SEA method to predict the vibro-acoustic behaviour of aluminium extrusions. In their study, an extruded panel was represented by a single global mode subsystem and three subsystems representing the local modes of the various strips which occur for frequencies typically above 500 Hz. To calculate the modal density and radiation efficiency, an approximate model for the modal density of extruded panels was developed [59] and verified by using FE calculations. Besides, the formula for modal average radiation of a lightly damped plate produced by Maidanik [59] was slightly modified to give a better estimation for long thin strips [60]. Xie et al.'s SEA model gave good prediction of the panel vibration levels but there were some differences with the experimental data in terms of sound radiation efficiency. Zhang et al. [27] used the SEA method to analyse the noise transmission through train wall structures and the contributions of high-speed train interior noise. In their research, a full vehicle model was created in the commercial software 'VA One', including many details such as windows, passenger seats and interior panels, and windshields on the two ends of the coach. The noise sources included bogie area noise, car-body structural vibration, noise from auxiliary equipment and aerodynamic noise from the pantograph and others. All these sources were characterised by measurements. In their SEA model, the train wall structures were modelled very simply by using a thin plate instead of a combination of strips and stiffeners. The wall structure's radiation ratio and sound transmission loss were obtained by measurements. Their SEA model gave a good agreement with the measured data. However, their SEA model does not give insight into the mechanism of noise transmission through the train wall structures, and the conclusions obtained are not sufficiently general to be easily applicable in practice.

The waveguide approach, also known as the 2.5D method, has been developed and applied to noise transmission through extruded panels using a coupled 2.5D FE/BE method by

Nilsson et al. [55, 56]. This 2.5D method is promising to study noise transmission through waveguide structures (with uniform properties in one direction) with complex cross sections. It only considers the cross-section of the structure by considering the third direction in terms of a spectrum of wavenumbers, which will greatly reduce the computational time compared with their corresponding 3D numerical models. Besides, it gives the vibrational behaviour of the structures which could explain the vibro-acoustic performance. The 2.5D method has been applied in the literature to study a variety of problems successfully, including composite plates [61], thin-walled beams [62], rib-stiffened plates [63], and extrusions [64, 65].

Numerical predictions by means of 2.5D FE/BE methods were made to predict the sound radiation efficiency and sound transmission loss of train wall structures well [55, 56]. Calculated results indicate good agreement with measurements as well as providing means that aid interpretation of the physics of the system. Kim et al. [64, 65] also predicted the radiation efficiency from and sound transmission through a complex extruded panel using the 2.5D FE/BE method. Part of an actual train wall structure was studied. It consisted of a 1 m wide and infinitely long extruded panel and included stiffeners, beams and a stiff rubber layer on the receiving side. The predicted radiation ratio and sound transmission loss agreed well with measured results at high frequency. Some differences in the sound transmission loss appeared at low frequency in reference [65] and were believed to be caused by the differences in the boundary condition. In their experiments, the extrusion was 1.5 m long and its boundary was approximately clamped, whereas, in their numerical models, the extrusion was infinitely long and simply supported at the ends and sides. After applying a window the agreement at low frequency improved [66]. Zhang et al. [66] used coupled 2.5D FE/BE to study the acoustic performance of extruded panels in order to determine the sound transmission loss. In their studies, an extensive parametric study was carried out to investigate the effect of different reinforcement rib styles on the sound transmission loss (STL). The effect of using extruded panels with rectangular, triangular and trapezoidal truss-core sections was studied in detail. They found out that the number of bays in a given width has a great influence on the sound insulation, and structures with better STL usually have fewer free wavenumbers below the acoustic wavenumber.

Previous research has shown that the 2.5D FE/BE method is suitable for acoustical modelling of extruded panels. However, in Kim's model [64, 65], the width of the extruded cross section was only 1 m. The total number of degrees of freedom in that model were 1364

including 1012 for FEs and 352 for BEs. To represent the whole train cross-section, a much larger number of elements would need to be used. This increases the difficulties in creating the model and increases the computational time significantly as well. Moreover, it is not suitable to use the 2.5D FE/BE method in the early design stage as it is not flexible to handle design changes.

Compared with the SEA method, the 2.5D FE/BE method is computationally expensive and it is not flexible to handle design changes. However, the SEA method has its own drawbacks, such as the difficulties to derive the essential parameters for a complicated structure. The 2.5D FE/BE method is able to calculate the dynamic response of the extrusions, which is used to derive the SEA parameters, and the 2.5D FE/BE method can also predict the sound radiation ratio and transmission loss with a good quality [64, 65], which can be used to validate the SEA model.

Orrenius et al. [5] modelled the acoustic transmission through extruded profiles of railway vehicles by using SEA combined with the 2.5D FE/BE method. In their SEA model, at low frequency, an equivalent plate was used to represent the extrusion by assuming that the orthotropic properties of the extrusion are not significant for its sound reduction, while above the cut on frequency of local modes (modes of attached strips), these were included in the model. Orrenius et al.'s method gave an good prediction of sound reduction through a floating floor, but their SEA model is complicated and the vibrational levels of the panel were not well estimated.

In recent years, new strategies for predicting the noise transmission through extruded walls with the influence of mean flow on the outer surface [67] and including porous materials [68] have also been developed. All these have increased the understanding of how sound is transmitted through complicated extruded structures that are commonly used in trains or aeroplanes. However, as well as the sound transmission through the walls that are enclosing the interior of a vehicle, it is necessary to know the distribution of sound pressure on the exterior surfaces of the vehicle to be able to predict the interior noise.

2.3   Review of studies of the interior noise

The noise inside railway vehicles is an important aspect of passenger comfort. Noise from various sources is transmitted into the vehicle by both airborne and structure-borne paths [2, 4]. For the airborne paths, the sound field beneath the vehicle is important in determining

the sound incident on the floor. Besides, the gangway region often has poor sound insulation so that the sound incident on the gangway region may contribute importantly to the interior noise. The noise incident on the side surfaces of the train is also important. For structure-borne paths, the vibration transmitted from the rail/wheel region to the bogie and then to the train body needs to be considered.

Established approaches that can be used to predicted train interior noise are summarised in [26]. The FE/BE method can be used at low frequency, hybrid FE-SEA approach at medium frequency and SEA at high frequency. Kim and Ih [69] employed the FE/BE method to study noise in an enclosed space at low frequency. The vibrational velocity, sound pressure, and acoustic power on the vibrating boundary comprising an enclosed space were reconstructed by the boundary element method. A half-scaled automotive cabin was considered as an example for validating and demonstrating the proposed reconstruction process. It was noted that the method they used can improve the resolution of the reconstructed field; thus vibro-acoustic parameters of the vibrating boundary can be estimated with reasonably good precision. Shorter et al. [70] provided a qualitative definition of the mid-frequency problem and suggested that a statistical description of the local dynamic properties of a system is an essential element of any mid-frequency prediction method. A hybrid approach to the mid-frequency problem was described in [70] which employs a statistical description of the local modal properties of various subsystems in a system. Experimental investigations of the spatial statistics of a frame-panel structure were presented and measurements of the acoustic power radiated by the structure were compared with numerical predictions. Reasonable agreement was found. Application of SEA to solve interior problems is common [71-73]. For instance, Sadri et al. [72] used the SEA model to predicted the noise inside a passenger vehicle, see Figure 2.5. The use of the SEA method to predict noise inside a railway vehicle has its advantages because the train cabin is very large. Even at relatively low frequency, there are a large number of acoustic modes involved in the train cabin. SEA has the reputation of solving problems associated with large structures, with little computational effort. It has been used by many researchers to investigate the sound distribution in the train cabin.
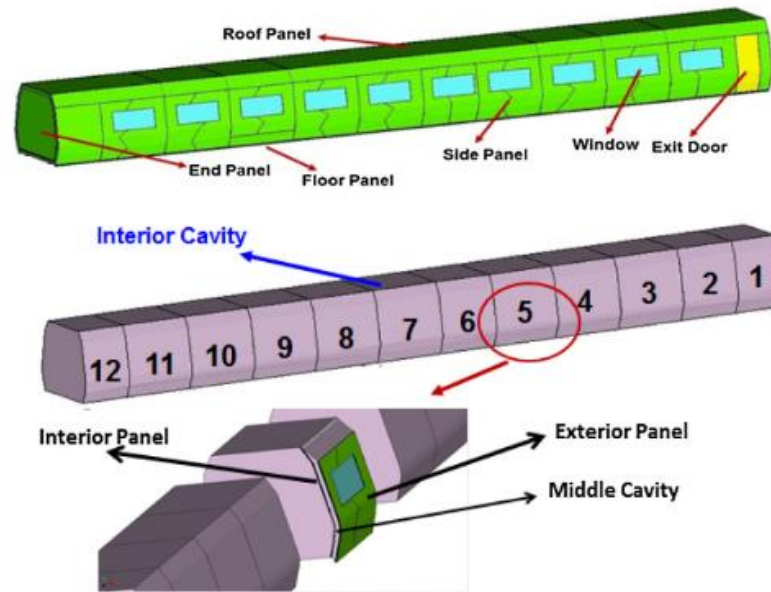
Figure 2.5. SEA model developed by Sadri et al. for a passenger vehicle [72].

Forssén et al. [73] employed an SEA model to predict the noise inside a 1:5 scale railway vehicle for the whole frequency range of interest by subdividing it into five coupled subsystems. As the usual SEA solution only gives the average energy of each system, in their work the spatial decay within a subsystem was adjusted using formulas from the literature on sound decay in corridors. They analysed the sound in the vehicle in the one-third octave bands between 125 and 4000 Hz (at full scale). The SEA predicted sound pressure levels in the train cabin along its axis were in reasonable agreement with the measured results at most frequencies. Forssén et al. [73] adopted noise sources located inside the train whereas the most important noise sources located outside were not considered.

Zheng et al. [26] proposed a statistical energy flow method to predict the full spectrum sound inside a railway vehicle. Their models included most rolling noise and aerodynamic noise. Due to the large size of the train and the complexity of the source modelling, they modelled the interior noise at low, by using finite element analysis (FEA) or boundary element analysis (BEA), at medium frequencies by using a hybrid finite element analysis-statistical energy analysis (FE-SEA) and at high frequencies by using statistical energy analysis (SEA). Rigid multi-body dynamics, fast multi-pole BEA, and large-eddy simulation with indirect boundary element analysis were first employed to extract the multi-physical-field excitations, which include the wheel/rail interaction forces and the secondary suspension forces, the wheel/rail rolling noise, and aerodynamic noise. A model of a fully-trimmed FE carriage was constructed to validate the model shapes and acoustic excitations. The combination of models and methods were coupled with the statistical acoustic energy flow method that they

proposed in [26] to predict the interior noise. The predictions had good agreements with measured data with differences less than 3 dB in terms of overall sound pressure levels. When Zheng et al. modelled the rolling noise and aerodynamic noise sources and their sound power incident on the train external surfaces, full-scale 3D models were created, thus leading to very large computational times. The strength of the noise sources and the transmission from the sources to the train walls were obtained mainly from measurements or from commercial software simulations based on boundary element analysis or computational fluid dynamics; however, the details of the modelling strategies of the sources were not given in detail. Zhang et al. [27] used an SEA model to study the train interior noise based on experimental or estimated parameters, including the sound transmission loss, modal densities, damping and coupling loss factors. They analysed the contributions from factors such as the vibration of sidewalls, the sources in the bogie area, and the transmission loss of the floor. They found bogie area noise has a greater effect on interior noise than aerodynamic noise. The results from their SEA model were in good agreement with experimental measurements. Kohrs et al. [74] compared different approaches and methods, including BEM, ray tracing and SEA to calculate the pressure field around the car body for either artificial sources or real operation in free field and in tunnel. Acceptable accuracy was achieved although various simplifications and assumptions had to be made and there were uncertainties in the various parameters involved. Apart from those predictive methodology, Deng et al. [75] investigated the sound absorption seats in high speed trains. Seats that made of high-performance absorbing materials were designed and installed in high speed trains for reducing interior noise. The test results showed that the installation of the sound absorption seats decreased the noise level at the standard point in the passenger compartment by 1.5 dB compared with the train equipped with normal seats.

Even though the SEA approach has shown its advantage for predicting the interior noise, there are some problems in using SEA to model acoustic environments that are extended in one or more dimension, such as a train cabin or the region below the floor. Fahy [76] noted that the SEA assumption of 'weak coupling' would not be valid for two coupled cavity subsystems without any impedance mismatch at the open boundary between them. However, he suggested that if the sound field within a vehicle compartment approximates to a diffuse field in the 'mid-frequency' range, it could nevertheless be acceptable to divide the enclosed air volume into arbitrarily small subsystems. Jang and Hopkins [77] compared an SEA model and ray tracing model for the prediction of sound transmission in long spaces with a point source at one end. They showed that predictive SEA that includes only direct coupling

between subsystems tends to over-predict the decrease in sound pressure level compared with the results of ray tracing at low frequency while under-predicting it at high frequency. However, if SEA is used with modified coupling loss factors that include indirect coupling it can give good agreement with ray tracing model.

Different from the traditional methods mentioned above, Orrenius et al. [78] compared the 2.5D FE/BE method and the periodic cell method in which a small finite element model of a periodic cell is used to create an infinite structure when determining the sound transmission loss of composite sandwich structures for interior noise prediction. They showed that the 2.5D method gave better prediction of sound transmission loss below 500 Hz than the periodic cell method while the periodic cell method is more efficient than the 2.5D method. In the same reference, Orrenius et al. also used the 2.5D FE/BE method to predict the noise inside a train cabin, see Figure 2.6. They obtained the cross-section of the train and generated 2D geometry with thick plate elements for the structure which is coupled with fluid elements in the cabin. They compared the numbers of degrees of freedom (DOF) and efficiency of the 2.5D model and the corresponding 3D model with a length of 4 m in the third direction. These had 15000 DOFs and three million DOFs respectively. A direct calculation with 3 million DOFs under the excitation of hundreds of incident angles of sound waves in a wide frequency range is hardly possible, whereas with the 2.5D model it is achievable with high efficiency. Even though there is no data to validate their 2.5D FE/BE model, it shows the efficiency of the method for structures that can be approximated by extruding a representative cross-section, of e.g. a railway vehicle. However, they did not consider the actual noise sources associated with a railway vehicle. In their work, only plane waves were considered as the acoustic excitation.
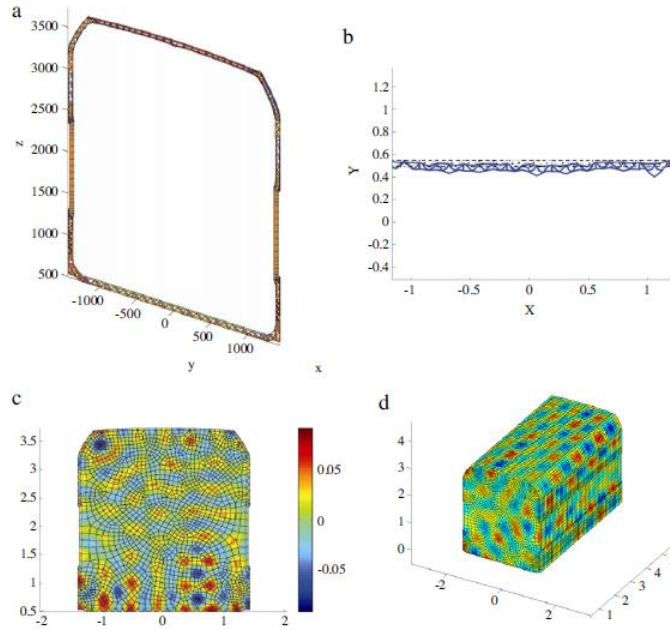
Figure 2.6. 2.5D FEM calculation of a train car-body section excited by an oblique incident plane wave. (a) Mesh of the railway car cross-section; (b) deformation of the panel at 900 Hz; (c) pressure field at $x = 1$ m at 900 Hz; (d) interior pressure field at 900 Hz. [78].

For both the traditional methods like the SEA, FE/BEM and the recently developed 2.5D approach, one of the main challenges is a correct prediction of the external noise sources and the sound incident on the train external surfaces. When Zheng et al. [26] modelled the rolling noise and aerodynamic noise sources and their sound power incident on the train external surfaces, full-scale 3D models were created, thus greatly increasing computational times. Bistagnino et al. [79] adopted a Fast Multipole BEM and Beam-tracing technique to predict the sound pressure on the train walls due to rolling noise, but the noise source was simplified as a point source with measured strength beneath the train, which is not able to precisely predict the noise from the rail and sleepers. To develop a comprehensive modelling approach for the interior airborne noise of modern railway vehicles is the aim of the thesis.

2.4   Summary

To predict the noise inside a railway vehicle, various existing models are avaliable, for instance, the FE/BE method and SEA approach. They can be successfully used for a particular frequency range. Besides, the 2.5D FE/BE coupled method can also predict the interior noise for a wide frequency range. However, a big challenge in the process to predict the noise inside a railway vehicle is to model the exterior noise sources and their transmission through the train wall structures.

Rolling noise has been well studied and the mechanism of the noise generation from wheel/rail interaction is relatively clear. Established models based on those understanding and knowledge are able to predict the rolling noise precisely. However, the sound environment beneath the train floor and the sound incident on the train side surfaces have not been studied in as much detail. One reason is because of the complexity of the configuration of the train floor due to the equipment mounted on it, the acoustical behaviour beneath the train floor is not easy. Another reason maybe thanks to the development of commercial software, which can be used to obtain the results directly, so the mechanism of this part is ignored by researchers. As a consequence, the existing approaches in the literature are either computationally expensive or over-simplified, for instance, the rolling noise was very simplified by a point source with measured sound power in [79].

The aerodynamic noise from the bogie is not easy to separate from the rolling noise experimentally. The aerodynamic noise from the pantograph has been extensively studied. Computational fluid dynamics with the component based approach can be used to predict the far field sound pressure and total sound power of the pantograph with reasonable accuracy. Like the rolling noise, however, the sound transmission from the pantograph to the train external surfaces is lacking investigation, especially when flow is present. No relevant research or understanding is available on this.

Besides, more work is needed to investigate the vibro-acoustic performance of the train floor and wall structures and to model their sound radiation efficiency governing the sound due to structural excitation, and sound transmission loss governing the air-borne sound transmission from exterior sources to the interior. Predictive models like SEA, ray tracing, FE/BE method can be successfully used in a certain range of frequency to predict the interior noise in a railway vehicle, but they can be more accurate to predict the interior noise if they are connected to the exterior excitation.

In this thesis, a combination of existing methods will be adopted and used to predict the noise inside a railway vehicle. These methods are chosen based on the overall consideration of accuracy, efficiency and convenience. The equivalent source model [16] and the SEA method are used to calculate the noise beneath the train floor to handle the complexity of the configuration of the auxiliary equipment. The 2.5D BE method is introduced with the aim of predicting the sound pressure on the train external surfaces due to rolling noise to achieve the accuracy and efficiency in comparison with the SEA and the FE/BE method. The CFD

method and the component based approach are employed to calculate the noise from the pantograph and the 2.5D BE method and the raying tracing method are used to model its transmission to the train external surfaces. An SEA model with parameters determined by the 2.5D FE model is used to investigate the noise transmission through the train wall structures with the purpose of improved efficiency and easy modification of the model at an early design stage. All the studies of exterior noise and transmission will benefit the internal SEA model in predicting the interior noise inside the railway vehicle.

Chapter 3 Rolling noise on train floor

The noise inside railway vehicles is an important aspect of passenger comfort. Noise from various sources beneath the train floor is transmitted into the vehicle by both airborne and structure-borne paths [2, 4]. For the airborne paths, the sound field beneath the vehicle is important in determining the sound incident on the floor. One of the most important noise sources in this region is the rolling noise radiated by the wheels and track.

When rolling noise is generated, some of the noise below the vehicle is absorbed by the ballast, some propagates away from the vehicle through gaps at the sides, and the rest is incident on the floor. Because the floor is nearly rigid, the sound reaching the floor is mostly reflected back underneath the train. It is common that auxiliary equipment is mounted under the train floor, see Figure 3.1.
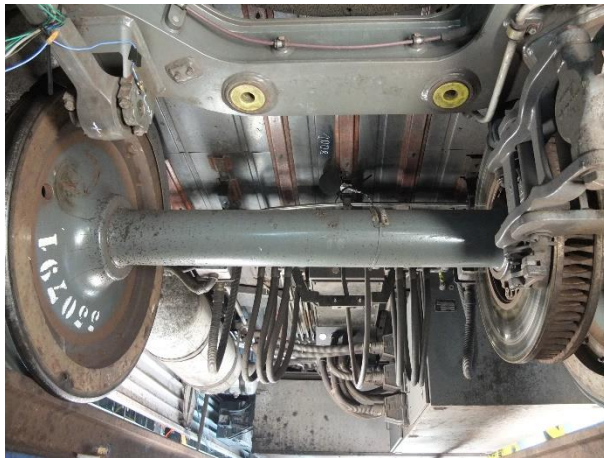
Figure 3.1. View from below of a train floor. Photo provided by Vibratec.

The equipment under the train adds additional reflection and scattering and a reverberant sound field can be developed underneath the vehicle [24]. This is illustrated in Figure 3.2(a) and Figure 3.2(b). This can also be enhanced by the presence of fairings along the underside of the vehicle, which cause further reflections into the region, leading to a stronger reverberant volume beneath the train, see Figure 3.2(c).
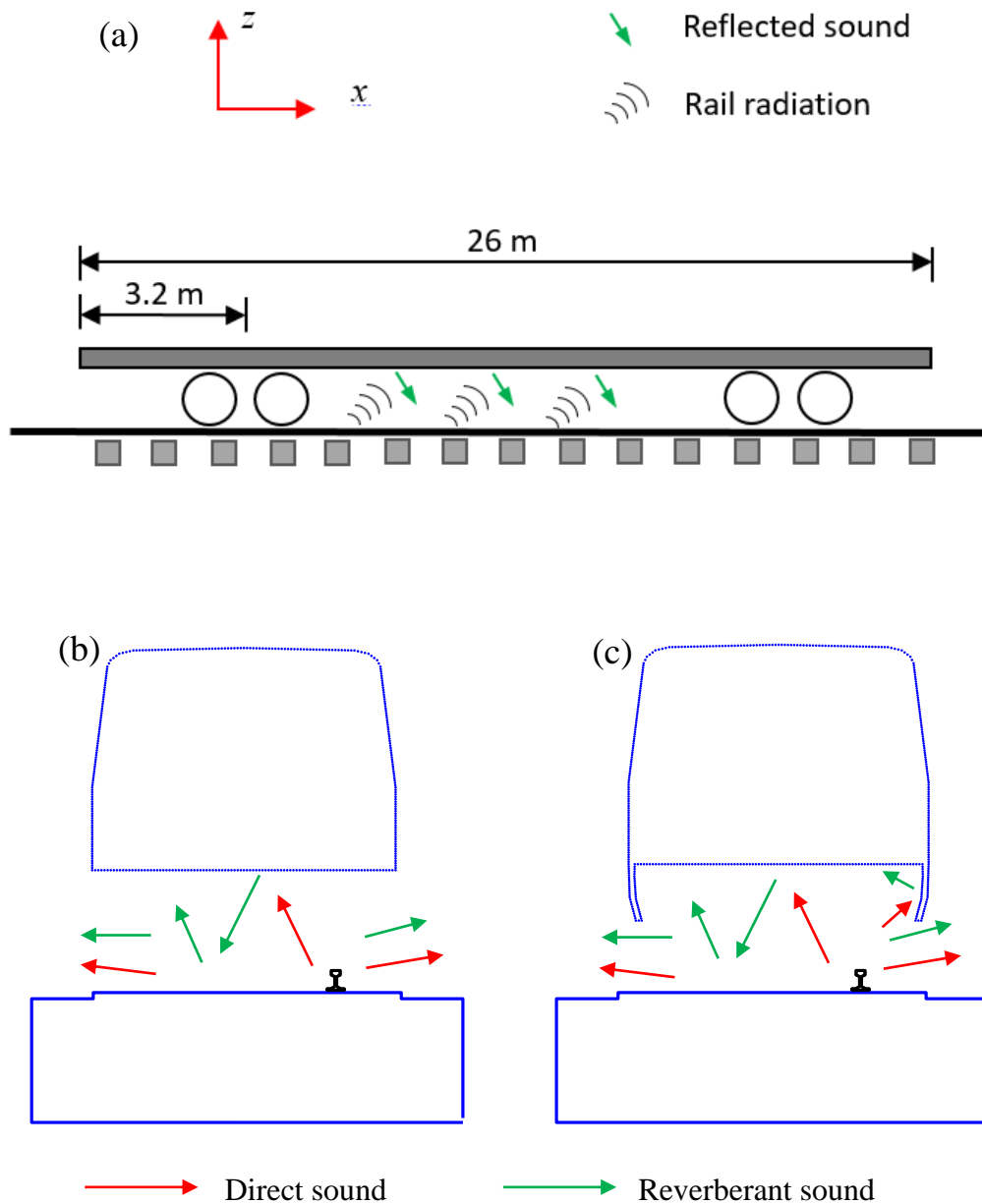
Figure 3.2. Sound reflection and absorption below the train. (a) reverberant sound field below the vehicle (side view), (b) end view, (c) end view with fairing.

Understanding and improving the acoustic environment beneath the vehicle can help in controlling the airborne component of interior noise that would be transmitted through the train floor as well as the exterior noise. To achieve this goal, this chapter builds upon existing knowledge for rolling noise modelling and proposes a method to predict the sound field under the train floor. Jones et al. [24] assumed that the sound beneath a train is composed of a direct and a reverberant part. The same assumption is used in this work. Equivalent sources [16] will be used to study the direct sound due to the wheel, the rail and the sleepers. The

SEA method can be adopted to study the noise in regions of space characterised by a diffuse field.

3.1   Sound power of the rolling noise

The prediction presented in this section is carried out for an example wheel with a straight web and radius 0.435 m running on a typical ballasted track fitted with a UIC 60 rail. The rail pads have a vertical dynamic stiffness of 100 MN/m, and lateral dynamic stiffness of 13 MN/m, corresponding to a relatively soft support. A typical measured rail roughness spectrum is used in the TWINS model [10] to predict the sound power. A summary of the theory in TWINS can also be found in **Appendix A**. The main parameters of the wheelset are listed below in Table 3.1 and those for the track in Table 3.2.

Table 3.1. Parameters used to represent the wheel.

Wheel radius	0.435 m
Width of tyre	0.135 m
Width of web	0.032 m
Tyre inner radius	0.36 m
Hub radius	0.135 m
Wheelset gauge	1.5 m
Wheelset mass	1100 kg

Table 3.2. Parameters used to represent a railway track (UIC60).

	Vertical	Lateral
Rail bending stiffness (Nm^2)	6.42×10^6	1.07×10^6
Rail shear coefficient	0.4	0.4
Rail damping loss factor	0.02	0.02
Mass per length (kg/m)	60	
Pad stiffness (N/m)	100×10^6	13×10^6
Pad loss factor	0.2	0.2
Sleeper mass (half, kg)	140	
Distance between sleepers (m)	0.6	
Ballast stiffness (N/m)	200×10^6	35×10^6
Ballast damping loss factor	1.0	2.0

The roughness of the rail that is used is based on previous measurements at Fishbourne in the UK, and is shown in Figure 3.3.
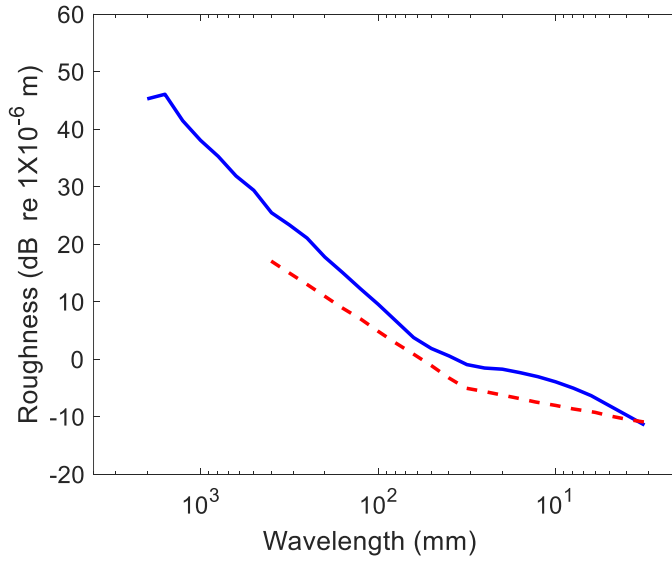
Figure 3.3. Roughness spectrum on the running surface of the rail. ——: Fishbourne measurements; - - -: ISO 3095:2013 limit curve [80].

Based on these parameters, the sound power predicted using the TWINS model is shown in Figure 3.4. These results are for a single wheel and the corresponding track vibration (one rail). Due to the soft rail pads, the rail is the largest source of sound power and dominates the spectrum from the 315 Hz band to the 2 kHz band. Below this frequency range the sleeper is the most important source while the wheel becomes significant at high frequency [10].
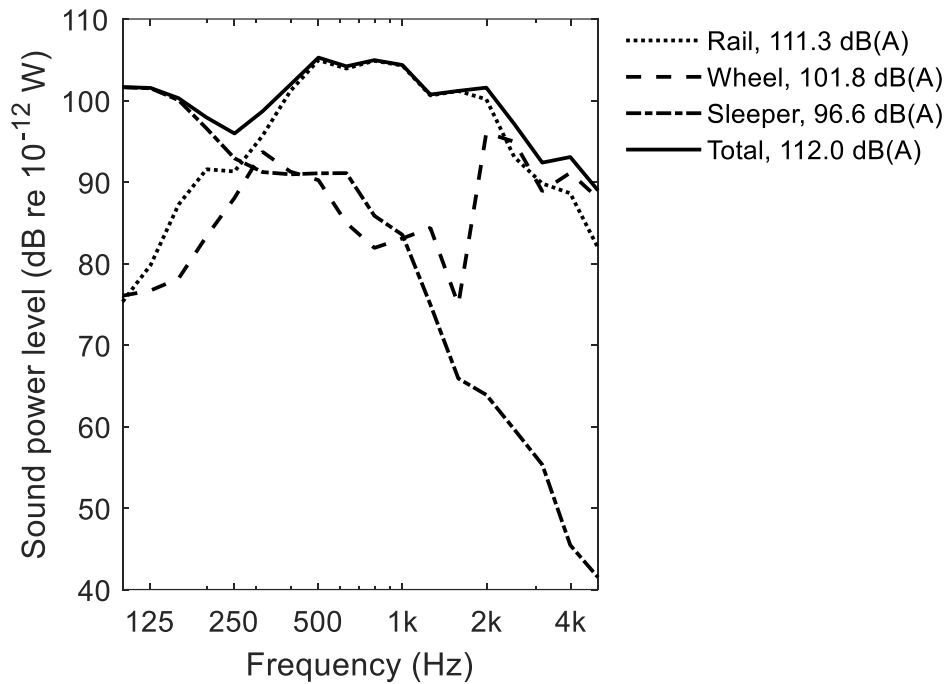
Figure 3.4. Sound power of rolling noise obtained from TWINS model based on parameters from Tables 3.1 and 3.2.

In the modelling approach outlined below, the procedure is based on the sound power from a single wheel and the corresponding track vibration as shown here. The total contribution from all the wheels in a vehicle can be obtained by combining the results for different wheels assuming they are incoherent sources [81].

After the sound power of rolling noise have been derived, the next step is to derive the sound pressure on the train floor due to rolling noise. The direct component and the reverberant part will be discussed separately.

3.2   Direct sound

3.2.1   Modelling wheel noise by using point sources model

The sound power from the wheel can be divided into components associated with its radial and axial vibration. Generally, for the radial direction, the sound pressure field around the wheel can be adequately approximated by an omni-directional source, whereas, for the axial motion of the wheel, a dipole approximation is more reasonable [2]. Therefore, a monopole and a lateral dipole are used to model the directivity of the sound radiated by the radial and axial components of the wheel motion, respectively.

The methodology used to calculate the direct sound incident on the train floor due to the wheel is illustrated in Figure 3.5. The point source (S_q in Figure 3.5) is located at the geometrical centre of the wheel, which is assumed in this example to be 0.61 m above the sleepers and ballast (the height of the rail plus the wheel radius). For harmonic motion at circular frequency ω, the amplitude of the sound pressure incident on the train floor from a monopole source is expressed as [51]

$$p(\mathbf{r}_m) = ikc_0\rho_0 Q \frac{e^{-ikR_{S_q m}}}{4\pi R_{S_q m}} \tag{3.1}$$

where Q is the volume velocity amplitude of the monopole, $R_{S_q m}$ is the distance from the source location (S_q) to the receiver location (m) on the train floor, $k = \omega/c_0$ is the acoustic wavenumber, ρ_0 is the air density, c_0 is the speed of sound and ω is the angular frequency. In the numerical model the source strength is initially set to be unity and the mean square pressure is later adjusted by using the sound power calculated in TWINS (see Section 3.3). The particle velocity of the sound incident on the train floor is

$$\mathbf{u}(\mathbf{r}_m) = (1 + ikR_{S_q m}) \frac{Q(\mathbf{r}_m - \mathbf{r}_{S_q})}{4\pi R_{S_q m}^3} e^{-ikR_{S_q m}} \tag{3.2}$$

The sound pressure and particle velocity of the sound incident on the ground surface due to this source can be calculated similarly. The sound power from the source (representing the wheel) incident on the ground will be discussed later in the reverberant sound part in Section 3.4. The sound pressure and particle velocity due to a dipole are calculated in a similar way but including the dipole directivity factor.
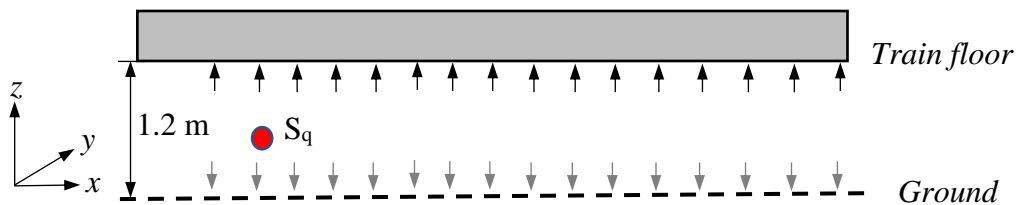
Figure 3.5. Direct sound from wheel, ➤: to the train floor, ➤: sound from the wheel to the ground.

3.2.2 Modelling rail noise by using equivalent source model

The rail noise radiation is also treated separately for the vertical and lateral vibration directions [2]. For vibration in the vertical direction, the rail is replaced by a line array of N correlated monopoles located with equal spacing D along its axis. Based on [16], the source separation D is set to be smaller than a quarter of the acoustic wavelength at the frequency of interest, as well as less than a quarter of the structural wavelength. A different source spacing is chosen for each frequency according to this criterion. For the lateral direction a similar approach is used but the rail is represented by an array of lateral dipoles.

The volume velocity amplitude of source n is denoted by Q_n and its location by $\mathbf{r}_n$. A series of receivers located on the train floor is considered, defined by vectors $\mathbf{r}_m$. The distance between source n and receiver location m is denoted by $R_{mn} = |\mathbf{r}_m - \mathbf{r}_n|$. The methodology to calculate the direct sound at the train floor due to the rail is illustrated in Figure 3.6.
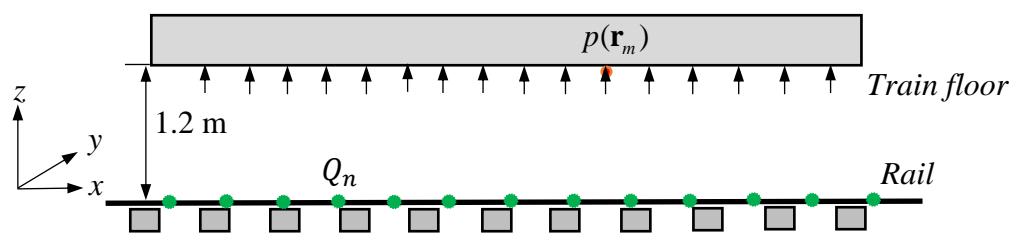
Figure 3.6. The equivalent noise source model for the rail. ●: point sources, ➤: to the train floor.

For each direction and frequency, ω, the sources representing the rail are assumed to be mutually coherent, so that their relative phase must be taken into account [51]. The sound pressure amplitude at receiver location m due to rail vertical vibration is given by

$$p(\mathbf{r}_m) = \sum_{n=1}^{N} \left(i\rho_0 c_0 k \frac{Q_n}{4\pi R_{mn}} e^{-ikR_{mn}} \right) \tag{3.3}$$

When calculating the sound pressure at the floor location (the floor is omitted in calculating the incident sound), the ground reflection and absorption are considered. This is not shown in the above Equation (3.3) but is incorporated in the source term that is obtained from the TWINS model [10]. When using the sound power of rolling noise to adjust the equivalent source models, the ground reflection and absorption is thus included. By differentiating Equation (3.3), the particle velocity can be written as

33

$$\mathbf{u}(\mathbf{r}_m) = \sum_{n=1}^{N} (1 + ikR_{mn}) \frac{Q_n(\mathbf{r}_m - \mathbf{r}_n)}{4\pi R_{mn}^3} e^{-ikR_{mn}} \tag{3.4}$$

The complex volume velocity amplitudes Q_n are chosen to correspond to the vibration velocity of the rail at each position along the rail due to a unit force at $x = 0$, calculated according to the transfer mobility of the rail.

$$Q_n = Q_0 Y(x_n) \tag{3.5}$$

where x_n is the distance from the excitation point and Q_0 is a 'calibration factor' which depends on the separation between the sources, the size of the rail cross-section and the frequency. The transfer mobility $Y(x)$ of the rail is derived from a model of a Timoshenko beam on a continuous support [2], expressed as

$$Y(x) = u_1 e^{-ik_r|x|} - iu_2 e^{-\beta|x|} \tag{3.6}$$

where k_r is the wavenumber corresponding to the predominantly propagating wave and β corresponds to the evanescent wave. u_1 and u_2 are the corresponding wave amplitudes. These wavenumbers and amplitudes include the effect of the support layers [2]. The results in this Chapter are calculated with the data shown in Table 3.2, which correspond to a UIC60 rail in a track with concrete sleepers. The sleepers are represented by an equivalent continuous layer of mass. The real part of k_x corresponds to the propagating waves, they are plotted in Figure 3.7(a). The imaginary part of k_x corresponds to the decay with distance along the rail, which can be expressed as a decay rate in dB/m as:

$$\Delta = -8.686 \text{Im}(k_x) \tag{3.7}$$

The vertical and lateral decay rates of the rail for the current parameters are plotted in Figure 3.7(b).
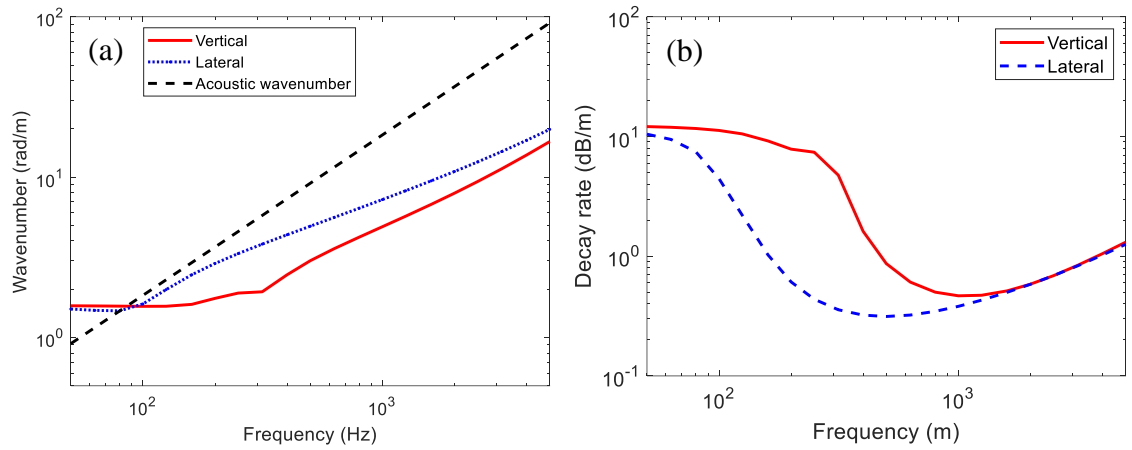
Figure 3.7. (a) Real part of the wavenumbers of the propagating waves, (b) calculated decay rates of the rail for vertical and lateral vibration. Based on Table 3.2.

The transfer mobility of the rail from Equation (3.6) is a function of x and its real and imaginary parts are illustrated at two example frequencies in Figure 3.8. Figure 3.8(a) shows the results at 100 Hz where the decay rate is relatively high, while Figure 3.8(b) shows the results at 2000 Hz with a relatively low decay rate.
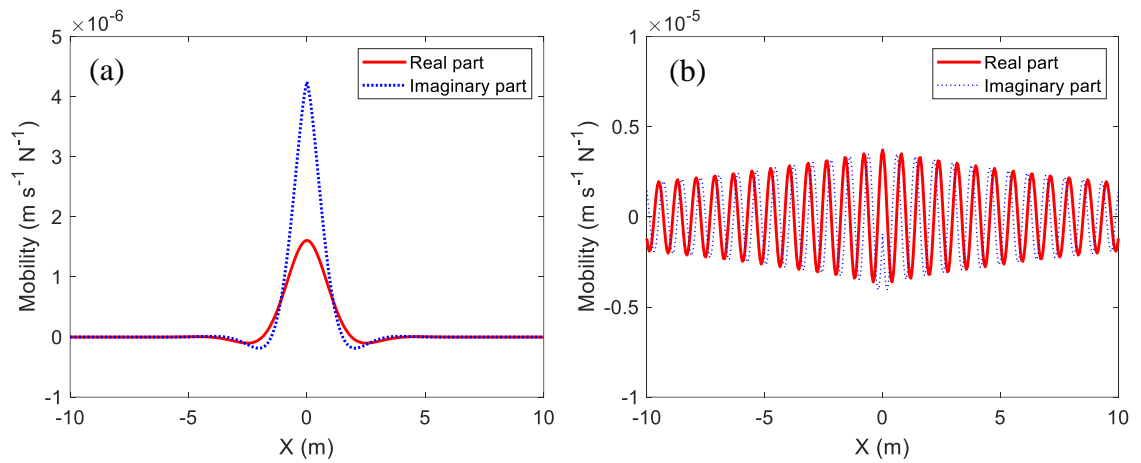
Figure 3.8. Rail mobility as a function of x in the spatial domain, (a) 100 Hz; (b) 2000 Hz.

3.2.3 Sleeper noise

Sleepers are typically about 2.5 m long and 0.2 to 0.25 m wide. When the vibration is transmitted from the rail to the sleepers, it causes the sleepers to vibrate mainly in the vertical direction. The distribution of the sleeper vibration in the x-direction (i.e. along the track) can be derived from the rail transfer mobility and the ratio of the sleeper displacement to that of the rail, based on assumption that the sleeper is represented as a mass, which is given by [2]

$$r = \frac{s_p}{s_p + s_b - \omega^2 m_s} \tag{3.8}$$

where s_p is the pad stiffness in vertical direction, s_b is the ballast stiffness and m_s is the sleeper mass. Damping is introduced by making the stiffnesses complex. From the rail transfer mobility and this ratio, the sleeper vibration velocity can be obtained. In this work, the sleepers are treated as rigid bodies and are represented acoustically by sets of monopole sources radiating noise into a half space. Five equally-spaced monopole sources are used to replace each half sleeper.

3.3 TWINS adjustment

The direct sound pressure incident on the train floor is calculated due to each point source as described above. The strength of the point sources used in the previous calculations are based on a unit force acted on the rail at all frequencies. Thus, the calculated sound distribution on the train floor only gives the decay pattern but not the actual sound level. The latter is also of interest. To obtain it, the results from the equivalent point source model need to be calibrated by comparison with results from the TWINS model.

The sound power obtained from the TWINS model is used to adjust these results according to the ratio of the sound power obtained from the TWINS model to that from the point source models used to replace the wheel, the rail and the sleepers. The adjustment is performed based on the relation below:

$$\overline{p_r^2} = \overline{p_{eq}^2} \frac{W_{TWINS}}{W_{eq}} \tag{3.9}$$

where W_{TWINS} is the sound power of the rolling noise components obtained from the TWINS model and it is considered as the actual sound power of the rolling noise. W_{eq} is the sound power calculated from the equivalent source model under unit force (for the rail and sleepers) and unit vibrational velocity (for the wheel). $\overline{p_{eq}^2}$ is the mean square pressure on the train external surfaces calculated from the same equivalent source model. $\overline{p_r^2}$ refers to the mean square pressure on the train external surfaces during running. The aim of the adjustment is to find $\overline{p_r^2}$ according to the other three terms. Because the effect of the ground on the radiation of rolling noise from the rail and sleeper has been incorporated in the source

term (W_{TWINS}) that is obtained from the TWINS model [10], it is not included in the equivalent source model.

The adjustments are determined separately for each source (wheel axial and radial, rail vertical and lateral, and sleepers) and each frequency band and applied to the corresponding mean square pressure. The sound power from the equivalent source models W_{eq} is found by integrating the sound intensity over a suitable far-field surface: the sound power of the equivalent sources representing the wheel is calculated by enclosing the point sources by a virtual sphere (radius 5 m) and integrating the sound intensity; for the rail, the radiating length is limited to 60 m on either side of the excitation position and this part of the rail is enclosed in a virtual cylinder with radius 2.5 m and length 60 m on each side of the excitation, see Figure 3.9. This length ensures that, even for the lowest decay rate, the contribution from the parts of the rail not included in the calculation is negligible. In fact, at the lowest decay rate, 0.3 dB/m at 500 Hz in the lateral direction (see Figure 3.7(b)), the vibration has decayed by 18 dB after 60 m.
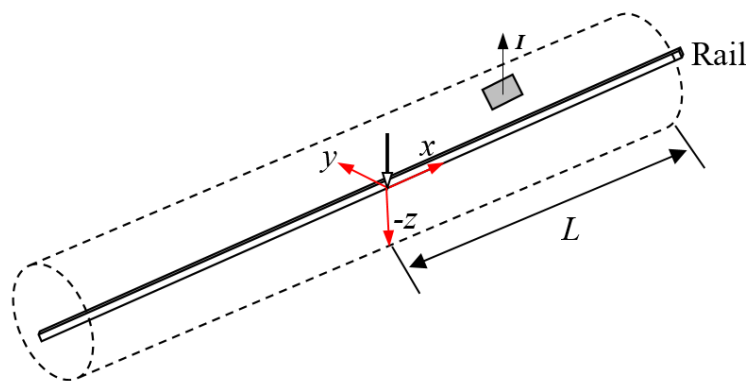
Figure 3.9. Calibration of the equivalent source model by integrating the sound intensity over a virtual cylinder with radius 2.5 m and length $L = 60$ m on each side of the excitation.

3.4   Reverberant sound

3.4.1   SEA model

The reverberant component of the sound beneath the train is studied by using Statistical Energy Analysis (SEA) [82]. This is an efficient method for obtaining the average response

of complicated structures. The space beneath the vehicle floor is subdivided into several segments as indicated in Figure 3.10. The length of a train coach is normally in the range 17 to 26 m. Here, a 26 m long train coach without fairings is used as an example. The centre of the bogie is assumed to be 3.2 m from its end. The width of the underfloor cavity is assumed to be 3.6 m and the height of the train floor above the ballast and sleepers is taken as 1.2 m. The region beneath the train floor is divided into seven segments, as shown in Figure 3.10. The length of segments 1 and 7 is taken as 5 m to include the whole bogie region; the remaining five segments are 3.2 m long. These lengths are sufficient to ensure that the number of acoustic modes in each one-third octave band is large enough to allow SEA to be used (here there are more than five modes in the frequency bands above 160 Hz) but they are also small enough to give an adequate resolution of the sound distribution beneath the vehicle.
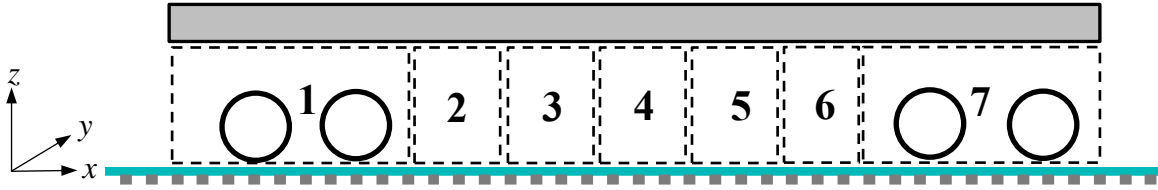
Figure 3.10. SEA model for investigating acoustic behaviour below the train.

The power balance for the SEA system is given by [82]

$$
\begin{bmatrix} P_{\text{in},1} \\ P_{\text{in},2} \\ \vdots \\ P_{\text{in},7} \end{bmatrix} = \omega \begin{bmatrix} \eta_1 + \eta_{12} + \cdots & -\eta_{21} & \cdots \\ -\eta_{12} & \eta_2 + \eta_{21} + \eta_{23} + \cdots & -\eta_{32} & \cdots \\ \vdots & \vdots & \cdots \end{bmatrix} \begin{bmatrix} E_1 \\ E_2 \\ \vdots \\ E_7 \end{bmatrix} \qquad (3.10)
$$

where $P_{\text{in},i}$ is the power input to subsystem i, E_i is the energy in the respective subsystem, ω is the angular frequency, η_{ij} are coupling loss factors between subsystems i and j ($i \neq j$) and η_i is dissipation loss factor in subsystem i. If the input powers, coupling loss factors and dissipation loss factors are known, the energy in each subsystem can then be calculated. Expressions for the dissipation loss factor η_i in each subsystem and the coupling loss factors η_{ij} between two acoustic subsystems can be found in [82]

$$
\eta_i = \frac{c_0 S_i \alpha_i}{4 \omega V_i} \qquad (3.11)
$$

$$\eta_{ij} = \frac{c_0 S_{ij} \tau}{4\omega V_i} \tag{3.12}$$

where c_0 is the speed of sound, S_i is the total surface area of subsystem i, α_i is its average absorption coefficient, V_i is the volume for subsystem i, $S_{ij} = S_{ji}$ is the area of the boundary between cavities i and j. τ is transmission coefficient through them. As there is no partition between adjacent subsystems, it can be assumed that τ can be set to 1 [73].

To calculate the dissipation loss factor, the absorption coefficient of the surfaces of each volume is required. As the sides are open, the 'absorption coefficients' of the open areas are expected to be 1. If there are fairings on the train sides, an appropriate absorption coefficient should be used for these surfaces. The absorption coefficient on the train floor (and the fairings) is set to be 0.2. For the absorption coefficient of the ballast, measured values from [83] are used, see Figure 3.11. The sleepers are made of concrete in most cases, so their absorption coefficient is set to be 0. The average absorption coefficient of the ground takes account of the respective areas of the ballast and the sleepers. The respective areas of the ballast and sleepers depend on particular design of the track. It is common that the sleeper spacing is 0.6 m and the sleeper width is 0.2 m, therefore the ballast takes 2/3 of the ground area and the sleepers cover the remaining 1/3 in this work.
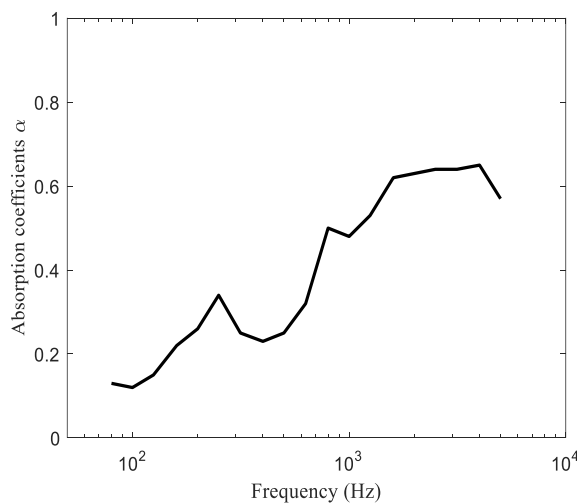
Figure 3.11. Absorption coefficient of 33 cm layer of ballast [83].

3.4.2   Input power and reverberant sound

The power input to the SEA system is calculated from the direct sound after the first reflection, allowing for the absorption coefficient of the surface. This is done for the train floor, the fairings and the ground. The sound power incident on the train floor can be calculated by

$$W = \int_{y_1}^{y_2} \int_a^b I_z \mathrm{d}y \mathrm{d}x \qquad (3.13)$$

where y is the coordinate in the width direction, extending from y_1 to y_2 relative to one rail, and a, b are the limits of x for each segment in the train length direction. I_z is the normal component of the sound intensity incident on the train floor

$$I_z = \frac{1}{2} \mathrm{Re}(p u_z{}^*) \qquad (3.14)$$

where p and u_z are the sound pressure and normal velocity amplitudes of the sound incident on the train floor. These are calculated for each source separately as described in Section 3.2. The sound power reflected by the ground consists only of the contribution from the wheels. This is because the direct sound radiated by the rails (and sleepers) is calculated allowing for the ground reflection and absorption. The sound power incident on the ground surface due to the wheel can be calculated in a similar manner to Equation (3.13) and (3.14). The power reflected from the ground (allowing for its absorption) is finally added as an input for each segment. The same is done for fairings if they are present. The final power input to each subsystem of the SEA model is expressed as

$$P_{in} = W_f(1 - \alpha_f) + W_b(1 - \alpha_b) \qquad (3.15)$$

where W_f is the sound power incident on the train floor, and the fairings if present, W_b is the sound power from the wheel incident on the ground, α_f and α_b are the absorption coefficients of the floor and ground. Figure 3.12(a) shows the input power for each subsystem for several example one-third octave bands. The relative levels of the different bands correspond to the inputs determined from the TWINS results and the sound power decays with distance at different rates in each band. By solving the SEA problem as given in Equation (3.10), the energy in each subsystem can then be calculated. This is shown in Figure 3.12(b) for the same example frequency bands.
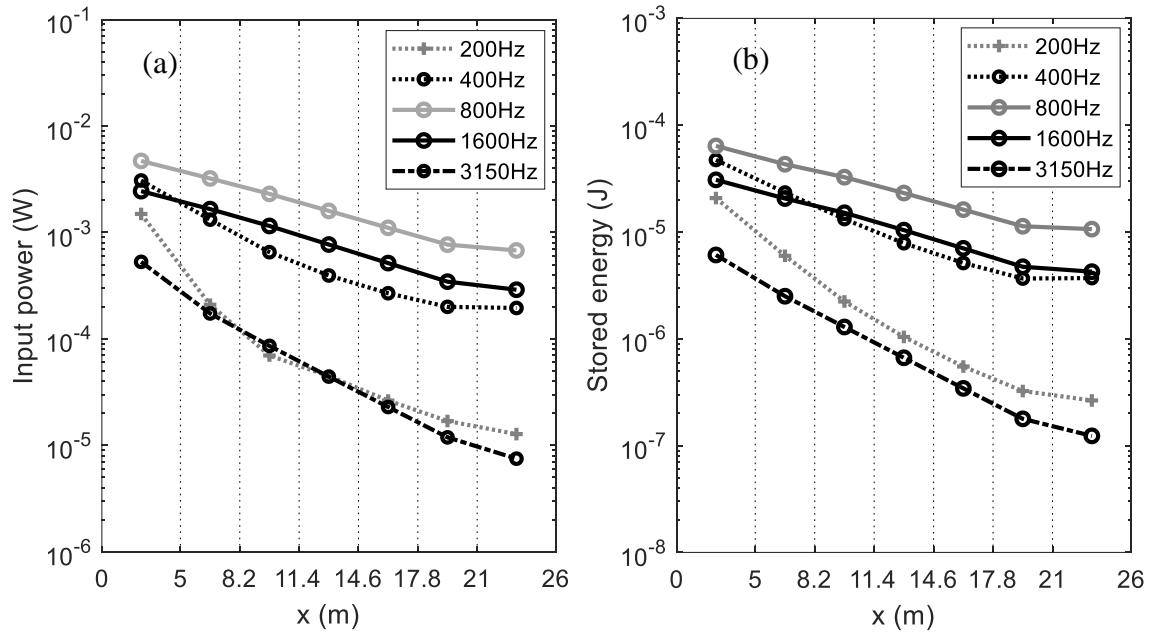
Figure 3.12. (a) Power input to each segment in the SEA system due to one wheel and associated track vibration, (b) Stored energy in each subsystem of the SEA system ($x = 0$ is the end of the carriage).

The spatially-averaged mean-square sound pressure in each subsystem is calculated from

$$\overline{p_{rev,i}^2} = \frac{\rho c_0^2 E_i}{V_i} \qquad (3.16)$$

which forms the reverberant component of the sound.

3.5 Discussion

The direct sound incident on the train floor is determined by summing the mean-square sound pressures from the wheels, rails and sleepers. The total direct sound pressure incident on the train floor in three example frequency bands is shown in Figure 3.13, in which the end of the vehicle is at $x = 0$ and the wheel/rail contact location is at (3.2 m, 0 m). The reverberant sound incident on the train floor is plotted in Figure 3.14.
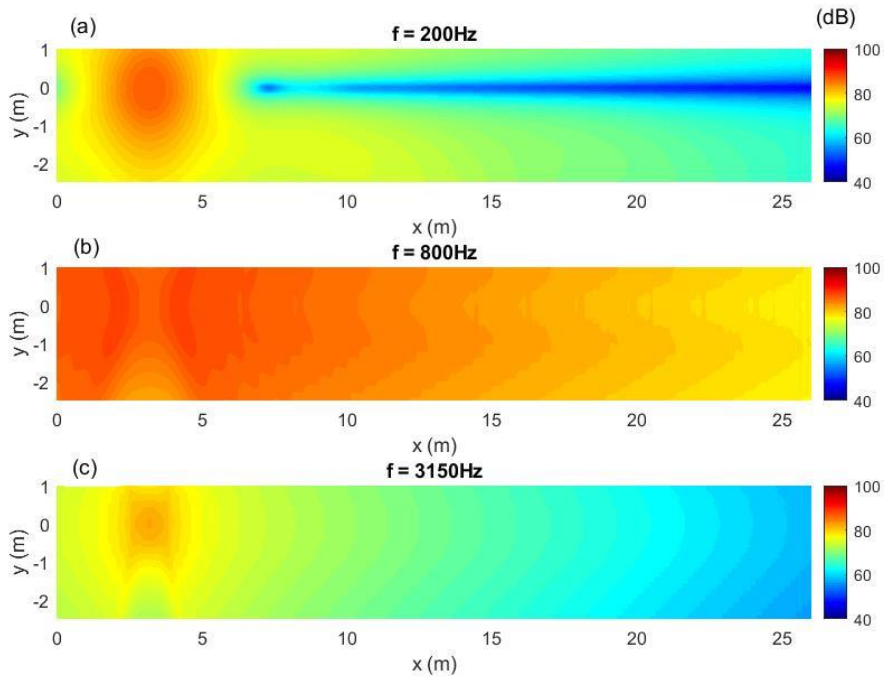
Figure 3.13. Direct sound pressure level on the train floor, dB re 2.0×10^{-5} Pa. (a) 200 Hz, (b) 800 Hz, (c) 3150 Hz.
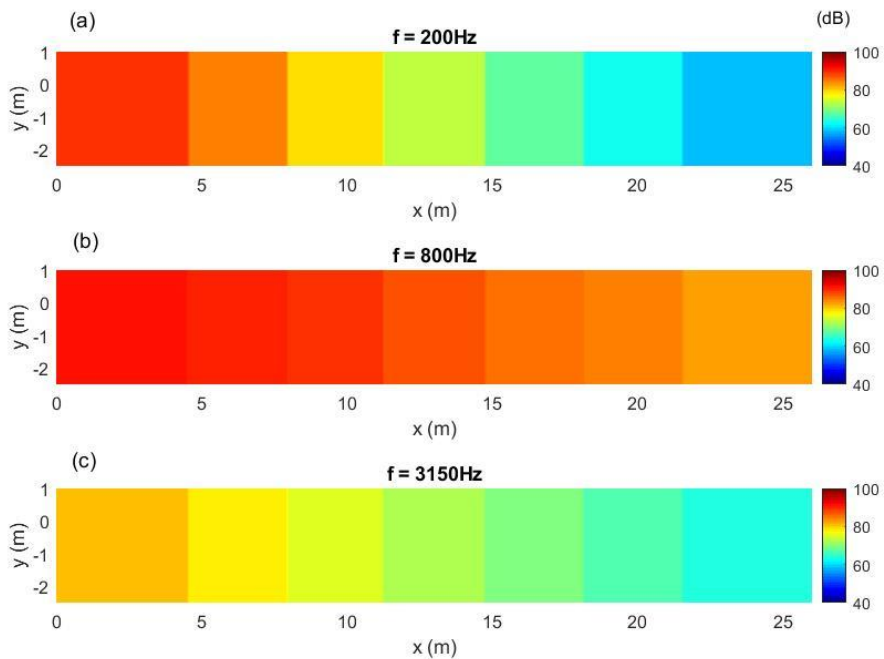
Figure 3.14. Reverberant sound pressure level on the train floor, dB re 2.0×10^{-5} Pa. (a) 200 Hz, (b) 800 Hz, (c) 3150 Hz.

At 200 Hz, the sleeper radiation is dominant (see Figure 3.4), and the direct sound pressure at the train floor decays quickly with distance (Figure 3.13(a)). At 800 Hz, the rail is dominant in terms of sound power; the decay of sound pressure levels with distance along the train floor corresponds to the low decay rate of the rail vibration at this frequency

(illustrated in Figure 3.7(b)). At 3150 Hz, the wheel contribution becomes significant and the sound pressure decays quickly away from the source (Figure 3.13(c)). The reverberant sound distribution on the train floor shown in Figure 3.14 has similar trend with the direct one.

The sound pressure levels at the train floor along the train centreline at four example frequency bands are plotted in Figure 3.15. The direct sound shown here is the incident sound field, which represents the sound pressure at the floor position without allowing for the reflection from the floor. Again only the noise from one wheel and the noise from the track excited by one wheel are considered here. The SEA model gives the average sound pressure for each subsystem, so the reverberant sound pressure levels are assumed constant within a given subsystem.
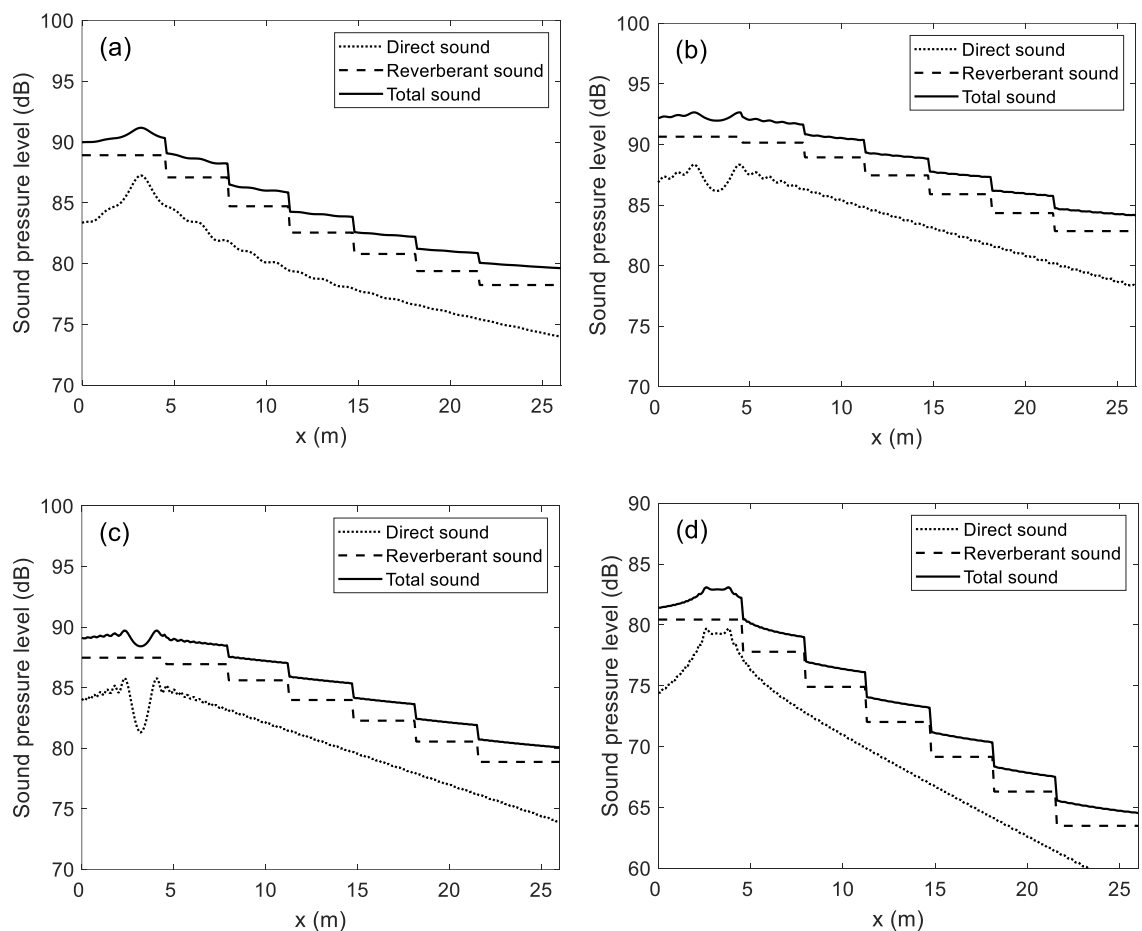
Figure 3.15. Incident sound pressure levels on the centreline of the train floor in example one-third octave bands, (a) 400 Hz, (b) 800 Hz, (c) 1600 Hz, (d) 3150 Hz.

Figure 3.16 shows spectra of the contributions of the direct sound and reverberant sound to the total sound pressure levels at the train floor for selected subsystems. The direct sound is calculated at the centre of the floor for each subsystem and the reverberant sound is the average for that subsystem.
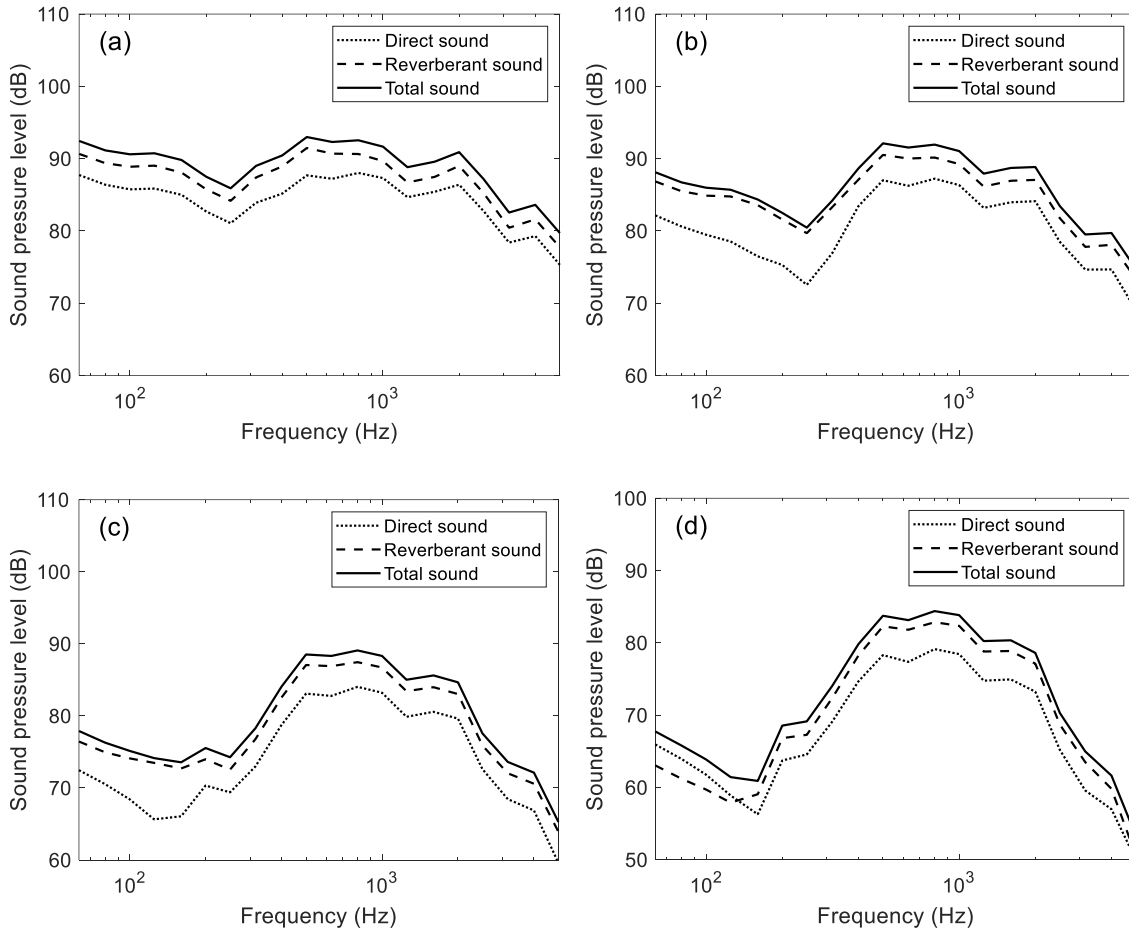
Figure 3.16. Comparison of the direct sound and reverberant sound in each subsystem, dB re 2.0×10^{-5} Pa. (a) Subsystem 1, (b) subsystem 2, (c) subsystem 4, (d) subsystem 7.

Figure 3.17 shows the relative contributions of the direct and reverberant components of the overall sound power incident on the train floor. The direct sound power incident on the train floor is calculated from Equation (3.13). The reverberant sound power incident on the train floor is obtained by [51]

$$W = \overline{\langle p_{rev}{}^2 \rangle} \frac{S}{4\rho_0 c_0} \tag{3.17}$$

where S is the area of the train floor.
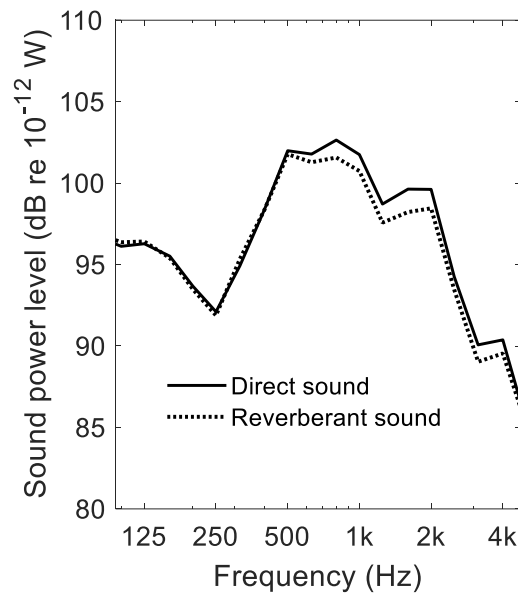
Figure 3.17. Relative contribution of direct and reverberant sound to the overall sound power incident on the train floor.

Although the reverberant sound pressure levels are higher than the direct sound pressure levels, as seen in Figure 3.16, the reverberant sound power is slightly lower than the direct sound power in Figure 3.17. This is a consequence of the fact that the relation between the sound pressure and the incident intensity is different for the direct field (approximately plane waves) and the reverberant field (Equation (3.17)).

3.6   Comparison with laboratory measurements

3.6.1   Experimental set-up

Experiments were conducted to measure the sound distribution on the floor of a 1:5 scale train model, including the scale track [84] and the scale train body [85], which were developed in previous projects at ISVR. For the measurement, a 1:5 scale ballasted track was installed in the anechoic chamber at the ISVR, University of Southampton and mounted on wooden panels to represent an acoustically reflecting ground (see Figure 3.18). A 1:5 scale simplified car body, made of a dense foam which was sealed with varnish, was set up above the track using wooden supports; the track and the car body were not in contact. The track model is 2 m long and 0.8 m wide, and the train is 2.5 m long, 0.56 m wide and 0.45 m tall. The distance from the top of the sleepers to the train floor was about 0.23 m.

In the measurements, a sound source is used that consists of a driver connected to a stiff tube with a nozzle of diameter 1.5 cm. The sound emitted from the tube is approximately omnidirectional and has a volume velocity that is independent of the source location. This arrangement allows the source to be placed at a precise location within the model. The source was excited with white noise, although the sound emitted is modified by the acoustic properties of the tube. The nozzle was located directly above the rail at 0.32 m from one end. A microphone was used to measure the sound pressure along the centreline of the bottom surface of the train body with a spatial resolution of 0.1 m.
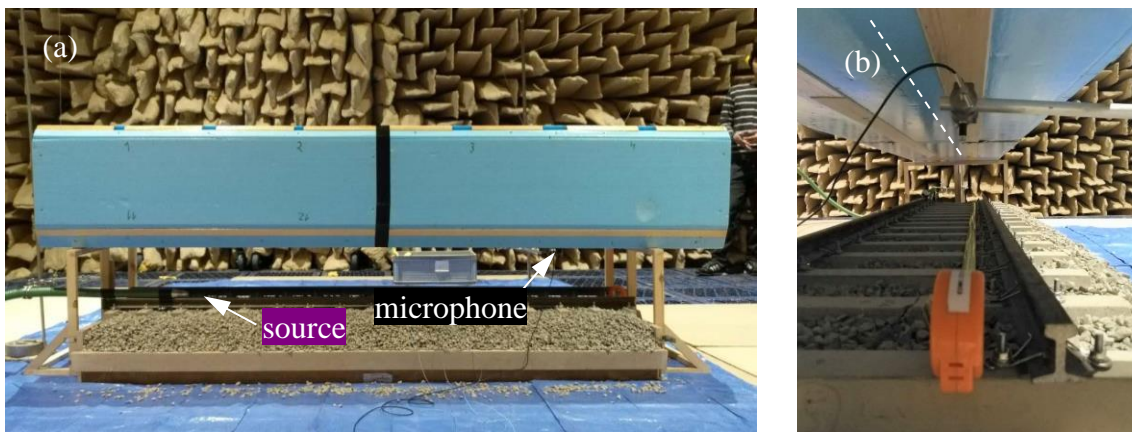
Figure 3.18. Experimental set up in anechoic chamber, (a) front view, (b) end view (note the microphone was located on the centreline of the train floor in the measurement, shown by the dashed line).

3.6.2   Comparison of numerical and experimental results

In the measurements, the sound pressure spectrum at the train floor was measured and was converted to 1/3 octave bands. For comparison, the sound field was predicted using the model with a monopole source with a source strength (volume velocity) determined from free-field measurements of the source. The absorption coefficient of the reduced scale ballast has been measured [86]. The absorption coefficient of the train floor has not been measured but it is set to 0.2 to be consistent with the field measurements in the next section. The direct and reverberant sound at the train floor have been calculated and their mean square pressures are added to obtain the total sound on the train floor. The results have been calculated in the frequency region between 1 and 5 kHz, corresponding to a range of 200-1000 Hz at full scale. The lower frequency limitation is chosen at 1 kHz as the signal-to-noise ratio is not sufficient below it in the measurement. Results in each one-third octave band are shown in Figure 3.19. The average differences in terms of the spatial sound pressure levels at each frequency band between the predictions and the measurements are shown in Table 3.3.
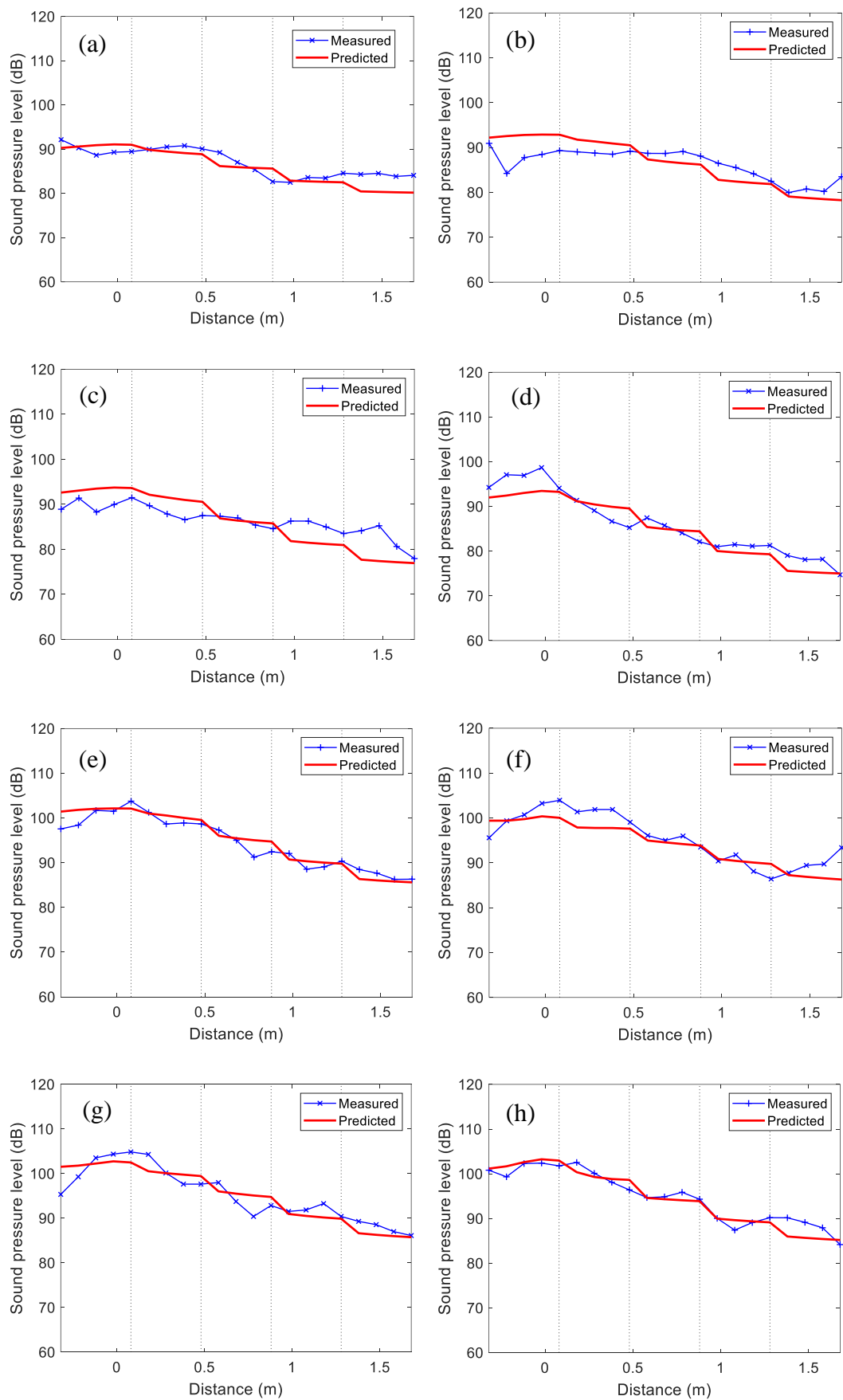
Figure 3.19. Comparison of sound pressure levels on the train floor obtained from the numerical simulation and experiment. (a) 1000 Hz, (b) 1250 Hz, (c) 1600 Hz, (d) 2000 Hz, (e) 2500 Hz, (f) 3150 Hz, (g) 4000 Hz, (h) 5000 Hz.

Table 3.3. Average difference in terms of the sound pressure level between the predictions and measurements (dB).

	1 kHz	1.25 kHz	1.6 kHz	2 kHz	2.5 kHz	3.15 kHz	4 kHz	5 kHz
Average difference	-0.9	0.2	-0.2	-1.1	0.5	-1.3	-0.1	-0.3

From these results it can be concluded that the SEA model combined with the equivalent source model is able to predict the sound beneath the train floor for frequencies above 200 Hz at full scale.

3.7   Comparison with field measurements

Field measurements have been performed on a metro train. More details can be found in **Appendix B.2** and **B.3**. The vehicle tested had a length of 17.92 m. In a first step an artificial source was introduced beneath the floor and the spatial decay of the sound was measured. In a second step measurements were made during train operation and the results were compared with predictions from the model.

3.7.1   Measurement on a stationary train

Field measurements have been performed to measure the sound decay below a stationary train due to a source located below the train floor [87], details included in **Appendix B.2**. The field measurement is shown in Figure 3.20(a). The diameter of the source is 0.45 m. This was excited by broadband noise and the sound pressure results were expressed in one-third octave bands between 100 and 5000 Hz. The microphones were placed 0.32 m above the sleepers at positions along the vehicle centreline with a spatial interval of 1.0 m (Figure 3.20(b)). The first microphone position was 2 m from the source.
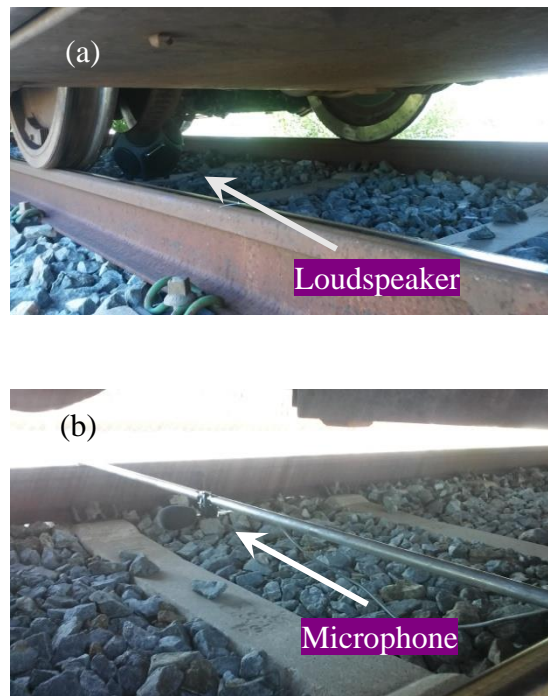
Figure 3.20. Field measurements on a stationary train. (a) Source location, (b) microphone locations. Photos provided by UPV.

Various pieces of equipment are mounted under the train floor, which will tend to weaken the direct sound and strengthen the reverberant one. The bottom of the equipment was 0.38 m above the sleepers while the train floor was 1.2 m above the sleepers. The equipment was simplified in the model as shown by the darker coloured areas in Figure 3.21. For this case, the area below the vehicle is divided into eight subsystems. Subsystems 1 and 8 are below the gangways at the two ends, subsystems 2 and 7 are for the two bogie areas and subsystems 3-6 are for the middle region.
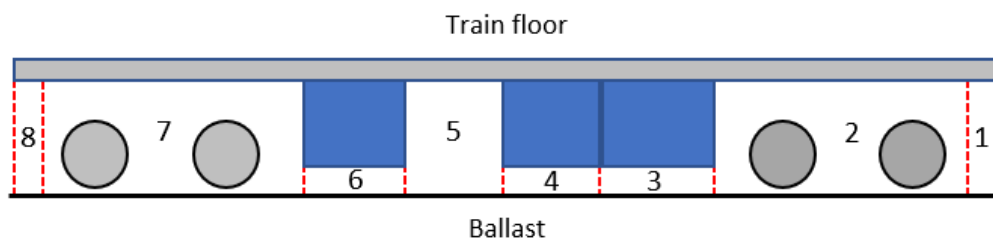
Figure 3.21. Subdivision of the region below the vehicle (not to scale).

The source is located in subsystem 7. It is represented in the model by a monopole in a similar manner to the wheel noise described in Section 3.2. Account is also taken of the end surfaces of the equipment in subsystem 6 which can also reflect sound into the reverberant field in subsystem 7. An equivalent sound absorption coefficient 0.2 is used for the train floor and the equipment boxes. The predicted spatial decay beneath the train floor is

compared with the measurements. As the source strength of the loudspeaker in the measurement is unknown, the predicted sound pressure levels have been shifted so that the predictions and measurements correspond to each other at the first position, $x = 2$ m, to allow direct comparison. The results for example one-third octave frequency bands are shown in Figure 3.22; other bands show similar results.
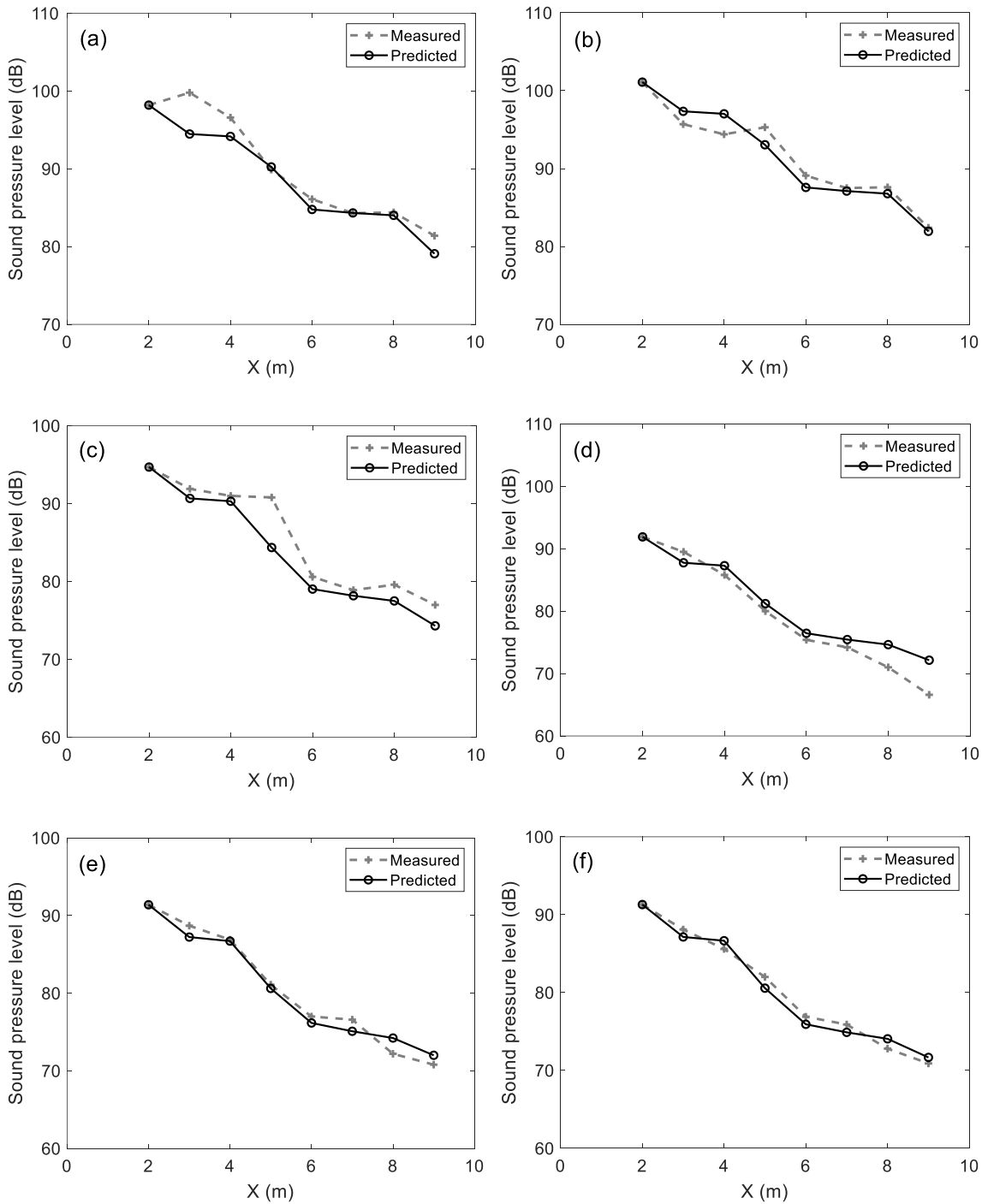
Figure 3.22. Comparison of sound pressure levels between predictions and field measurements on stationary train, (a) 160 Hz, (b) 315 Hz, (c) 630 Hz, (d) 1250 Hz, (e) 2500 Hz, (f) 5000 Hz.

3.7.2 Measurement on a running train

Field measurements were performed to measure the sound pressure below the same train during operation at 50 km/h [87]. More details can be found in **Appendix B.3**. The sound pressure was recorded at various positions, including six microphones located below the train floor which are used here. These are labelled as 1002, 1007, and 1008 which were in the bogie area, microphone 1003 below the gangway and microphones 1012 and 1013 in the central part below the vehicle, see Figure 3.23.
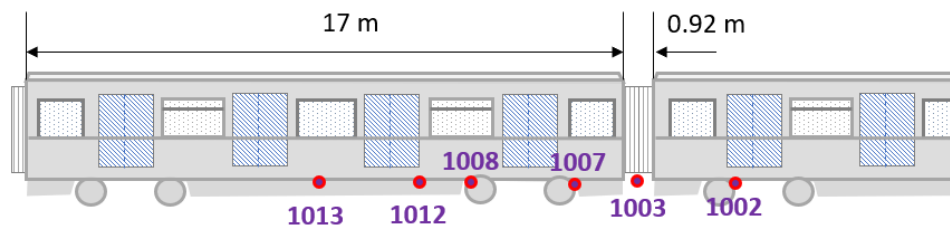
Figure 3.23. Measurement set up for microphone locations below the train.

Because of the presence of the underfloor equipment, direct sound is assumed only to reach the train floor region belonging to subsystems 1, 2, 5, 7 and 8. The equipment also blocks the direct sound from one end of the carriage from reaching the other end; therefore when calculating the direct sound on the train floor for these subsystems, only the sources below these subsystems are considered. The sound pressure impinging on the bottom of the equipment is assumed to be reflected into the corresponding subsystem and to contribute to the reverberant sound. The sound pressure below the vehicle is predicted following the procedure outlined in Sections 3.2~3.4. Although point 1002 was measured below the adjacent carriage, it is compared with an equivalent location in segment 7 as the configuration of the equipment below each coach is similar (the adjacent carriage had a motor bogie but the motor did introduce noise as it was switched off for the tests).

The sound power of the rolling noise was obtained from the TWINS model and used to adjust the results. The track parameters are listed in the **Appendix B.1**. The wheels had a nominal diameter of 860 mm and were fitted with dampers. The predictions of the sound pressure levels at the measurement positions below the floor are compared with field measurements, as shown in Figure 3.24. Points 1002, 1007 and 1008 are located in the same

subsystem in the bogie region, so the predictions at the three points are nearly the same, and they are compared together in Figure 3.24(a).
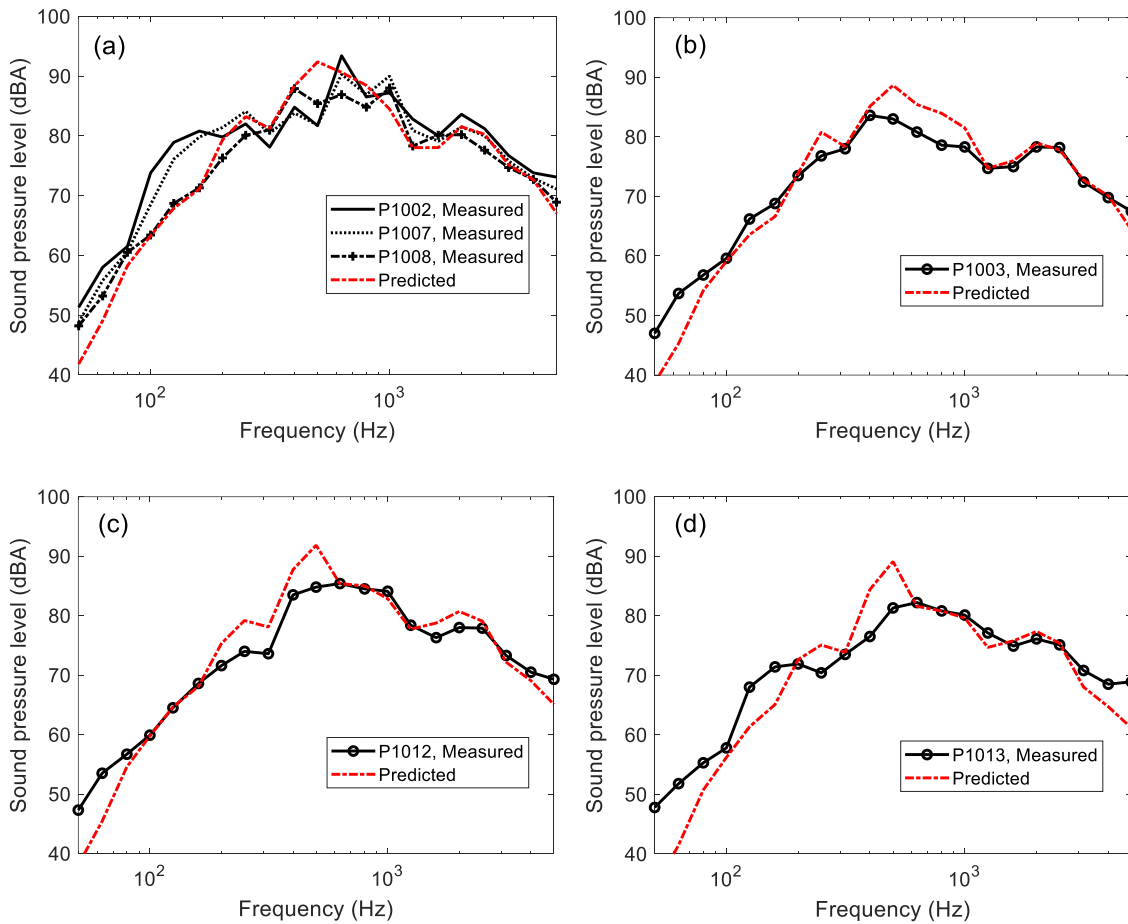
Figure 3.24. Comparison of sound pressure levels between predictions and field measurements, (a) comparisons at the bogie area, (b) comparison at point 1003, (c) comparison at point 1012, (d) comparison at point 1013.

The overall sound pressure levels and the average differences between the predictions and the measurements are shown in Table 3.5. The predictions of sound pressure levels at the three positions in the bogie area (1002, 1007 and 1008) agree well with the measurements; the relative error of their overall sound pressure levels is less than 2 dB. For the two positions, 1012 and 1013, in the middle region of the vehicle, the predictions agree well with the measurements apart from the region between 250 Hz and 500 Hz, where the predictions are higher. At point 1003, the one below the gangway, very good agreement is found but again in the middle frequency region, in this case between 500 and 1000 Hz, some differences appear. The differences in overall level at these three locations outside the bogie area are between 2 and 3 dB, see Table 3.4.

Table 3.4. Overall sound pressure levels on train floor (dB(A)).

	Point 1002 (bogie)	Point 1003 (gangway)	Point 1007 (bogie)	Point 1008 (bogie)	Point 1012 (centre)	Point 1013 (centre)
Prediction	96.7	93.2	97.2	96.8	94.8	91.6
Measurement	96.9	90.3	96.1	94.9	92.5	89.1
Difference	-0.2	2.9	1.1	1.9	2.3	2.5

3.8 Summary

A methodology has been presented to predict the sound pressure beneath a train floor due to rolling noise during train operation. It can also be used for other sources such as traction and auxiliary equipment if the corresponding sound powers are known. The sound is separated into the direct and reverberant components, with a set of equivalent sources being used to predict the direct sound and SEA being used for the reverberant sound. The source strengths of the wheel, the rail and the sleepers have been determined by using sound powers obtained from the TWINS model. The sound pressure on the train floor is highest in the bogie region and decays with increasing distance from the source, but the decay rate is dependent on frequency.

Comparisons have been made with both laboratory and field measurements of sound pressure below a vehicle. In the laboratory measurements, performed on a 1:5 scale model, the sound pressure distribution along the train floor centreline was found to agree well with the predicted results above 200 Hz (full scale frequency). Field measurements on a static train using an omindirectional source also show good agreement with the sound pressure decay under the vehicle. For a train in running operation, the sound pressure spectrum measured at six locations below the vehicle was in reasonable agreement with the predictions, with overall sound pressure levels differing by less than 3 dB.

This approach can benefit the prediction of train interior noise as the incident sound on the train floor is an essential component for interior noise calculations. The sound incident on the side and roof of the train is also important so this is addressed in the next chapter.

Chapter 4   Rolling noise on train side and roof

When calculating the train interior noise, the sound incident on the train sides and roof may also be important. It is therefore necessary to know the distribution of sound pressure on the side surfaces of the vehicle to be able to predict the interior noise. In this chapter, a wave-domain boundary element model, which is also called the 2.5D BE model is introduced with the aim of predicting the sound pressure on the train side surfaces due to rolling noise. One of the first applications of the 2.5D BE method was made by Duhamel [88] to predict the sound pressure around a noise barrier and it showed high efficiency to solve that three dimensional acoustic problem. In this work, the noise sources, the wheel, the rail and the sleepers, are represented in a 2.5D BE model that accounts for the train cross-section and includes the presence of the ground.

For use in a railway noise study this method needs to handle discrete compact sources, such as the wheels of the train, as well as extended sources, such as the rail. One of the challenges is to represent discrete sources in a 2.5D BE model, where by definition the different components of the model extend indefinitely in the x direction. This is achieved by applying suitable wavenumber spectra to equivalent extended sources, as outlined in the next section. The track, in contrast, extends in the x direction and can readily be represented as an infinite structure.

The numerical approach is briefly described in Section 4.1. Section 4.2 explains how the rolling noise sources are represented in a 2.5D model. Section 4.3 presents the 2.5D model for predicting the noise incident on the train external surfaces. Sections 4.4 and 4.5 verify the validity of this approach by means of comparison with laboratory tests on a scale model in an anechoic chamber and field tests on a metro vehicle.

4.1   Numerical method

4.1.1   2.5D boundary element method

The derivation of the 2.5D BE method starts from a three-dimensional (3D) problem. Assuming time-harmonic variations with dependence $e^{i\omega t}$, the boundary integral for a 3D acoustic problem is [89]

$$p(x', y', z') = - \int_S \Bigg(i\rho\omega v(x, y, z)\psi(x, y, z|x', y', z')$$
$$+ p(x, y, z)\frac{\partial\psi(x, y, z|x', y', z')}{\partial n}\Bigg)\mathrm{d}S \tag{4.1}$$

where S is the surface of the vibrating boundaries, $p(x', y', z')$ is the sound pressure amplitude at a receiver P, ρ is the density of air, $v(x, y, z)$ and $p(x, y, z)$ are the normal velocity and pressure amplitudes on the vibrating surface and $\psi(x, y, z|x', y', z')$ is the Green's function. If the geometry of the problem can be considered uniform and of infinite length in one direction, e.g. x, Equation (4.1) can be conveniently solved in the 2D domain for a range of wavenumbers k_x in the x direction. To achieve this, the Fourier transform pair for the sound pressure $p(x, y, z)$ with respect to x can be expressed as

$$\tilde{p}(k_x, y, z) = \int_{-\infty}^{\infty} p(x, y, z)\, e^{ik_x x}\mathrm{d}x \tag{4.2}$$

$$p(x, y, z) = \frac{1}{2\pi}\int_{-\infty}^{\infty} \tilde{p}(k_x, y, z)\, e^{-ik_x x}\mathrm{d}k_x \tag{4.3}$$

Equation (4.3) indicates that the sound pressure at a receiver P has the form of a sum of harmonic waves with angular frequency ω, propagating in the x direction with wavenumbers k_x. The distribution of sound pressure can therefore be obtained from Equation (4.3) once $\tilde{p}(k_x, y, z)$ is determined. This can be achieved through a 2.5D formulation of Equation (4.1) where pressure, velocity and the Green's function are expressed as functions of k_x, y and z and the boundary integrals are solved over the perimeter of the boundary region Γ in the y-z plane. The wavenumber domain integral equation therefore becomes:

$$\tilde{p}(k_x, y', z') = - \int_\Gamma \Bigg(i\rho\omega\tilde{v}(k_x, y, z)\psi(k_x, y, z|y', z')$$
$$+ \tilde{p}(k_x, y, z)\frac{\partial\psi(k_x, y, z|y', z')}{\partial n}\Bigg)\mathrm{d}\Gamma \tag{4.4}$$

$\tilde{v}(k_x, y, z)$ in Equation (4.4) is the normal particle velocity in the wavenumber domain, which is obtained by applying the Fourier transform to the normal velocity in the spatial domain,

$$\tilde{v}(k_x, y, z) = \int_{-\infty}^{\infty} v(x, y, z) e^{ik_x x} \, dx \tag{4.5}$$

In Equation (4.4), the wavenumber in the x direction, k_x, is not dependent on y, z and the Green's function $\psi(k_x, y, z | y', z')$ takes the same form as the 2D fundamental solution [88]

$$\psi(k_x, y, z | y', z') = -i\frac{1}{4} H_0^{(2)} ((k_0^2 - k_x^2)^{1/2} r) \tag{4.6}$$

with $H_0^{(2)}(x)$ being the Hankel function of the second kind of order 0, and k_0 the wavenumber in air. If $k_x > k_0$, the wavenumber in the 2D domain is imaginary, and the sound waves will decay exponentially with distance $r = (y^2 - z^2)^{1/2}$.

The presence of the ground can be taken into account by means of an image source located symmetrically beneath the ground. If a rigid ground is considered, the fundamental solution takes the form

$$G = -\frac{i}{4} H_0^{(2)} ((k_0^2 - k_x^2)^{1/2} r) - \frac{i}{4} H_0^{(2)} ((k_0^2 - k_x^2)^{1/2} r') \tag{4.7}$$

where r is the distance from the actual source to the receiver, and r' is the distance from the image source to the receiver. The phase difference between the two sources is therefore included automatically in this equation.

Partially absorbing boundaries can be modelled through their surface normal impedance, which can be obtained by means of analytical or empirical models. In this case the corresponding part of the boundaries is meshed using boundary elements. For simplicity, the Delany-Bazley model for the impedance [90] is adopted in the current work to model the sound reflection from a partially absorbing ground surface:

$$z_n' = 1 + 9.08 \left(\frac{1000f}{\sigma_e}\right)^{-0.75} - 11.9i \left(\frac{1000f}{\sigma_e}\right)^{-0.73} \tag{4.8}$$

where z_n' is the surface normal impedance normalised by the impedance of air $\rho_0 c_0$, σ_e is the equivalent flow resistivity and f is the frequency.

Chapter 4

4.1.2   Monopole sources in 2.5D

In 3D, monopole sources can be represented with pulsating spheres, see Figure 4.1(a), but this is not possible in a 2.5D waveguide approach. An equivalent result can be found by using a circle in the y-z plane, see Figure 4.1(b). The boundaries of the circle are given unit normal velocity and a spatial window is applied in the x direction with its shape set through its wavenumber spectrum. The distribution of the velocity is chosen to be constant in the x direction over a length corresponding to twice the radius of the circle a, such that:

$$v_n(x) = \begin{cases} 1 & x \in [-a, a] \\ 0 & x \notin [-a, a] \end{cases} \tag{4.9}$$

The corresponding velocity in the wavenumber domain is given by

$$\tilde{v}_n(k_x) = 2\frac{\sin(k_x a)}{k_x} \tag{4.10}$$

As a consequence, the source in 2.5D corresponds to a pulsating cylinder of radius a and length $2a$. Additionally, as the geometry of the source extends indefinitely in the x direction, the numerical model contains a cylinder that is rigid for $|x| > a$. The pulsating sphere and the corresponding 2.5D model have the same source strength.

(a)   (b)
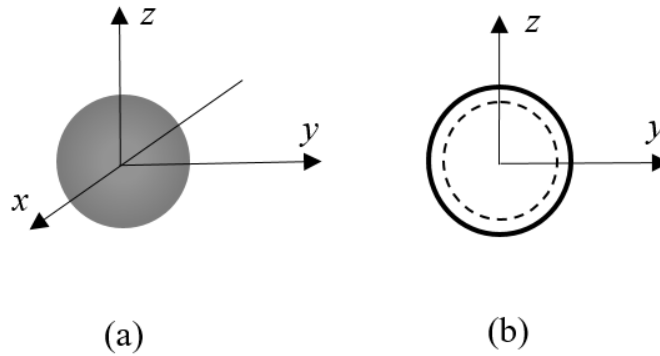
Figure 4.1. A sphere and its cross-section in y-z plane. (a) A pulsating sphere; (b) the cross-section in the y-z plane.

The velocity distribution in the x direction and in the wavenumber domain are plotted below in Figure 4.2(a) and (b) respectively.
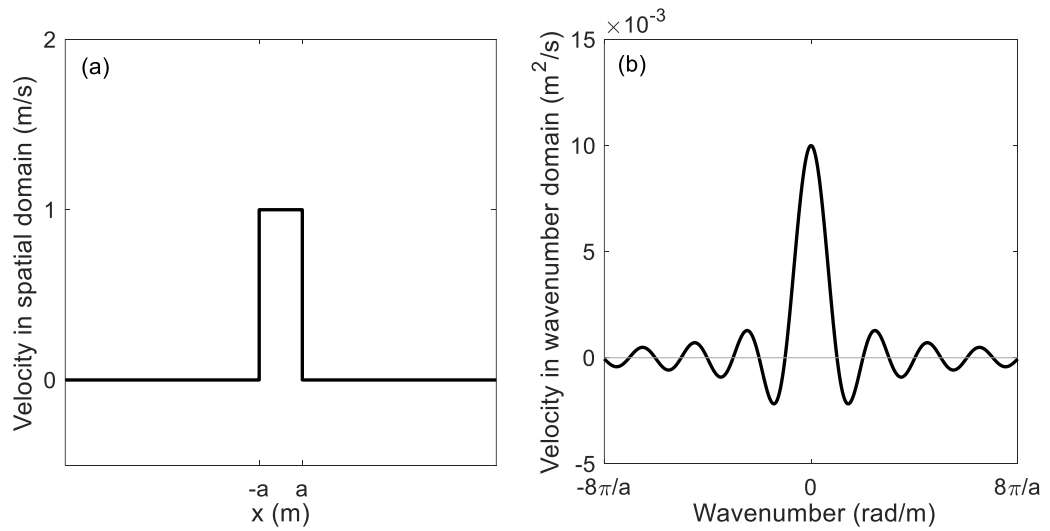
Figure 4.2. (a) Velocity distribution of the monopole source in the *x* direction and (b) its wavenumber spectrum.

To verify the validity of this representation of the source, the sound pressure levels around the monopole-like source calculated by using the 2.5D model (36 linear elements were used to represent the source) were compared with the theoretical results for a pulsating sphere [51]. In the 2.5D model, the volume velocity was fixed as 10^{-5} m^3/s and the source radius was varied from 0.001 m to 0.1 m. The frequency varies from 100 Hz to 5 kHz. The comparisons were first made in terms of the sound pressure levels at a set of receivers at different distances from the source in the *x-y* plane and in the *y-z* plane, and second receivers were on a circle 5 m away from the source centre, in both the *x-y* and *y-z* planes. The definition of the two planes is illustrated in Figure 4.3.
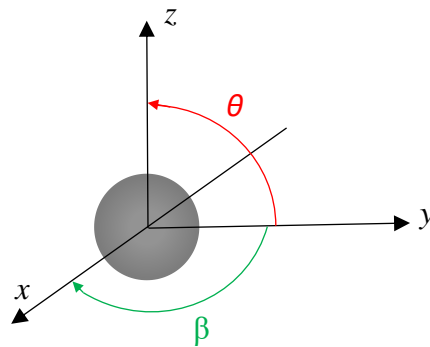
Figure 4.3. The definition of the coordinates for the source.

Figure 4.4 shows the sound pressure at different distances from the source centre in both the *x-y* and *y-z* planes obtained by fixing the volume velocity but varying the source radius from

0.001 m to 0.02 m. It is found that the numerically predicted sound pressure levels are almost identical to the analytical values within less than 0.3 dB difference and the influence due to the radius of the circle is negligible as long as it is small enough.
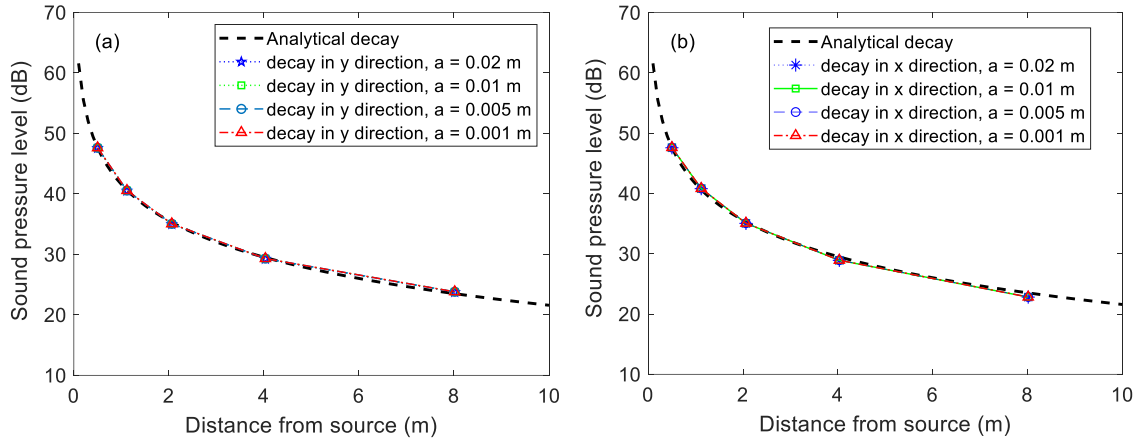
Figure 4.4. Sound decay comparisons (in dB) around a pulsating sphere with volume velocity 10^{-5} m^3/s in corresponding 2.5D model, radius 0.005 m, at 200 Hz. (a) in the *y-z* plane along the *y* direction. (b) in the *x-z* plane along the *x* direction.

The comparisons were also made in terms of the sound pressure levels at the receivers on a circle 5 m away from the source centre, in both the *x-y* and *y-z* planes. A similar trend was found. Figure 4.5 gives an example of the sound pressure levels obtained from the 2.5D model compared with the analytical solutions at 1000 Hz for a source radius of 0.005 m. In the *y-z* plane, the 2.5D prediction and the analytical solution are almost the same. In the *x-y* plane, the prediction has some fluctuations at around 90° and 270°, but the maximum errors between the prediction and the analytical values are still close within 0.3 dB difference. The results at other frequencies are similar, not shown here. The comparisons demonstrate that the 2.5D model proposed for a monopole source can be used reliably.

(a)   (b)
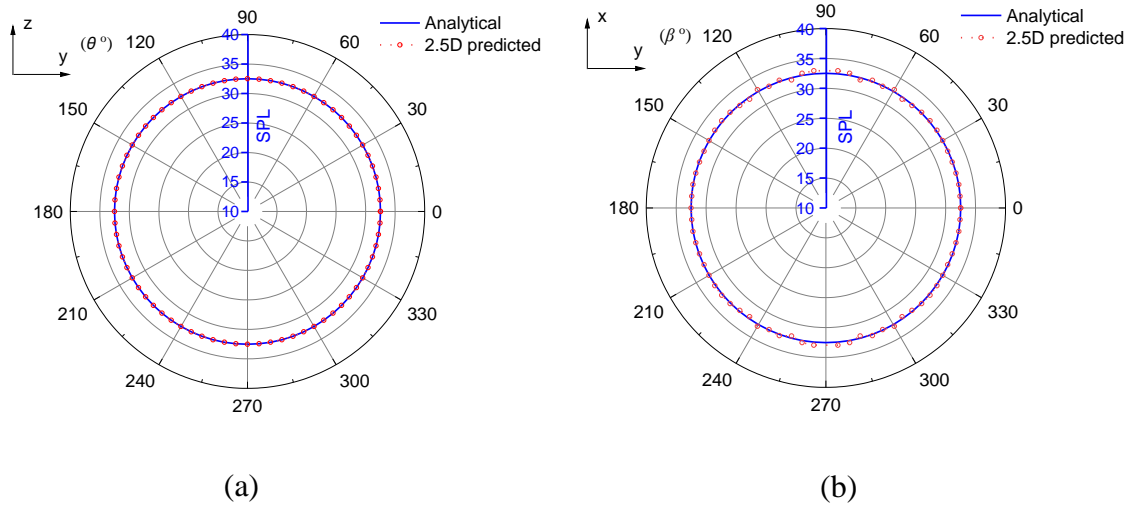
Figure 4.5. Sound pressure level distribution (in dB) around a pulsating sphere with volume velocity 10^{-5} m^3/s and corresponding 2.5D model, radius 0.005 m, at 1000 Hz. (a) In *y-z* plane; (b) in *x-y* plane.

The maximum errors between the 2.5D predictions and the analytical solutions are plotted against the product of the acoustic wavenumber and the radius of the source in Figure 4.6.
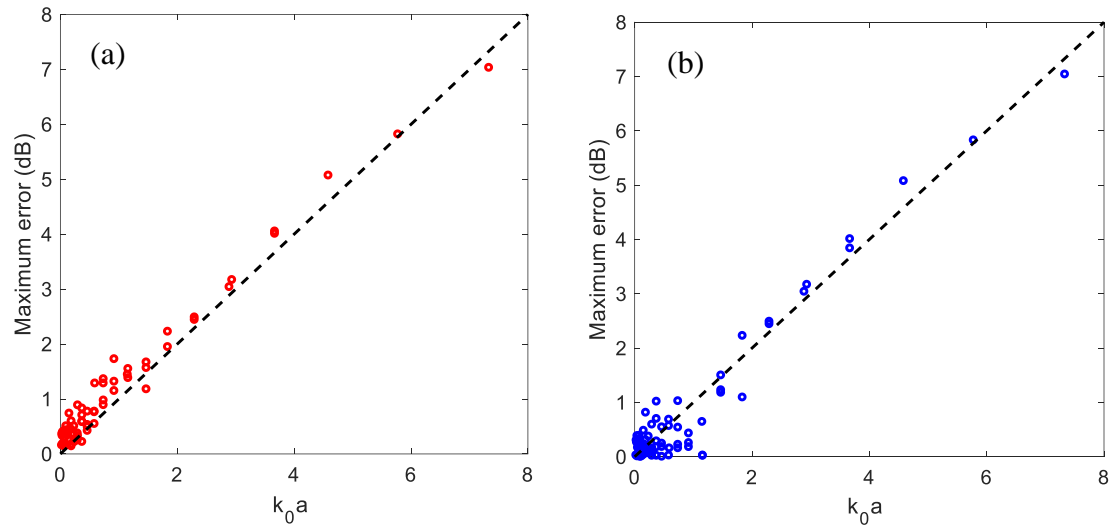
Figure 4.6. (a) Maximum errors for receivers in the *x-y* plane, (b) maximum errors for receivers in the *y-z* plane.

It is found from Figure 4.6 that the difference between the predictions and the analytical solutions increases with increasing $k_0 a$. It is suggested to make $k_0 a$ less than 0.5 to achieve less than 1 dB error. Because the frequency bands are fixed, by making *a* small, its influence can be minimised.

4.1.3   Dipole sources in 2.5D

In a similar way, a dipole source in 3D is represented by an oscillating sphere, see Figure 4.7(a). It is simulated in the 2.5D model by applying the velocity pattern of an oscillating sphere to a circle in 2.5D, see Figure 4.7(b). The normal velocity in the y-z plane can be expressed as $v_n(y,z) = v\cos\theta$, where θ is the angle between the vector that is in the circle's normal direction and the oscillating axis. The velocity distribution in the x-z plane is the same as that in y-z plane, just replacing y by x. Similar to the monopole source, the 2.5D model represents approximately an oscillating cylinder of radius a and length $2a$ for the dipole source. Additionally, as the geometry of the source extends indefinitely in the x direction, the numerical model again contains a cylinder that is rigid for $|x| > a$.

(a)   (b)
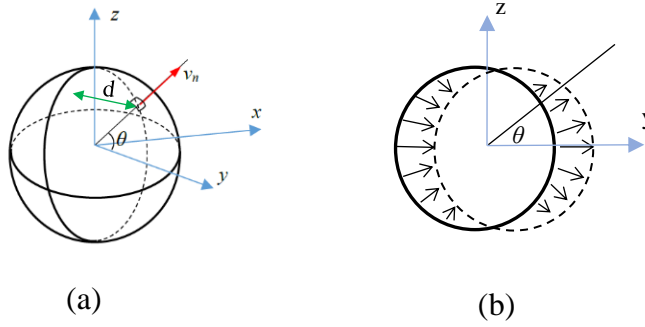
Figure 4.7. (a) An oscillating sphere, (b) the cross-section in the y-z plane.

For the convenience of applying the Fourier transform to the velocity in the x direction, the velocity distribution in the x-z plane is expressed as a function of x, as

$$v_n(x) = \begin{cases} v\cos\left(\dfrac{2\pi}{4a}x\right) & x \in [-a, a] \\ 0 & x \notin [-a, a] \end{cases}$$
(4.11)

and the corresponding velocity in the wavenumber domain is given by

$$\tilde{v}_n(k_x) = v\left[\frac{\sin\left[\left(k_x + \dfrac{\pi}{2a}\right)a\right]}{k_x + \dfrac{\pi}{2a}} + \frac{\sin\left[\left(k_x - \dfrac{\pi}{2a}\right)a\right]}{k_x - \dfrac{\pi}{2a}}\right]$$
(4.12)

The representation of the velocity in the spatial and in the wavenumber domain is shown in Figure 4.8(a) and (b) respectively.
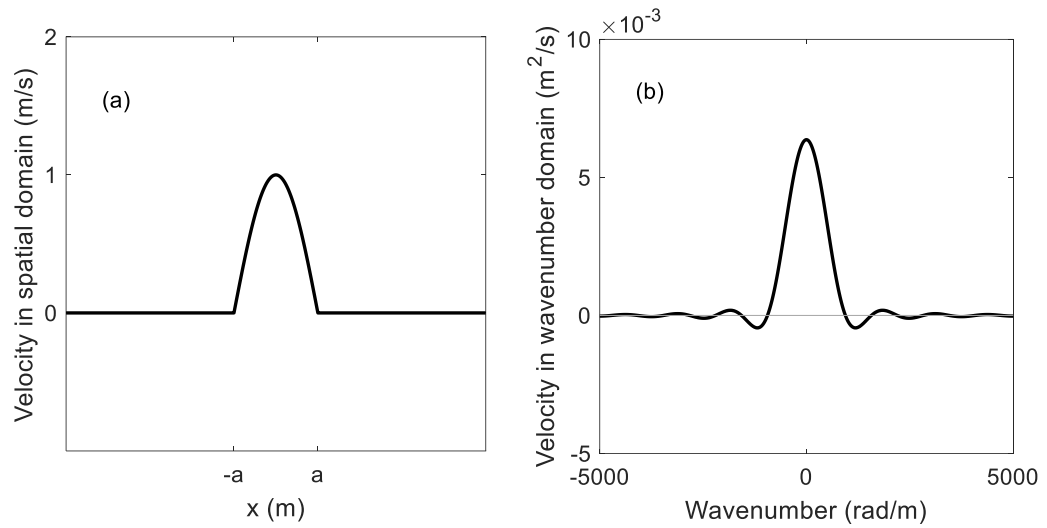
Figure 4.8. (a) Velocity distribution of the dipole source in the *x* direction and (b) its wavenumber spectrum.

As the source strength of a dipole depends on the distance between the positive and negative parts of the source as well as their individual strengths, its size should be taken into account in determining the source strength to be used in the 2.5D model that corresponds to a particular dipole. Assuming that the amplitude of the oscillating velocity of the surface is $\mathbf{V}$, the dipole source strength of the oscillating sphere (or of the 2.5D model) can be calculated by

$$Q = \int_S (\mathbf{V} \cdot \mathbf{d}) \mathrm{d}S \qquad (4.13)$$

where $\mathbf{d}$ is the distance vector to the surface from its centre and S is the surface area. The dipole source strength of an oscillating sphere of radius a is $\pi a^3 V$ (where V is the magnitude of the oscillating velocity) and that of the 2.5D model is $4a^3 V$. Thus, for an oscillating sphere and the corresponding 2.5D model of the same radius, a factor of $\pi/4$ is required between their velocities.

To check the validity of the 2.5D model, it has been used to predict the sound distribution around an oscillating sphere with different radii and at different frequencies. It is found that the maximum error between the 2.5D predictions and the analytical solutions increases with the product of the acoustic wavenumber and the source radius, similar to what has been found for the monopole case. Figure 4.9 gives an example of the sound pressure levels obtained from the 2.5D model compared with the analytical solutions at 1000 Hz for an

oscillating sphere with radius 0.005 m (36 linear elements were again used to represent the source in the 2.5D model). The sound distribution at the receivers on a circle 5 m away from the source centre around the dipole with fixed oscillating velocity 1 m/s is calculated. The numerically predicted sound distribution in either the *y-z* plane or the *x-y* plane is almost identical to the analytical values. As expected there are some fluctuations when β is approaching 90º and 270º, which can be seen from Figure 4.9(b), but as the sound pressure levels at these angle regions are small, they will not affect the validity of the 2.5D model. The results at other frequencies are similar, not shown here.

(a) (b)
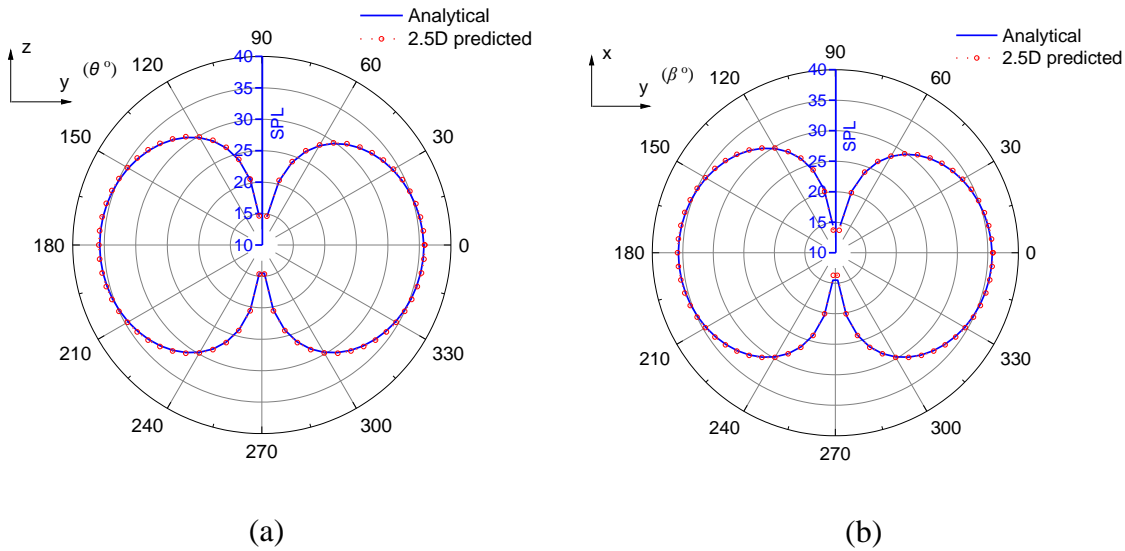
Figure 4.9. Sound pressure level distribution (in dB) around an oscillating sphere and corresponding 2.5D model, oscillating velocity 1 m/s, radius 0.005 m, at 1000 Hz. (a) In *y-z* plane, (b) in *x-y* plane.

4.2 Rolling noise

4.2.1 Modelling wheel noise by using 2.5D model

The sound radiation from a train wheel can be divided into the axial and the radial components [2] and they can be represented approximately as a monopole and a horizontal dipole respectively, which has been explained in Chapter 3. In the 2.5D model, the radial component is modelled by implementing a monopole-like source and the axial component is modelled by giving a lateral oscillation to the same fundamental source (equivalent to a dipole). In the 2.5D BE model, the velocities of the sources are set to unity and the final results are re-scaled by the sound power levels calculated in TWINS.

As in Chapter 3, a wheel with diameter of 0.86 m is studied, and it is represented in the 2.5D model by using a point source located at its geometrical centre. This has been compared with a model in which three point sources at different heights were used to represent the wheel, but it is found that the sound pressure spectra at the receivers on the train side surfaces above the bogie obtained from the two models are similar. The difference in terms of overall sound pressure levels at those receivers was less than 0.5 dB. Therefore only a single point source is used in this work to reduce the computational cost.

4.2.2   Modelling rail noise by using 2.5D BE model

The rail is an extended source in the longitudinal direction which can be represented directly by its vibrating surface using the 2.5D BE method. For simplicity cross-section deformation of the rail [2] is not included in this study, although it could be included by using a 2.5D FE model of the rail [17] instead of the Timoshenko beam model. The noise radiation from the vertical and lateral vibration of the rail are considered separately. The response of the rail to a unit force is calculated in terms of the transfer mobility $Y(x)$ of the rail at a distance x from the excitation point and circular frequency ω from a model of a Timoshenko beam on a continuous two-layer foundation [2]. The expression of the transfer mobility is given in Equation (3.6) in Section 3.2.2. Mobilities at two frequencies are shown in Figure 3.8.

Applying a Fourier transform to the mobility in the spatial domain (Equation (3.6)), the velocity in the wavenumber domain due to a unit force can be expressed as

$$\tilde{Y}(k_x) = u_1 \left(\frac{1}{\mathrm{i}(k_r + k_x)} + \frac{1}{\mathrm{i}(k_r - k_x)} \right) - \mathrm{i}u_2 \left(\frac{1}{\beta + \mathrm{i}k_x} + \frac{1}{\beta - \mathrm{i}k_x} \right) \qquad (4.14)$$

where k_x is the wavenumber in the x direction introduced by the Fourier transform, which runs from $-\infty$ to ∞. The mobilities in the wavenumber domain corresponding to the mobilities in the spatial domain in Figure 3.8 are shown in Figure 4.10. At high enough frequency, once the waves have cut on in the rail, the wavenumber spectrum is dominated by the free wavenumber in the rail; at 2 kHz this can be seen as the peak at about 8 rad/m (compare Figure 3.7(a)). However, below 300 Hz waves have not cut on in the rail and no distinct peak is seen in the wavenumber spectrum.
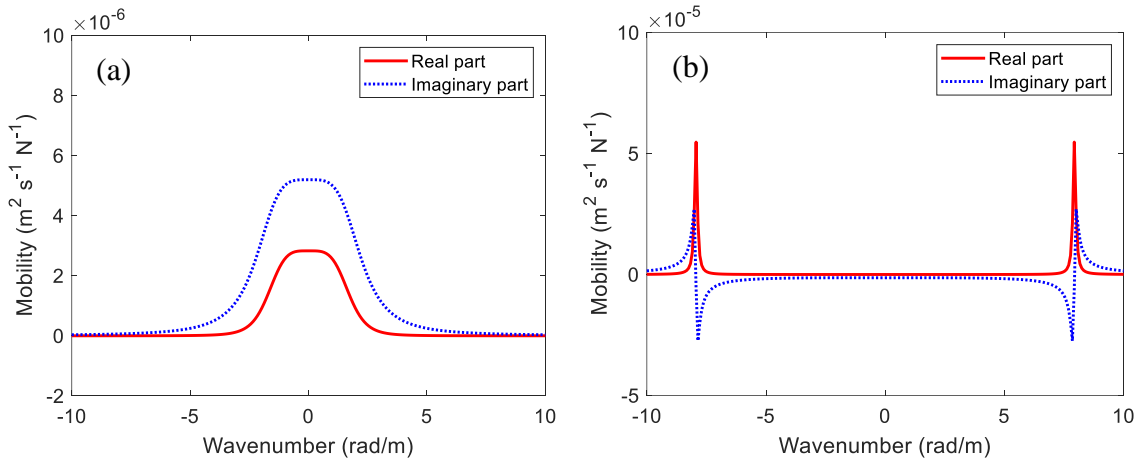
Figure 4.10. Rail mobility in the wavenumber domain, (a) 100 Hz; (b) 2000 Hz.

When k_x is smaller than the wavenumber in the air, the structural waves will produce propagating sound waves. In such a situation, the vibration of the rail radiates sound efficiently. However, when k_x is greater than the wavenumber in air, near-field sound waves will be generated and these structural waves radiate sound inefficiently. However, the near-field sound waves cannot be neglected, especially at low frequency and in the region relatively close to the source. Neglecting them would introduce errors in the inverse Fourier transform when converting the sound pressure back to the spatial domain.

Finally, to obtain the radiation from the rail, the mobility in the wavenumber domain is applied as a velocity boundary condition to the boundary elements representing the rail cross-section. The rail cross-section is assumed to move uniformly in either vertical or lateral direction; the vibration in the vertical and lateral directions is dealt with separately. The boundary conditions are visually represented in Figure 4.11(a) for the vertical direction and in Figure 4.11(b) for the lateral one.
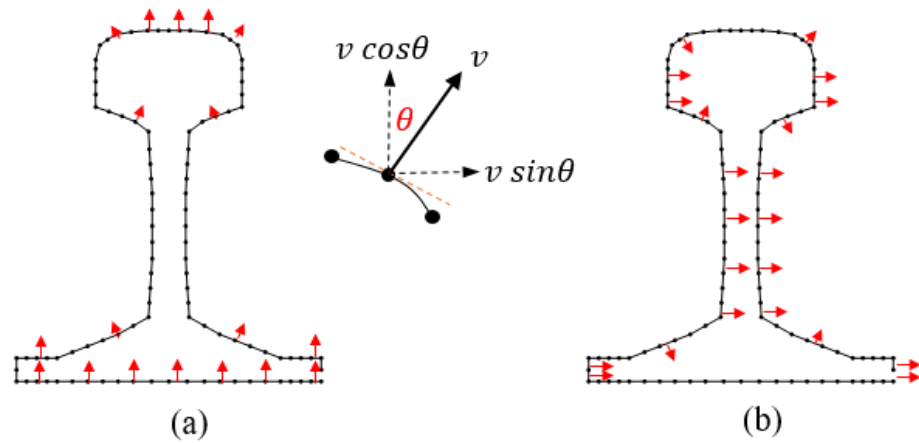
Figure 4.11. General view of velocity on the rail cross-section, the vertical and lateral components are studied separately. (a) Vertical vibration, (b) lateral vibration.

To verify the validity of the 2.5D rail model in predicting its sound radiation, a simple case is used. A single rail is represented in the 2.5D model and it is radiating in free space, see Figure 4.12. Comparison of the sound pressure distribution along the rail is made between the 2.5D model and the equivalent source model [16] that has explained in Section 3.2.2. The parameters used for the rail are taken from [16] for comparison. A receiver is located at $(y, z) = (1, 1.3)$ m in the plane of the cross-section of the rail to calculate the sound pressure in the wavenumber domain and this was transformed to the spatial domain to obtain the spatial decay of the sound along the rail axis direction (the x direction).
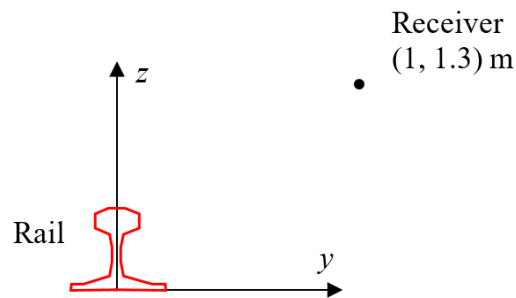
Figure 4.12. Noise from the rail by using the 2.5D model.

The comparisons are made in terms of the sound pressure due to the vertical vibration of the rail, and the results are plotted in Figure 4.13. Results are shown at two frequencies as example. The results at other frequencies are similar, so not shown here. In the equivalent source model the spacing of the point sources is chosen as $1/k_0$ (k_0 is the acoustic wavelength at the considered frequency) and in the 2.5D BE model the spacing of wavenumber is $\pi/100$.

From Figure 4.13, it can be concluded that the sound pressure levels predicted by the 2.5D model and by the equivalent source model have very close agreement although with small differences in sound pressure levels. At 125 Hz there is a difference of about 1 dB at 15~20 m and at 1600 Hz some fluctuations appear at 0~2 m causing a maximum difference of 1.2 dB.
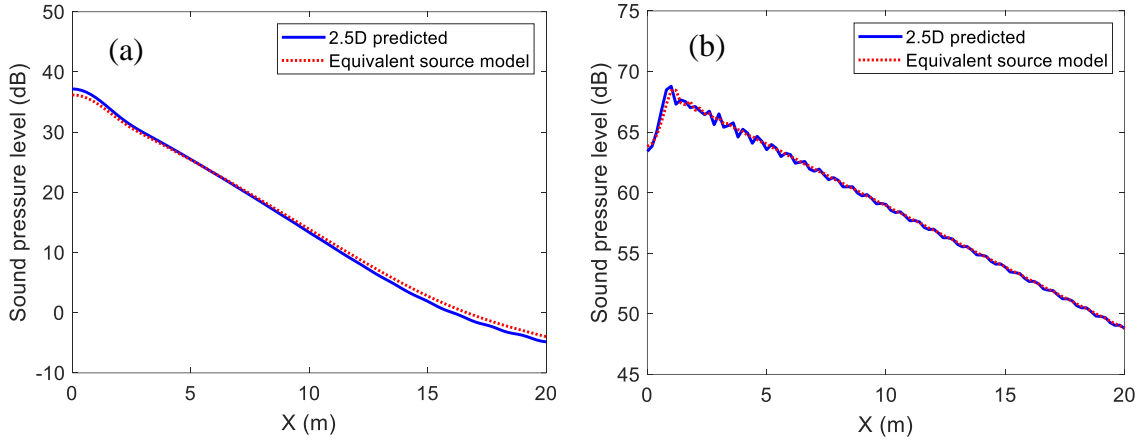
Figure 4.13. Comparison of sound pressure between 2.5D BE model and the equivalent source model. (a) 125 Hz, (b) 1600 Hz.

4.2.3   Modelling the sleeper noise by using a 2.5D model

The vibration of the sleepers is also required to determine their contribution to the noise in the 2.5D model. The vibration of the sleepers can be derived from the rail mobility and from the ratio of the sleeper displacement to that of the rail. This has been explained in Section 3.2.3 and the expression of the ratio is presented in Equation (3.8).

In ballasted track, the sleepers are embedded in ballast, so the vibrational velocity is only given to their top surfaces. Moreover, the 2.5D model treats the sleepers as a continuous medium in the x direction. To account for their discrete distribution and for the spacing between them, scaling factors are needed to adjust the sound power calculated from the 2.5D model. It was found that [91], at high frequency where the acoustic wavelength is smaller than the sleeper spacing, the sound power needs to be adjusted by a factor corresponding to the ratio of the sleeper width to the sleeper spacing. At low frequency, where the wavelength is larger than the sleeper spacing, the scaling factor corresponds to the square of that ratio. In this case the sleeper spacing is 1 m and the sleeper width is 0.2 m. The scaling factor is $1/5$ above 340 Hz and $1/5^2$ below it. The sound power obtained with the Rayleigh integral

approach [92] and the 2.5D BE model prediction after being corrected with the scaling factor are compared in Figure 4.14. The results obtained by the 2.5D model and the Rayleigh integral approach have close agreements above 800 Hz and with some difference at low frequency. The averaged difference in sound power level between the two models is 2 dB.
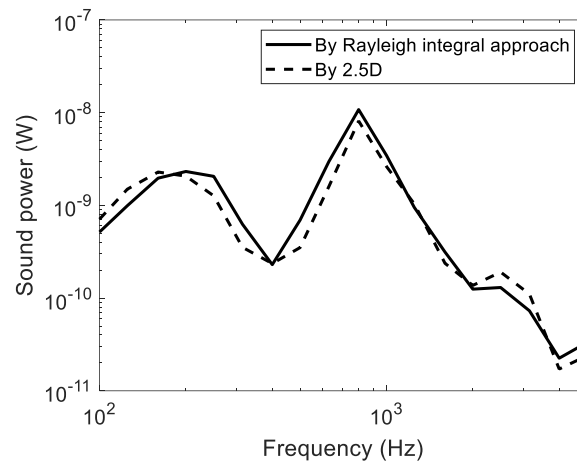
Figure 4.14. Sound power from the sleepers for a unit force on the rail.

4.3   2.5D model for noise on train side and roof

Rolling noise is generated beneath the train floor, so it cannot propagate directly to the train sides and roof, see Figure 4.15. Sound incident on the sides and roof is caused by diffraction. 2.5D BE models have been created to predict the noise on the train external surfaces. In the 2.5D models, the train is represented by its cross-section. The equipment mounted on the train floor is ignored, so the sound incident on the train floor obtained by the 2.5D models is expected to be less accurate than the SEA model introduced in Chapter 3. The 2.5D models are only used to calculate the sound incident on the train sides and roof.

The train cross-section is represented by boundary elements. A part of the ground is also modelled by boundary elements and they are assigned impedance boundary conditions. In these numerical models, the modified Green's function is used, which represents a half-space ground extending beyond the absorptive region.

The wheels, the rails and the sleepers are considered as separate sources in the 2.5D models and the different components. The rail is represented by its cross-section and the wheel is represented by point sources with small radius. The size of the elements needs to be at least

less than a quarter of the acoustic wavelength at the frequency of interest and they also should be dense enough to represent the profile of the rail or circle.
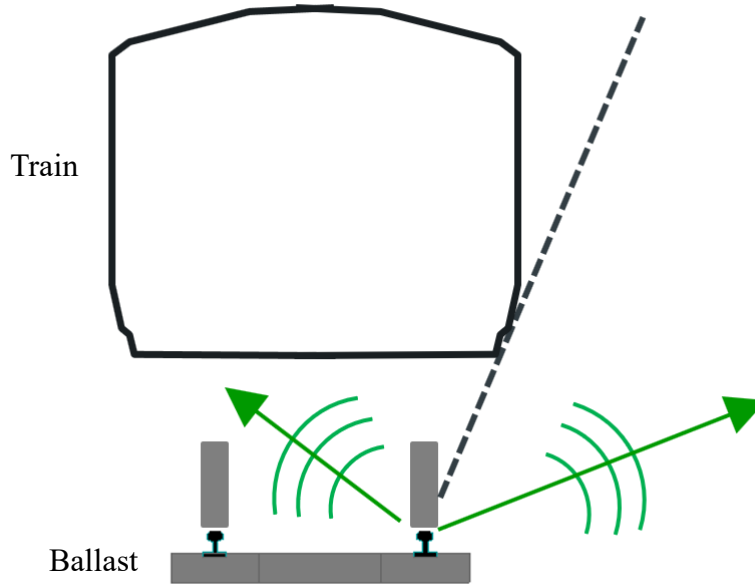
Figure 4.15. 2.5D model for calculating sound incident on train external surfaces.

The 2.5D models give the sound pressure on the train cross-section in the wavenumber domain. After applying the inverse Fourier transform, the sound pressure distribution in the spatial domain is obtained. Then the sound pressure on the train surfaces is determined from an incoherent sum of the contributions of the wheel radial and axial components, the rail vertical and lateral components, and the sleepers.

4.4   Experimental validation using laboratory measurements

To validate the modelling approach used to predict the sound distribution on the train external surfaces, results from two different sets of measurements have been used. First, laboratory measurements were performed in the anechoic chamber at the University of Southampton, which are presented in this section. The 1:5 scale model has been introduced in Section 3.6 and a similar experimental set up is used here, shown in Figure 4.16(a). With this arrangement, the sound pressure distribution around the scale model railway vehicle was determined.

4.4.1 Point source

The same compact source has been used as described in Section 3.6. The orifice of the source was located beneath the train floor, directly above one of the rails and 0.32 m from one of its ends, see Figure 4.16(b). Microphones were located along the centrelines of the four external surfaces of the train: floor, two walls and roof. On each surface, there were 21 measurement locations with a spacing of 0.1 m, which are illustrated as points P1, P3, P4, P5 in the corresponding numerical model in Figure 4.17. Another set of microphones was placed along the upper right corner on the side face, illustrated as P2.
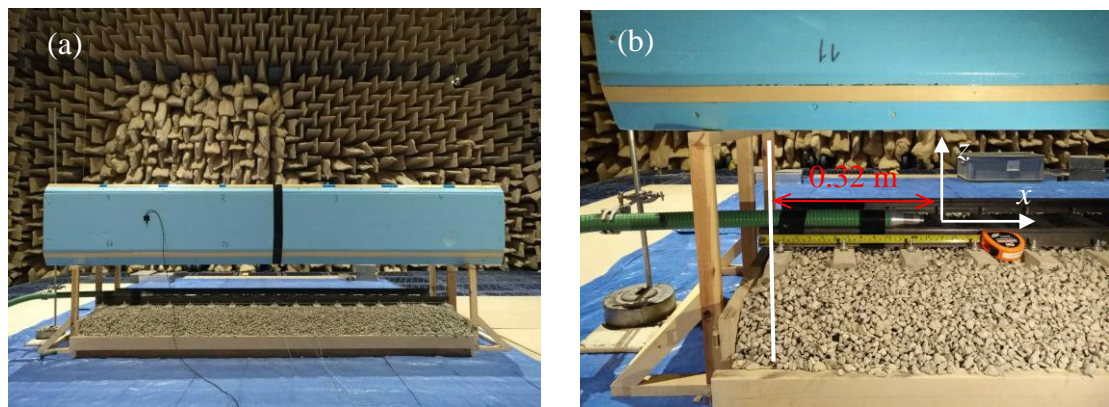
Figure 4.16. Measurement arrangement in laboratory test for point source, (a) overview and (b) source location.

The receivers in the numerical model were located at the same locations as those in the measurements. The source was represented in the 2.5D model by a monopole, as described in Section 4.1, with a radius of 0.005 m. Its source strength was derived to give the same sound power spectrum in one-third octave bands as the source in the experiments. The ground (at height 0 m in Figure 4.17) was set to be rigid in the 2.5D model and the ballast was modelled by a rectangular box with an impedance boundary condition on its top surface and with rigid condition on the sides. The impedance of the scale ballast is calculated by the Delany-Bazley model [90] with measured ballast properties [93]. Linear boundary elements are used to create these models. 36 elements are used to model the fundamental sources representing the wheel. The sizes of the elements used for the train cross-section and the ballast box are 0.01 m, which should be sufficient for frequencies up to 5 kHz. Five 'CHIEF' points are set inside the train, and three are in the ballast box to overcome the non-uniqueness problem associated with resonances of the corresponding interior problem [94].
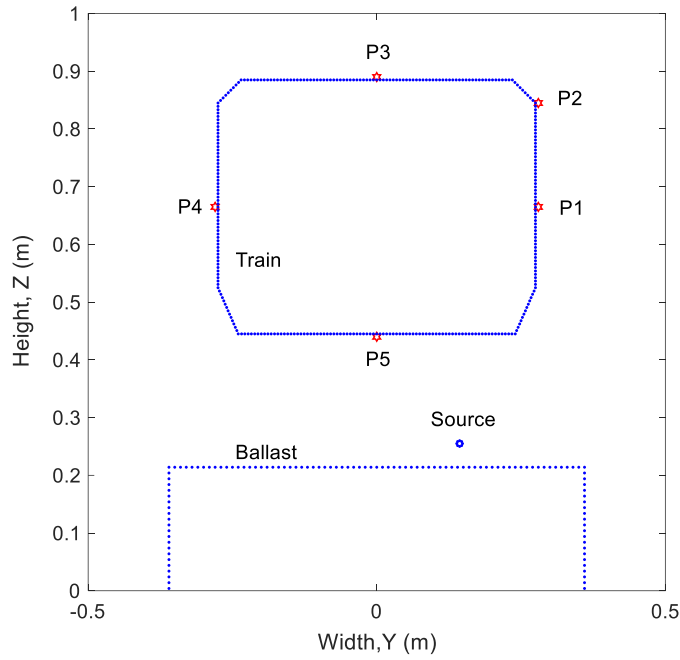
Figure 4.17. Geometry of the 2.5D BE model used for predicting wheel noise on train outside surfaces of the scale model.

Figure 4.18 shows a comparison of the predicted sound levels with the measured ones at P2 (the upper right corner position) for these four frequency bands. The distance x is shown relative to the location of the source. These results are shown for the 1000 Hz, 1600 Hz, 2500 Hz, and 4000 Hz one-third octave bands for the scale train model. These correspond to 200 Hz, 315 Hz, 500 Hz and 800 Hz at full scale. In the numerical models, results were calculated at three frequencies in each band and averaged to obtain the sound pressure level in the band.
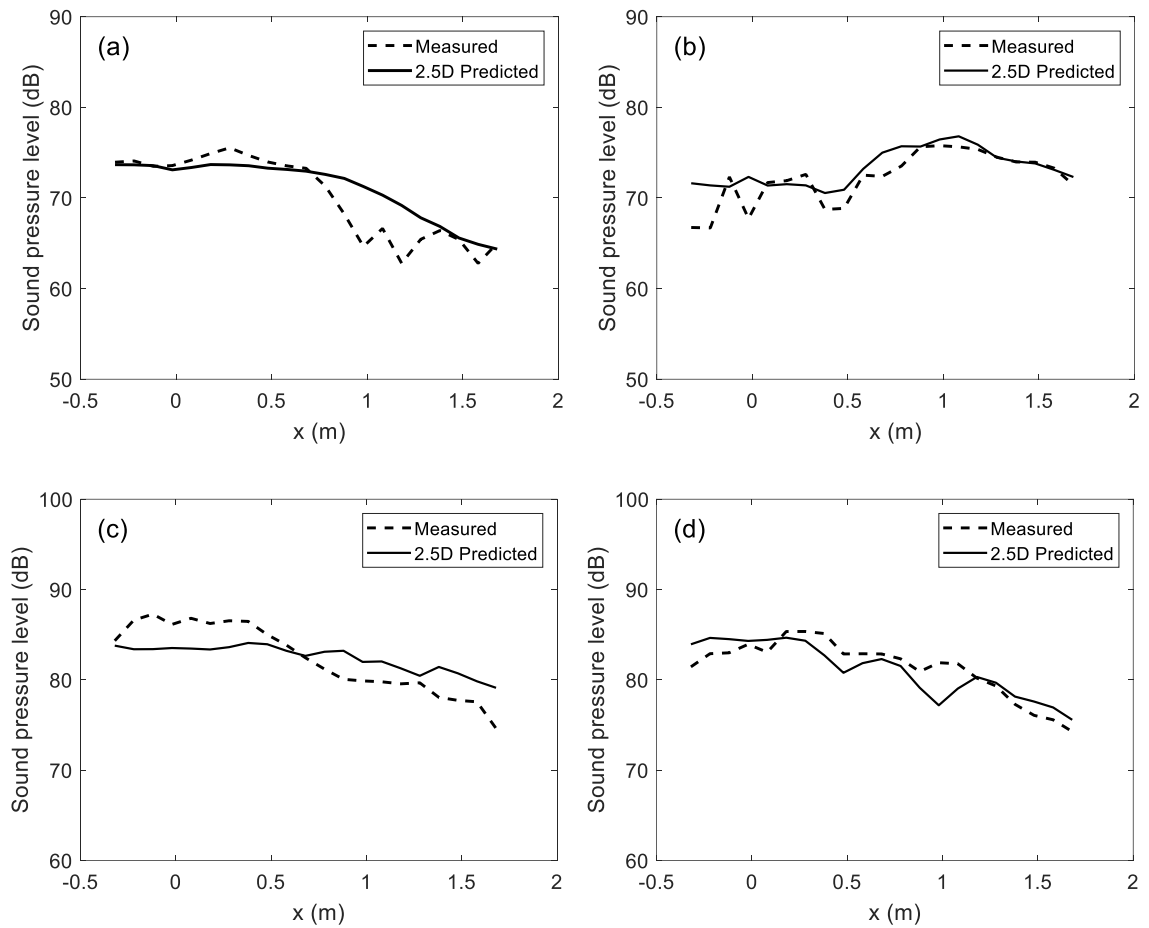
Figure 4.18. Sound decay comparison in four one-third bands at the right up corner point. (a) 1000 Hz, (b) 1600 Hz, (c) 2500 Hz, (d) 4000 Hz.

Figure 4.19 shows the equivalent results for receivers on the four different train surfaces. These results are given for the 4 kHz one-third octave band as an example, the results in the other one-third octave bands being similar.
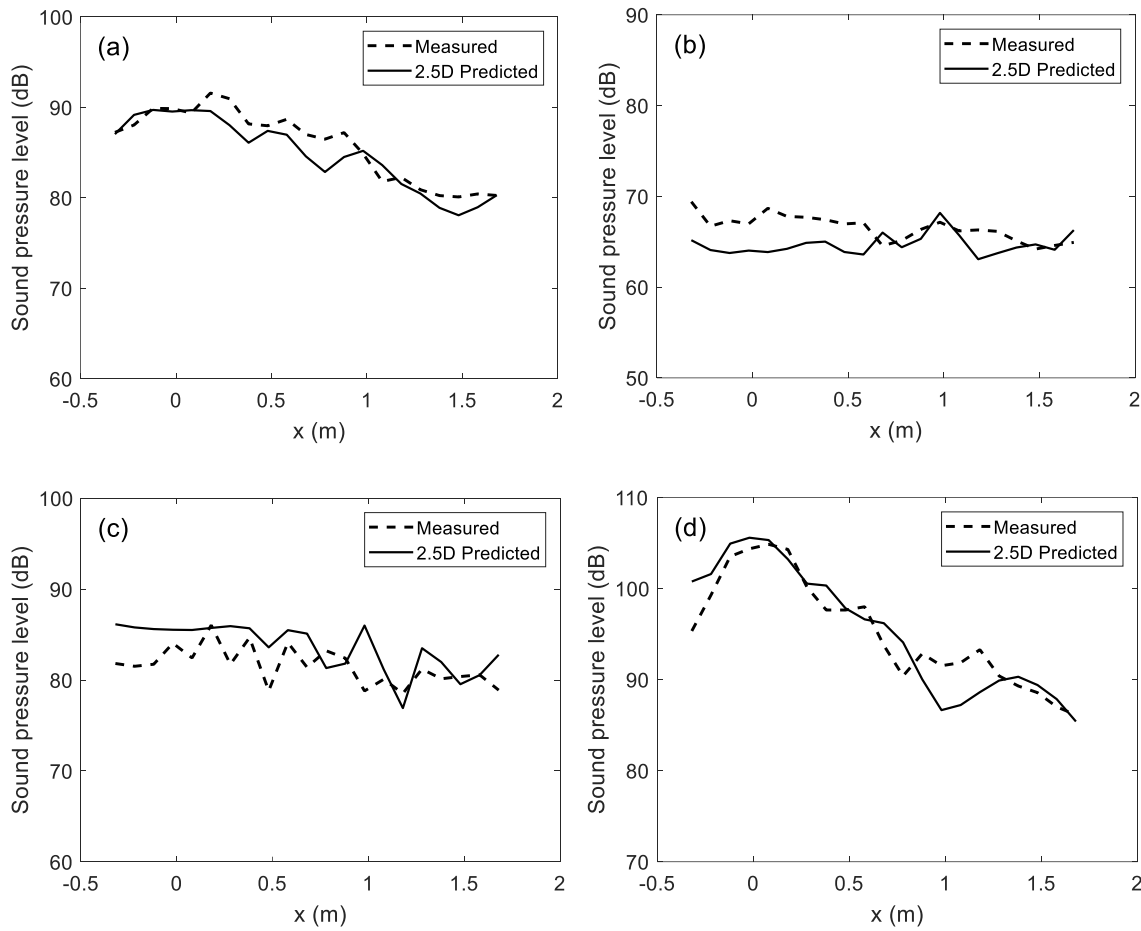
Figure 4.19. Sound decay comparison at the four surfaces in the 4 kHz band. (a) On the right side, P1, (b) on the top, P3 (c) on the left side, P4, (d) on the bottom, P5.

From Figure 4.18 and Figure 4.19, it can be concluded that the 2.5D BE approach is able to give reasonable predictions of the sound pressure levels on the train external surfaces due to a point source below it. The maximum errors at each measured position (predicted level-measured level) and the average level difference between the predictions and the measurements are listed in Table 4.1 for each frequency band. As the 2.5D model corresponds to an infinite carriage, the truncation at the end of the carriage might affect the agreement, so when calculating the difference between the predictions and the measurements, the two data points at each end are ignored. At the upper right corner position P2, the average difference between the prediction and the measurement is less than 3 dB in most of the 1/3 octave bands. The maximum difference at position P2 is found in the 2000 Hz one-third octave band and at the measurement positions located close to one of the ends of the carriage. The results in Table 4.1 indicate that the 2.5D model gives better predictions of the sound pressure on the bottom and the side surface that is closer to the source. Larger errors are found at the receivers on the top and the side that is further from the source.

Table 4.1. Level differences between predictions and measurements for point source below the scale model train body (dB). Maximum and average difference over 17 points at each location.

Position Freq (Hz)	P 1 Near side		P 2 Upper corner		P 3 Top		P 4 Far side		P 5 Floor	
	Max.	Ave.	Max.	Ave.	Max.	Ave.	Max.	Ave.	Max.	Ave.
1000	8.3	2.8	6.6	1.1	11.1	-3.8	4.6	2.0	2.9	-1.7
1250	5.7	-1.7	5.3	-0.9	4.5	0.2	3.0	-1.2	6.3	-2.9
1600	2.8	0.2	4.6	0.8	6.9	-0.7	5.6	2.4	4.9	1.0
2000	8.3	3.1	7.6	2.6	6.7	-2.3	10.7	4.8	4.2	-1.5
2500	3.5	-1.2	3.9	-0.1	10.4	-3.6	6.6	1.7	7.1	2.9
3150	5.7	1.1	7.3	1.9	6.8	-2.6	6.4	2.6	9.0	3.6
4000	3.6	-1.2	4.7	-0.7	4.8	-1.9	7.1	1.8	4.8	-0.3

4.4.2   Sound radiated by the rail

Measurements were also carried out on the 1:5 scale model to determine the sound pressure caused by vibration of the rail, see Figure 4.20. A reciprocal approach [95] was followed to infer the sound pressure distribution on the train external surfaces due to a vibrating rail. According to the principle of vibro-acoustic reciprocity, the transfer function between a point force F acting on a structure at a point A and the resulting sound pressure p at a receiver B is identical to the transfer function between a volume velocity Q of a point monopole located at the point B and the resulting vibration velocity v produced at the original excitation point A. Thus, if a unit force is acting on the rail, the resulting sound pressure on the train external surfaces can be obtained by placing a source on the train surfaces and then measuring the vibration velocity of the rail as excited by the sound field. The source orifice was located at various positions along the right upper corner line and on the centreline of the bottom surface and the rail vibration was measured by accelerometers located on the rail measuring in both vertical and lateral directions, see Figure 4.20(b). However, in the present work only the vertical accelerometer is used.
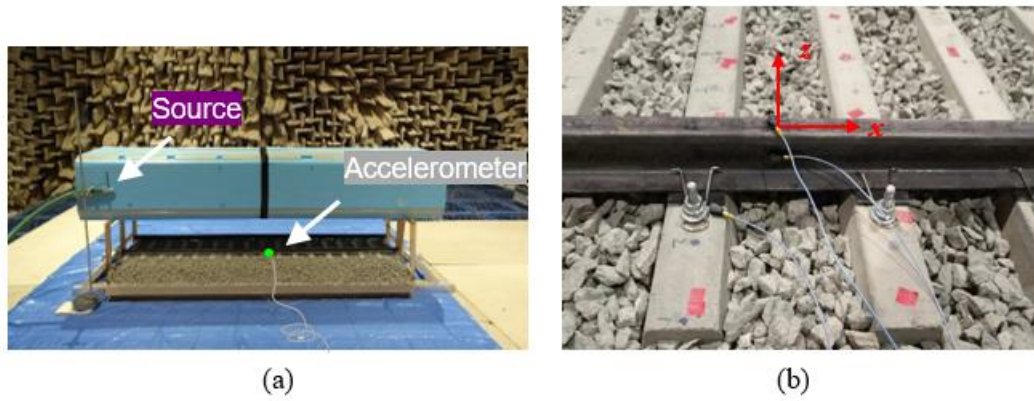
Figure 4.20. Measurement arrangement for the laboratory test for rail source and the accelerometer locations on the rail. (a) Overview, (b) close-up view of accelerometers.

A numerical model was created with the same geometry as that in the measurement, see Figure 4.21. The velocity of the rail under a unit force obtained from the Timoshenko beam model was assigned to the boundary elements representing the rail in the numerical model. The properties used for the track are listed in Table 4.2. The velocity of the sleeper was derived using the method given in Section 4.2.3. The absorption property of the ballast was modelled by using its impedance in the same way as before but this was only applied in the region outside the sleepers.
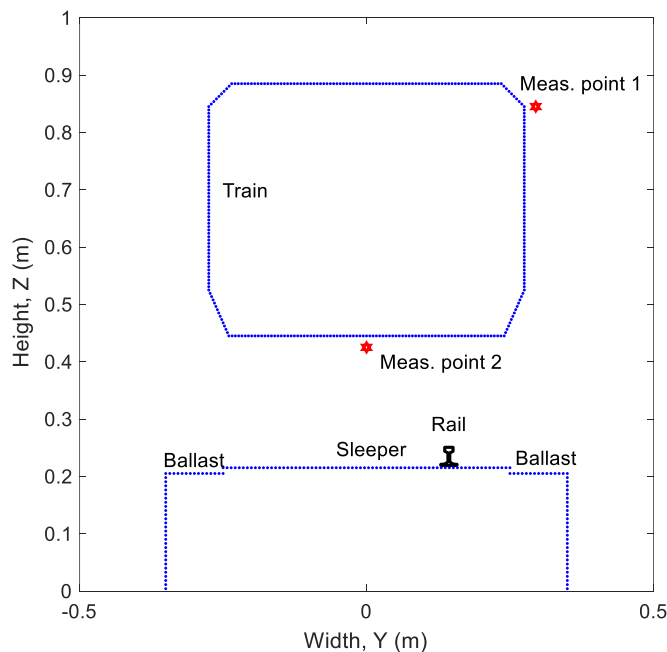
Figure 4.21. Geometry of the 2.5D BE model for predicting rail noise on train outside surfaces of the scale model.

Table 4.2. Parameters used for vertical motion of the 1:5 scale track [93].

Young's modulus	2.1×10^{11} N/m^2
Rail bending stiffness	0.01 MNm^2
Rail mass per unit length	3.4 kg/m
Rail damping loss factor	0.05
Rail density	7850 kg/m^3
Pad stiffness	15 MN/m
Pad damping loss factor	0.2
Sleeper mass (half)	1.41 kg
Sleeper spacing	0.12 m
Ballast stiffness (per half sleeper)	1.0 MN/m
Ballast damping loss factor	1.0

The comparisons between the predictions and the measurements were made for two positions, as shown in Figure 4.21. One, P1, is at the upper right-hand corner and the other, P2, is on the bottom of the train body. Based on the principle of reciprocity, the results obtained from the measurement correspond to the ratio of the sound pressure and the force, so they are compared with the predicted sound pressure on the train outside surfaces due to a unit force on the rail. These results are shown in Figure 4.22 for frequency bands between 1250 and 4000 Hz (between 250 and 800 Hz full scale). The spatial distribution of the rail vertical vibration is also plotted in the figure, from which it can be seen that the finite length leads to significant spatial variations that are not captured by the model of the infinite rail but the overall decay with distance is mostly captured.
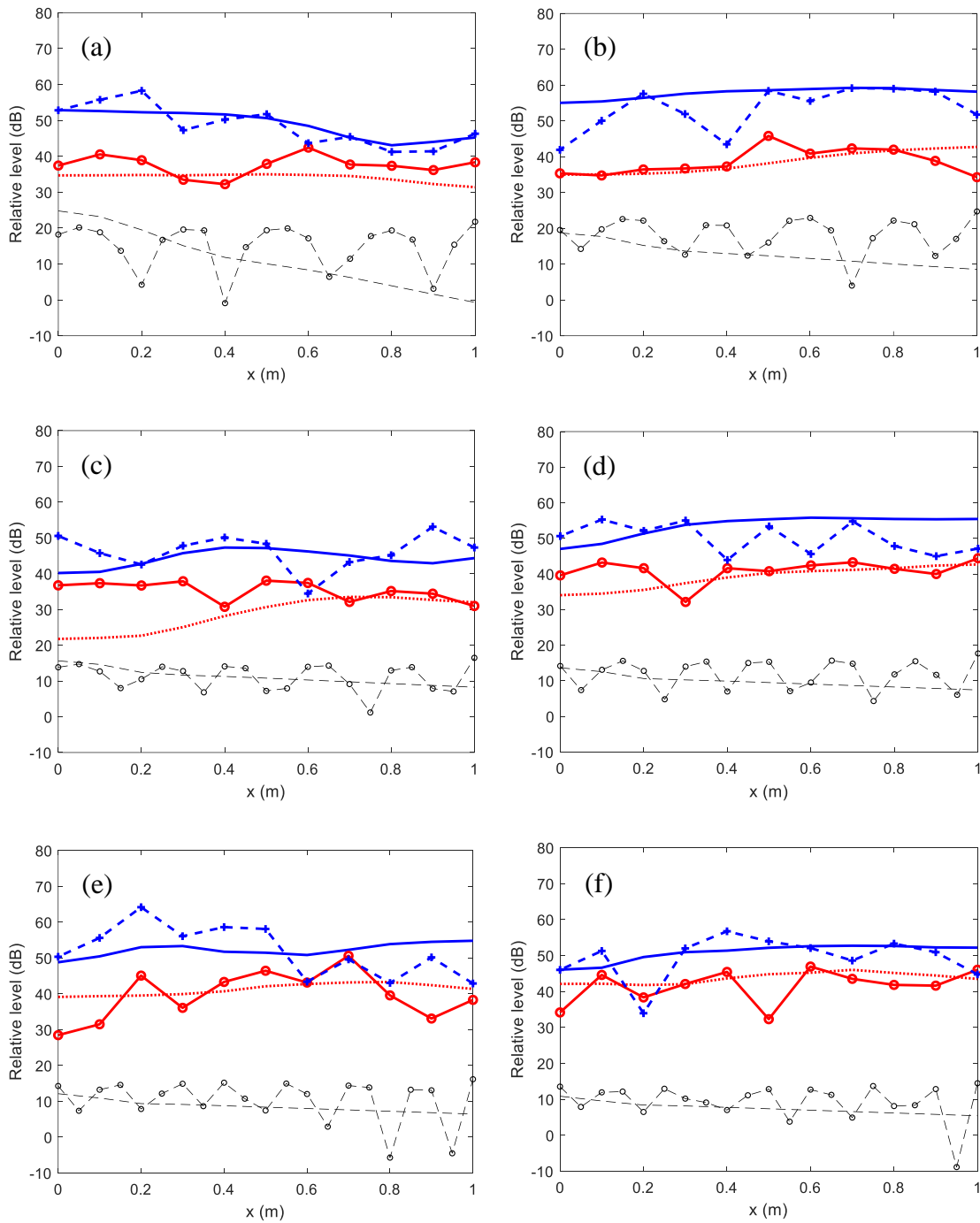
Figure 4.22. Comparisons between predictions and measurements of the sound pressure level (SPL) on the train external surfaces in one-third octave bands, where *x* is relative to the force location. dB re 2.0×10⁻⁵ Pa. ⋯⋯⋯: SPL at P1, 2.5D; —o—: SPL at P1, measured; ——: SPL at P2, 2.5D; – + –: SPL at P2, measured; – – –: rail vibration, predicted; – • –: rail vibration, measured. (a) 1250 Hz, (b) 1600 Hz, (c) 2000 Hz, (d) 2500 Hz, (e) 3150 Hz, (f) 4000 Hz.

The predictions from the 2.5D model have similar average levels and decay trends as in the measurements, but the measured values contain large variations. An important difference between the measurements and the prediction is that the 2.5D waveguide approach is based on an infinite rail, whereas in the measurements the rail is finite with a length of only 2 m. The wave reflections at the ends of the rail therefore lead to the spatial variations seen here.

4.5   Experimental validation using field measurements

4.5.1   Measurements on a stationary train

Within the scope of the RUN2Rail EU project, field measurements were carried out[1] on a metro train in Madrid, Spain [87] to measure the sound pressure distribution on the train sides when a loudspeaker was located beneath the train floor, see Figure 4.23. More details can be found in **Appendix B.2.** These are used to validate the 2.5D models. Five microphone positions are located on the train side surface right above the loudspeaker. The height of the first position is 0.1 m above the bottom edge of the sidewall, and the relative vertical separation between microphone positions is 0.5 m. Each microphone position was measured twice.

Figure 4.23. Measurements of sound pressure on a stationary train. (a) Loudspeaker location, (b) microphone positions, (c) separation of microphones. Photos provided by Polytechnic University of Valencia.

---

[1] These measurements were carried out by Polytechnic University of Valencia in collaboration with Metro de Madrid

A 2.5D BE model was created to predict the sound distribution along the vertical direction on the train sides. The geometry of the train profile in the numerical model corresponds to the train in the tests but the details of the train floor are simplified in the model. The bogie is also omitted. The surface normal impedance of the ballast is calculated based on the Delany-Bazley model with an equivalent flow resistivity of $50 \, \text{kPa} \cdot \text{s/m}^2$ [93]. A half-space ground is considered outside this region. The source in the numerical model has the same size as the loudspeaker and same location relative to the train corresponding to the field test. Although the source diameter is much larger than the fundamental sources considered in Section 4.1, the response is only considered here in the plane at $x = 0$ m so no strong effect is expected.

Linear boundary elements are used to create the model with element size 0.02 m, which allows the calculation up to 4 kHz. Five field points are set on the side surface of the train (4 mm away from the side surface) in the 2.5D models to represent the microphones in the measurements (wind balls were used to cover the microphones in the tests, the microphones were supposed to be about 2 cm away from the train). As the source strength of the loudspeaker used in the field test is not available, the predictions are shifted to correspond to the measured sound pressure levels for ease of comparison. The cross-section of the train and the source and the comparisons of the predicted and the measured sound pressure levels in one-third octave bands (averaged over three frequencies in each one-third band for the prediction) are shown in Figure 4.24. It can be seen that the sound pressure levels decrease with the increasing height on the side surfaces and the predictions match the measurements well.
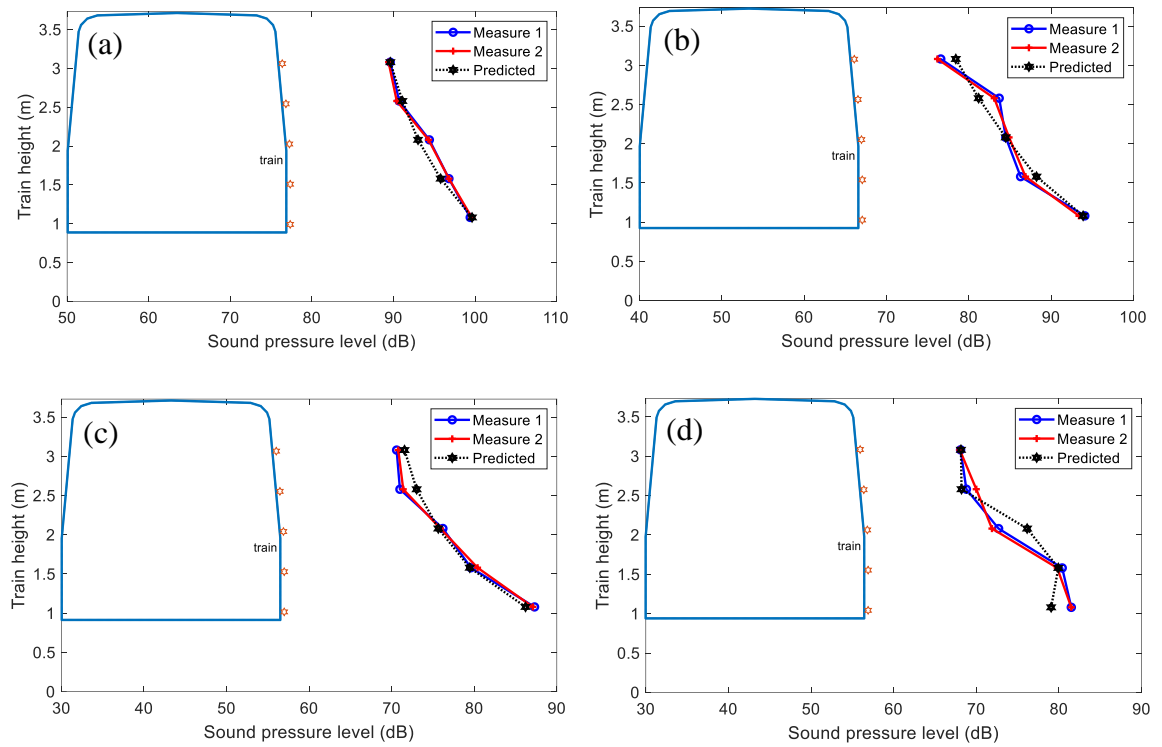
Figure 4.24. Comparison of prediction and measurement of sound distribution on the train side in one-third octave bands. (a) 200 Hz, (b) 400 Hz, (c) 800 Hz, (d) 1600 Hz.

4.5.2   Measurements on a running train

The sound pressure distribution was measured on the external surfaces of the metro train when the train was running at 50 km/h on a test track. More details can be found in **Appendix B.3.** Four surface microphones were located on the train side above the bogie area, see Figure 4.25. They are numbered as points 1006, 1009, 1010 and 1011. Microphones 1006, 1009, 1011 are all 0.7 m above the bottom edge of the sidewall whereas microphone 1010 is 1.5 m above it.

Figure 4.25. Field measurements to measure sound distribution on the train outside surface. Photo provided by Vibratec.

The sound power spectra of the rail, the wheel and the sleepers were calculated using the TWINS model. They are given in **Appendix B.1**. These TWINS predicted source strengths are then used in combination with the 2.5D predictions to determine the sound pressure levels at the four positions on the train external surfaces.

2.5D numerical models are created based on the actual train cross-section. Figure 4.26(a) shows the cross-section of the 2.5D model used for investigation of the noise transmission from the wheel to the train external surfaces, with the wheel located 0.61 m above the ballast. Figure 4.26(b) shows the cross-sections adopted to calculate the contribution of the rail, with the rail located 0.02 m above the ballast. In the 2.5D models for the wheel and the rail, the sleepers are omitted and the ballast is replaced by a rectangular box sitting on the ground with a height of 0.05 m. The cross-section adopted to calculate the contribution from the sleepers is shown in Figure 4.26(c). The upper surface of the sleepers in the numerical models is modelled as before in Section 4.5.1. The velocity of the rail/sleepers in the wavenumber domain is calculated as described in Section 3.2 and is assigned to the models as described before in Section 4.4. In these three numerical models, as before, a half-space ground extending beyond the region modelled using boundary elements.

As before in Section 4.4, the train bodies in all three models are made of linear boundary elements with size 0.02 m, as well as the rectangular box used for the ballast in Figure 4.26(a) and (b) and for the sleepers in Figure 4.26(c). Elements with different sizes are used for the

wheel and rail. As before, 36 elements are used to model the fundamental sources representing the wheel in Figure 4.26(a), which are modelled by using a circle of radius 0.005 m. 100 elements are used to model the rail cross-section in Figure 4.26(b). Five 'CHIEF' points are used inside the train and three are used in the rectangular box below it which represents the ballast or sleepers. The train cross-section in Figure 4.26(a) does not include the side fairings whereas side fairings are present in Figure 4.26(b) and Figure 4.26(c). This is because the train adopted in the validation tests described in Figure 4.25 did not have fairings to cover the bogie area and the model approximates this by using different cross-sections for the models of the wheel and track components of noise.
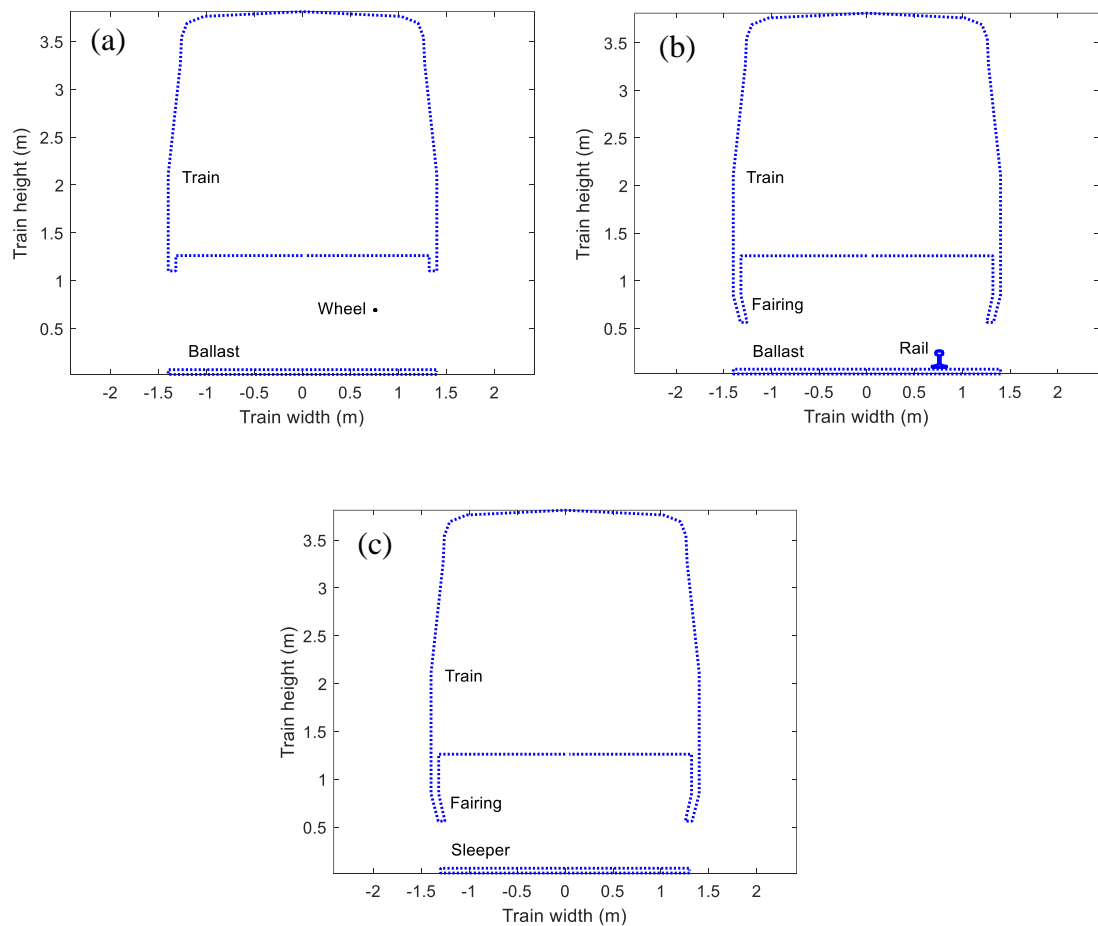
Figure 4.26. 2.5D models for (a) the wheel, (b) the rail, (c) the sleepers.

The total sound pressure on the train surfaces is determined from the incoherent sum of the contributions of the wheel radial and axial components, the rail vertical and lateral components, and the sleepers. Overall A-weighted sound pressure levels on the train external surfaces due to a single bogie (four wheels) are shown in Figure 4.27. The length of the carriage is 17.92 m and the centre of the bogie is 2.95 m from the carriage end. This sound pressure distribution shows that the highest levels of sound are incident on the train floor.

Moreover the presence of the fairings helps to create a partially reverberant enclosure below the train, as discussed in Chapter 3. However, noise can also diffract from the edge of the cover to the side surfaces of the train. The sound level reduces with increasing height. The noise on the train roof due to the wheel and rail is less significant and is estimated to be around 30 dB lower than the noise impinging on the floor.
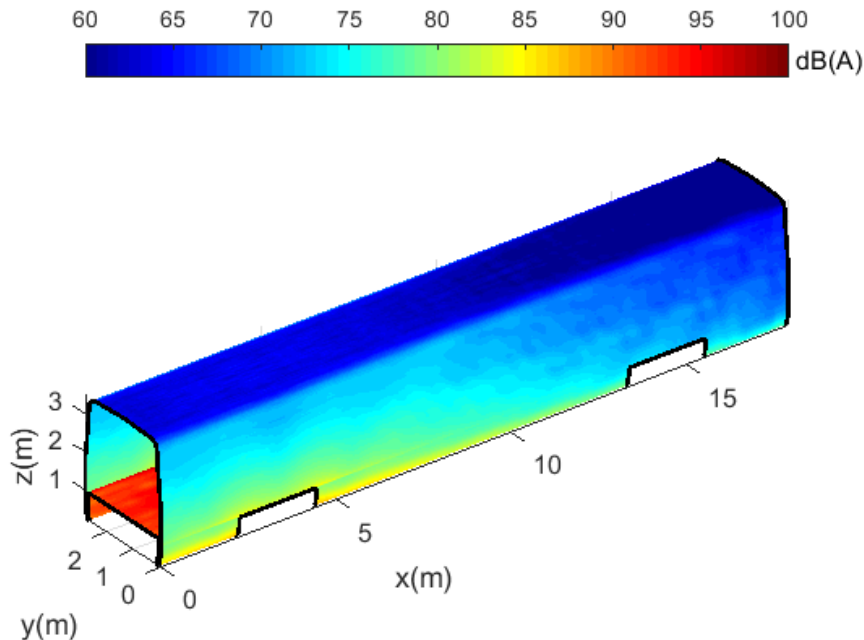
Figure 4.27. Overall sound pressure levels on the train outside surfaces. The bogie considered here is on the left.

To compare the prediction with the measurements, the predicted sound pressure levels were calculated by including the contribution from the two bogies below the carriage on which the microphones were mounted and the closest bogie from the adjacent carriage on either side. The comparisons with the measurements are shown in Figure 4.28.

The predictions capture the main trend of the sound pressure spectra compared with the measurements. However, at low frequency, the predictions are lower than the measurements, whereas they are higher at high frequency. Comparison with the sound power obtained from the TWINS model in Figure B.5 from **Appendix B.1** indicates that the peak at 500 Hz is dominated by lateral motion of the rail which may be overpredicted due to the neglect of torsion.

At high frequency, the predictions are higher than the measurements. One possible reason is because the simplified model could not consider the complex interaction between the source

and the equipment beneath the vehicle. Besides, there is no fairing in the model used for the wheel noise while in reality there is also a bogie frame which will shield the noise to some extent. The overall sound pressure levels from the predictions and the measurements, together with the relative error between them, are given in Table 4.3. The relative errors in terms of the overall sound pressure levels are less than 3 dB at these four measurement positions, which shows that the 2.5D model captured the main trend of the sound spectrum with acceptable errors.
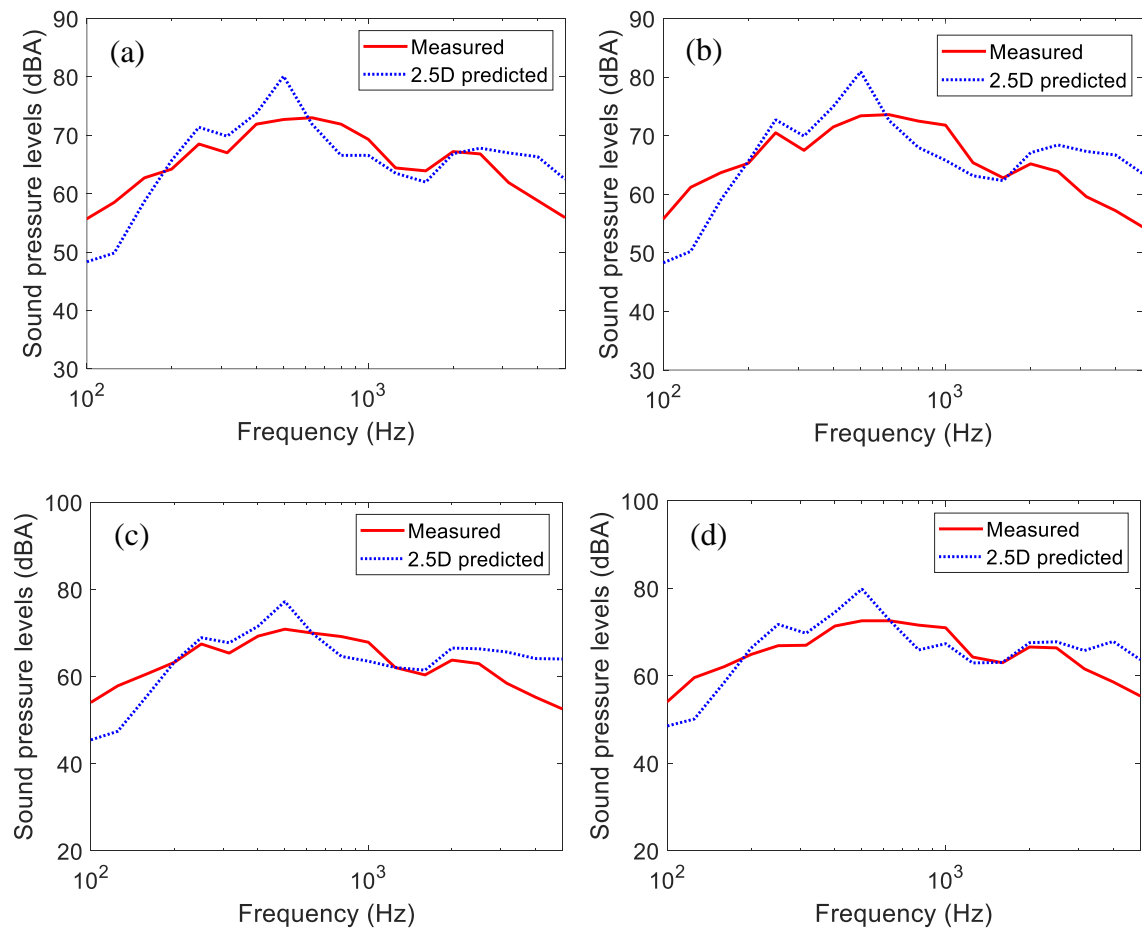
Figure 4.28. Comparisons between the 2.5D predictions and the measurements, (a) Point 1006, (b) Point 1009, (c) Point 1010, (d) Point 1011.

Table 4.3. Overall sound pressure levels on the train sides.

	P 1006	P 1009	P 1010	P 1011
Prediction (dB(A))	83.2	83.1	79.7	82.9
Measurement (dB(A))	80.6	81.1	78.3	80.4
Difference (dB(A))	2.6	2.0	1.4	2.5

4.6   Summary

A 2.5D BE approach has been developed to calculate the noise propagation from the wheel, rail and sleepers to the external surfaces of a train. The wheel was modelled by using approximations to a monopole and a dipole in the 2.5D models. The rail and the sleepers were modelled by their cross-section in the 2D domain and their wavenumber spectrum in the third direction. An inverse Fourier transform was used to convert the sound pressure from the wavenumber domain back to the spatial domain. The TWINS model was used to determine the sound powers of the individual components which were then used to adjust the source levels in the 2.5D model predictions. The overall sound pressure level on the train external surfaces was obtained by adding the various components incoherently. Comparisons were made with measurements of sound pressure levels on the external surfaces of a 1:5 scale model train in an anechoic chamber and on a full-scale metro train, both statically and in running operation. The comparisons with the laboratory test show that the predicted sound pressure levels from the 2.5D model and the measured ones have a similar decay trend along the train axis direction and the average difference of the sound pressure levels is less than 3 dB. For the field measurement on a stationary train, the predicted sound pressure distribution along the train height on the train side is close to that obtained by measurement. In the field measurement on a running train, the predictions and the measurements agree fairly well in terms of sound pressure spectrum and the overall sound pressure levels have less than 3 dB error. The 2.5D boundary element model can therefore be used to predict the sound pressure on the external surfaces of a train due to rolling noise. In the next chapter the aerodynamic noise from the pantograph is considered.

Chapter 5 Aerodynamic noise from the pantograph on train external surfaces

The pantograph is chosen to illustrate the modelling approach of aerodynamic noise and how to model its propagation to the train external surfaces by using the 2.5D method in this chapter, also the influence of flow to noise propagation is considered. The pantograph is composed of many different components. The most representative components within a typical pantograph are the contact strips, horns, stroke limiting cage, control rod and pantograph arms, as shown in Figure 5.1 and detailed in reference [50].
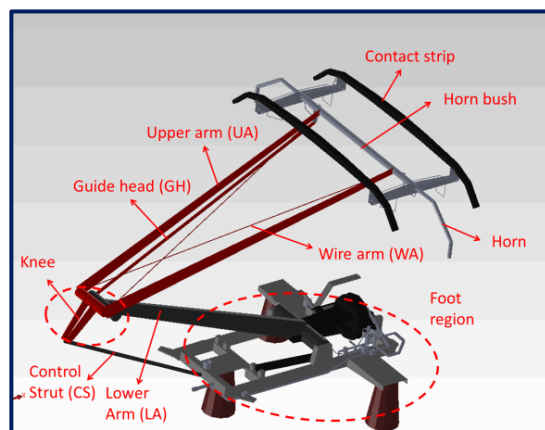
Figure 5.1. Configuration of the pantograph DSA350 [48, 50].

The common thing among the various components is they can be simply modelled by cylinders or square bars with different dimensions and different yaw angles towards the flow. The sound radiation from each component is assumed to be the result of the fluctuating dynamic force on the cylinder caused by the interaction of the flow and the structure [34]. In previous research, aerodynamic noise from single components has been modelled by using CFD [48, 50] and a database related to the main factors of influence has been created based on these simulations and associated measurements [96]. The total sound power from the pantograph can be calculated from this database using the component-based approach.

When calculating the sound propagation from the pantograph to the train external surfaces, Lei et al. [44] used a three-dimensional boundary element model. This is able to represent the complicated structure of the pantograph, but it would be computationally expensive. The influence of flow on the sound propagation was not considered in their work. Besides, a thorough understanding of mechanism of pantograph noise propagation was not achieved.

Chapter 5

In this Chapter, the aerodynamic noise properties of the sound around a single cylinder are briefly reviewed first, which are helpful to understand the aerodynamic noise from a whole pantograph; the total sound power from a pantograph is then discussed. The 2.5D BE method is employed to solve the pantograph noise propagation to the train external surfaces. The pantograph is modelled by several equivalent dipole sources. The waveguide boundary element model gives the sound pressure on the train cross-section in the wavenumber domain. An inverse Fourier transform is applied to obtain the sound pressure distribution in the spatial domain.

The influence of flow on the sound propagation is modelled using two methods. At low frequency, when the acoustic wavelength is larger than the thickness of the turbulent boundary layer, the flow is modelled as a uniform mean flow, whereas at high frequency it is modelled by a velocity profile through the boundary layer. Equivalent sound speeds are determined to model the influence of flow on sound propagation. The turbulent boundary layer itself is an acoustic source, but here only its influence on pantograph noise propagation is considered and the noise radiation from the turbulent boundary layer is not taken into account. Laboratory experiments and the ray tracing approach are used to verify the 2.5D models for predicting the pantograph noise propagation.

5.1   Review of aerodynamic sound pressure from flow over a cylinder

Aerodynamic noise from a moving object is generated from the interaction of the fluid and the structure. The aerodynamic noise sources caused by interaction with a structure surface are classified as monopole and dipole sources [34]. The sound field generated by the monopole and dipole source terms can be calculated by [34]

$$p(\mathbf{x}, t) = \frac{\partial}{\partial t} \int_S \frac{Q(\mathbf{y}, \tau)}{4\pi D |\mathbf{x} - \mathbf{y}|} d\mathbf{y} - \frac{\partial}{\partial x_i} \int_S \frac{F_i(\mathbf{y}, \tau)}{4\pi D |\mathbf{x} - \mathbf{y}|} d\mathbf{y} \qquad (5.1)$$

where $\mathbf{x}$ and $\mathbf{y}$ are the vectors to represent the receiver and source positions. t is the receiving time at the receiver and τ is the emission time at the source. They are related as

$$t = \tau + \frac{|\mathbf{x} - \mathbf{y}(\tau)|}{c_0} \qquad (5.2)$$

Q and F_i are the monopole and dipole source terms. They are defined as below and can be obtained by simulations or measurements.

88

$$Q = \rho(u_n - v_n) + \rho_0 v_n \qquad F_i = \rho\mathbf{u}(u_n - v_n) + p\mathbf{n} - \boldsymbol{\tau} \cdot \mathbf{n} \tag{5.3}$$

where ρ is the fluctuating density of air, ρ_0 is the equilibrium density of air, u_n and v_n are the flow velocity and object moving velocity in the direction normal to the surface. $\mathbf{n}$ is the unit vector normal to the surface and $\boldsymbol{\tau}$ is the viscosity stress tensor. If the object is not permeable, it yields $u_n = v_n$. When an object is moving at a constant speed, the time derivative of the monopole source in Equation (5.1) is zero. If the viscosity stress is ignored and the divergence term in Equation (5.1) is rearranged and rewritten as a time derivative form for the dipole source, the sound pressure from a moving structure in the air can be expressed as

$$p(\mathbf{x}, t) = \int_S \frac{1}{4\pi c_0 |\mathbf{r}| D^2} \frac{\mathbf{r}}{|\mathbf{r}|} \cdot \frac{\partial \mathbf{F}}{\partial \tau} d\alpha \tag{5.4}$$

where D is the Doppler factor, given by

$$D = 1 - \frac{\mathbf{v}_s(\tau) - \mathbf{u}_0}{c_0} \cdot \frac{\mathbf{r}}{|\mathbf{r}|} \tag{5.5}$$

$\mathbf{v}_s(\tau)$ is the velocity at the source. $\mathbf{u}_0$ is the flow velocity. $\mathbf{r} = \mathbf{x} - \mathbf{y}$. In Equation (5.4) α is the source area. The dot product $\mathbf{r} \cdot \mathbf{F}$ in Equation (5.4) introduced a dipole directivity to the sound field caused by flow crossing a cylinder. Pantographs are composed of cylinders and bars with different dimensions. It is well known that the aerodynamic noise radiated from them is characterised by tonal noise related to vortex shedding behind them [97]. Figure 5.2 shows an example of the flow structure behind a cylinder [50]. Obvious vortex shedding can be found in the rear region.
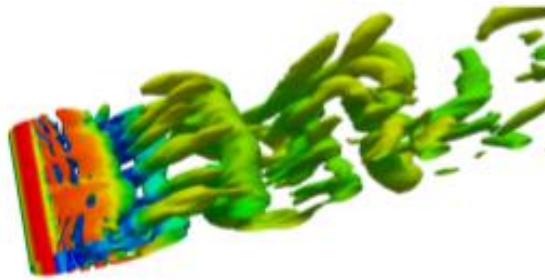
Figure 5.2. Example of vortex shedding behind a cylinder [50].

The periodic vortex shedding behind the cylinder causes fluctuating lift and drag forces on the cylinder. From Equation (5.4) it is known that the related lift and drag forces on the cylinder surface provide dipole source terms perpendicular to the cylinder. For a receiver in the far field, such that the distance from the source is much larger than the dimension of the source, the cylinder can be treated as a compact source, and the total fluctuating force on the surfaces can be calculated first by integrating the pressure over the surface of the cylinder.

Figure 5.3 illustrates an example of the sound distribution around a cylinder. This has been calculated for the case of a cylinder with diameter $d = 0.05$ m and flow speed $u_0 = 15$ m/s, similar to the case considered in reference [50]. It corresponds to a Reynolds number of 5×10^4 where $Re = \rho u_0 L/\mu$, with ρ the fluid density, L the characteristic length and μ the fluid viscosity. The lift and drag forces on the cylinder were extracted from the CFD simulation on the platform OpenFoam following the set up explained in [50]. The sound pressure field caused by the lift and drag forces due to the flow over this cylinder is then calculated using Equation (5.4) and plotted in Figure 5.3. The influence of flow on the sound transmission is not considered in Figure 5.3. Both the lift and drag forces provide a dipole-like source term but it is clear that the lift force is dominant, causing higher sound amplitudes in the y direction.
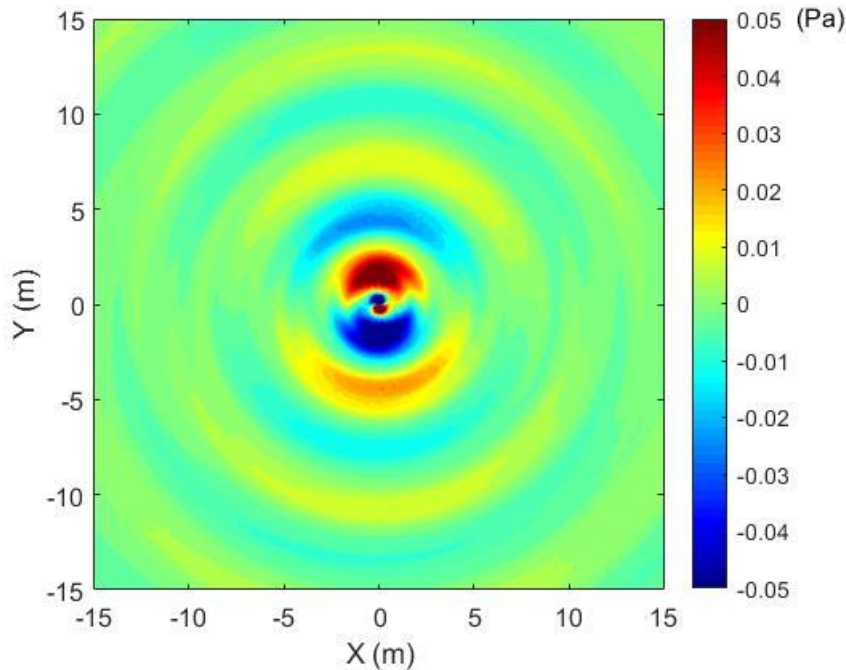
Figure 5.3. Instantaneous sound pressure distribution around a cylinder. ($u_0 = 15$ m/s from left to right, $Re = 5\times10^4$).

5.2   Pantograph sound power

In the prediction of the noise from the whole pantograph, if it is assumed that noise contributions from each component are not correlated, the mean square sound pressure radiated by the whole pantograph can be predicted by the incoherent sum of the spectra of each individual strut. This is the basis of the component-based approach [48, 50]. It is assumed that the pantograph and receiver are both stationary and the flow is moving. This is equivalent to a moving train and moving receiver in stationary air. The sound pressure in the far field due to the pantograph is expressed as [48]

$$\overline{p^2}(f) = (\rho_0 c_0^2)^2 M^6 \sum_i \frac{\eta_i S_i F_i(f)}{R_i^2} \frac{D_{rad,i}(\varphi, \psi)}{(1 - M \cos \theta)^4} \tag{5.6}$$

where the subscript i refers to each strut, M is the Mach number, S_i is the total surface area of each component of the pantograph. $F_i(f)$ is a normalized spectrum obtained using empirical relations. $D_{rad,i}(\varphi, \psi)$ is the directivity of the noise radiated by each strut, where φ is the radiation angle in the vertical plane parallel to the flow direction and ψ is the radiation angle in the vertical plane normal to the flow direction. The directivity function for a theoretical dipole source is used for the peak noise at the vortex shedding frequency while the broadband noise is assumed to be omnidirectional [48]. The distance R between the cylinder and the receiver is defined separately for each cylinder. The Doppler factor $(1 - M \cos \theta)^4$ accounts for the effect of the convective amplification for a dipole source, depending on the observer position, where θ is the angle between the direction of the flow and the observer position and M is the Mach number. η_i is the amplitude factor, given by

$$\eta = \frac{St^2 C_{l,rms}^2 L l_c d}{16S} \tag{5.7}$$

where St is the Strouhal number to describe oscillating flow mechanisms, defined by $St = fd/U$ (f is the frequency of vortex shedding and d the cylinder diameter), $C_{l,rms}$ is the rms fluctuating lift coefficient, (the lift coefficient C_l defined as $C_l = F_l/(0.5\rho U^2 dL)$ with F_l being the lift force). L is the length of the cylinders, l_c is the spanwise correlation length, normalised by the cylinder diameter, d. Each component of the pantograph is modelled independently by choosing an appropriate normalized spectrum $F_i(f)$. This allows prediction of the far-field noise spectrum based on empirical databases of S_t, $C_{l,rms}$ for different cases of cylinders, rather than relying only on measurements or simulations of noise.

Chapter 5

The normalized spectrum, $F_i(f)$, is determined in different ways for peak and broadband noise [48].

The component-based approach has previously been validated by wind tunnel measurements of noise due to the pantograph. Figure 5.4 shows the predicted sound pressure at a receiver placed in the plane parallel to the pantograph head at half the height of the pantograph and a distance of 5 m from the centre of the pantograph head (type DSA350). The predictions were made at 170 km/h, 280 km/h and 400 km/h using the latest version of the component-based approach [50] and they are compared with the measurements from reference [96]. The comparisons indicate that the component-based model is reliable to predict both the peak and broadband noise from the pantograph in a wide frequency range; besides, it is qualified to predict the noise at a wide speed range.
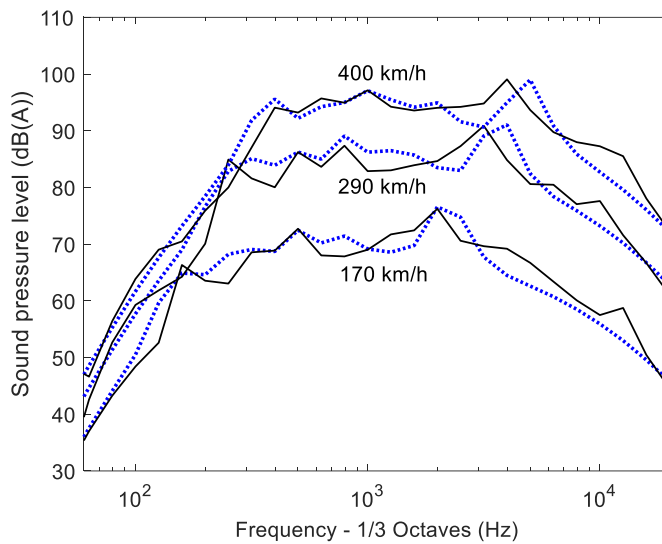
Figure 5.4. Comparison of A-weighted noise spectra at a receiver placed in the plane parallel to the pantograph head (half height of the pantograph and 5 m from the pantograph centre) between the predictions and the measurements for a full-scale pantograph DSA350 with different flow speeds. ⋯⋯: Liu model [50]; ——: Measurement from [96].

The total sound power from the pantograph can be determined from the sound pressure level over a surface by assuming a compact source in free space radiation. A directivity factor is needed in this case as the pantograph noise has a dipole property. For simplicity in this work, the sound power of the pantograph is calculated from the sound pressure by using a sphere (radius, 5 m) enclosing the pantograph, taking the assumption that it is a compact source and

using the approximate expression for the time-averaged sound intensity in the far field ($\bar{I} = \overline{p^2}/\rho_0 c_0$). The sound power from the pantograph is expressed as

$$W = \int_S \bar{I} \mathrm{d}s \tag{5.8}$$

where W is the sound power of the pantograph and $\bar{I}$ (sound intensity) is on normal to the spherical surface. The sound directivity is considered when calculating the sound pressure ($\overline{p^2}$) by using Equation (5.6). This approach can also be applied to calculate the sound power from each part of the pantograph. Figure 5.5 illustrates the total sound power from the pantograph DSA350 at train speed 290 km/h and the contributions from the head, the horns, the upper and lower arms.
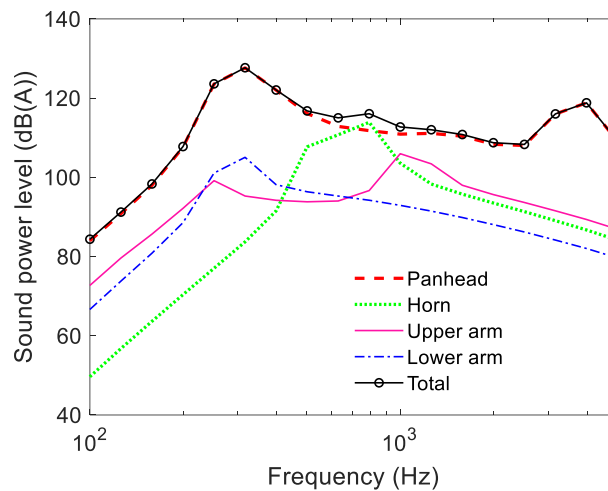
Figure 5.5. Predicted sound power from the pantograph and contributions from each part, 290 km/h.

From Figure 5.5, it can be seen that most of the sound power is due to the head of the pantograph. It has a spectral peak at about 200 Hz, which is due to the contact strips (with bigger thickness) within the head. There is another peak at 4000 Hz in the power spectrum of the head, which is from the components with very small radius.

5.3   2.5D BE model for the pantograph noise

Due to the complexity of the pantograph structures, a 2.5D BE model is proposed to model the noise propagation from the pantograph to the train external surfaces. The 2.5D BE model was introduced in Chapter 4 where it was used to model the rolling noise propagation to the train external surfaces. The concept used to model the wheel in Chapter 4 is employed here

to model the dipole sources on the pantograph. The train is again represented by its cross-section.

However, to use the 2.5D model to model the pantograph, it needs to be noticed that the pantograph is a distributed source. Whether it can be treated as a compact source depends on the source dimension, the relative distance from the source to the receiver and the frequency. If the pantograph is subdivided into several segments, each segment has a relatively small dimension compared with the distance from the source to the train external surfaces, thus, they will roughly meet the geometrical far field assumption. The distance from the pantograph head to the train roof is estimated as 1.4 m from its configuration in [50], and the sound power of the pantograph is concentrated above 200 Hz when it runs at 290 km/h, which can roughly meet the acoustical far field condition ($k\,r \gg 1$). In this work, the pantograph is therefore regarded as an array of dipole sources as each of its components has a dipole property in terms of sound radiation.

The pantograph is broken down into the panhead, the arms, and the horn, and each of them is modelled by using multiple dipole sources. When replacing the pantograph by an array of dipole sources, the locations and number of the dipoles should be chosen based on the correlation length of the components and the frequency and the direction of the dipole should be consistent with the reality, see Figure 5.6(a). The final 2.5D models are indicated in Figure 5.6(b). Five dipole sources are used to model the pantograph head, two inclined at 45 degrees are used to model the horn and another two horizontal dipoles are used to model the upper arms. Their relative locations are listed in Table 5.1. The knee and the foot parts of the pantograph are located in the boundary layer and their contributions to the total sound power are small compared with the pantograph head, so they are ignored in this work. The various sources are assumed to be incoherent, so they are created in separate 2.5D BE models. A typical train cross-section is included in the model with the roof of the train about 4 m above the ground. The modified Green's function is used in the 2.5D models, which represents a half space ground, although it is far enough away that it could be neglected.

Linear boundary elements with length 0.01 m are used to represent the train cross section. Each source is represented by a circle in the 2.5D models and the radii of the sources are 0.005 m. As before 36 elements are used for each source. The boundary condition of the sources is given by a unit oscillating velocity. The oscillating direction is along the axis direction of the dipole in terms of its radiation directivity. The sound power of each part of

the pantograph obtained from the component-based approach is used to adjust the source levels later. For this exterior problem, five 'CHIEF' points are introduced inside the train body to avoid the non-uniqueness problem [94]. The relative locations of the nine dipoles above the roof are listed in Table 5.1.

(a)

(b)
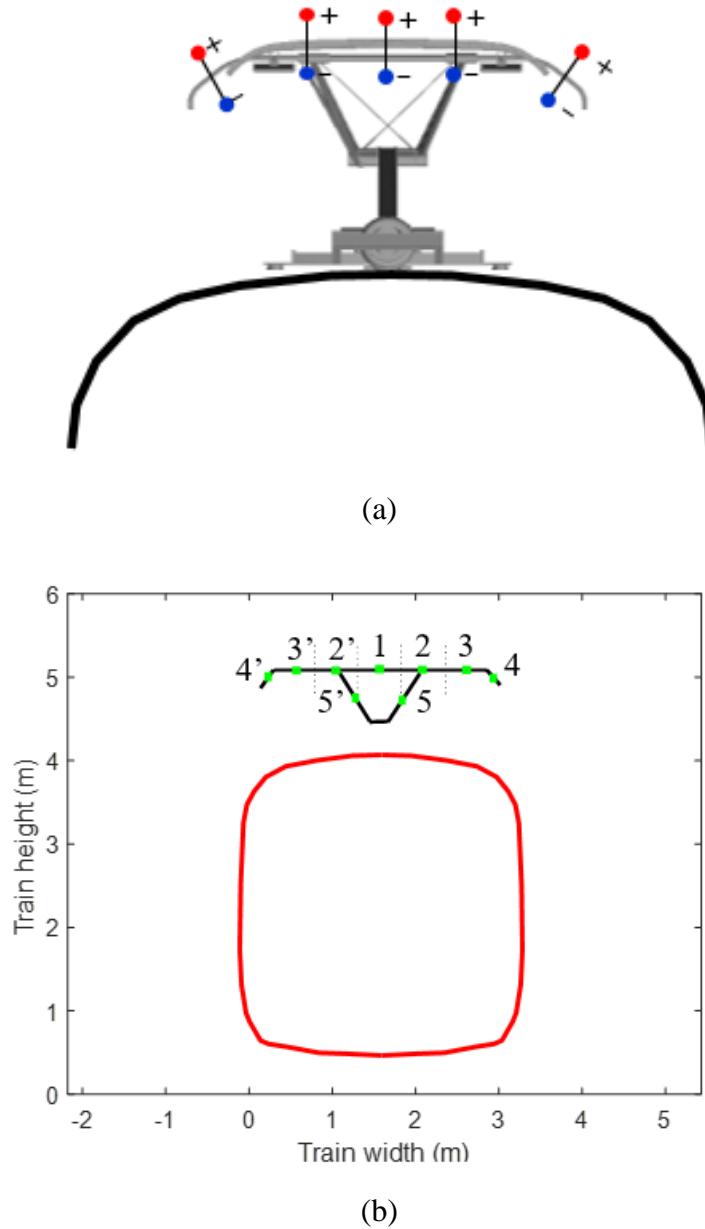
Figure 5.6. (a) Pantograph on train roof, (b) the 2.5D model for pantograph noise, (an enclosure is used to represent a typical train cross-section).

Table 5.1. Locations of the dipole source above the train roof.

Points	Location (y, z), m	Orientation	Part of
1	(0, 5.4)	Vertical	Head
2 and 2'	($\pm$0.271, 5.4)	Vertical	Head
3 and 3'	($\pm$0.542, 5.4)	Vertical	Head
4 and 4'	($\pm$0.808, 5.27)	Inclined at 45°	Horn
5 and 5'	($\pm$0.280, 5.08)	Lateral	Upper arm

By using the 2.5D BE model, the pressure on the train external surfaces can be obtained as a function of wavenumber and frequency. The spatial distribution of sound at each frequency can be calculated by the inverse Fourier transform

$$p(x, y, z) = \frac{1}{2\pi} \int_{-k_0}^{k_0} \tilde{p}(k_x, y, z) \, e^{-ik_x x} dk_x \tag{5.9}$$

in which the integral is chosen from $-k_0$ to k_0, with k_0 being the acoustic wavenumber in air at rest. In Equation (5.9), the integral limitation should be from $-\infty$ to ∞ when applying the inverse Fourier transform, but here it is limited from $-k_0$ to k_0 since larger values than k_0 nearly produce no radiated power to the far field. However, this might have some effect on the near field solution, especially at low frequency as their acoustic wavenumbers are relatively small. Truncating infinite wavenumbers to the region $(-k_0, k_0)$ will introduce discontinuities to the near field sound pressure spectra as a function of the wavenumber. Fluctuations will appear in the corresponding sound pressure in the spatial domain.

5.4   Sound pressure on the train external surfaces

The pantograph is symmetrical about the train centreline. The noise from point sources 1, 2, 3, 4 and 5 on the train external surfaces is calculated and the others are obtained by symmetry. Figure 5.7 shows the sound pressure on the train external surfaces in the spatial domain due to point sources 1, 3, 4 and 5.
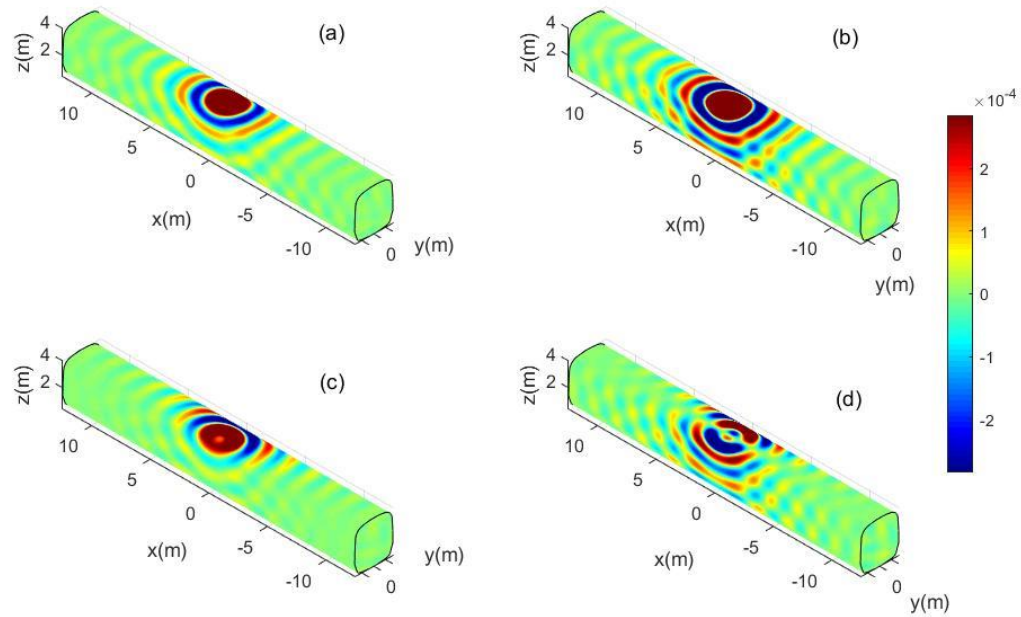
Figure 5.7. Real part of the sound pressure (Pa) on the train external surfaces due to dipoles with unit oscillating velocity. (a) From point source 1, a vertical dipole located in the middle of the contact strip, (b) from point source 3, a vertical dipole close to one end of the contact strip, (c) from point source 4, a dipole inclined at 45° to the vertical direction for the horn (d) from point source 5, a lateral dipole for the upper arm.

A scale factor is used to adjust the sound power from the 2.5D prediction to correspond to the actual value obtained from the component-based model. As before, this is defined as the ratio of the sound power from each part of the pantograph to that of the dipole sources.

$$\gamma_i = \frac{W_i}{nW_{dipole}} \tag{5.10}$$

where W_{dipole} is the sound power of a single dipole source in the 2.5D models (unit velocity is used in the predictions), W_i is the sound power from the component and n is the number of dipole sources used to model each of them. Five were used for the head, and two each for the horn and the upper arms. The total sound pressure level distribution on the train external surfaces is due to the contributions from all the three parts and calculated by adding their mean square pressures together. Figure 5.8(a) gives the sound pressure level at 200 Hz on the train external surfaces and Figure 5.8(b) is the overall sound pressure level. It can be seen that the sound pressure levels on the two sides of the pantograph are the same if the convective effect is ignored. In Figure 5.8(a), some ripples appear at the ends of the segment

that created to represent the vehicle. They are introduced in the inverse Fourier transform process. These ripples can be avoided by including the near field sound waves (whose wavenumbers are greater than k_0) in Equation (5.9).
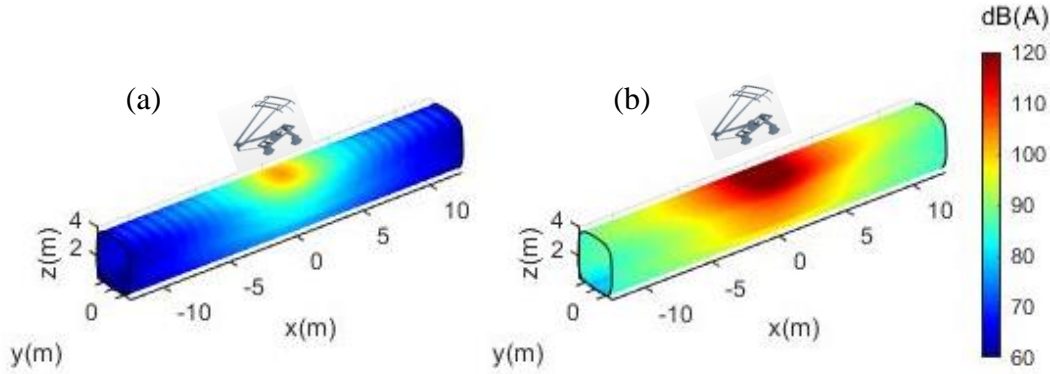
Figure 5.8. Sound pressure on the train external surfaces due to a pantograph at 290 km/h, (a) 200 Hz, (b) overall sound pressure level. dB(A), re 2.0 ×10⁻⁵ Pa.

5.5   Boundary layer on train external surface

In reality the pantograph is moving with the train, and the sound propagation from the pantograph is therefore considered as a moving source in a largely static medium. However, it is easier to consider it as a stationary source in a wind that is flowing in the opposite direction. Because of the viscosity of the air and the presence of the train surfaces, a turbulent boundary layer is generated when the train runs at high speeds. Detailed measurements on the boundary layer development over the roof of a train is limited in the literature study. A short series of measurements were made above a scale four-car ICE2 model in [98] but the scale effects and the lack of realistic roof roughness inherent in those measurements make their results difficult to interpret. Theory of flow over a flat plate is adopted in this work. In terms of the Reynolds number, when $Re > 5 \times 10^5$ the flow becomes unstable and transition to a turbulent boundary layer occurs if considering fluid flow over a flat plate [99]. For the flat plate case, the mean velocity profile in the boundary layer can be described by a power law [99]

$$\overline{U}_1 = U \left(\frac{z}{\delta}\right)^{\frac{1}{7}} \tag{5.11}$$

where U is the train speed, z is the distance from the train surface in its normal direction, δ is the thickness of the turbulent boundary layer which grows according to [99]

$$\delta \simeq 0.37 \, x \, Re^{-1/5} \tag{5.12}$$

where $Re = \rho U x / \mu$. The thickness δ thus varies along the train axis direction. For the boundary layer on the train roof, x is the distance from the location of the pantograph to the front of the train. The inter-coach gap is narrow and so it is assumed that it will not affect the growing trend of the boundary layer thickness. For a train with eight carriages, generally there are two pantographs mounted on the train roof: one typically is at the end of the second coach, about 40 m from the front of the train, the other is on the sixth coach about 160 m from the front. If the train runs at 80 m/s (290 km/h), the corresponding Reynolds numbers at the two pantograph positions are 2.1×10^8 and 8.5×10^8, indicating that the flow is fully developed into turbulence. Therefore, the expressions for the boundary layer thickness and mean velocity profile in the turbulent boundary layer are assumed to be valid for the train case.

The thickness of the boundary layer at these two positions can be calculated from Equation (5.12) by applying these different values of x. In this work, the pantograph at 40 m from the front of the train is studied for a train speed of 80 m/s (about 290 km/h), which leads to a turbulent boundary layer thickness of about 0.35 m. Substituting this thickness back into Equation (5.11), the mean velocity profile in the turbulent boundary layer can be estimated. Figure 5.9 shows the estimated thickness of the boundary layer when the train runs at 80 m/s (about 290 km/h) and the velocity profile at the positions 40 m and 160 m from the front of the train. It can be seen that the thickness of the boundary layer increases with increasing distance from the front of the train and the velocity profiles varies.
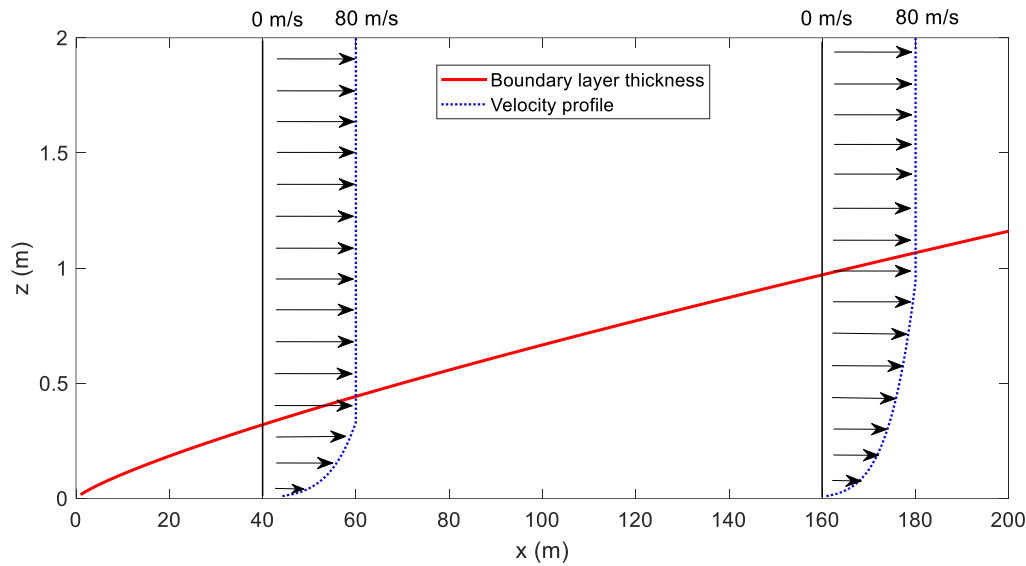
Figure 5.9. Thickness of the turbulent boundary layer and the velocity profile at 40 m and 160 m from the front of the train for a train speed of 80 m/s (about 290 km/h).

When sound travels through the boundary layer, the influence of the flow causes a change of the wave direction and the amplitude of the sound pressure. The influence is known to be highly related to the wind speed and wind gradient in the turbulent boundary layer and the ratio of the wavelength to the thickness of the turbulent boundary layer. To consider this the frequency range is divided into two. When the acoustic wavelength is greater than the thickness of the boundary layer (which occurs below about 1 kHz for the position at 40 m from the front of the train), it is considered as low frequency and otherwise it is considered as high frequency. The influence of the flow on the sound propagation will be considered separately at low and high frequency.

5.6   Modelling of flow influence at low frequency

At low frequency (below 1 kHz), the acoustic wavelength is larger than the thickness of the turbulent boundary layer. It is assumed that when the sound propagates through the boundary layer to the train roof the velocity gradient in the boundary layer will not change it significantly. Thus, the influence of the turbulent boundary layer is ignored, and a uniform mean flow is used to model the influence from the wind.

With a mean flow, the apparent movement of the wave front is the combination of the acoustic propagation and the convective effect of the mean flow. In comparison with no flow, see Figure 5.10(a), it is found that in the upstream direction the acoustic propagation and the convective effect cancel each other to some extent, see Figure 5.10(b) and in the down-

stream direction the two effects add up, see Figure 5.10(c). The two effects together can be modelled by an equivalent phase speed.
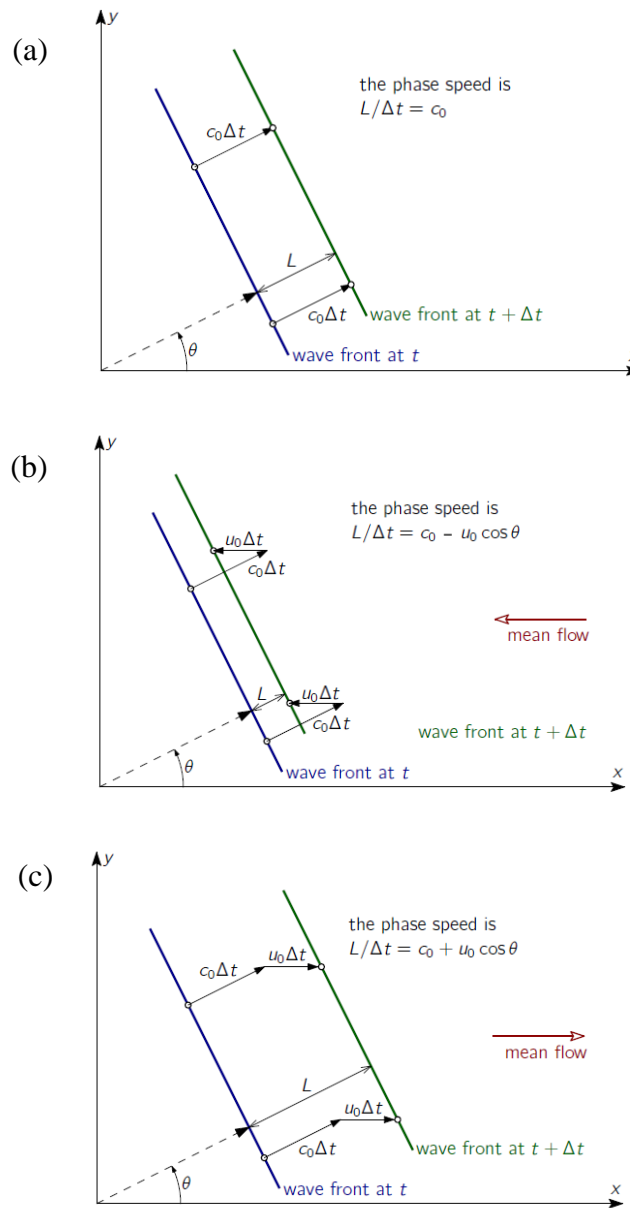
Figure 5.10. (a) propagating with no flow, (b) upstream propagation with mean flow, (c) downstream propagation with mean flow [100].

Figure 5.11(a) shows the wave fronts due to a point source in static air. Figure 5.11(b) shows the wave fronts in a uniform mean flow with flow direction from the left to the right. From Figure 5.11, it can be seen that the wind carries the waves to the downstream. The waves are squeezed in the upstream direction and stretched in the downstream direction.

(a)   (b)
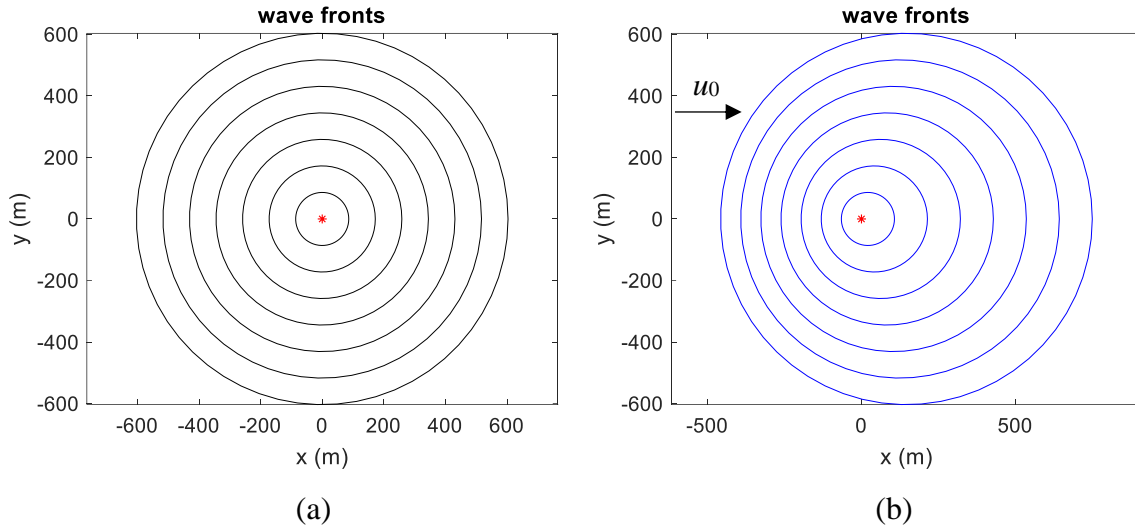
Figure 5.11. (a) Wave fronts in static air, (b) wave fronts in uniform mean flow, 80 m/s to the positive x direction.

Analogously, the sound propagation in a uniform mean flow can be modelled by an equivalent direction-dependent phase speed in a static air medium, see Figure 5.12.
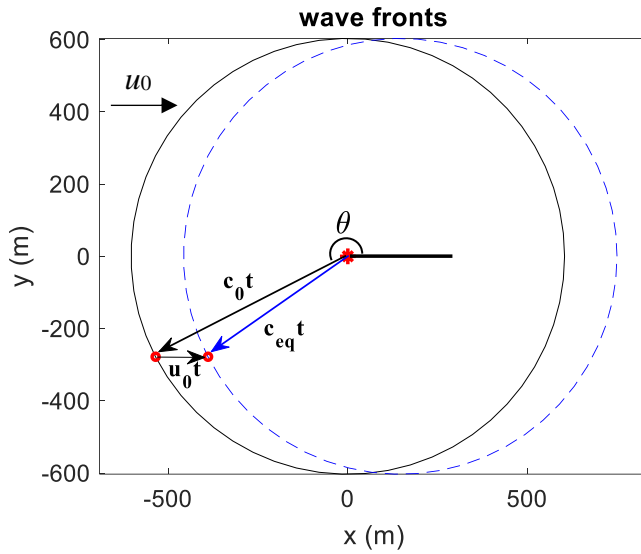
Figure 5.12. The stretching of the sound wave fronts in static air and in mean flow.

The equivalent phase speed and the resulting equivalent acoustic wavenumber are expressed as

$$c_{eq} \approx c_0 + u_0 \cos\theta; \qquad k_0' = \frac{\omega}{c_{eq}} \tag{5.13}$$

where c_0 is the sound speed in air at rest, u_0 is the wind speed, θ is the original sound wave direction, c_{eq} is the equivalent sound speed, in which the wind is considered, and ω is the

angular frequency. In the upstream direction, $\cos\theta$ is negative, which makes $c_{eq} < c_0$, while in the downstream direction, $\cos\theta$ is positive, which makes $c_{eq} > c_0$. As a consequence, in the upstream direction, $k_0' > k_0$, the equivalent wavenumber is greater than the wavenumber in air at rest, the wind turns previously evanescent waves (which do not radiate sound) at wavenumbers between $k_0' - k_0$ into propagating waves; on the contrary in the downstream direction $k_0' < k_0$, the wind turns those waves at wavenumbers $k_0 - k_0'$ from propagating waves into evanescent waves in the y-z plane. The sound pressure on the train external surface in a mean flow can be calculated by

$$p(x) = \frac{1}{2\pi}\int_{-k_0'}^{k_0'}\widetilde{p}'(k_x)\,\mathrm{e}^{-\mathrm{i}k_x x}\mathrm{d}k_x \tag{5.14}$$

Alternatively, in the upstream direction, it can be written as

$$p(x) = \frac{1}{2\pi}\left\{\int_{-k_0}^{k_0}\widetilde{p}'(k_x)\,\mathrm{e}^{-\mathrm{i}k_x x}\mathrm{d}k_x \right.$$
$$\left. + \left(\int_{-k_0'}^{-k_0}\widetilde{p}'(k_x)\,\mathrm{e}^{-\mathrm{i}k_x x}\mathrm{d}k_x + \int_{k_0}^{k_0'}\widetilde{p}'(k_x)\,\mathrm{e}^{-\mathrm{i}k_x x}\mathrm{d}k_x\right)\right\} \tag{5.15}$$

On the contrary in the downstream direction, it can be written as

$$p(x) = \frac{1}{2\pi}\left\{\int_{-k_0}^{k_0}\widetilde{p}'(k_x)\,\mathrm{e}^{-\mathrm{i}kx}\mathrm{d}k_x \right.$$
$$\left. - \left(\int_{-k_0}^{-k_0'}\widetilde{p}'(k_x)\,\mathrm{e}^{-\mathrm{i}k_x x}\mathrm{d}k_x + \int_{k_0'}^{k_0}\widetilde{p}'(k_x)\,\mathrm{e}^{-\mathrm{i}k_x x}\mathrm{d}k_x\right)\right\} \tag{5.16}$$

The adding of the two components in Equation (5.15) will increase the sound pressure in the upstream direction while the omission of the two segments in equation (5.16) will contribute to the reduction of the sound pressure in the downstream direction. In the case with flow, the acoustic wavenumber has been modified to k_0'. Therefore the sound pressure $\widetilde{p}'$ is solved in the 2D model with a spectrum of wavenumbers k_x in the x direction and with the corresponding transverse wavenumbers $\sqrt{(k_0')^2 - (k_x)^2}$ in the y-z plane. The convective effect of the sound pressure amplitude is hidden in Equation (5.14). After applying the correction, the sound pressure (real part) on the train external surfaces at one example frequency (200 Hz) is shown below in Figure 5.13(a) and the sound pressure levels at this frequency band on the train external surfaces in Figure 5.13(b). It can be noticed that because of the convective effect, the sound pressure levels in front of the pantograph is higher than that behind.
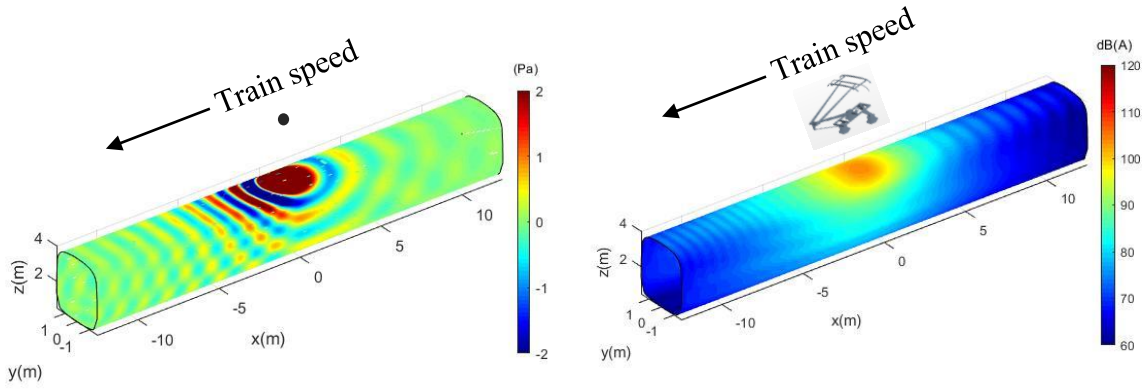
Figure 5.13. (a) Real part of sound pressure on train external surface due to a point source (unit oscillating velocity) in a uniform mean flow at 200 Hz, (b) sound pressure level on train external surface due to the pantograph in a uniform mean flow for 200 Hz band, dB(A) re 2×10⁻⁵ Pa. Train speed 290 km/h.

5.7 Modelling of flow influence at high frequency

At high frequency, which is here the region above 1 kHz, the acoustic wavelength is smaller than the thickness of the turbulent boundary layer and the effect from the wind gradient cannot be ignored. It is complicated to derive the sound propagation through the boundary layer to the train roof by theoretical methods. Here the ray tracing method [101] is employed to study the influence of the boundary layer on the sound propagation, which is known as a high frequency method. The diffraction of sound in the boundary layer can be illustrated by the sound ray trajectories. The governing equations for the ray trajectories are expressed as [101]

$$\frac{d\mathbf{x}_p}{dt} = \mathbf{u}_0 + \frac{c_0^2 \mathbf{s}_p}{1 - \mathbf{u}_0 \cdot \mathbf{s}_p} \tag{5.17}$$

$$\frac{d\mathbf{s}_p}{dt} = \frac{\mathbf{u}_0 \cdot \mathbf{s}_p - 1}{c_0} \nabla c_0 - \sum_j s_j \nabla u_{0j} \tag{5.18}$$

where the function $\mathbf{x}_p(t)$ is a ray trajectory, $\mathbf{u}_0$ is the flow velocity, $\mathbf{s}_p$ is defined as a wave-slowness vector normal to the wavefront. Solving the two equations in a time-stepping procedure can give the sound rays' locations and directions at each time step. The ray tracing

method is used to predict the sound propagation in three cases: in air at rest; in a medium with a uniform flow of speed 80 m/s; and in a boundary layer with a particular mean velocity profile. The flow is from the negative x direction to the positive x direction. The source location is 1.4 m above the train roof. The time step is set at 8×10^{-6} s and the ray spacing is 1°. The velocity profile in the boundary layer is determined in Section 5.5. The rays' locations and directions indicate the propagation of sound in the turbulent boundary layer. Their ray trajectories are shown in Figure 5.14. The gradient of the wind makes the sound rays bend away from the train roof in the upstream direction while it makes them bend towards the roof in the downstream direction.
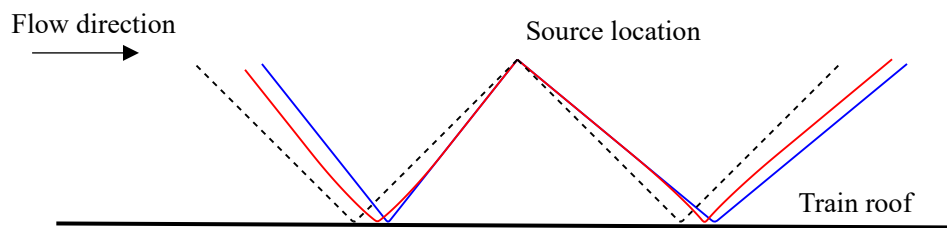
Figure 5.14. Ray trajectories, ┄┄: in air at rest; ──: in boundary layer, 80 m/s; ──: in uniform flow, 80 m/s; flow direction is from the left to the right.

Because in the upstream direction the velocity gradient within the boundary layer makes the sound rays bend away from the train roof, within a particular range of incident angles in the upstream direction, the velocity boundary might make the sound rays fully reflect before they reach the roof. A quiet area will therefore be generated in the upstream direction. However, because in the downstream direction the velocity gradient bends the sound rays towards the roof, the sound can always reach the train roof for all incident angles. Here, to illustrate the full reflection caused by the velocity gradient in the boundary layer in the upstream direction, the velocity profile is assumed to be symmetrical about $y = 0$ m to allow the sound rays to enter the region $y < 0$. The sound rays are plotted in Figure 5.15. It can be seen that in the area about $x < -2.5$ m the sound rays are fully reflected by the velocity boundary layer before they reach the roof.
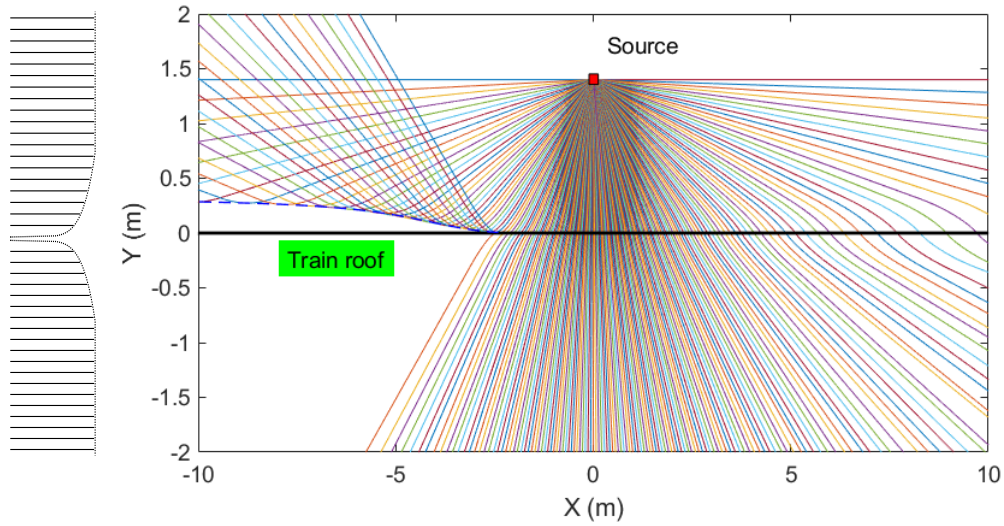
Figure 5.15. The ray trajectories in a flow speed of 80 m/s, flow from the left to the right.

Based on the Blokhintzev's invariant [102, 103], the mean square sound pressure in the medium is proportional to the area of the ray cluster. The area of the ray cluster can be obtained from the ray trajectories after they are solved, see Figure 5.16.
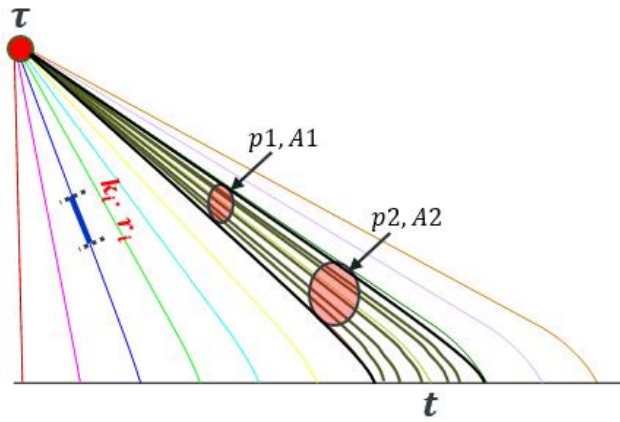
Figure 5.16. Rays in non-uniform flow.

Therefore, if the pressure at position 1 indicated in Figure 5.16 is chosen as a reference, the pressure at another position 2 can be calculated based on the relation

$$p_1^2 A_1 = p_2^2 A_2 \tag{5.19}$$

where p_1 and A_1 are the sound pressure and area of the rays at position 1 and p_2 and A_2 are those at position 2. The sound pressure phase is determined by the travelling time of the sound rays in the medium [101]. This can be derived from the term

$$e^{-ikr} = \prod_{i=1}^{n} e^{-ik_i \cdot r_i} = \prod_{i=1}^{n} e^{-i\frac{\omega}{c_i} \cdot r_i} = \prod_{i=1}^{n} e^{-i\omega \Delta t} \qquad (5.20)$$

where Δt is the time step in the calculation and n is the number of time steps. r is the total distance that the sound ray has travelled. k_i is the average acoustic wavenumber in the ith time step in the direction of the ray, r_i is the distance that the ray has travelled in that time step and c_i is the average sound speed in that time step.

The current 2.5D BE model cannot deal with curved rays or variable wave speeds when modelling sound diffraction and scattering. To model the sound pressure incident on the train external surface considering the influence of the velocity boundary layer in the 2.5D models, an equivalent acoustic wavenumber needs to be found when applying the inverse Fourier transform. Based on [101], analogously, it can be assumed that the influence of the velocity boundary layer can be modelled by an equivalent mean flow with a uniform velocity. The equivalent mean flow will convey the sound rays to the same locations on the train roof as the velocity boundary layer does, which will make the sound ray clusters have similar area when they reach the train roof. The resulting equivalent acoustic wavenumber is given by

$$k_0' = \frac{\omega}{c_0 \pm \overline{u_{\text{eq}}} \cos \theta} \qquad (5.21)$$

According to the Blokhintzev's invariant [102], the equivalent mean flow in Equation (5.21) will give a relatively precise prediction of the sound pressure amplitude. However, as the phase of the sound pressure is related to the propagation time in the medium, the equivalent mean flow is not able to give a precise prediction of the phase information because the velocity gradient within the boundary layer will bend the sound rays whereas the mean flow will not, so the actual travelling time of the sound in the velocity boundary layer will not be predicted by the equivalent mean flow.

Another way to find the equivalent acoustic wavenumber is to assume that the equivalent sound speed is equal to the distance that the sound rays travel between the emission time at the source and the receiving time when it reaches the train surface divided by the propagation time. The equivalent wavenumber is then given as

$$k_0' = \frac{\omega}{L/(t-\tau)} \tag{5.22}$$

where L is the length of the ray trajectory before they reach the train surfaces, t and τ are the emission time at the source and the receiving time at the receiver on the roof. They can all be determined by using the ray tracing method. Equation (5.22) considered the time difference from the source to the receiver but it does not consider the area of the ray clusters. It therefore will not model the sound pressure amplitude precisely.

Because even a small error in propagation time will cause a large error in the phase at high frequency, the priority is given to model the propagation time when finding the equivalent sound speed. In this work, therefore, the equivalent acoustic wavenumber is determined by Equation (5.22) rather than Equation (5.21). Figure 5.17 shows the equivalent speed of sound in the boundary layer calculated by Equation (5.22) and compared with the results from Equation (5.21) and the analytical value in a uniform mean flow. They are all calculated for the case with flow speed of 80 m/s. It can be seen that the phase speed of sound decreases in the upstream direction while it increases in the downstream direction. For $x < $ -2.5 m in the upstream direction the sound rays are reflected by the boundary layer. For -2.5 $< x < 0$ m, the sound pressure levels will increase while in the downstream direction they will decrease compared with the case without flow. At $x = 0$ m the incident angle is 90° to the flow direction, the wind does not affect the sound speed, thus there is no convective amplification right below the pantograph.

When using Equation (5.22) to calculate the equivalent phase speed of sound, at about 4 m away from the pantograph in the downstream direction, the equivalent speed of the sound in the mean flow and in the boundary layer have a nearly constant difference of about 6 m/s. This will not cause an obvious difference in the sound pressure levels between using a uniform mean flow and using a boundary layer to model the influence of flow. However, the two models will make an obvious difference in terms of the incident angles of the sound rays to the train roof (the angle between the rays and the roof surface), which will cause a significant difference to the sound power incident on the train roof. When using Equation (5.21), the predicted equivalent acoustic speed is about 50 m/s lower than the value obtained analytically from a uniform mean flow.
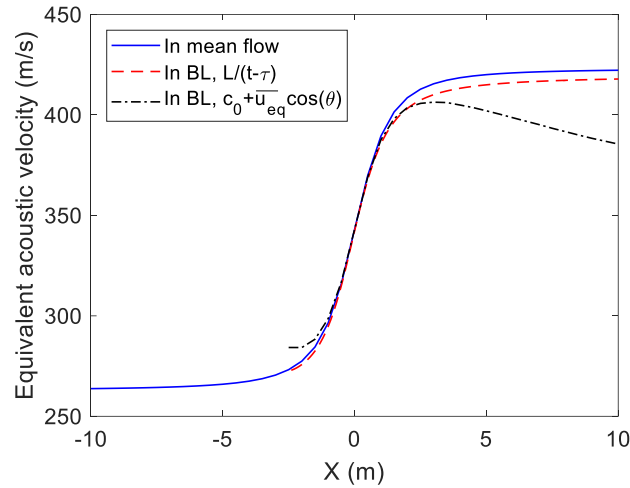
Figure 5.17. Equivalent phase speed of sound, in the uniform mean flow and in boundary layer calculated by the raying tracing method, flow speed 80 m/s, from the left to the right.

Substituting the equivalent sound wavenumber into the inverse Fourier transform, Equation (5.14), the sound pressure on the train external surfaces considering the velocity boundary layer can be obtained. Figure 5.18(a) shows the real part of the sound pressure at 1600 Hz on the train external surfaces due to the pantograph above the roof. Figure 5.18(b) shows the sound pressure levels at this frequency due to the pantograph. The train speed is set to be 290 km/h. It can be seen that a quiet area exists in the upstream direction.
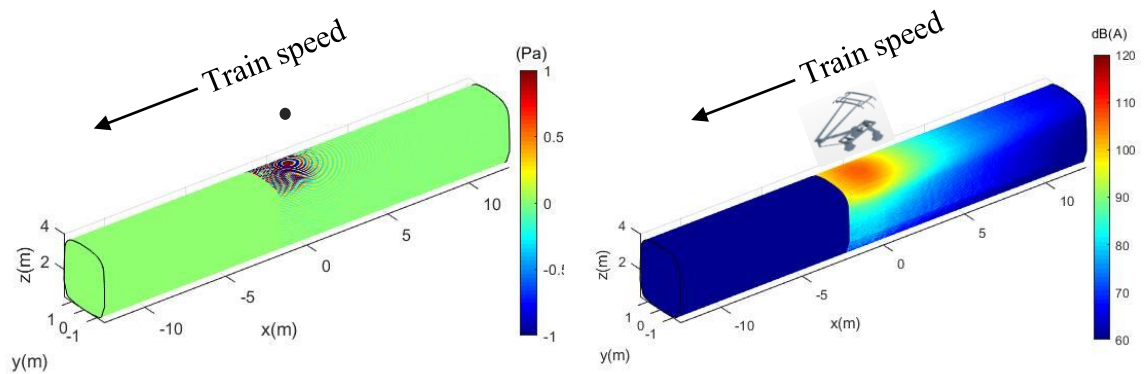
Figure 5.18. Real part of sound pressure on train external surface due to a point dipole source (unit oscillating velocity) considering influence of flow at 1600 Hz, (b) sound pressure level on train external surface due to the pantograph considering influence of flow for 1600 Hz one-third octave band, dB(A) re 2×10^{-5} Pa. Train speed 290 km/h.

After the flow influence has been modelled at both low and high frequency, the overall sound pressure distribution on the train external surfaces can be calculated by summing the

contributions from each one third octave frequency band. Because the amplification of sound pressure amplitude caused by flow is independent of frequency the convective amplification will be consistent in each frequency group. Using the uniform mean flow to model the flow influence, the sound can reach all the roof surface while using the ray tracing method there is always a quiet area in the upstream direction (depends on train speed and on distance from the front of the train, the conclusion is made for this case with train speed 290 km/h at the 40 m position). Around the frequency where the acoustic wavelength equals the thickness of the boundary layer, in this case 1 kHz, the influence of the flow on the sound pressure on the train external surfaces can be modelled by both approaches, but there is a discontinuity in terms of the sound distribution on the train external surfaces at 1 kHz as the frequency range changes from one to the other.

5.8   Validation of the 2.5D boundary element model

To validate the 2.5D BE models for predicting the sound distribution on the train external surfaces, experiments were performed in the anechoic chamber at ISVR, University of Southampton, to measure the sound pressure on the external surfaces of the 1/5 scale model train. The influence of flow on the noise transmission cannot easily be replicated in the measurements. The effect of the flow is therefore validated separately by comparison with analytical solutions at low frequency and with the ray tracing model at high frequency.

5.8.1   Validation of the 2.5D BE model by measurements

Laboratory measurements were performed in the anechoic chamber at the University of Southampton to validate the 2.5D BE models. The measurement set up is the same as that in section 3.6.1. The rail and ballast are not essential in this test, but they can provide more representative absorptive properties below the train. The pantograph is modelled by a single point source located 0.24 m above the train roof and in the middle of the train cross-section to evaluate the sound pressure distribution around the train body in the experiment, see Figure 5.19(a). The point source is a horn driver as described before in Section 3.6.1. It gives a monopole-like sound distribution, rather than a dipole source, but if the 2.5D model can predict the sound distribution on the scaled train model due to a monopole source above it, it can also be trusted to predict the sound pressure from a dipole source. Microphones are located along the centrelines of the train roof and one side surface. On each surface, there are 11 measurement locations between the middle of the carriage and one of its ends, with a spacing of 0.1 m.

Figure 5.19(b) shows the corresponding numerical model. The train and ballast box are modelled by linear boundary elements with element size 0.01 m (allowing the calculation to be carried out up to 5 kHz based on six elements per wavelength). The boundary condition of the train surface is set as rigid while for the ballast an acoustic impedance boundary condition is given to the top surface and the sides are rigid. The source in the numerical model is represented by a circle with radius 0.005 m and 36 boundary elements. The source strength is derived from the sound power of the source used in the measurement. 'CHIEF' points are added in the model to solve the non-uniqueness problem for exterior problems, as for the previous model in Chapter 4. The measured locations are illustrated as points P_1, P_2 (now the names are different from those in Chapter 4) in the corresponding numerical model, see Figure 5.19(b).
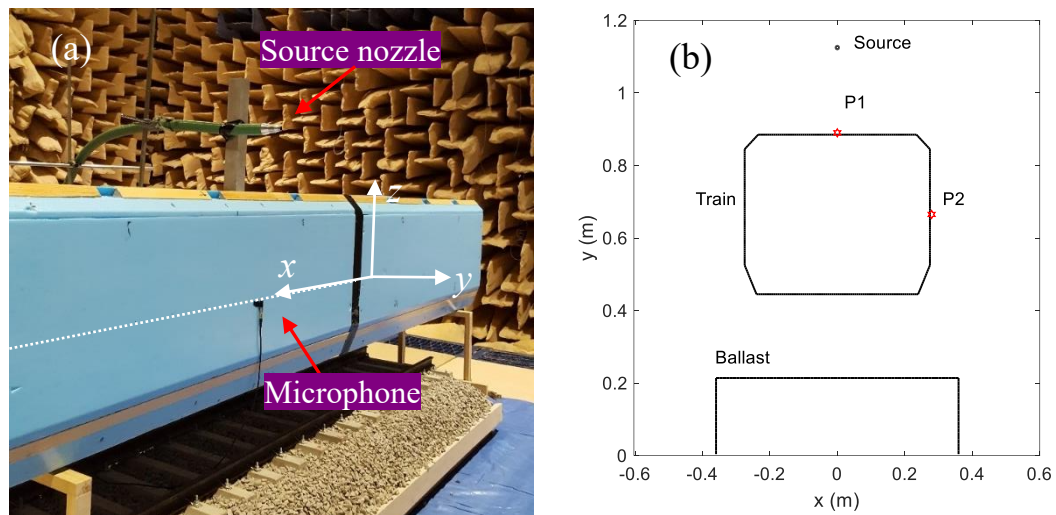
Figure 5.19. (a) Model in the measurement, (b) the corresponding 2.5D BE model.

The predictions and the measurements are compared in one-third octave bands between 1 and 5 kHz (200 to 1000 Hz at full scale). In the predictions, five frequencies are used in each one-third octave band to obtain the results. The comparisons are shown in Figure 5.20. The predictions show that the sound pressure level on the train roof decays faster than that on the side, and directly below the source the sound pressure level on the roof is about 20 dB higher than that on the side.
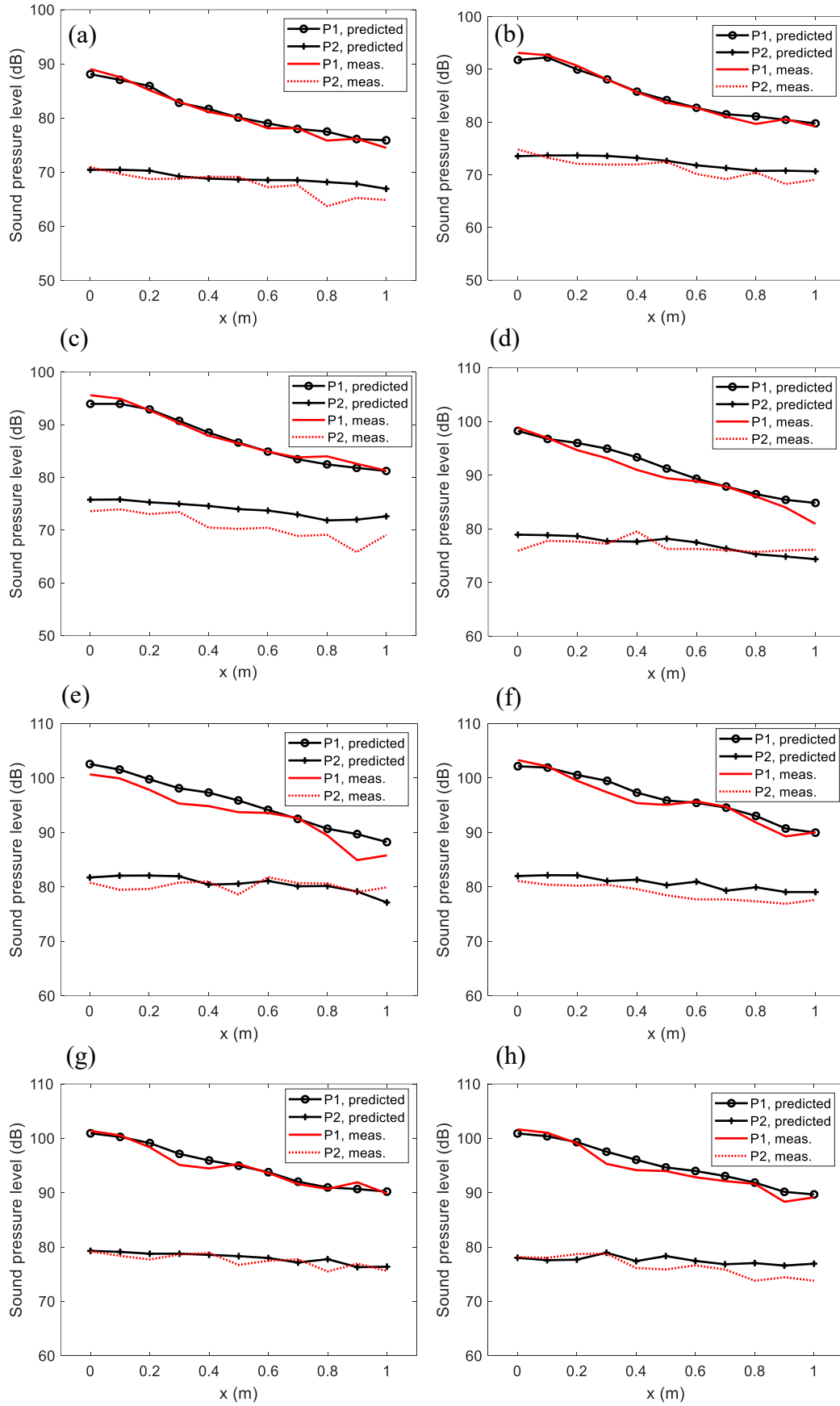
Figure 5.20. Comparison between predictions and measurements. (a) 1000 Hz, (b) 1250 Hz, (c) 1600 Hz, (d) 2000 Hz, (e) 2500 Hz, (f) 3150 Hz, (g) 4000 Hz, (h) 5000 Hz.

The maximum level difference between the predictions and the measurements (prediction minus measurement) and the average between them are listed in Table 5.2. The predictions agree well with the measurements. The average errors at these measured locations are mostly less than 1 dB except the 1600 Hz band which has about 3 dB difference. The comparisons indicate that the 2.5D model is sufficiently reliable.

Table 5.2. Relative error between predictions and measurements (dB).

Freq (Hz)	P1 (roof)		P2 (side)	
	Max.	Ave.	Max.	Ave.
1000	1.6	-0.3	4.4	-1.2
1250	1.4	-0.1	2.5	-1.1
1600	1.6	0.4	6.1	-3.2
2000	3.9	-1.2	3.0	-0.3
2500	4.8	-2.0	2.7	-0.4
3150	2.1	-0.6	3.2	-1.8
4000	2.0	-0.3	2.3	-0.5
5000	2.2	-0.8	3.2	-1.1

5.8.2 Validation of the flow influence

In modelling of the influence of flow, the 2.5D BE method with equivalent wavenumber and the ray tracing model are used. For sound propagation in a uniform mean flow, there is an analytical solution to calculate the sound pressure [34]. A Doppler factor can be used to model the amplification. In reality the source (the pantograph) and receiver (the train external surfaces) are moving at the same speed and the surrounding medium is stationary. As explained earlier in this Chapter, in this work it is assumed that the pantograph is stationary whereas the wind is moving in the opposite direction. The two cases are equivalent in terms of sound propagation.

To validate the flow influence at low frequency, a fluctuating force source (i.e. dipole) is considered to radiate sound in a free space, Figure 5.21(a). Receivers with coordinates (x_i, 0, -1.4) are set along the x direction to collect the sound pressure from the source. The modelling of a dipole source in the 2.5D BE model is explained in Section 4.1.3. In the corresponding 2.5D model, a circle with radius 0.01 m is created to represent the source, see Figure 5.21(b). The oscillating velocity of the dipole in the 2.5D model is set to be 1 m/s. A single receiver (y, z) = (0, -1.4) is set in the 2.5D model to get the sound pressure in wavenumber domain which is then converted to spatial domain. To compare with the results

113

obtained from the 2.5D BE model, the analytical sound pressure is calculated from Equation (5.4) by assuming the fluctuating force (a compact source) is harmonic with the form $\mathbf{F}e^{i\omega t}$. The force amplitude, $|\mathbf{F}|$, is adjusted to achieve the same source strength as that in the corresponding 2.5D BE model. In the 2.5D BE model the influence of flow is modelled by the equivalent acoustic wavenumber and in the analytical model it is modelled by the Doppler factor in Equation (5.5).
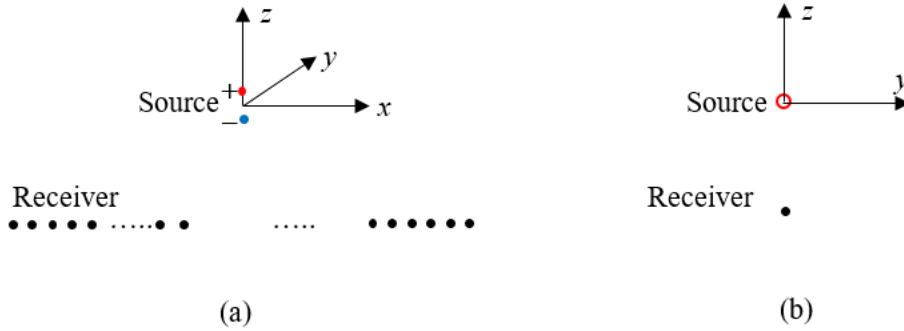
Figure 5.21. (a) A dipole source radiating in free space, (b) the corresponding 2.5D BE model.

The first case considered is without flow. The source is radiating sound in static air. Therefore the Doppler factor is equal to unity. The analytical solution in free space and the 2.5D prediction are compared at 200 Hz in Figure 5.22. The sound pressure levels on the two sides of the pantograph are identical. The 2.5D prediction and the analytical solution are nearly equal, with differences less than 0.5 dB.

In the second case the flow speed is set to 80 m/s ($v_s = 0, u_0 = 80$ m/s). The sound distribution at the receiver from the 2.5D BE model prediction and from the analytical model are compared at the same frequency in Figure 5.22. Because of the presence of the flow, the sound pressure level in the upstream direction has increased while that in the downstream direction has decreased. The 2.5D prediction has a good agreement with the analytical results with differences less than 1.0 dB, which shows the 2.5D model is reliable to model the influence of a uniform mean flow on noise propagation, indicating it is applicable to the train application at low frequency. Because the amplification/attenuation is not frequency dependent, results at other frequencies in the low frequency region (below 1 kHz) are not given.
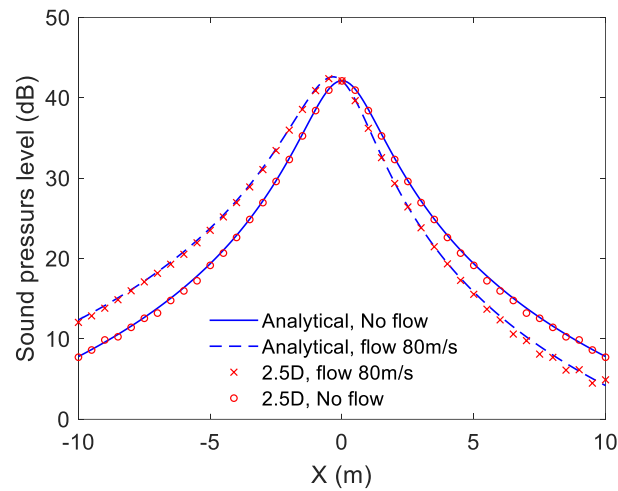
Figure 5.22. Sound pressure levels from a point dipole with and without uniform mean flow at 200 Hz. flow speed 80 m/s, from left to right.

At high frequency, the sound pressure in the velocity boundary layer cannot be calculated analytically. The modelling of the influence of the boundary layer is validated by using the ray tracing model. The source strength in the ray tracing model is equated to that used in the 2.5D model. Again, the wind flow is set at 80 m/s, the source is located at 1.4 m above the train roof. The sound pressure level on the train roof along the train centre line obtained from the ray tracing model at 1600 Hz is plotted in Figure 5.23 together with the prediction from the 2.5D BE model. In this validation, the train roof is not included so the results are just the incident sound pressure. With a rigid train roof, the sound pressure will be doubled. In Figure 5.23, there is a quiet area in the upstream direction at $x < -2.5$ m; the sound pressure levels are compared between -1.5 m and 10 m in the x direction (between -2.5 m and -1.5 m the sound rays are nearly at grazing incidence to the train surface, so the results from the ray tracing model are not reliable as it is calculated based on the area of the rays). Figure 5.23 shows that the sound pressure levels on the train roof obtained from the 2.5D BE model and from the ray tracing model are similar with differences of less than 1.3 dB in the upstream area and with a difference of about 1.6 dB at 10 m away from the source in the downstream direction. This verifies the modelling of the flow influence at high frequency. If using Equation (5.21) to calculate the equivalent acoustic wavenumber, the sound pressure is indicated by the blue dotted line in Figure 5.23. The sound pressure level at 10 m from the source in the downstream direction will increase by 1.2 dB compared with the values obtained by using Equation (5.22).
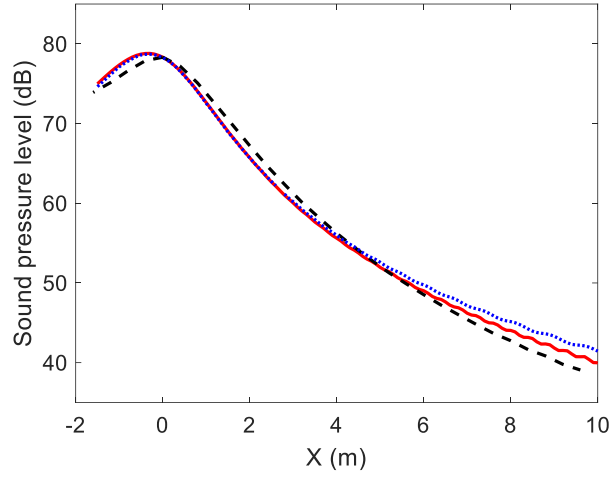
Figure 5.23. Comparison of sound pressure level between 2.5D and ray tracing model at 1600 Hz. ——: 2.5D model with $k_0' = \omega(t - \tau)/L$; ⋯⋯⋯: 2.5D model with $k_0' = \omega/(c_0 \pm \overline{u_{eq}} \cos \theta)$; - - -: ray tracing model. Flow speed 80 m/s, from left to right.

5.8.3   Total sound pressure on the train external surfaces in flow

The total sound pressure on the train external surfaces caused by the pantograph when the train is running at 290 km/h is calculated by adding the mean square sound pressure in each one-third octave band together. The overall A-weighted sound pressure on the train external surfaces at 290 km/h is indicated in Figure 5.24. It can be seen that the sound pressure in the upstream direction is higher than that in the downstream direction. The amplification and attenuation are caused by the convective effect of the flow and they depend on the train speed.
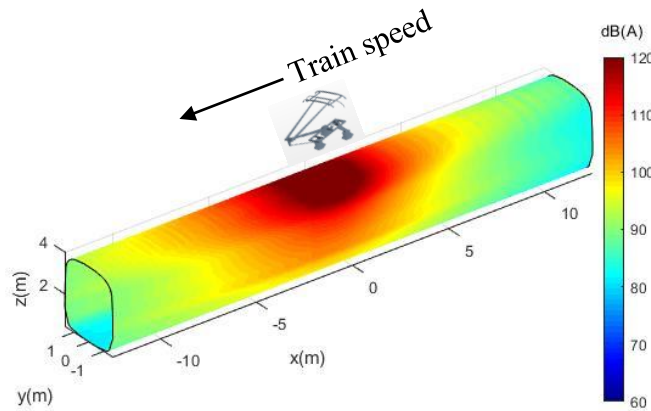
Figure 5.24. Overall sound pressure levels on the train external surfaces due to the pantograph with considering the influence of flow, train speed 290 km/h.

To understand how significant the effect of the flow is on the sound pressure amplitude, the overall sound pressure levels on the train roof along the centre line are plotted in Figure 5.25 and they are compared with the case in which the influence of flow is ignored. The sound pressure levels have some fluctuation at 5 m away from the pantograph and with increasing distance, the fluctuation becomes more obvious. This is introduced by the inverse Fourier transform in the 2.5D model when converting the wavenumber domain sound pressure to the spatial domain (truncation of the wavenumber). From the comparison in Figure 5.25, it can be seen that when the train is running at 290 km/h, the flow convective effect increases the sound pressure levels on the train roof surface in the upstream direction (10 m away) by about 3 dB while it decreases them in the downstream direction by about 3~4 dB.
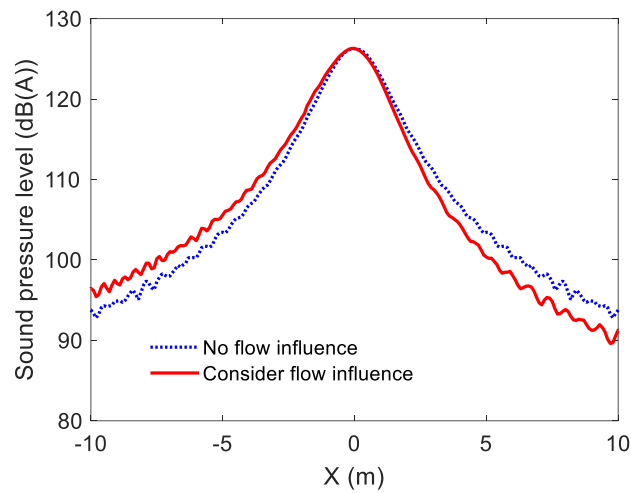
Figure 5.25. Overall A-weighted sound pressure level on the train roof along the centre line (train speed 290 km/h towards the right).

5.9   **Summary**

In this chapter, the noise propagation from the pantograph to the train external surfaces has been studied. The pantograph is replaced by several dipole sources and the sound propagation is modelled by using 2.5D BE method. In the 2.5D BE model, the dipole source and the train body are created in a 2D domain and the third direction is considered as a wavenumber integral. The sound power from the pantograph is calculated from the component-based approach and used to adjust the source level in the 2.5D BE model. The influence of flow on the noise propagation is considered differently at low and high frequency. At low frequency where the sound wavelength is larger than the thickness of the turbulent boundary layer, the boundary layer is ignored, and the wind is simply considered as a mean flow. However, at high frequency, the boundary layer profile is predicted by using a power law, and the sound propagation through it is modelled by using the ray tracing model. This is then used to determine an equivalent wave speed for use in the 2.5D model. Laboratory measurements are used to validate the 2.5D model.

The sound pressure on the train external surfaces from the 2.5D model shows that the pantograph noise is quite localised directly below the pantograph, where the sound pressure level on the train surface is high, but with increasing distance from the pantograph, it decreases rapidly. The simulation on the scale model train shows that the difference between the sound pressure level on the train roof and on the sides is about 20 dB in the plane of the pantograph. The levels gradually converge with increasing distance and there is about 10 dB difference at a distance of 1 m for the scale train model (5 m for full scale). The experimental measurements show a similar trend.

The wind will cause amplification or attenuation in the sound pressure levels. In the upstream direction the sound waves are squeezed and sound pressure is enhanced while in the downstream direction the sound wavelength increases and sound pressure is reduced. The wind gradient in the boundary layer will change the direction of the sound, thus making the sound rays bend away from the train surfaces in the upstream direction and towards the train surfaces in the downstream direction. Therefore, a quiet shadow area is formed in the upstream direction at high frequency. The validation of the influence of flow is performed by comparing the results obtained from the 2.5D BE models with an analytical solution at low frequency and with the numerical results obtained from the ray tracing model at high frequency. This shows that the 2.5D BE model with an estimated equivalent acoustic

wavenumber can predict the noise propagation through the boundary layer from the pantograph to the train external surfaces.

Combined with the laboratory experimental validation for the case without flow, it can be concluded that the 2.5D models can predict the pantograph noise propagation both with and without considering the influence of flow.

Chapter 6   2.5D FE/BE method for noise transmission through extruded panels

To predict the interior noise in a train cabin, the vibro-acoustic performance of the train wall structures should be investigated. In this chapter, the vibrational behaviour of a typical train wall structure, an extruded aluminium panel, is studied. For structures with an invariant cross-section such as extruded panels, wave-based methods become suitable for predicting their vibro-acoustic performance. In this chapter, the 2.5D FE/BE method is used to predict the noise radiated from, and transmitted through, an extruded panel. Specifically, a 2.5D model of the extruded aluminium panel is created in the 'WANDS' software developed at ISVR, University of Southampton [104].

6.1   Wavenumber domain analysis for extruded panels

6.1.1   2.5D FE model

The railway rolling stock manufacturing industry has adopted a method of construction using double-skinned, rib-stiffened extrusions of aluminium for the whole length of a carriage. The 2.5D FE/BE approach for an extrusion was presented by Nilsson et al. [17] and other researchers. In this wavenumber domain method, only a two-dimensional cross-section of the structure is meshed, assuming harmonic dependence on time and on the third direction in space. The equation of motion is originally formed by using Hamilton's principle expressions for strain and kinetic energies and by assuming test functions and trial solutions with dependence on the x-direction. The governing equation of the 2.5D FEs for a waveguide structure (isotropic property in one direction) modelled with plate elements is given by

$$\left[\mathbf{K}_4 \frac{\partial^4}{\partial x^4} + \mathbf{K}_2 \frac{\partial^2}{\partial x^2} + \mathbf{K}_1 \frac{\partial}{\partial x} + \mathbf{K}_0 - \omega^2 \mathbf{M}\right] \mathbf{\Phi}(x) = \mathbf{F}(x) \qquad (6.1)$$

where $\mathbf{K}_i$ are the stiffness matrices, $\mathbf{M}$ is the mass matrix, ω is the angular frequency, $\mathbf{F}(x)$ is a vector of forces, and $\mathbf{\Phi}(x)$ is the nodal displacement vector in the spatial domain. If a Fourier transform is applied to the x-direction, the nodal displacements can be expressed as

$$\tilde{\boldsymbol{\Phi}}(k_x) = \int_{-\infty}^{\infty} \boldsymbol{\Phi}(x)e^{ik_x x}dx \tag{6.2}$$

Its inverse Fourier transform is

$$\boldsymbol{\Phi}(x) = \frac{1}{2\pi}\int_{-\infty}^{\infty} \tilde{\boldsymbol{\Phi}}(k_x)e^{-ik_x x}dk_x \tag{6.3}$$

Meanwhile, the nodal force vector in the wavenumber domain is given by

$$\tilde{\mathbf{F}}_s(k_x) = \int_{-\infty}^{\infty} \mathbf{F}(x)e^{ik_x x}dx \tag{6.4}$$

Its inverse Fourier transform is

$$\mathbf{F}(x) = \frac{1}{2\pi}\int_{-\infty}^{\infty} \tilde{\mathbf{F}}_s(k_x)e^{-ik_x x}dk_x \tag{6.5}$$

Substituting Equation (6.2) and (6.4) into Equation (6.1)gives

$$[\mathbf{K}_4(-ik_x)^4 + \mathbf{K}_2(-ik_x)^2 + \mathbf{K}_1(-ik_x)^1 + \mathbf{K}_0 - \omega^2\mathbf{M}]\tilde{\boldsymbol{\Phi}} = \tilde{\mathbf{F}}_s \tag{6.6}$$

Positive values of the structural wavenumber k_x correspond to waves propagating in the positive x direction and negative values to waves propagating in the negative x direction.

6.1.2 Geometrical model

Kim et al. [64] studied the vibro-acoustic behaviour of an extrusion based on the waveguide method and relevant measurements were performed in reference [105]. In this work, Kim's geometry model is used and it is shown in Figure 6.1(a). This extruded panel is a typical floor panel of a railway vehicle, made of aluminium with the bottom[2] surface covered with a stiff rubber layer. The assumed properties and dimensions of the extruded panel are listed in Table 6.1. The geometry of numerical model created for this work is shown in Figure 6.1(b). In the numerical model, the cross-section of the extruded panel is modelled by using plate finite elements. It has dimensions of 1 m in width and 67.5 mm in height. Both the

---

[2] The bottom surface of the extrusion is actually the surface that faces the inside of the train. The top surface faces the ground.

lower plate and upper plate have 101 nodes while 130 nodes are used for the middle stiffeners. The damping loss factor of the aluminium panel and its mass density are based on Kim et al.'s model. The density of aluminium is 2700 kg/m^3 and the density of the rubber is 1500 kg/m^3. When the rubber layer is attached to the bottom plate, the rubber will increase its mass and the damping loss factor. Keeping the thickness of the strip unchanged, an equivalent mass density of 5062 kg/m^3 is used to allow for the rubber layer. The damping loss factor of the layer with and without rubber was measured by Zhang et al. [66]. A mean value of 0.005 is chosen for top plate without rubber and 0.02 for the bottom plate with the rubber layer. The air cavities inside the extrusion are not taken into account in this study; the influence from the air cavities was found by Zhang et al. not to be significant [66].

In this work, the 'extruded panel' refers to the whole structure, while the 'strips' refer to the narrow thin plates that make it up, like strips A, B, C in Figure 6.1(b). If the whole structure is represented by an equivalent plate model which has the mass per unit area and bending stiffness of the extruded panel, the modes/waves in this equivalent plate are defined as global modes/waves, while those in the strips are called local modes/waves.
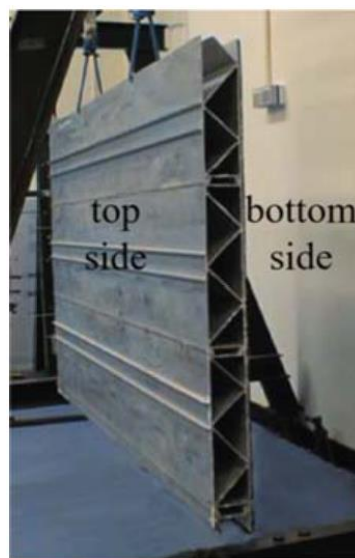
(a)
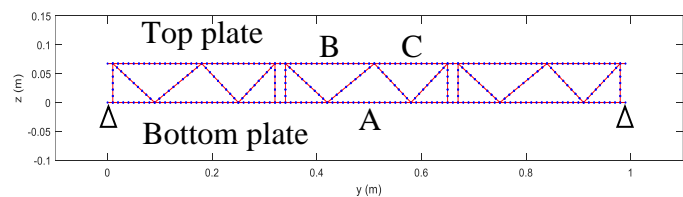
(b)

Figure 6.1. (a) An example of an extruded panel from a railway vehicle [64, 105], (b) The cross-section model of the extrusion. Red lines represent the geometrical shape of the extrusion cross-section, the dots '.' represent the plate finite element nodes in the 2.5D model.

Table 6.1. Properties and dimensions of the extruded panel [64].

Properties	Young's modulus (E) N/m²	Poisson's ratio (v)	Density (ρ) kg/m³	Thickness (t) mm	Loss factor (η)	Height (H) m
Aluminium	7.0×10^{10}	0.3	2700	2.54	0.005	0.067
Rubber	-	-	1500	4	0.02	-

6.1.3   Dispersion relations

To study wave propagation in this extruded panel, the dispersion curves can be helpful. For free vibration, $\tilde{\mathbf{F}} = \mathbf{0}$, Equation (6.6) can be rewritten as

$$[\mathbf{K}_s(k_x) - \omega^2 \mathbf{M}]\tilde{\mathbf{\Phi}} = \mathbf{0} \tag{6.7}$$

where $\mathbf{K}_s(k_x) = \mathbf{K}_4(-ik_x)^4 + \mathbf{K}_2(-ik_x)^2 + \mathbf{K}_1(-ik_x)^1 + \mathbf{K}_0$. The eigenvalue problem related to Equation (6.7) can be solved for ω at given real wavenumbers or can be solved for k_x at given angular frequencies. As the latter is a quadratic eigenvalue problem, the former approach is adopted here. The eigenvalue problem provides dispersion relations of waves propagating along the x direction.

The dispersion relations of this extruded panel with free boundary conditions at the edges are illustrated in Figure 6.2 and those for simply supported boundary conditions (as indicated in Figure 6.1(b)) are illustrated in Figure 6.3. The result with clamped boundary conditions is also shown in Figure 6.4. These correspond to the free waves in an undamped panel which can be obtained in each case by giving a real wavenumber k_x (the resolution of k_x is $\pi/20$) in Equation (6.7) and solving for the real values of angular frequency ω. The red lines in the figures represent the acoustic wavenumber. From the three diagrams, it can be concluded that the effects of the boundary condition on the waves in this extruded panel are more significant at low frequencies. In the case of free-free boundary conditions, illustrated in Figure 6.2, there are several waves at low frequency. However, in the case of simply supported boundary conditions, see Figure 6.3, there are no waves below around 150 Hz. For the clamped case, see Figure 6.4, no waves exist below 250 Hz. At high frequency, local waves in the strips are excited and become dominant, thus the dispersion curves of the three cases are similar.
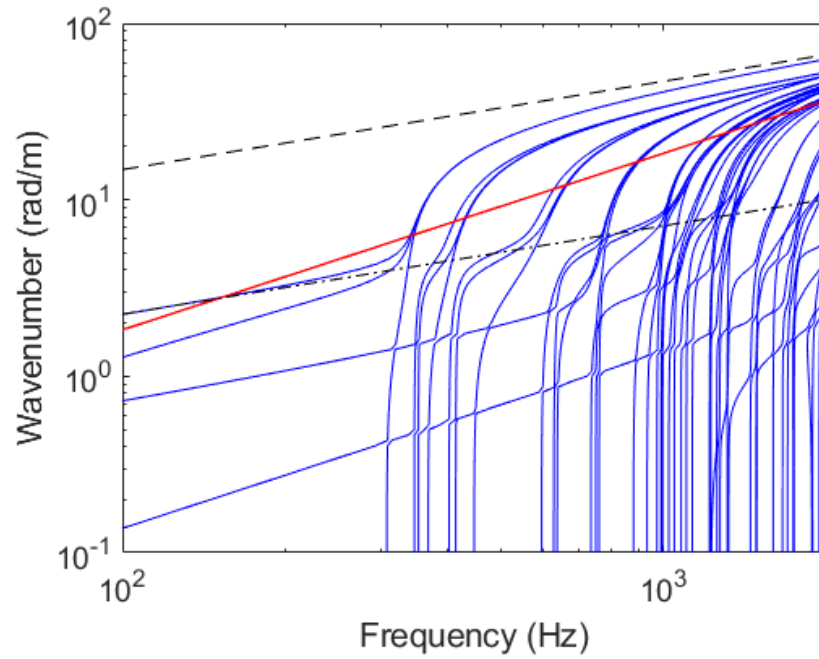
Figure 6.2. Dispersion curves for a free-free extruded panel. ——: structural wavenumbers in the full structure; ——: acoustic wavenumbers; ⎯·⎯·⎯: free bending waves in an equivalent plate which represents the whole structure; ⎯ ⎯ ⎯: free bending waves in an equivalent plate which represents the strips.
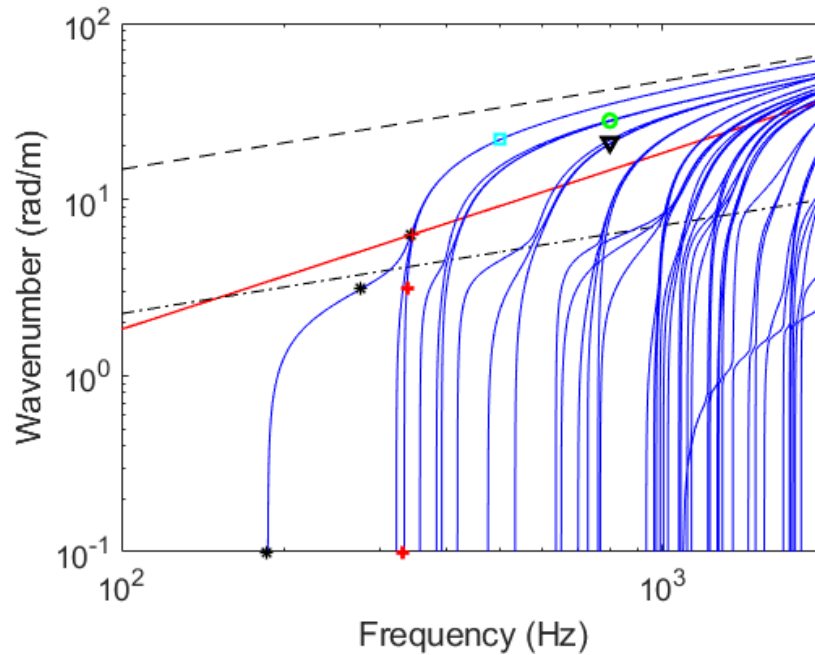
Figure 6.3. Dispersion curves for a simply supported extruded panel. ——: structural wavenumbers in the full structure; ——: acoustic wavenumbers; ⎯·⎯·⎯: free bending waves in an equivalent plate which represents the whole structure; ⎯ ⎯ ⎯: free bending waves in an equivalent plate which represents the strips.
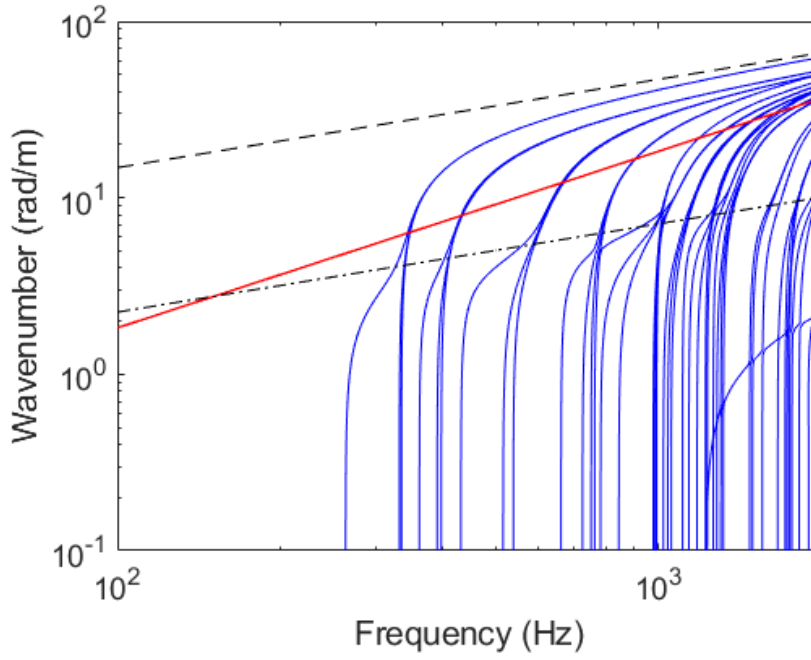
Figure 6.4. Dispersion curves for a clamped extruded panel. ——: structural wavenumbers in the full structure; ——: acoustic wavenumbers; –·–·–: free bending waves in an equivalent plate which represents the whole structure; – – –: free bending waves in an equivalent plate which represents the strips.

The vibro-acoustic behaviour of the extruded panel can be divided into global behaviour (or global waves) and local behaviour (or local waves) [63]. As stated above, the global behaviour corresponds to waves propagating in an equivalent plate which has the same mass per unit area and bending stiffness as the whole extruded panel. The local behaviour is considered as waves propagating predominantly in individual strips. Based on reference [106], two asymptotic lines can be calculated to represent the free wavenumber in the strips and in the equivalent plate. They are calculated by

$$k = (\omega)^{\frac{1}{2}} / \left(\frac{u}{B}\right)^{\frac{1}{4}} \tag{6.8}$$

where μ is the mass per unit area, 12.86 kg/m^2 for the strips (with the rubber layer) and 30.93 kg/m^2 for the whole structure. B is the bending stiffness, being calculated as 4.77×10^5 Nm for the whole structure and 105.05 Nm for the strips. These free bending waves are the black lines illustrated in Figure 6.3. The dashed asymptotic line denotes the free bending wavenumbers of the local waves in the strips and the dash-dot line represents the free wavenumbers of the global bending waves.

In the dispersion diagram, each line represents waves with approximately sinusoidal shapes in the *y* direction analogous to a thin homogeneous plate strip (some are global waves while most of them are local waves). With increasing frequency, higher-order waves in the *y* direction appear. For a homogeneous plate strip with simply supported boundaries at the ends, the wavenumber in the *y* direction is expressed as

$$\alpha_n = n\pi/(2b), (n = 1,2,3\cdots) \tag{6.9}$$

where $2b$ is the width of the strip, $n = 1$ corresponding to the first cut on wave and $n = 2$ corresponding to the second cut on wave, illustrated in Figure 6.4.

(a)   (b)
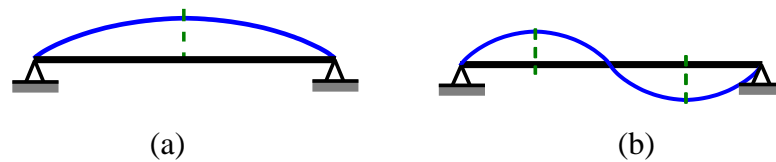
Figure 6.5. The mode shape of waves in the *y* direction, (a) *n* = 1, (b) *n* = 2.

For a homogeneous plate strip with simply supported boundary conditions at two opposite edges, the wavenumber of guided waves in the *x* direction can be expressed as

$$k_x = (k^2 - \alpha_n{}^2)^{\frac{1}{2}} \tag{6.10}$$

where k is wavenumber of free flexural waves in the homogeneous plate strip. At the cut on frequency of the corresponding wave, the wavenumbers in the *x* direction (k_x) are zero by definition. Therefore, the cut on frequencies can be calculated by setting $k_x = 0$ in Equation (6.7) and also can be read directly from Figure 6.3. The first six cut-on frequencies of the extruded panel are listed in Table 6.2.

Table 6.2. First six cut-on frequencies of the extruded panel with simply supported boundary conditions.

n^{th}	1	2	3	4	5	6
Frequency (Hz)	186.6	322.4	333.6	356.5	382.5	391.4

Figure 6.6 shows the mode shapes of different modes at their corresponding cut-on frequencies listed in Table 6.2. From this it can be seen that the first cut-on frequency corresponds to a global wave, and the rest of these cut on frequencies correspond to local waves.
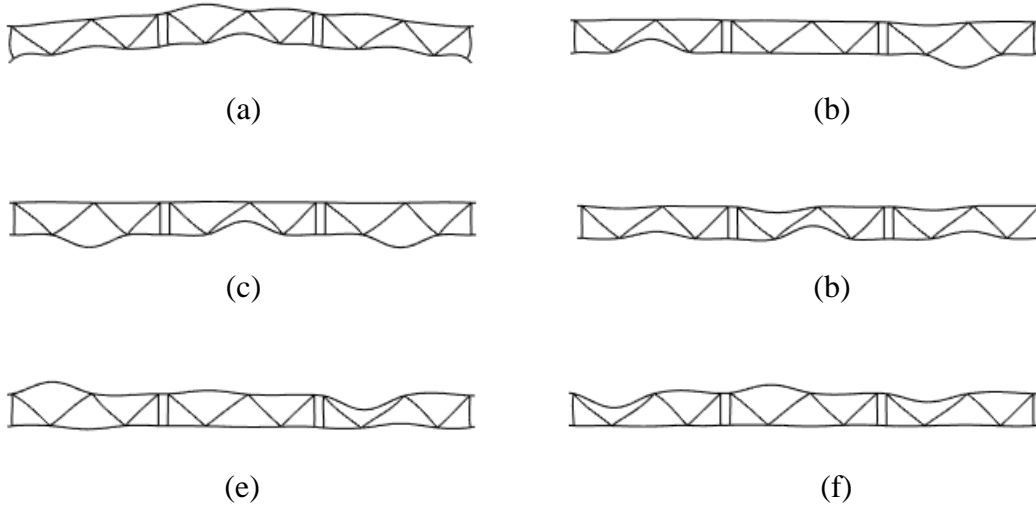
Figure 6.6. Mode shapes of different modes at their corresponding cut-on frequencies given in Table 6.2. (a) 186.6 Hz, (b) 322.4 Hz, (c) 333.6 Hz, (d) 356.5 Hz, (e) 382.5 Hz, (f) 391.4 Hz.

Above the corresponding cut-on frequencies, the axial wavenumber firstly increases rapidly with increasing frequency. Then, the slope of the curve gradually decreases, and increases again around the first asymptotic line. At higher frequencies, the curves finally tend asymptotically to the dispersion curves for free local waves in the attached strips. This shape of the dispersion curves can be explained by considering that the waves change their forms in the extrusion due to the stiffeners. This phenomenon is different at different wavelengths. Figure 6.7 and Figure 6.8 illustrate the evolution of particular mode shapes as frequency increases. The mode shapes are plotted by using the deformation in the 2D cross-section multiplied by the term $e^{-ik_x x}$. k_x is fixed but x varies from 0 to 1 m. Figure 6.7(a) represents a global wave in the structure first (indicated by the first dispersion curve in Figure 6.3), but with increasing frequency the global wave tends to become local waves in the strips, see Figure 6.7(b) and (c). Some curves representing local modes do not have this change as they are not affected by the stiffeners. See for instance, the third curve in Figure 6.3 which represents a purely local wave; its shape is shown in Figure 6.8 for three different wavenumbers.
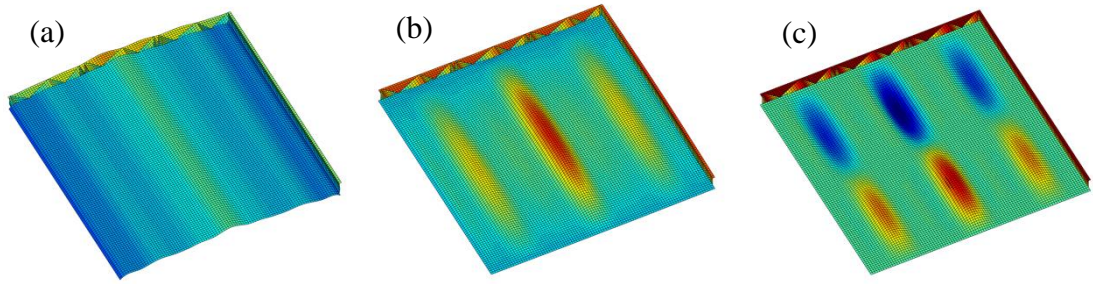
Figure 6.7. Evolution of the mode shape corresponding to '*' in Figure 6.3 as frequency increases, the real part of the displacement is plotted, (k_x, rad/m), (a) $f = 186$ Hz, $k_x = 0$, (b) $f = 276$ Hz, $k_x = \pi$, (c) $f = 343$ Hz, $k_x = 2\pi$.
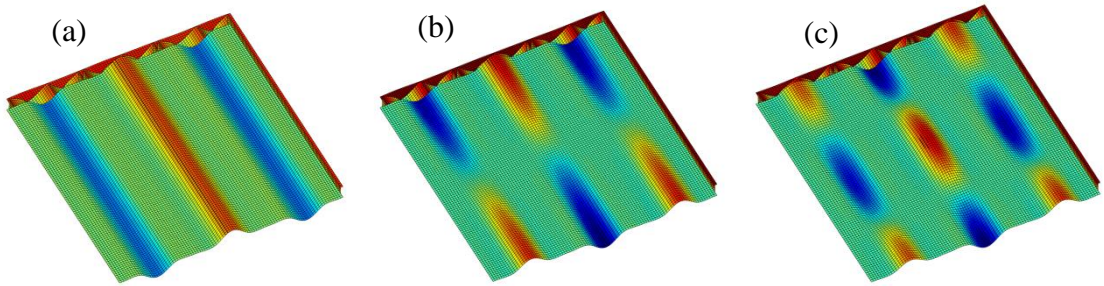
Figure 6.8. Evolution of the mode shape corresponding to '+' in Figure 6.3 as frequency increases, the real part of the displacement is plotted, (k_x, rad/m), (a) $f = 332$ Hz, $k_x = 0$, (b) $f = 337$ Hz, $k_x = \pi$, (c) $f = 346$ Hz, $k_x = 2\pi$.

Above the lower dash-dot asymptotic line in Figure 6.3, local modes are dominant. Orrenius et al. [63] defined this as the 'plate region'. In the plate region, the dispersion curves are clustered in groups as seen in Figure 6.3. Each group contains three waves as the structure has three identical bays. In the mode shapes of the modes within the same group, the different bays may be vibrating in phase or out of phase. This is illustrated in Figure 6.9, which shows the mode shapes in the first group at frequency 500 Hz; in (a) the three bays are in phase, in (b) they vibrate in an anti-symmetrical manner and in (c) they are out of phase with adjacent bays.
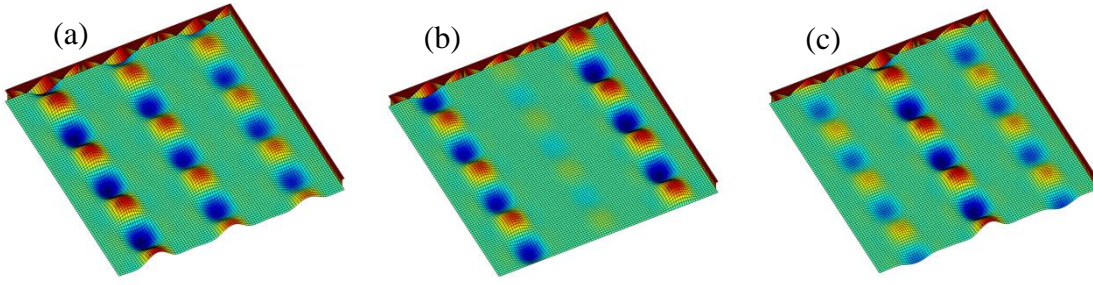
Figure 6.9. The real part of displaced shape for waves in the first group (strips on the bottom plate) at frequency 500 Hz, corresponding to '▫' in Figure 6.3. (k_x, rad/m), (a) $k_x = 21.807$, (b) $k_x = 21.802$, (c) $k_x = 21.796$.

Figure 6.10 and Figure 6.11 show the local waves on the top plate. Figure 6.10 is for modes in the group of wider strips (there are three) with a width of 0.17 m and Figure 6.11 is for the group of narrower strips with a width of 0.14 m. The local waves in each figure are not vibrating completely in phase or out of phase, but equivalent strips have similar modal shapes. They do not vibrate like the strip in Figure 6.9 because the three strips in each group on the top plate do not have exactly the same boundary condition. The difference in boundary conditions might cause them to vibrate slightly differently, instead of completely in phase or out of phase.
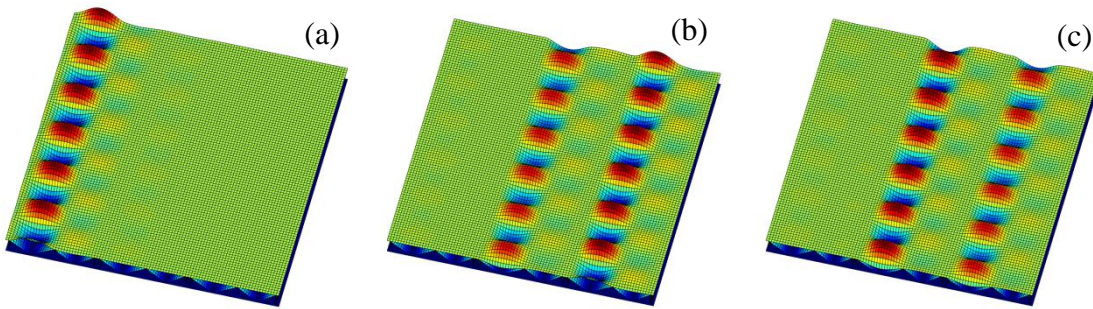
Figure 6.10. The real part of displaced shape for waves in the second group (strips on the top plate) at frequency 800 Hz, corresponding to 'o' in Figure 6.3. (k_x, rad/m), (a) $k_x = 28.17$, (b) $k_x = 28.01$, (c) $k_x = 28.00$.
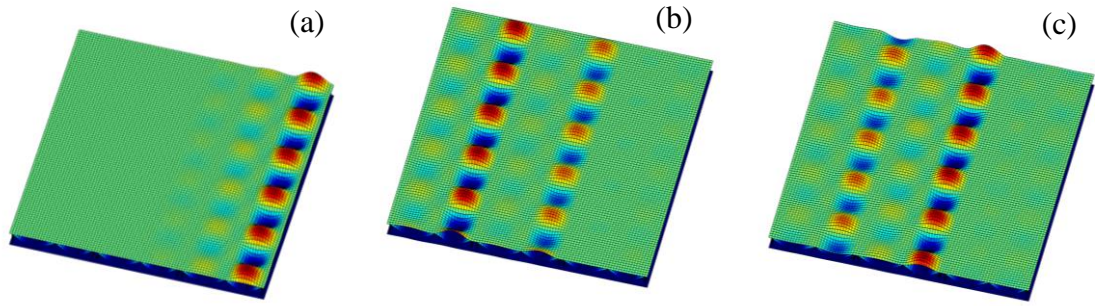
Figure 6.11. The real part of displaced shape for waves in the third group (strips on the top plate) at frequency 800 Hz, corresponding to '∇' in Figure 6.3. (k_x, rad/m), (a) $k_x = 22.04$, (b) $k_x = 21.11$, (c) $k_x = 21.02$.

6.1.4 Forced response

If the structure is excited by a mechanical force vector $\tilde{\mathbf{F}}$, the governing equation becomes

$$[\mathbf{K}_s(k_x) - \omega^2 \mathbf{M}]\tilde{\boldsymbol{\Phi}} = \tilde{\mathbf{F}} \tag{6.11}$$

Then the displacements $\tilde{\boldsymbol{\Phi}}$ of the structure can be obtained by

$$\tilde{\boldsymbol{\Phi}} = [\mathbf{K}_s(k_x) - \omega^2 \mathbf{M}]^{-1}\tilde{\mathbf{F}} \tag{6.12}$$

At a given frequency, the displacement in the spatial domain can be calculated by applying an inverse Fourier transform to the displacement in the wavenumber domain. This is expressed in Equation (6.3). Then the forced response of the structure will be obtained and it can be used to calculate the radiated sound. Figure 6.12(a) shows an example of the forced response of the structure when a unit mechanical force is applied to a strip on the top plate at a frequency 500 Hz. Figure 6.12(b) shows the forced response when the force is applied to a stiffener. The displacements in Figure 6.12 are the real part of the displacement multiplied by a scaling factor. In the x direction, the extrusion in this figure extends from -1.0 m to 0.0 m.
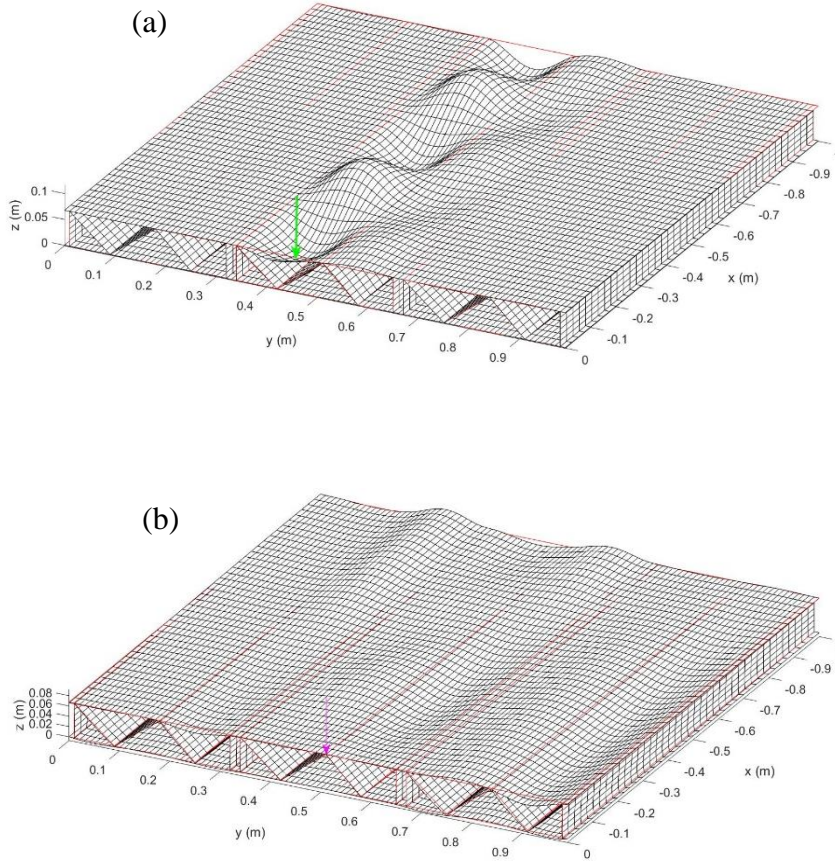
Figure 6.12. Real part of the spatial response of the structure to a unit force at an example frequency of 500 Hz, a length of 1.0 m is shown. (a) A strip is excited, scaling factor 1×10^4, (b) a stiffener is excited, scaling factor 1×10^5.

6.2   Coupled 2.5D FE/BE model

For a waveguide structure coupled with fluid domains, boundary elements are introduced to model the fluids, and they are connected to the 2.5D FEs. If the fluid-coupled structure is excited by a mechanical force **F** and also by acoustical pressure **P**, the governing equation of the 2.5D FE/BE model is [104]

$$[\mathbf{K}_s(k_x) - \omega^2 \mathbf{M}]\widetilde{\boldsymbol{\Phi}} = \widetilde{\mathbf{F}} + i\omega\rho_0 \mathbf{C}_1 \widetilde{\boldsymbol{\psi}} \tag{6.13}$$

where $\mathbf{C}_1$ is the complex matrix representing coupling between 2.5D FEs and 2.5D BEs. $\widetilde{\boldsymbol{\psi}}$ denotes the acoustic velocity potential vector defined at the nodes of the boundary elements. The continuity condition at the coupled degrees of freedom is given by

$$I_2 \frac{\partial \widetilde{\boldsymbol{\psi}}}{\partial \mathbf{n}} - i\omega \mathbf{C}_2 \widetilde{\boldsymbol{\Phi}} = \mathbf{0} \tag{6.14}$$

where $\mathbf{n}$ is the normal directional vector of the boundary elements connected to the 2.5D FEs, $\mathbf{I}_2$ is an identity matrix and $\mathbf{C}_2$ is a matrix allocating fluid-coupled degrees of the freedom in $\widetilde{\boldsymbol{\Phi}}$. $\widetilde{\boldsymbol{\Phi}}$ can be obtained from Equation (6.11) if only excited by a mechanical force and from Equation (6.13) if both mechanical and acoustic excitation are considered.

The velocity potential $\widetilde{\boldsymbol{\psi}}$ and the normal velocity $\partial \widetilde{\boldsymbol{\psi}} / \partial \mathbf{n}$ of the fluid at the coupled boundary can be determined by the following boundary integral equation

$$[\mathbf{H}]\widetilde{\boldsymbol{\psi}} - [\mathbf{G}] \frac{\partial \widetilde{\boldsymbol{\psi}}}{\partial \mathbf{n}} = 0 \tag{6.15}$$

where $\mathbf{H}$ and $\mathbf{G}$ are matrices of Green's functions. This equation has some differences compared with the one presented by Wu [89]. In the traditional 2D BE method, the equation involves the velocity and sound pressure directly rather than the velocity potential and its normal derivative. For BEs not coupled with FEs, boundary conditions need to be specified. For each uncoupled BE node, the boundary condition can be defined in the wavenumber domain by

$$\mathbf{C}_a \tilde{p} + \mathbf{C}_b \tilde{v}_n = \mathbf{C}_c \tag{6.16}$$

$\mathbf{C}_a$, $\mathbf{C}_b$ and $\mathbf{C}_c$ are the coefficients when assign the boundary conditions. The pressure and normal velocity can then be determined from the velocity potential $\widetilde{\boldsymbol{\psi}}$.

$$\tilde{p}(k_x) = i\omega \rho_0 \widetilde{\boldsymbol{\psi}} \tag{6.17}$$

$$\tilde{v}(k_x) = -\frac{\partial \widetilde{\boldsymbol{\psi}}}{\partial \mathbf{n}} \tag{6.18}$$

The matrix form of the coupled finite/boundary element model is

$$\begin{bmatrix} \mathbf{K} - \omega^2\mathbf{M} & -i\omega\rho_0\mathbf{C}_1 & 0 \\ 0 & \mathbf{H} & -\mathbf{G} \\ -i\omega\rho_0\mathbf{C}_2 & 0 & \mathbf{I}_2 \\ 0 & i\omega\rho_0\mathbf{C_a} & -\mathbf{C_b} \end{bmatrix} \begin{Bmatrix} \widetilde{\mathbf{\Phi}} \\ \widetilde{\mathbf{\Psi}} \\ \dfrac{\partial\widetilde{\mathbf{\Psi}}}{\partial\mathbf{n}} \end{Bmatrix} = \begin{Bmatrix} \widetilde{\mathbf{F}} \\ 0 \\ 0 \\ \mathbf{C_c} \end{Bmatrix} \tag{6.19}$$

By solving these equations, the pressure $\tilde{p}(k_x)$ and normal velocity $\tilde{v}(k_x)$ obtained on the fluid boundary are obtained in the wavenumber domain.

The coupled 2.5D FE/BE model for the extruded panel is shown in Figure 6.13. The fluid domain is on the two sides of the extruded panel. As this panel is assumed baffled on each side, the half space Green's function is used in the boundary integral Equation (6.15). To simulate the sound radiation, the extruded panel is set to be simply supported at the two edges of the bottom plate. Because this panel represents a train floor, there is no sound transmission from one side to the other one, so both the top and bottom plates are assumed to be rigidly baffled for $y < 0$ and $y > 1$ m.
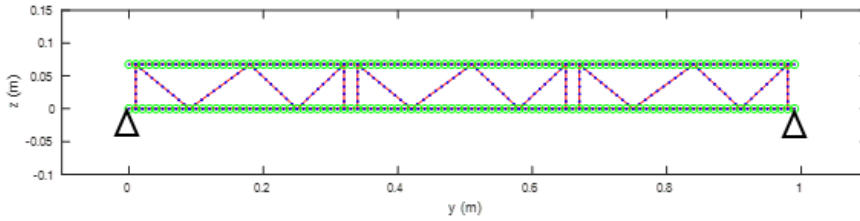
Figure 6.13. The coupled 2.5D FE/BE model. The red lines represent the geometry profile of the extruded panel. The blue dots represent the finite element nodes. The green circles denote the nodes of the fluid boundary elements.

6.3 Sound radiation efficiency

6.3.1 Numerical model

A mechanical force applied to one side of the extruded panel will cause the extruded panel to vibrate. The vibration of extruded panel will generate sound power. The radiation efficiency of the extruded panel is equal to the total radiated power divided by a normalised sound power. It can be calculated as

$$\sigma = \frac{W_{rad}}{\rho_0 c_0 \Gamma \left\langle \overline{v^2} \right\rangle_{inf}} \tag{6.20}$$

where W_{rad} is the total radiated sound power, $\left\langle \overline{v^2} \right\rangle_{inf}$ is the integral of the mean square velocity over the length and the average over the width. It can be calculated by [64]

$$\left\langle \overline{v^2} \right\rangle_{inf} = \frac{1}{2\pi\Gamma} \int_{-\infty}^{\infty} \int_{\Gamma} \frac{|\tilde{v}(k_x)|^2}{2} d\Gamma dk_x \tag{6.21}$$

where Γ is the width of the extruded panel in the y direction. The radiated power of the extrusion can be calculated in wavenumber domain as [64]

$$W_{rad} = \frac{1}{4\pi} \mathrm{Re}\left(\int_{-k_0}^{k_0} \int_{\Gamma} \tilde{p}(k_x)\, \tilde{v}^*(k_x) d\Gamma dk \right) \tag{6.22}$$

To calculate the mean square velocity in Equation (6.21), the integral over wavenumber should be calculated from $-\infty$ to ∞, while for the radiated sound power in Equation (6.22), the integral can be performed between $-k_0$ and k_0 (k_0 is the acoustic wavenumber). This is because the radiation properties of the waves in the extruded panel depend on the ratio of the structural wavenumber and the acoustic wavenumber. If the structural wavenumber is less than the acoustic wavenumber, far field sound will be generated. However, if the structural wavenumber is greater than the acoustic wavenumber, then the structural waves will generate only near field sound which will not propagate out to the far field. In this situation, the vibration is significant but the radiated power is negligible.

To demonstrate and verify the method adopted to calculate the radiated sound power, a simply supported single panel is considered as shown in Figure 6.14. The width of the plate is 1 m and thickness is 0.006 m. The material properties are Young's modulus 70 GPa, density 2700 kg/m^3, Poisson's ratio 0.332 and damping 0.1. The critical frequency of the current extrusion when the structural wavenumber is equal to the acoustic wavenumber, is expressed as

$$f_c = \frac{c_0^2}{2\pi}\sqrt{\frac{\mu}{B}} \tag{6.23}$$

where μ is the mass per unit area of the extruded panel and B is the equivalent bending stiffness of the extruded panel. Equation (6.23) gives the critical frequency 2025 Hz for the panel shown in Figure 6.14.

Figure 6.14. A single panel used to validate the integral limitations.

Figure 6.15(a) presents the dispersion curves of this panel. The red dashed line denotes the acoustic wavenumbers and the blue lines represent the structural wavenumbers. The mean square velocity of, and radiated sound power from this plate are calculated at some example frequencies shown below in Figure 6.15(b), (c) and (d).
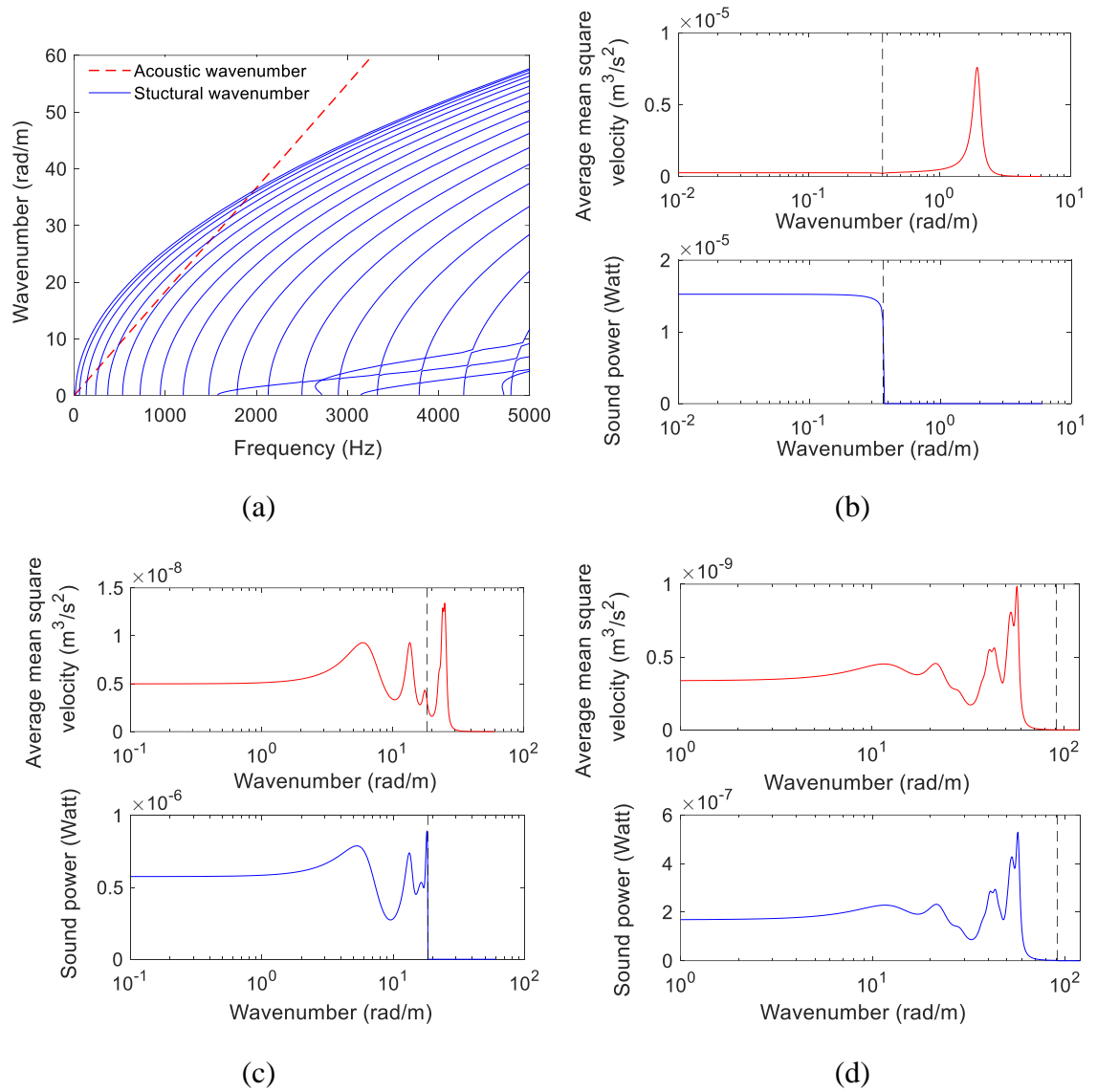
Figure 6.15. Dispersion relationship and sound power, average mean square velocity of a simply supported single plate. (a) Dispersion curves, (b) results at 20 Hz, (c) results at 1000 Hz, (d) results at 5000 Hz. The vertical dash lines in (b)~(d) are the corresponding acoustic wavenumber.

At a fixed frequency, for instance 20 Hz as shown in Figure 6.15(b), the mean square velocity of the plate in the wavenumber domain is significant up to 3 rad/m (free bending wavenumber at this frequency is 3.6 rad/m), while the sound power is significant only up to 0.36 rad/m. This is because at this frequency, the acoustic wavenumber is around 0.36 rad/m. The panel radiates sound only when the structure wavenumber is less than the acoustical wavenumber. Similar behaviour can be seen at 1 kHz as shown in Figure 6.15(c). Here, the acoustic wavenumber is around 18 rad/m (free bending wavenumber is 26 rad/m), and below 18 rad/m the sound power is significant. However, beyond this range, the vibration levels of the plate are still significant. That is why the integral should cover a wider wavenumber

range to calculate the mean square velocity than to calculate the radiated power. Above the critical frequency 2025 Hz, for instance at 5 kHz as shown in Figure 6.15(c), both mean square velocity and sound power are significant below 70 rad/m (free bending wavenumber 58.3 rad/m). The acoustic wavenumber is 90 rad/m. The same wavenumber range can be used to calculate both of them.

The sound power from the extruded panel under a mechanical force is determined using the WANDS software. For consistency, simply supported boundary conditions are used at the two edges of the bottom plate in the 2.5D FE model when calculating the sound power, see Figure 6.16.

To investigate the influence of force locations, three stiffener locations (F_2, F_5, F_8) and five strip locations (F_1, F_3, F_4, F_6, F_7) on the extruded panel are excited individually, as illustrated in Figure 6.16. The details are listed in Table 6.3.
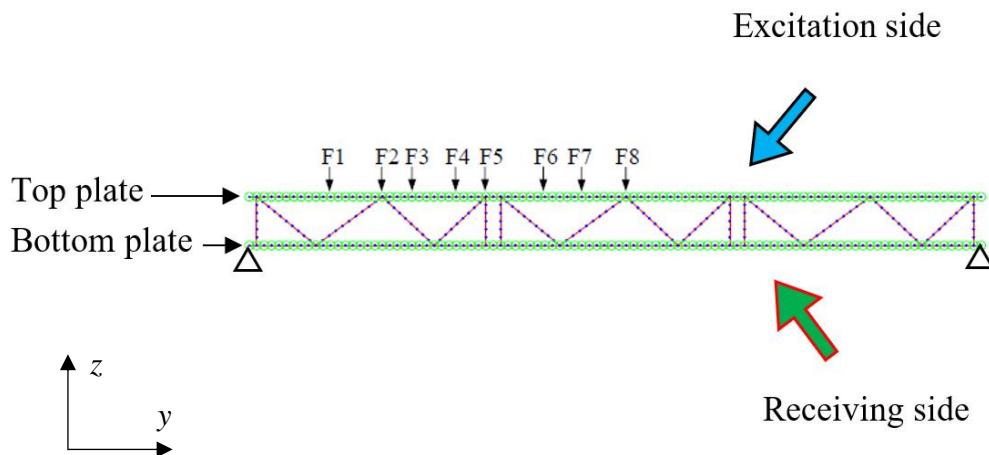
Figure 6.16. Force locations for noise radiation simulation.

Table 6.3. The locations of forces.

Excitation point	F_1	F_2	F_3	F_4	F_5	F_6	F_7	F_8
(y) m	(0.11)	(0.18)	(0.22)	(0.28)	(0.32)	(0.40)	(0.45)	(0.51)
Description	strip	stiffener	strip	strip	stiffener	strip	strip	stiffener

Comparisons are made with measurements of radiation efficiency of this extruded panel previously obtained at the ISVR, University of Southampton [64, 105]. The extruded panel

was suspended by a rope (see Figure 6.1(a)) and the excitation locations are illustrated in Figure 6.17. In the experiments, the extruded panel is under free boundary conditions, which is different from the boundary condition used in the 2.5D FE model. Also, in the 2.5D FE model, the two sides are baffled but in the experiment the panel is unbaffled.
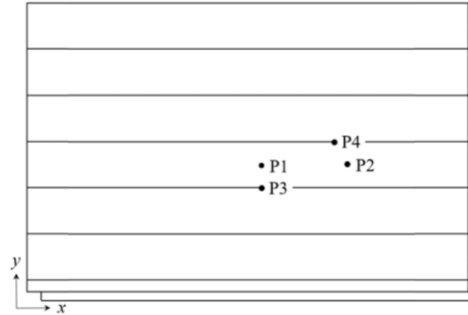
Figure 6.17. The locations of four excitation points on the top plate used in the experiments [64, 105].

6.3.2 Excitation on stiffeners

In the 2.5D FE model, the results are calculated at 100 logarithmically spaced frequencies from 50 Hz to 6 kHz. The number of wavenumbers used in the calculations is frequency dependent, ranging from 50 to 500. Figure 6.18 illustrates the mean square velocity of the extruded panel in one third octave bands when position F_2 is excited (the excitation side and the receiving side are defined in Figure 6.16). The force will excite the global vibration (global modes) of the extruded panel directly but does not directly excite the local vibration (local modes) in the strips. The global modes cut on at 186 Hz which is indicated in the figure. Because of the dominance of the global modes at low frequency, the mean square velocity on the two sides are similar. With increasing frequency, the local modes gradually cut on. The energy of the system is spreading from the global modes to the local modes. The mean square velocities on the two sides of the extruded panel begin to separate but their levels are similar.
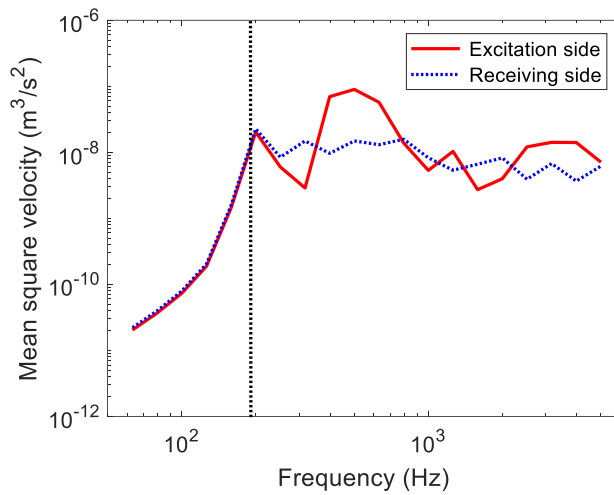
Figure 6.18. The mean square velocity of the extruded panel on its two sides with unit excitation at F_2 (on a stiffener, position indicated in Figure 6.16. The dot line refers to the cut-on frequency of the global modes, 186 Hz).

The radiated power on the two sides of the extruded panel has the same trend as its mean square velocity, see Figure 6.19. At low frequency, the radiated power on the two sides is similar, caused by global mode radiation. However, above the cut on frequency of local modes, the radiated power begins to diverge.
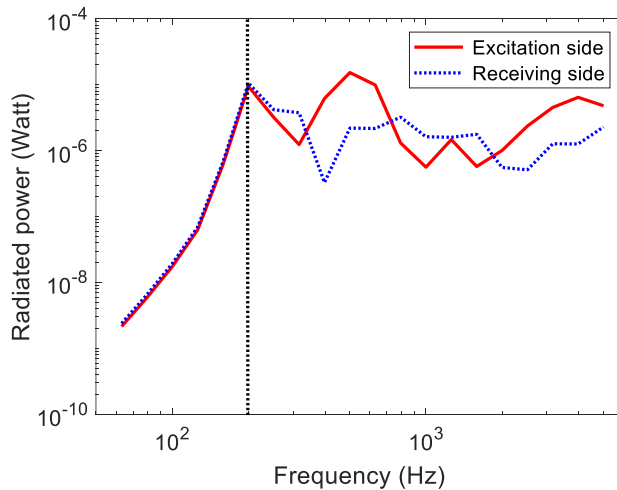
Figure 6.19. The radiated power of the extruded panel from its two sides with unit excitation at F_2 (on a stiffener, position indicated in Figure 6.16).

The radiation efficiency on the two sides of the extrusion when a mechanical force is applied to the stiffener at F_2 is shown in Figure 6.20 The cut on frequency of the local modes on the excitation side is 386 Hz, which is also indicated in the figure. At low frequency, the two sides have similar radiation efficiencies, while above the cut on frequency of the local modes, 140

the radiation efficiency on the two sides are different as the strips begin to contribute to the overall radiation efficiency. The numerically predicted radiation efficiency is similar to the measured one at high frequency. At low frequency, the error is probably caused by the difference of boundary conditions in the numerical models and in the experiments. Above the cut on frequency of local modes, the radiation efficiency drops because of the contribution of local modes. The critical frequency of the local modes on the excitation side is 4785 Hz calculated by Equation (6.23) above which the radiation efficiency trends to unity.
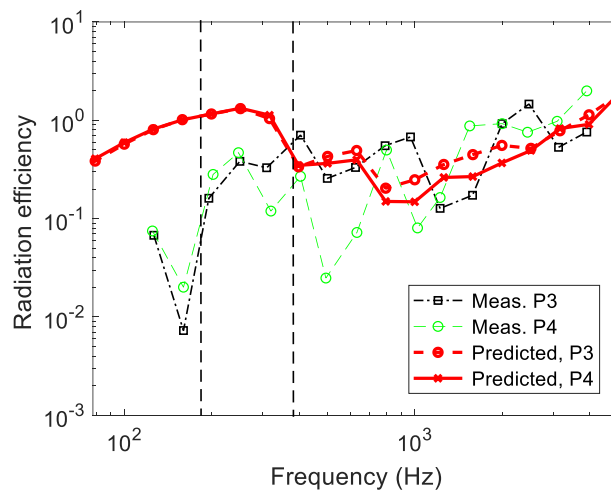
Figure 6.20. The radiation efficiency of the extruded panel for radiation from both sides with excitation on a stiffener. Comparison of prediction with measurement from [64, 105]. The dashed lines refer to the cut-on frequency of the global modes, 186 Hz, and the cut-on frequency of the local modes on the excitation side, 386 Hz.

To study the influence of excitation location on the results, another two stiffener positions, F_5 and F_8 are excited. The mean square velocity and radiated power of the extruded panel for the three excitation locations are shown in Figure 6.21 and Figure 6.22 respectively. The radiation efficiencies are shown in Figure 6.23. The results for the three excitation locations are similar in each case.
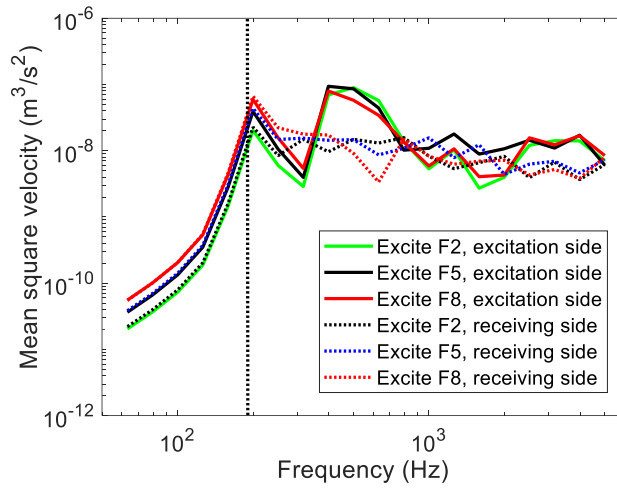
Figure 6.21. The mean square velocity of the extruded panel for three excitation positions (positions indicated in Figure 6.16).
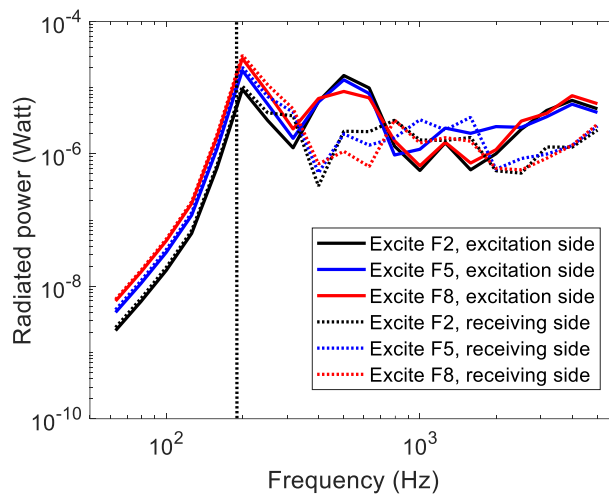
Figure 6.22. The radiated power of the extruded panel for three excitation positions (positions indicated in Figure 6.16).
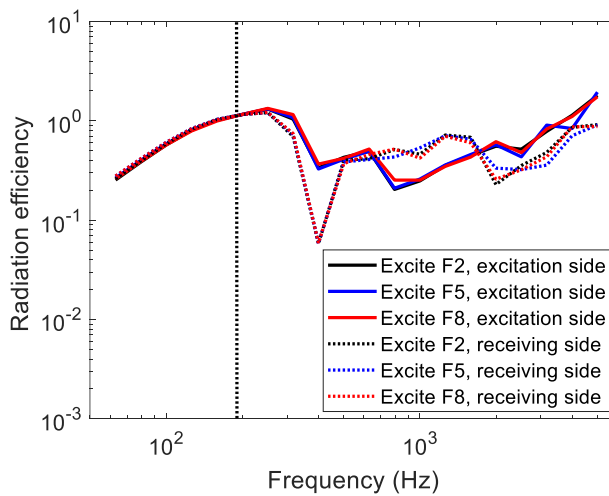
Figure 6.23. The radiation efficiency of the extruded panel for three excitation positions (positions indicated in Figure 6.16).

6.3.3 Excitation on strips

When a mechanical excitation is applied to a strip, the vibro-acoustic behaviour of the extrusion is different in comparison with the previous cases when a force is applied to a stiffener. The averaged mean square velocity on the excitation and the receiving side as shown in Figure 6.24. The local modes cut on at 386 Hz which is also indicated in the figure. Above this frequency, the mean square velocity on the excitation is higher than that on the receiving side.
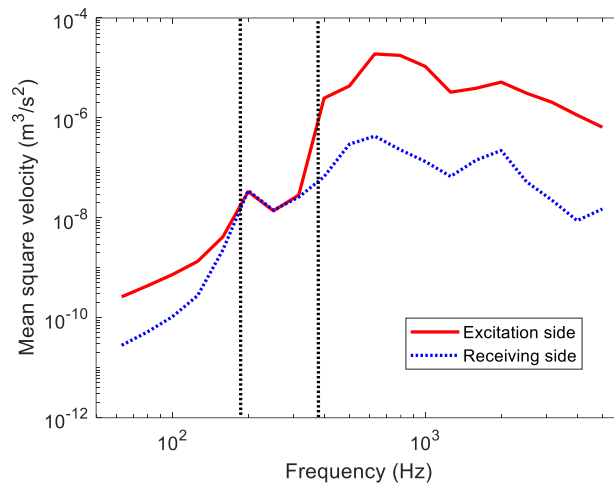
Figure 6.24. The mean square velocity of the extruded panel on its two sides for unit excitation at F_3 (on a strip, position indicated in Figure 6.16).

The mean square velocities on the two sides are only close around the first cut on frequency of the global modes (186 Hz). This is likely due to the dominance of the global response on both sides: see the real part of the deformation at 186 Hz in Figure 6.25.
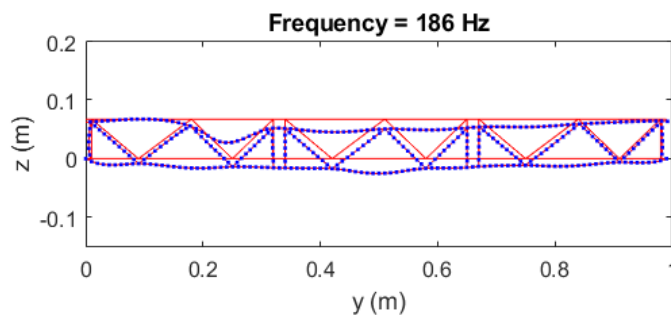
Figure 6.25. Normalised spatial response at 186 Hz for unit excitation at position F_3. (position indicated in Figure 6.16, scale factor 1×10^5).

Below the cut on frequency of the global modes, the mean square velocity of the extruded panel on the receiving side is dominated by global vibration. The mean square velocity on the excitation side is the sum of the global response and the forced local vibration of the strip where the force is applied. The forced response of the strip is more significant than the global response. That is why the mean square velocity on the excitation side is higher than that on the receiving side below the cut on frequency of global modes. One example at 100 Hz is shown in Figure 6.26.
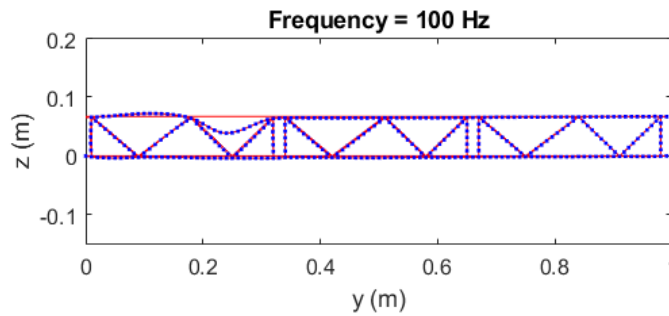
Figure 6.26. Normalised spatial response at 100 Hz for unit excitation at position F_3 (position indicated in Figure 6.16, scale factor 1×10^5).

Above the cut on frequency of local modes (386 Hz for the top plate strip which is excited), the mean square velocity on the excitation side becomes much higher again. This is likely due to the localisation of the vibration in the excited strip. One example at 800 Hz is shown in Figure 6.27.
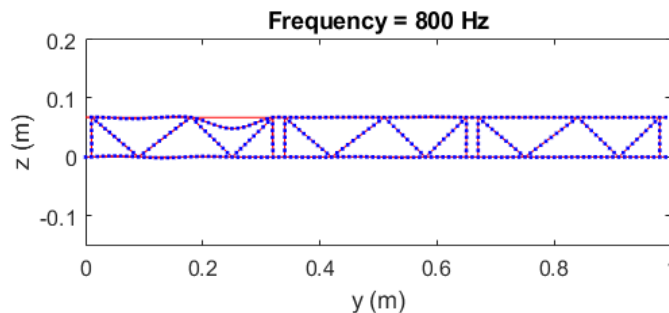
Figure 6.27. Normalised spatial response at 800 Hz for unit excitation at position F_3 (position indicated in Figure 6.16, scale factor 1×10^4).

The radiated power from the excitation side is only a little higher than that on the receiving side below the cut on frequency of the global modes as shown in Figure 6.28. This is due to the fact that the radiation efficiency of the local motion of the strips is quite small at low

frequency, even though its vibration level is high. At high frequency local modes are dominant, and the radiated power on the excitation side is higher than that on the receiving side.
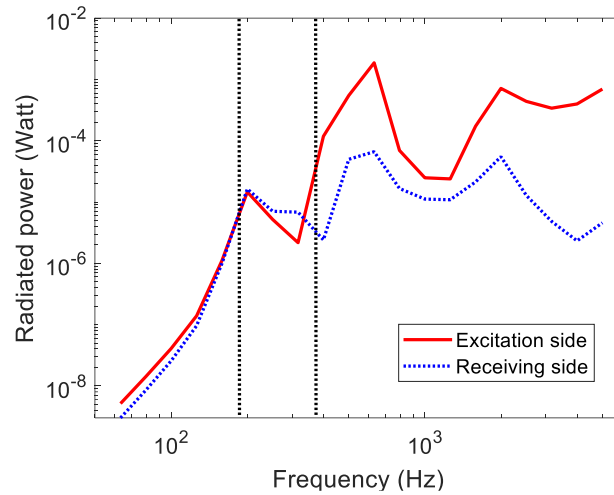
Figure 6.28. The radiated power of the extruded panel on its two sides with unit excitation at F_3 (on a strip, position indicated in Figure 6.16).

The radiation efficiency for excitation on a strip is shown in Figure 6.29. When the force is applied to a strip, the radiation efficiency of the extruded panel on the receiving side does not change much in comparison with the case when the force is applied to a stiffener. However, the radiation efficiency on the excitation side decreases. From Figure 6.24, below the cut on frequency of the global modes, the vibration levels on the excitation side are dominated by the strip to which the force is applied, which is higher than that on the receiving side. The radiated power spectra from the two sides of the extruded panel are similar. As a result, the overall radiation efficiency on the excitation side is lower than that on the receiving side. Between 200 Hz and 630 Hz, the radiation efficiencies of the two sides are similar. At around 1 kHz, the vibration level on the excitation side is high but the radiated power on that side is not much higher than on the receiving side, which causes a dip in the radiation efficiency curve on the excitation side.
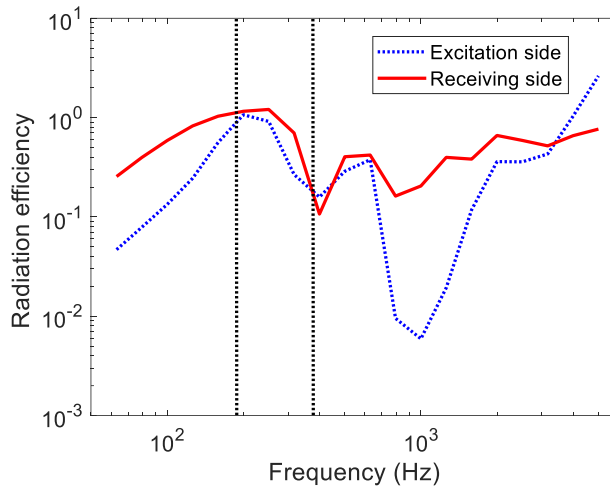
Figure 6.29. The radiation efficiency of the extruded panel on its two sides with excitation at F_3 (on a strip, position indicated in Figure 6.16).

Figure 6.30 and Figure 6.31 present the mean square velocities of the extruded panel on the two sides when the force is applied to different strips. When the force is applied to positions F_1, F_6 and F_7, (all three positions are on the wider strips with width 0.17 m), the mean square velocities are similar to each other and when the force is applied to positions F_3 and F_4 (these positions are on the narrower strip, with width 0.14 m), their results are again similar to each other. The first peak of the mean square velocity at 200 Hz is caused by the first global mode, while the others are caused by the local resonances of different strips.
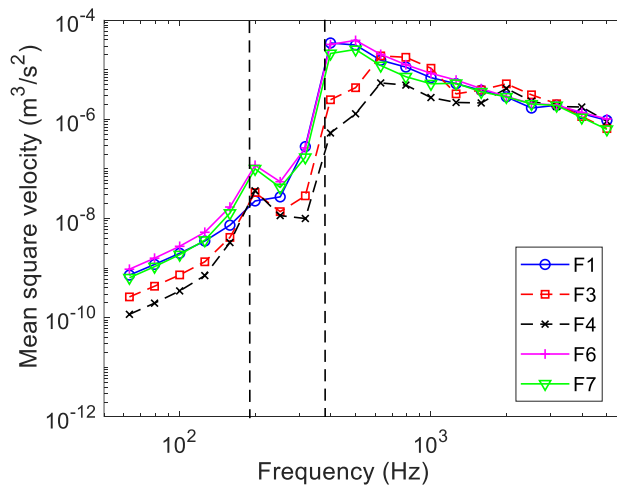
Figure 6.30. Mean square velocity on the excitation side for different force positions on a strip (positions indicated in Figure 6.16).
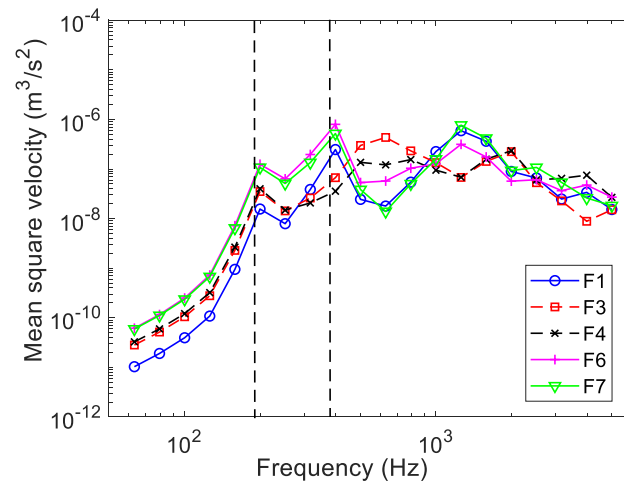
Figure 6.31. Mean square velocity on the receiving side for different force positions on a strip (positions indicated in Figure 6.16).

The power radiated from the extrusion for different force positions on the strips is shown in Figure 6.32 and Figure 6.33. As for the mean square velocity, the radiated power is similar when the force is applied to positions F_1, F_6, and F_7, and the power is also similar when the force is applied to positions F_3 and F_4.
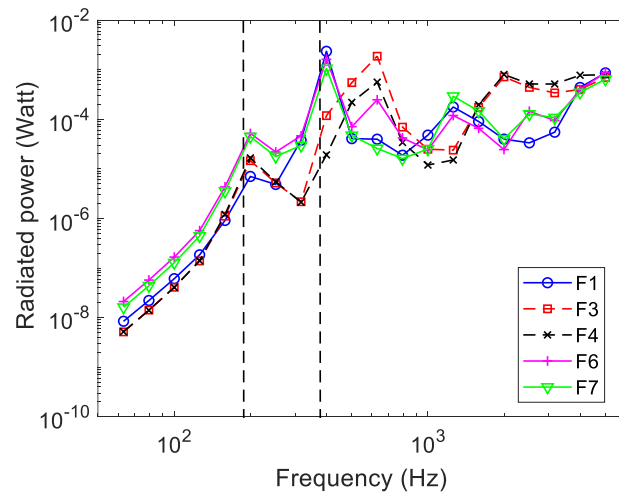
Figure 6.32. Radiated power on the excitation side for different force positions on a strip (positions indicated in Figure 6.16).
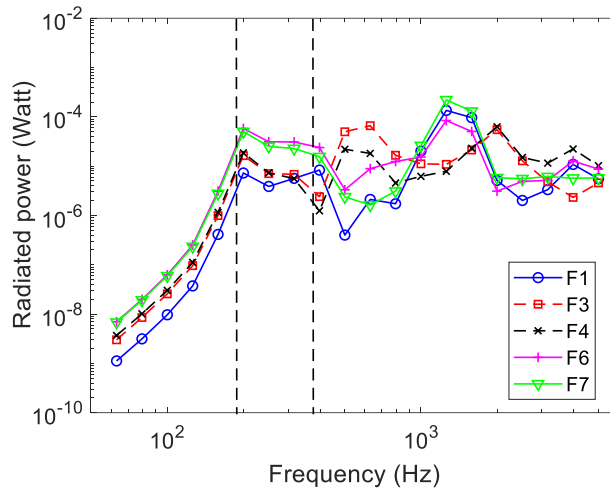
Figure 6.33. Radiated power on the receiving side for different force positions on a strip (positions indicated in Figure 6.16).

The resulting radiation efficiencies of the extrusion on the two sides are shown in Figure 6.34 and Figure 6.35. The results when the force is applied to positions F_1, F_6 and F_7 are similar, and when it is applied to F_3 and F_4 they are similar. Compared with Figure 6.35, it is shown that radiation efficiency is lower on the source side over a wide frequency range as there is more local vibration.
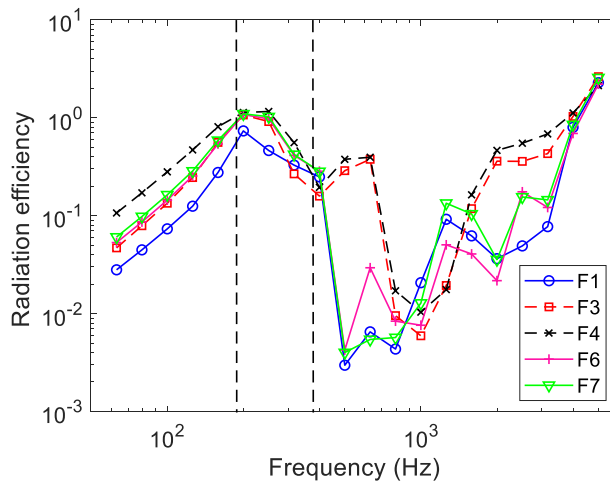
Figure 6.34. Radiation efficiency on the excitation side for different force positions on a strip (positions indicated in Figure 6.16).
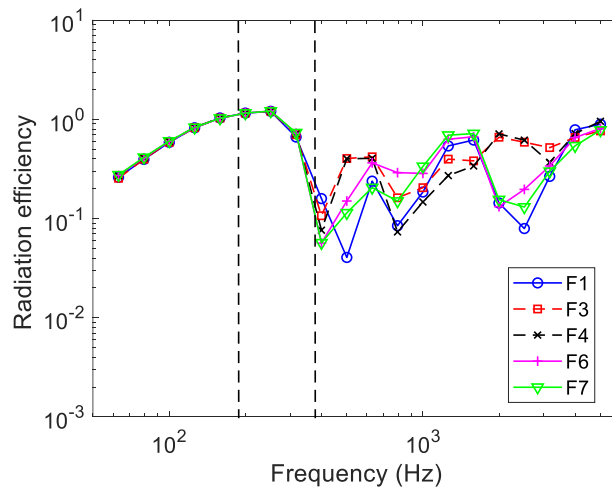
Figure 6.35. Radiation efficiency on the receiving side for different force positions on a strip (positions indicated in Figure 6.16).

The predicted radiation efficiency is compared with the measured data from reference [64, 105] in Figure 6.36. The radiation efficiency predicted by the 2.5D method is reasonably close to the measured data. The measured data includes the contributions from both sides while the results predicted by using the 2.5D model are the radiation efficiency on the excitation side.
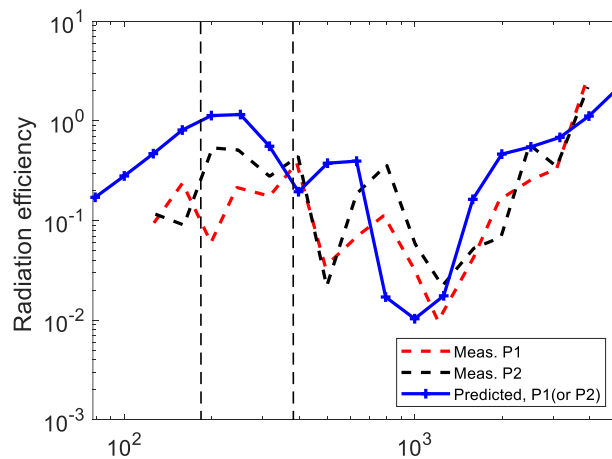
Figure 6.36. Radiation efficiency comparison between the 2.5D model and measured data [64, 105].

As noticed above, the radiation efficiency on the excitation side has a broad dip region between 500 Hz and 1250 Hz, which is also be found in the measured data in reference [64]. When the force is applied to positions F_1, F_6, and F_7, the first dip is around 500 Hz, and for positions F_3 and F_4, the first dip is around 800 Hz. The real part of the three-dimensional

149

spatial responses of the extrusion for excitation at positions F_1, F_4, and F_7 are shown in Figure 6.37~Figure 6.39 (1 m length in the *x* direction is shown). At these frequencies shown in the figures, local resonance occurs, which will cause high levels of vibration (see Figure 6.30) but also cause sound power cancellation (see Figure 6.32). Sound power cancellation at the local resonances of the strips below their critical frequency may cause these dips in the radiation ratio.
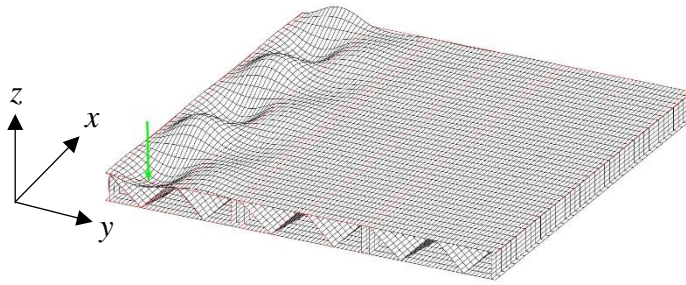
Figure 6.37. Spatial response at 516 Hz for unit excitation at position F1 (position indicated in Figure 6.16, scale factor 1×10^4).
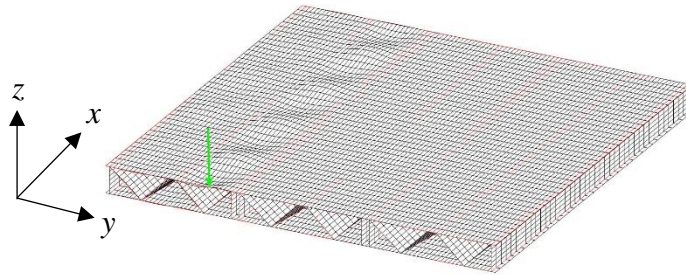
Figure 6.38. Spatial response at 996 Hz for unit excitation at position F_4 (position indicated in Figure 6.16, scale factor 1×10^4).
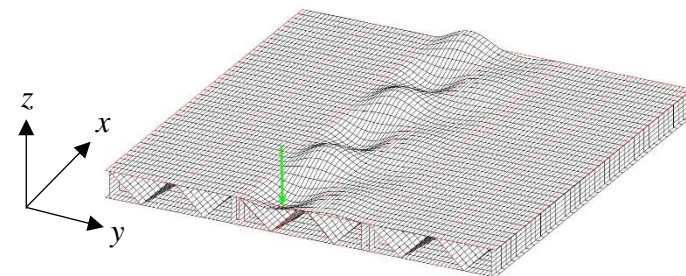
Figure 6.39. Spatial response at 548 Hz for unit excitation at position F_7 (position indicated in Figure 6.16, scale factor 1×10^4).

6.4   Sound transmission loss

When quantifying the air-borne transmission path, the sound transmission loss through the extrusion is of interest. Incident waves which excite the panel will be defined first. It is assumed that the sound is incident on one side of the panel with an angle α in the *y-z* plane and with an angle β about the *x* axis, as described in Figure 6.40. The acoustic pressure of the incident wave can be written as

$$p_i = Ae^{-ik_x x}e^{-ik_y y}e^{-ik_z z} \tag{6.24}$$

(a)   (b)
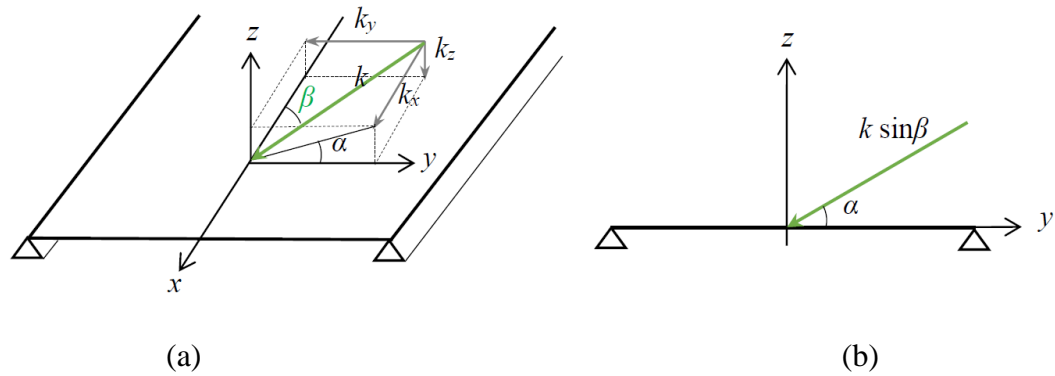
Figure 6.40. Coordinate system to define a wave incident on the plate (a) in 3D space and (b) in the y-z plane [64].

The directional acoustic wavenumbers k_x, k_y, k_z satisfy

$$k = (k_x^2 + k_y^2 + k_z^2)^{1/2} \tag{6.25}$$

These directional wavenumbers along *x, y, z* directions can be expressed in terms of the angles β and α as $k_x = k \cos \beta$, $k_y = k \sin \beta \cos \alpha$, $k_z = k \sin \beta \sin \alpha$. The incident power, W_i can be obtained in the wavenumber domain from [64]

$$W_i(\alpha, \beta) = \frac{1}{2} \int_\Gamma \frac{|\tilde{p}_i(k_x)|^2 \sin \alpha \cos \beta}{\rho_0 c_0} d\Gamma \tag{6.26}$$

where p_i is the incident sound pressure amplitude. For the extruded panel, the transmitted power W_t on the other side can be calculated by [64]

$$W_t(\alpha,\beta) = \frac{1}{2}\mathrm{Re}\left(\int_\Gamma \tilde{p}_t(\alpha,\beta)\tilde{v}_t^*(\alpha,\beta)\,\mathrm{d}\Gamma\right) \tag{6.27}$$

where $\tilde{p}_t$ and $\tilde{v}_t$ are the wavenumber domain pressure and normal velocity amplitude at the nodes of the panel. * indicates the complex conjugate. The transmission coefficient, τ is defined by the ratio between the incident and transmitted power as

$$\tau(\alpha,\beta) = \frac{W_i(\alpha,\beta)}{W_t(\alpha,\beta)} \tag{6.28}$$

For diffuse incidence, the transmission coefficient can be calculated by using

$$\tau_d = \frac{\int_0^{\pi/2}\int_0^{\pi/2}(\tau(\alpha,\beta)\sin^2\beta\sin\alpha)\,\mathrm{d}\alpha\mathrm{d}\beta}{\int_0^{\pi/2}\int_0^{\pi/2}(\sin^2\beta\sin\alpha)\,\mathrm{d}\alpha\mathrm{d}\beta} \tag{6.29}$$

Finally, the sound transmission loss in a diffuse field is determined using

$$R = 10\log_{10}\left(\frac{1}{\tau_d}\right) \tag{6.30}$$

The simulation of sound transmission loss through this extruded panel was conducted using the WANDS software. The sound waves are incident on the top plate of the extruded panel (as defined in Figure 6.16). Measurements of sound transmission loss of the current extruded panel were previously conducted between two reverberant chambers at the ISVR, University of Southampton [64, 105]. The panel was mounted between the two reverberation rooms, as illustrated in Figure 6.41. The boundary condition of the extruded panel in the experiments is somewhere between clamped and simply supported. So, in the simulation of sound transmission loss, clamped (C-C) and simply supported boundary (S-S) conditions are applied to the extruded panel individually. To represent a diffuse incident field, the angle spacing is set $10°$ for α and β after performing a convergence test (different angle spacings were used and it was found smaller than $10°$ did not make obvious difference in results). The results are calculated for 500 frequencies with log spacing from 10 Hz to 10000 Hz and then converted to one-third octave bands.

Figure 6.42 shows the sound transmission loss of the extrusion for diffuse sound incidence compared with the experimental data from Reference [64, 105]. The sound transmission loss

152

from the 2.5D FE/BE model has a dip at low frequency and this dip occurs at different frequencies for different boundary conditions. This is due to the fundamental panel resonance [51]. For a simply supported extruded panel (S-S), the first resonance frequency is around 186 Hz, see Figure 6.3. For a clamped extruded panel (C-C), its first resonance frequency is about 276 Hz, see the dispersion relation in Figure 6.4. According to the 2.5D FE/BE calculation, for the simply supported case, below the 200 Hz band (first natural frequency is 186 Hz) it is stiffness controlled. For the clamped case, below the 315 Hz band (first natural frequency 276 Hz) it is stiffness controlled. Some errors appear at low frequency. Kim et al. [65] applied a window function to allow finite length of the extruded panel, which improved the accuracy at low frequency. In this calculation the window is not involved. Above the first resonance frequency of the extruded panel, the predicted sound transmission loss agrees with the measured one.
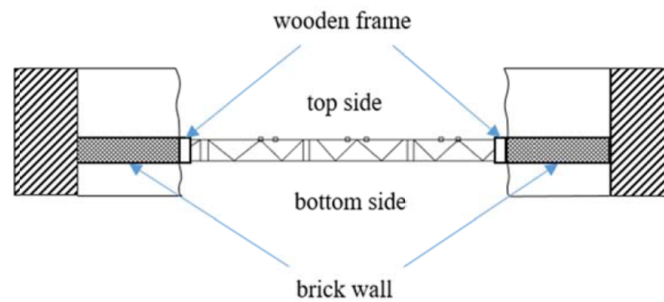
Figure 6.41. The cross-section of the extruded panel mounted between two reverberant rooms [64, 105].
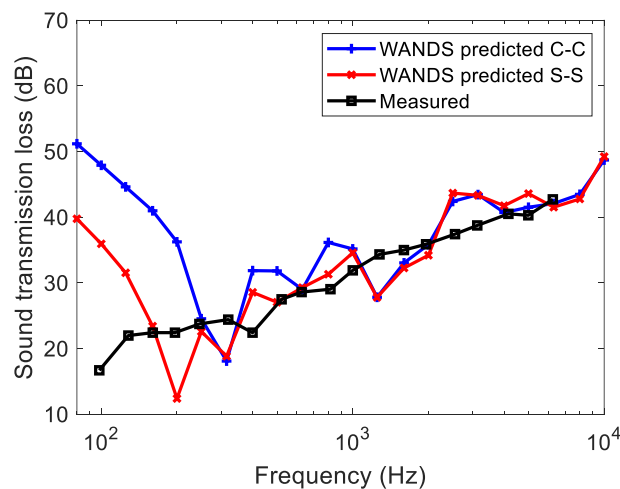
Figure 6.42. Sound transmission loss through the extruded panel for diffuse incidence compared with measurement from [64, 105].

6.5   Summary

A 2.5D FE/BE model was created, which only contains the cross-section of the extrusion, to study the vibro-acoustic performance of the extrusion, including the radiation efficiency and the sound transmission loss.

First, the wave modes of the extrusion were studied. The 2.5D finite element analysis of the extrusion shows that it has both global and local vibration. At low frequency, global vibration is dominant while at high frequency, the local modes dominate the vibration levels. The waves in the strips are clustered into groups. The number of waves in each group is equal to the number of identical bays in the extruded panel. In each group, the strips roughly vibrate in phase or out of phase. Acoustic pressure was used to excite the extrusion; the STL of the extrusion obtained by using the 2.5D FE/BE model is found to be close to the measured data. Besides, a mechanical force was applied to either the stiffeners or the strips of the extrusion to investigate the radiation efficiency. The simulation results show that, below the cut on frequency of the local modes, the global radiation is dominant, while above the cut on frequency of the local modes, local modes will dominate the vibration levels and radiation efficiency. The location of the force will affect the results. When the force is applied to the strips, on the excitation side, the radiation efficiency has a large dip in the 500 Hz to 1250 Hz frequency range. This is caused by the cancellation of the sound power radiated by the strips below their critical frequency. When the force is applied at the stiffeners, the radiation efficiency on the excitation side is relatively flat. The radiation efficiency on the receiving side does not have significant differences for the two different types of excitation position.

Chapter 7   SEA approach for noise transmission through extruded panels

The 2.5D FE/BE method introduced in Chapter 6 can give relatively accurate predictions in terms of sound transmission loss and sound radiation efficiency of the extruded panel; therefore, it has a wide range of application. In railway engineering, noise transmission through train walls has both air-borne and structure borne components. Different types of excitation for air-borne and structure borne noise transmission should be determined. For example, rolling noise can propagate or diffract to the train external surfaces, which will cause air-borne noise transmission, as discussed in Chapters 3 and 4. Meanwhile, structural vibration caused by wheel/rail interaction propagates through the bogie/suspension and can excite the train body to vibrate, causing structure-borne transmission. The air-borne and structure borne transmission has been studied by using the 2.5D FE/BE method in Chapter 6. Compared with the commonly used SEA method, the 2.5D FE/BE method is more computationally expensive and it requires bespoke software, which may limit the application of this method to predict noise transmission through train wall structures.

To propose a more efficient way to calculate the noise transmission through train wall structures, the SEA method is employed. Xie et al. [54] created an SEA model to investigate the vibro-acoustic behaviour of an extruded panel. This SEA model can approximately explain the complex mechanism of sound transmission through the extruded panel. In this work, Xie et al.'s SEA model will be employed and some modifications will be applied to this model. The 2.5D FE/BE calculations in Chapter 6 will be used to calibrate the input power, modal density, etc., for the SEA model.

7.1   The SEA model for noise transmission through extruded panels

The principle of the SEA method has been presented in Chapter 3, see also reference [82]. The SEA model created by Xie et al. [54] is shown in Figure 7.1. In this model there are six subsystems. Four subsystems were used to model the extruded panel: three subsystems are for local behaviour (the top plate, the bottom plate and the middle stiffeners), and one for the global modes, see Figure 7.2. Another two subsystems were used to model the two cavities on either side.
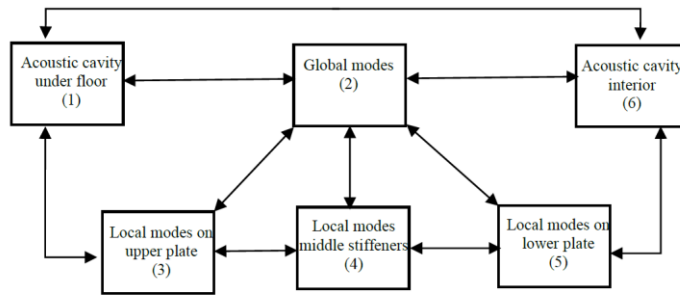
Figure 7.1. Xie et al.'s SEA model [54].
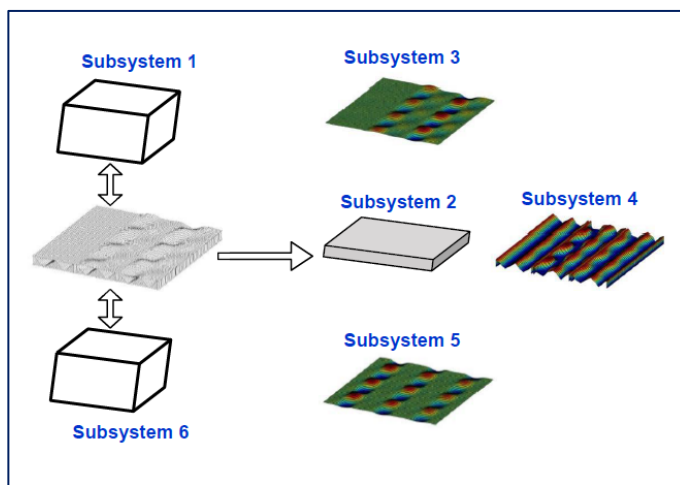
Figure 7.2. The subsystems used to model the extrusion, redrawn from [54].

Assuming that there is no direct coupling between the local modes on the two sides of the extruded panel, there are five different types of coupling in this SEA model; they are

1. Non-resonant sound transmission [82] between the two cavities through the extruded panel; in Figure 7.1, it is the direct coupling from cavity (1) to cavity (6).

2. Coupling between cavities and global modes: the coupling between cavity (1) and global modes (2), and between cavity (6) and global modes (2).

3. Coupling between cavities and local modes: the coupling between cavity (1) and local modes (3), and between cavity (6) and local modes (5).

4. Coupling between global modes and local modes within the panel; coupling between (2) and (3), (2) and (4), (2) and (5).

5. Coupling between local modes within the panel; (3) and (4), (4) and (5).

The non-resonant sound transmission between two cavities through panels depends mainly on the mass per unit area. According to [82], the pressure fluctuations in the source room

will cause the panel to vibrate and the vibrating panel will generate sound in the receiving room. However, the panel can vibrate in two ways. Above the critical frequency, free bending waves are excited which interact to cause resonances; the amplitude of these waves depend on the damping of the panel. Below the critical frequency, the pressure fluctuations force the panel to move in such a way that these free travelling bending waves are not generated. In this case, the mass of the panel is the most important property that determines the transmission. For simulation of transmission, both the resonant and non- resonant transmission are included. The resonant transmission is included in the SEA model by the coupling through the panel subsystems. The non-resonant transmission is modelled by the 'mass law' through the coupling between subsystems 1 and 6 because SEA is based on coupled modes so if a structure vibrates in a non-resonant way it cannot be represented by an SEA subsystem.

This SEA model is employed to investigate the sound transmission through an extruded panel from a train floor. The cross-section of the extruded panel is the same as the one considered in Chapter 6 in Figure 6.1. Figure 7.3 shows the strips involved in this panel that is used here. The widths of these strips are listed in Table 7.1 and their lengths are 20 m. The bottom plate is covered by a layer of stiff rubber. The material properties of the panel are the same as those in Chapter 6 and more details are listed in Table 6.1.
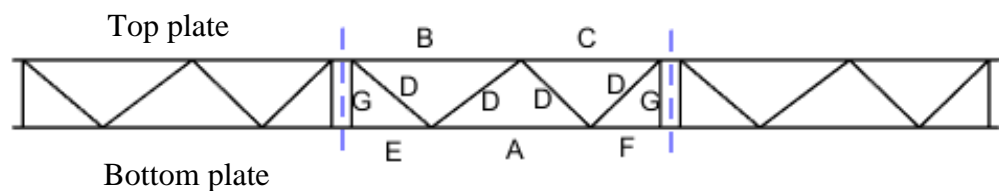
Figure 7.3. Schematic representation of the panel with names given to each strip.

Table 7.1. Geometrical details of the extruded panel.

	Strip A	Strip B	Strip C	Strip D	Strip E	Strip F	Strip G
Width (m)	0.16	0.17	0.14	0.10~0.11	0.08	0.07	0.067
Location	bottom plate (with rubber)	top plate	top plate	middle	bottom plate (with rubber)	bottom plate (with rubber)	middle

To apply the SEA model shown in Figure 7.1 to study the noise transmission through the train floor, the coupling loss factors are required. Apart from the coupling loss factors, the calculations of radiation efficiency and modal density are based on the bending stiffness of

the extruded panel (global modes) and the strips (local modes), so these bending stiffnesses should be determined first.

7.2   Determining equivalent bending stiffness

7.2.1   Calculation of bending stiffness

The extruded panel studied here is geometrically different along x and y axes, see Figure 7.4. The geometry of the panel results in a different bending stiffness along the two axes. In order to predict its modal density, radiation efficiency etc., the bending stiffness of the extruded panel along the x and y axes should be determined beforehand.

(a)   (b)
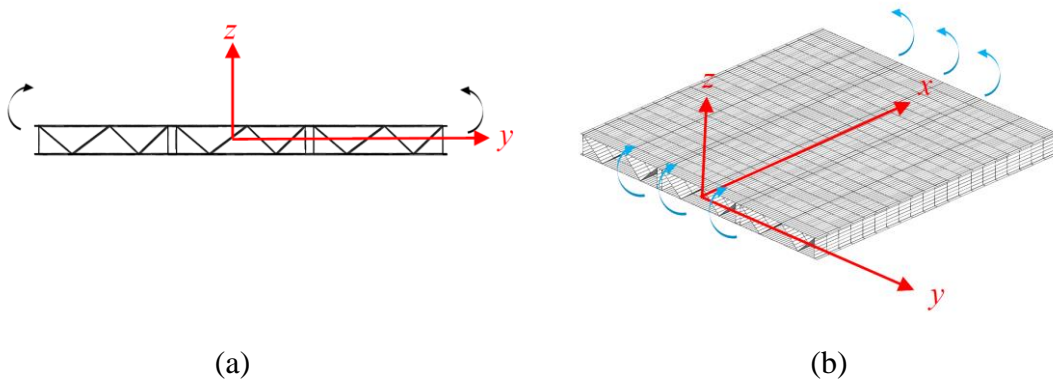
Figure 7.4. The extruded panel bends in different planes. (a) Bending along x axis, (b) bending along y axis.

The bending stiffness of the extruded panel along the x and y axes can be determined by

$$B_i = \frac{EI_i}{1 - v^2} \tag{7.1}$$

where E is the Young's modulus, I is the second moment of area per unit length (or width), v is the Poisson's ratio and i is the index for x and y. Based on the vibration level analysis in Section 6.3, the bending stiffness at different positions in the y direction might be different due to the inclined geometry of the stiffeners. When the stiffeners are close to the top or bottom plate, the bending stiffness is at its maximum and when the stiffeners are located in the middle, the bending stiffness is at its minimum. The representative value of the second moment of area was calculated by approximately setting the stiffeners at one quarter of the distance below the top plate, see Figure 7.5.
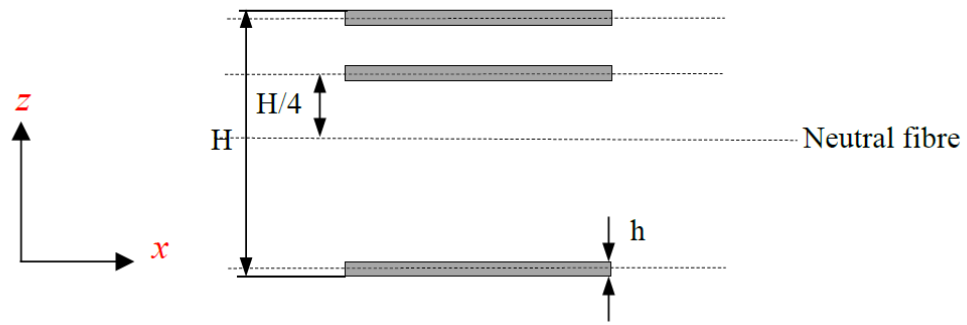
Figure 7.5. Cross-section of part of the extrusion along the *x* axis.

The second moment of the area about the *x* axis per unit length can be calculated as

$$I_x = 2\left[\frac{h^3}{12} + \left(\frac{H}{2} - \frac{h}{2}\right)^2 h\right] + \left[\frac{h^3}{12} + \left(\frac{H}{4}\right)^2 h\right] \tag{7.2}$$

where H, h are the thickness of the extruded panel, and thickness of the strips respectively. The second moment of area in the *y* direction can be considered as made of simpler components, such as those shown in Figure 7.6(right). Each component can be considered as an equivalent counterpart of a II section [107], shown in Figure 7.6(left).
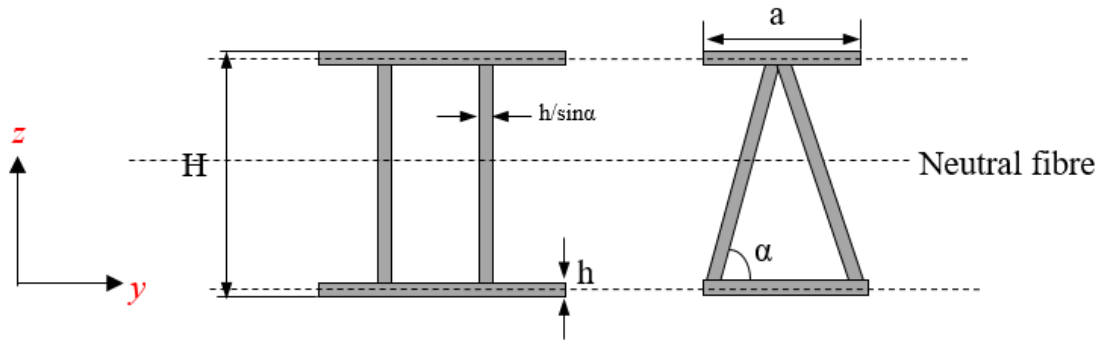
Figure 7.6. left: the cross-section of the equivalent II section; right: cross-section of the parts of the extrusion along the *y* axis.

The second moment of area for each component about the *y* axis can be calculated as [107]

$$I_{y,i} = 2\left[\frac{ah^3}{12} + ah\left(\frac{H}{2} - \frac{h}{2}\right)^2 + \frac{h(H - 2h)^3}{12\sin(\alpha)}\right] \tag{7.3}$$

where a is the spacing between each pair of stiffeners and α is the angle between the stiffener and the bottom plate. The extruded panel consists of nine equivalent components of the form shown in Figure 7.6. The second moment of area of the extruded panel about the y axis is the sum of the contribution from these components. The values for the extruded panel are given below in Table 7.2.

Table 7.2. Second mement of area and bending stiffness of the extruded panel.

Description	Second moment of area about the x axis (per unit length)	Second moment of area about the y axis (per unit width)	Bending stiffness along the x axis	Bending stiffness along the y axis
Symbol	I_x	I_y	B_x	B_y
Value	6.03×10^{-6} m³	6.37×10^{-6} m³	4.64×10^5 Nm	4.90×10^5 Nm

The bending stiffness of the strips is calculated by

$$B_l = \frac{Eh^3}{12(1 - v^2)} \tag{7.4}$$

The result is 105.05 Nm based on the parameters of the strip in Table 6.1.

7.2.2   Validation of bending stiffness

The bending stiffness of the extruded panel along the x axis could be validated by using the cut on frequency of the global modes. The cut on frequency of global modes obtained from the dispersion curve in Figure 6.3 is 186 Hz for simply supported boundaries. For comparison, the cut on frequency of the extruded panel can be calculated analytically by using a simply supported beam model as

$$f_1 = \frac{\pi}{2}\left[\left(\frac{1}{b}\right)^2\right]\sqrt{\frac{B_x}{\rho h}} \tag{7.5}$$

here $b = 1$ m is the width of the extruded panel. ρh is the mass per unit area of the extruded panel, calculated by using the total mass divided by the area of the extrusion. B_x is the bending stiffness along the x axis. The analytically calculated cut on frequency of the

extruded panel is 195 Hz, which is close to the value obtained from the FE calculation (with error 4.8%). The analytically calculated bending stiffness along the x axis is therefore acceptable.

The bending stiffness along the y axis can be validated by using the lower asymptotic line in Figure 6.3, which represents the global wavenumbers in the extruded panel. The natural frequencies of the extruded panel global modes can be calculated by using an anisotropic plate model [108], expressed as

$$\omega_{mn} = \frac{\pi^2}{a^2\sqrt{\rho h}}\sqrt{B_x m^4 + 2B_{xy}m^2 n^2 \left(\frac{a}{b}\right)^2 + B_y n^4 \left(\frac{a}{b}\right)^4} \tag{7.6}$$

where a is the length of the extruded panel, assuming it is 20 m to represent a train floor length and b is the width of the panel, 1 m. B_x and B_y are the bending stiffness along the x axis and y axis respectively. B_{xy} is the cross bending stiffness, calculated as [108]

$$B_{xy} = B_x v + 2B_k \tag{7.7}$$

$$B_k = \frac{Gh^3}{12} \tag{7.8}$$

$$G = \frac{E}{2(1+v)} \tag{7.9}$$

Orrenius et al. [5] concluded that the extruded panel could be approximately modelled by an equivalent plate. Then the natural frequencies of the train floor (the global modes) can be calculated by

$$f_{m,n} = \frac{\pi}{2}\left[\left(\frac{m}{a}\right)^2 + \left(\frac{n}{b}\right)^2\right]\sqrt{\frac{B}{\rho h}}, m, n = 1,2,3 \tag{7.10}$$

where B is the equivalent bending stiffness of the extruded panel, calculated by

$$B = \sqrt{B_x B_y} \tag{7.11}$$

The anisotropic plate model and the equivalent plate model with a bending stiffness $B = 4.77 \times 10^5$ Nm were used to predict the natural frequencies of the global modes by using Equations (7.6) and (7.10) respectively. The results are compared with those from the 2.5D model in Figure 7.7. Both of these models can predict the global natural frequencies quite well though the anisotropic one is slightly better, which means the analytically derived bending stiffness of the extruded panel along the y axis is also acceptable.
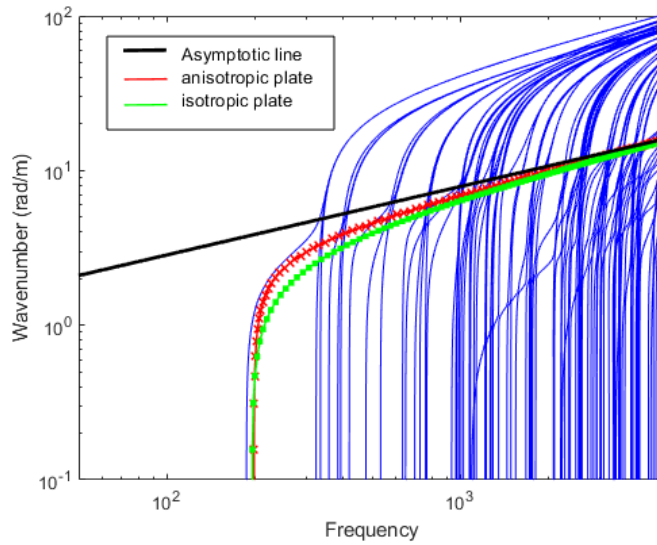
Figure 7.7. The natural frequencies of the extrusion, blue lines: from 2.5D model, red line: by using the equivalent anisotropic plate model, green line: by using the equivalent isotropic plate model.

For the current extruded panel, B_x and B_y have similar values. Using an equivalent isotropic plate to predict the natural frequencies of a 20 m long extruded train floor is less accurate than using the anisotropic plate model proposed by Leissa [108], but it is still acceptable. As using an isotropic plate to model the global modes will be more convenient to calculate the modal densities and radiation efficiency, the equivalent isotropic plate model will be used later in this work to calculate the modal density.

7.3   Determining the equivalent width of strips

To calculate the modal density of the local mode subsystems, the boundary conditions of the individual strips are important but they are not well defined. In this section the results for

various boundary conditions will be explored and compared with the results from the 2.5D model.

7.3.1   Cut on frequencies of the strips

The natural frequencies, especially the first few natural frequencies of the strips, are important to determine their radiation efficiency and modal density, etc. Because of the uncertainty of the boundary conditions, the natural frequencies of the strips are difficult to determine. From the analysis of dispersion relation in Chapter 6, each combination of (ω, k_x) corresponds to a wave mode for an infinite strip. By definition the wave mode of an infinite strip at $k_x = 0$ corresponds to its cut on frequency.

From Section 6.1.3, the strips can be assembled in groups in the 'plate' region. Each group has three curves. By plotting their wave modal shapes, it has been found that the dispersion curves marked with A, B, C, D in Figure 7.8 are corresponding to the wave modes of strip A, B, C, D indicated in Figure 7.3 respectively. Example waves (plotted at wavenumber $k_x = 1$ rad/m) in the four types of strips are shown in Figure 7.9(a~d).
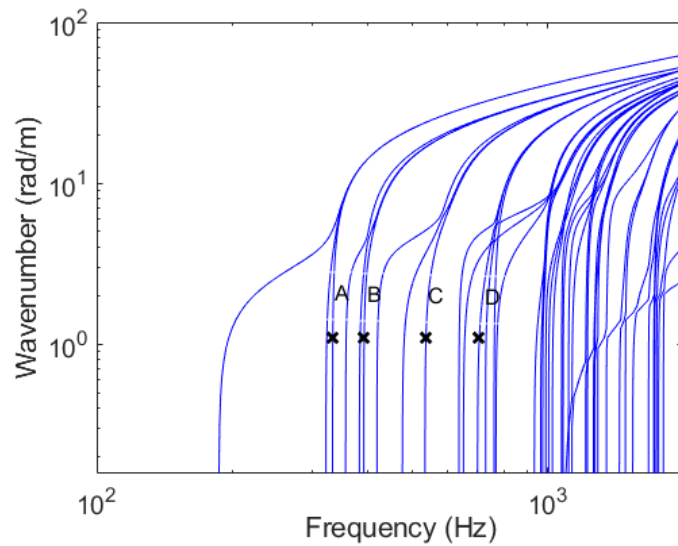
Figure 7.8. Dispersion curves of the extruded panel, lines marked with numbers A, B, C, D represent local wavenumbers in the strips.
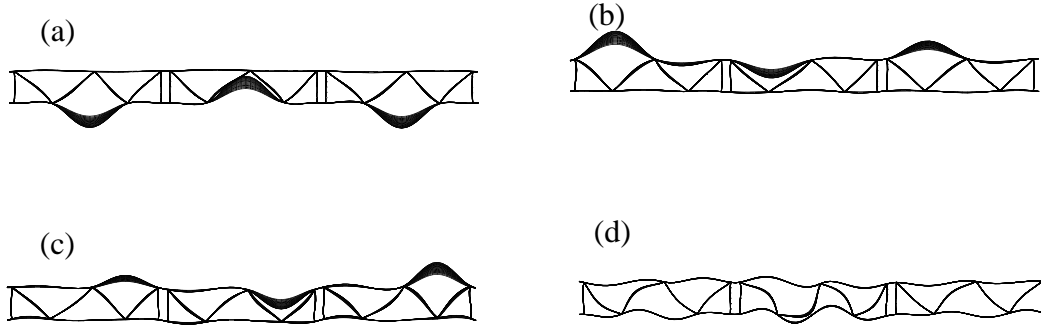
Figure 7.9. Waves in strips plotted at wavenumber $k_x = 1$ rad/m, indicated by 'X' in Figure 7.8. (a) Curve marked with A, (b) curve marked with B, (c) curve marked with C, (d) curve marked with D.

The cut on frequencies of the strips (by definition $k_x = 0$ rad/m) can be read from the four dispersion curves marked with A, B, C, D in Figure 7.8. They are 332 Hz for strip group A (identified in Figure 7.3); 386 Hz for strip group B; and 534 Hz for strip group C. The width of strip group D (the diagonal internal stiffeners) varies from 0.10 m to 0.11 m, the cut on frequencies of this group strips occur between 700~800 Hz. From dispersion curve strip D in Figure 7.8, the cut on frequency is read as 768 Hz.

To predict these cut on frequencies analytically, the boundary conditions of the strips are important. However, the actual boundary conditions of the strips when they are assembled in the extruded panel are not well defined: they are somewhere between simply supported and clamped. So, different combinations of boundary conditions have been tested to predict these cut on frequencies. For instance, (1) the strips are assumed to be simply suported on their two longer opposite edges and the two shorter sides are free (SFSF), (2) they are clamped on their two longer edges, setting the shorter edges simply supported (CSCS), and (3) clamped and simply supported on their two longer edges (CSSS). The natural frequencies under different boundary conditions can be estimated by [108]

$$\omega^2 = \frac{\pi^4 B}{a^4 \mu} \left\{ G_x^4 + G_y^4 \left(\frac{a}{b}\right)^4 + 2 \left(\frac{a}{b}\right)^2 [\nu H_x H_y + (1-\nu) J_x J_y] \right\} \qquad (7.12)$$

where a is the length of the strips, 20 m. b is the width of each strip. B is the bending stiffness and μ is the mass per unit area. G_x, H_x, J_x are functions determined from Table 7.3 according to the boundary conditions at $x = 0$ and $x = a$. The quantities G_y, H_y, J_y are obtained from Table 7.3 by replacing x by y and m by n.

Table 7.3. Frequency coefficients in Equation (7.12) [108].

Boundary condition	m	G_x	H_x	J_x
SS^a, SS^b	2, 3, 4…	$m-1$	$(m-1)^2$	$(m-1)^2$
C^a, C^b	2	1.506	1.248	1.248
	3, 4, 5…	$m-\dfrac{1}{2}$	$(m-\tfrac{1}{2})^2\left[1-\dfrac{2}{(m-\frac{1}{2})\pi}\right]$	$(m-\tfrac{1}{2})^2\left[1-\dfrac{2}{(m-\frac{1}{2})\pi}\right]$
C^a, SS^b	2, 3, 4…	$m-\dfrac{3}{4}$	$(m-\tfrac{3}{4})^2\left[1-\dfrac{2}{(m-\frac{3}{4})\pi}\right]$	$(m-\tfrac{3}{4})^2\left[1-\dfrac{2}{(m-\frac{3}{4})\pi}\right]$

*a means the boundary conditions at $x = a$, for example, SS^a means at $x = a$, it is simply supported.

The analytically calculated cut on frequencies of these strips are shown in Table 7.4, compared with the actual cut on frequencies from the FE calculation read from Figure 7.8. The simply supported and clamped-simply supported boundary conditions underestimate the cut on frequencies for each strip while the clamped-clamped boundary condition is too stiff, causing the cut on frequencies to be overestimated. None of the boundary conditions considered can consistently give the correct cut on frequencies.

Table 7.4. Cut on frequency of the extrusion's local modes.

	Boundary condition	strip group A	strip group B	strip group C	strip group D
(1)	SFSF	175 Hz	212 Hz	313 Hz	508 Hz
(2)	CSCS	397 Hz	482 Hz	711 Hz	1152 Hz
(3)	CSSS	274 Hz	332 Hz	490 Hz	793 Hz
(4)	2.5D FE calculation	322 Hz	386 Hz	534 Hz	768 Hz

* (1) the strips are assumed to be simply suported on their two longer opposite edges and the two shorter sides are free (SFSF), (2) they are clamped on their two longer edges, setting the shorter edges simply supported (CSCS), and (3) clamped-simply supported on their two longer edges (CSSS). (4) FE calculations are read from the curves A, B, C, D in Figure 7.8.

7.3.2   Determining the equivalent width for the strips

As these boundary conditions cannot predict the cut on frequencies of the strips correctly, an alternative approach is introduced which is to adjust the width of each strip. By assuming they are simply supported, an equivalent width for each strip can be determined to make their cut on frequencies close to the values obtained from the FE calculation. This is achieved

by applying the modified width (equivalent width) in Equation (7.12) to make their cut on frequency coincide with the actual values from the FE calculation, see Figure 7.10.
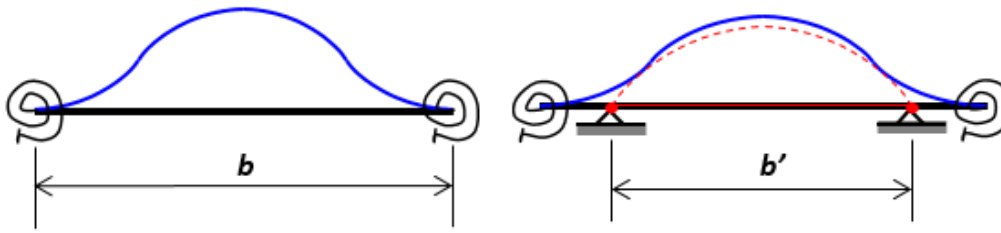
Figure 7.10. Equivalent width.

For example, strip A is of width $b = 0.16$ m, and their cut on frequency is 322 Hz, obtained from the FE calculation. Their width can be modified to a customized value $b' = 0.12$ m and using this value in Equation (7.12) (a is unchanged), the cut on frequency under simply supported boundary conditions is the same as the value obtained from the FE calculation. Similarly, the equivalent widths for group B, group C and group D are found to be 0.1275 m, 0.108 m, and 0.0904 m respectively, see Table 7.6. These equivalent widths are between 75% and 82% of the full width of the strips.

For the other shorter strips, such as strip E with width of 0.08 m, and strip F with width of 0.07 m, and also strip G with width of 0.0675 m, their cut on frequencies are relatively high and they vibrate together with other strips. It is difficult to recognise their cut on frequencies by plotting the mode shape. Their equivalent widths are therefore determined based on the averaged ratio (approximately 0.75) of the four groups of strips discussed above. The equivalent widths for them are listed in Table 7.5.

Table 7.5. The equivalent width of each strip.

Length	Group A	Group B	Group C	Group D	Group E	Group F	Group G
Original	0.16 m	0.17 m	0.14 m	0.11 m	0.08	0.07	0.0675 m
Equivalent	0.12 m	0.1275 m	0.108 m	0.0904 m	0.06 m	0.053 m	0.051 m
Ratio	0.75	0.75	0.77	0.82	0.75	0.75	0.75

To validate these equivalent widths, they are used to predict the natural frequencies of the strips under simply supported boundary conditions. The natural modes of the strips have sinusoidal shapes. At their natural frequencies, the length of the strips is equal to half the wavelength or a multiple of half the wavelength of the sinusoidal wave, which gives the

wavenumbers in the x direction, $k_x = m\pi/a$. The analytically predicted relationship between the natural frequencies and their corresponding wavenumbers is compared with the dispersion curves obtained from the 2.5D model in Figure 7.11. Using the equivalent width, the first few natural frequencies of the strips can be predicted quite well. The equivalent width is likely to slightly underestimate the modes with $n = 2$ in the width direction, but it is nearly impossible to identify the $n = 2$ modes from the dispersion curves in Figure 7.8 because there are so many waves occurring close together.
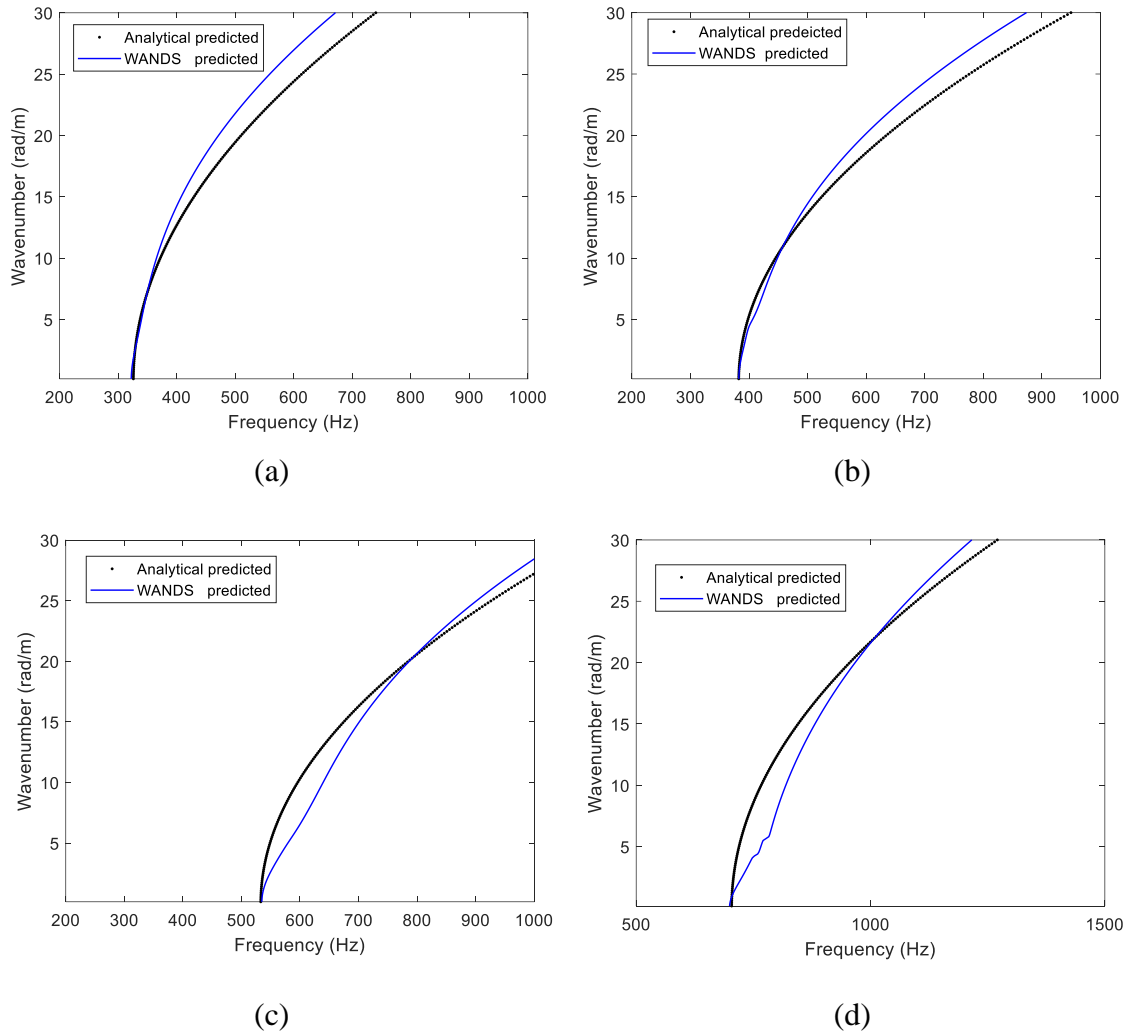
Figure 7.11. Natural frequencies of the strips, black circle dots represent the results calculated by using simply supported plate model with equivalent widths, blue lines denote the results extracted from the 2.5D FE model, (a) for strips Group A, (b) for strips Group B, (c) for strips Group C, (d) for strips Group D.

Although Equation (7.12) can give an accurate calculation of the equivalent widths, to simplify the procedure the same factor can be adopted for all the strips when using the equivalent width later in this chapter and this is chosen to be 0.75.

7.4   Determining modal density

Modal densities are important parameters in an SEA model. After the bending stiffness and equivalent widths of the strips are obtained, the modal density of the extruded panel can be calculated. Often in SEA modal densities are estimated based on asymptotic values. Here, however, it will be determined from the actual number of modes in each frequency band. Once the natural frequencies are obtained, the modal density can be calculated by

$$n(f) = \frac{\text{Number of modes}}{f_2 - f_1} \tag{7.13}$$

where f_1 and f_2 are the lower and upper limits of each frequency band. The number of modes for each strip in each one third octave band can be estimated by using an analytical plate model with simply supported boundary conditions. The width used for the strip is the equivalent width estimated in Section 7.3. The modal density of each subsystem is the sum of the contributions from its strips. The estimated modal densities of the extruded panel are shown in Figure 7.12.

The modal density of the extruded panel at around 400 Hz and 1000 Hz is relatively high. This is due to the cut on of local modes at these frequencies.
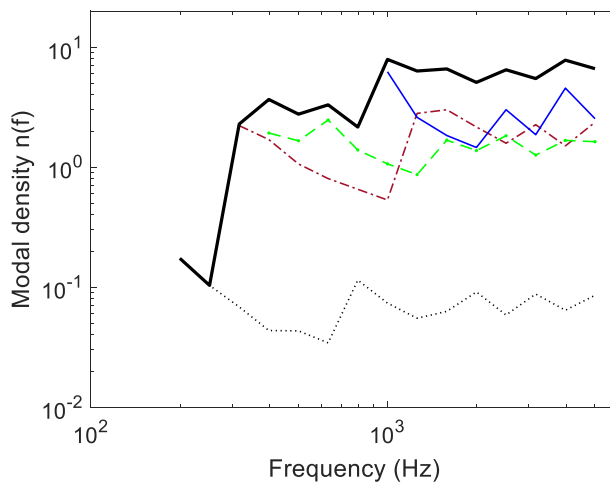
Figure 7.12. Modal density of the 20 m long extrusion obtained by using Equation (7.13). - - -: the modal densities of local subsystem 3; ——: the modal densities of local subsystem 4; -·-·-: the modal densities of local subsystem 5; ·······: the modal densities of global subsystem 2; ——: total modal density.

An analytical expression for the asymptotic modal densities of the global modes of an extruded panel was proposed by Xie et al. [54]

$$n_g(\omega) = \frac{S}{4\pi}\sqrt{\frac{M''}{B_g}} - \frac{1}{4}\left(\frac{M''}{B_g}\right)^{\frac{1}{4}}\left(\frac{a+b}{\pi}\right)\omega^{-\frac{1}{2}} \tag{7.14}$$

where S is the plate area, M'' is the equivalent mass per unit area, and B_g is the equivalent bending stiffness of the extruded panel. The first term corresponds to the plate area and the second term corresponds a correction due to the boundary length. For local modes, assuming a local subsystem contains $p+1$ strips (a rectangular plate divided by p intermediate constraints), the total modal density of the local subsystem is given by [54]

$$n_l(\omega) = \sum_{1}^{p+1} n_i \tag{7.15}$$

where n_i is the modal density of each strip. Once the modes of the strips have cut on, this has the following expression [54]

$$n_i = \frac{l_i a}{4\pi}\sqrt{\frac{m''}{B}} - \frac{l_i}{4\pi}\left(\frac{m''}{B}\right)^{\frac{1}{4}}\omega^{-\frac{1}{2}} - \frac{1}{2(p+1)}\left(p\delta + \frac{1}{2}\right)\frac{a}{\pi}\left(\frac{m''}{B}\right)^{\frac{1}{4}}\omega^{-\frac{1}{2}} \tag{7.16}$$

where l_i is the actual width of the strips, m'' is the mass per unit area of the strips, B is the bending stiffness of the strip. δ is the boundary effect of the intermediate constraints between strips. The first term of Equation (7.16) corresponds to the area of the strips. The others correspond to the boundary effects. The resulting modal densities of the extrusion are shown in Figure 7.13.
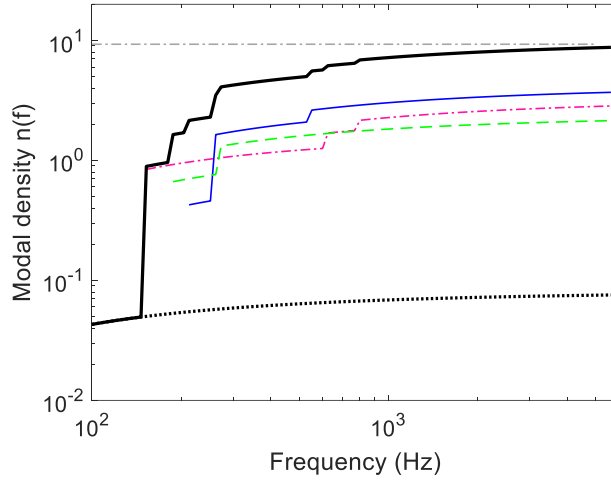
Figure 7.13. Modal density of the extrusion by using Xie et al.'s model. – – –: the modal densities of local subsystem 3; —: local subsystem 4; –·–·: local subsystem 5; ·········: global subsystem 2; ▬▬: total modal density; ----: simple plate.

The natural frequencies of the extrusion can also be obtained by using the FE calculation. In the dispersion curve of the extruded panel, the frequencies at $k_x = m\pi/a$ correspond to the natural frequencies of the extrusion assuming the simply supported boundary conditions at the ends, where a is the length of the extruded panel. This allows the modal density of the extruded panel to be calculated.

The dispersion relation analysis for an infinitely long extrusion can be used to deduce the vibration modes of a simply supported panel with a finite length. Because the modal shape of a simply supported panel provided by the eigenvalue analysis has a sinusoidal wave shape in the x direction (the x direction in the 2.5D model has an infinite length). When the length of the train floor equals half the wavelength or a multiple of half the wavelength of these waves, the corresponding frequency is one of the natural frequencies of the train floor. In the case of the length of the train floor, L is assumed to be 20 m long. Therefore, at the natural frequencies of a 20 m extruded panel, the wavenumbers in the x direction will be

$$k_x = \frac{n\pi}{L} \tag{7.17}$$

Each dot in Figure 7.14(a) represents a natural frequency of the 20 m long train floor. The corresponding modal density in one-third octave bands is shown in Figure 7.14(b).
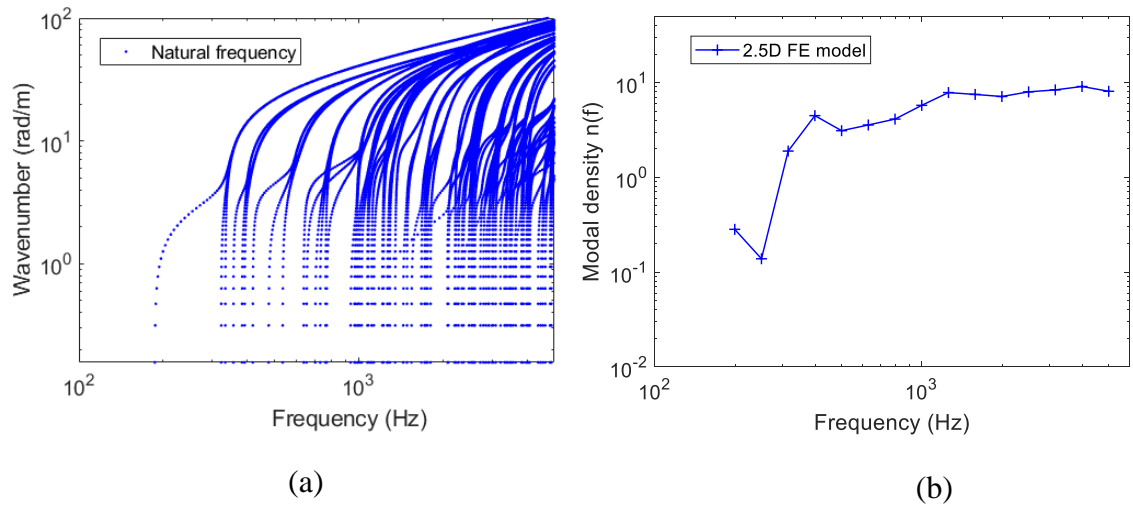
Figure 7.14. (a) Natural frequencies of a 20 m long train floor obtained by the dispersion curve and modal analysis, (b) modal density calculated from the 2.5D FE model.

The total modal density of this extruded panel calculated by using Xie et al.'s model and the one obtained by using Equation (7.13) are compared with the one obtained from the 2.5D FE calculation in Figure 7.15. The modal density obtained from the 2.5D FE calculation is considered as a reference. The relative error is calculated by the difference between the predictions and the 2.5D FE calculation divided by the 2.5D FE calculation. From Figure 7.15(a), Xie et al.'s model can predict the total modal density of the extruded panel quite well at high frequency. However, that model gave cut on frequencies 187 Hz, 225 Hz and 255 Hz, for local modes in subsystems 5, 3 and 4 respectively, which are lower than the actual values from the 2.5D FE calculation. Equation (7.13) with the equivalent width of the strips can predict the modal density well at low frequency attributing to that the equivalent width is chosen to fit their cut on frequency. From Figure 7.15(b), Xie et al.'s model gives better prediction above 800 Hz whereas below it the errors can be up to 10 times bigger than the actual values. Using the equivalent widths in Equation (7.13) for modal density prediction gives an average error of about 20% throughout the frequency range. It is better than Xie et al.' s model below 800 Hz. At high frequency using equivalent widths with Equation (7.13) underestimates the modal density. This is because the modified width of the strips cannot fit their higher order cut-on frequencies. Due to the big errors that Xie et al.'s model has at low frequency, Equation (7.13) with the equivalent width of the strips will be used to calculate the modal densities.
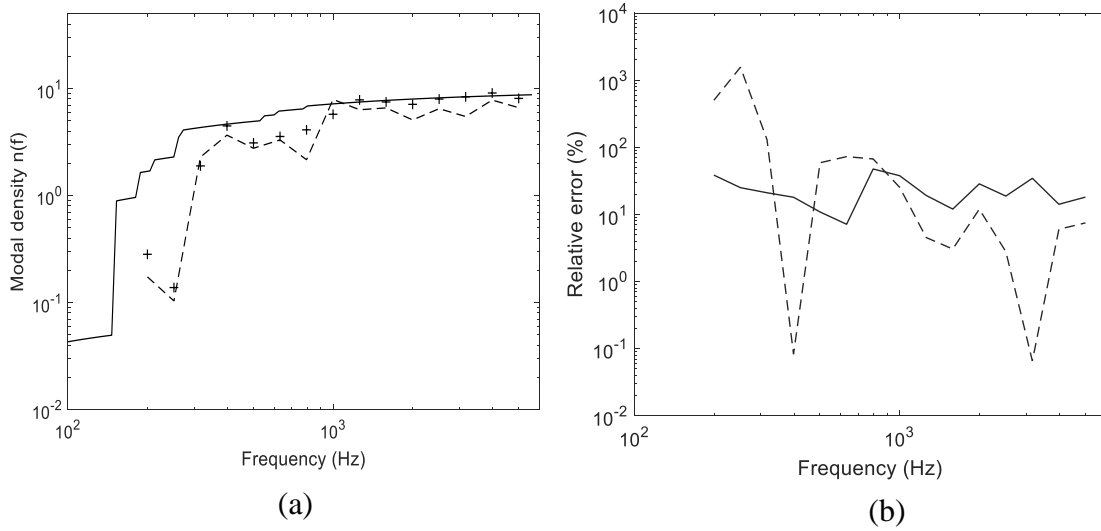
Figure 7.15. (a) Modal density comparison among Xie's model, FE calculation and the definition method. $+$: 2.5D FE calculation; $---$: Equation (7.13) with equivalent strip width; $—$: Xie. et al.' s model, (b) $—$: error of Xie et al.' s model; $---$: error of using equivalent widths in Equation (7.13).

7.5 Determining coupling loss factors

Having obtained the bending stiffness and the modal density of the extruded panel, the coupling loss factors (CLFs) in the SEA model can be calculated. The five types of coupling introduced in Section 7.1 will be discussed individually in this Section.

7.5.1 CLFs between two cavities

The direct coupling between the source room and the receiving room represents the non-resonant transmission path. This path is only significant below the critical frequency of the extrusion. The critical frequency of the global modes is calculated as 151 Hz, close to the value of 175 Hz given in Reference [60]. For the local modes, their bending stiffness is 105.05 Nm, the density of the layer without rubber is 6.86 kg/m^2 and that of the layer covered by rubber is 12.86 kg/m^2. Their critical frequencies are 4785 Hz and 6551 Hz.

The direct coupling between the source room and the receiving room in the SEA model is modelled by using the coupling loss factor η_{sr} between two cavities through a plate [82]

$$\eta_{sr} = \frac{c_0 S}{4\omega V_s} \tau_{sr} \tag{7.18}$$

where S is the area of the plate, V_s is the volume of the source room, and τ_{sr} is the transmission coefficient from the source room to the receiving room, which can be estimated from the sound transmission loss $R = 10 \log_{10}(1/\tau)$, where R is the sound transmission loss through a plate under diffuse incidence sound field. In this work the sound transmission loss is calculated based on the 'mass law' [51] in the whole frequency range of interest, given by

$$R \approx 20 \log_{10} \left(\frac{\omega \mu}{2 \rho_0 c_0} \right) - 5 \tag{7.19}$$

where ρ_0 is the density of air, c_0 is the acoustic velocity, and μ is the mass per unit area. This coupling path is applied in the SEA model in the whole frequency range considered in this work.

7.5.2 CLFs between cavities and the extruded panel

The coupling loss factor from a plate to an acoustic cavity can be modelled in terms of the radiation efficiency of the structure. It is expressed as [82]

$$\eta_{gc}, \eta_{lc} = \frac{\rho_0 c_0 \sigma}{\omega \mu} \tag{7.20}$$

In this equation, σ is the radiation efficiency. For the global modes, the radiation efficiency is obtained by using a modal summation approach (assuming the plates are simply supported) which averages the results over forcing points [109], as is shown in Figure 7.16.
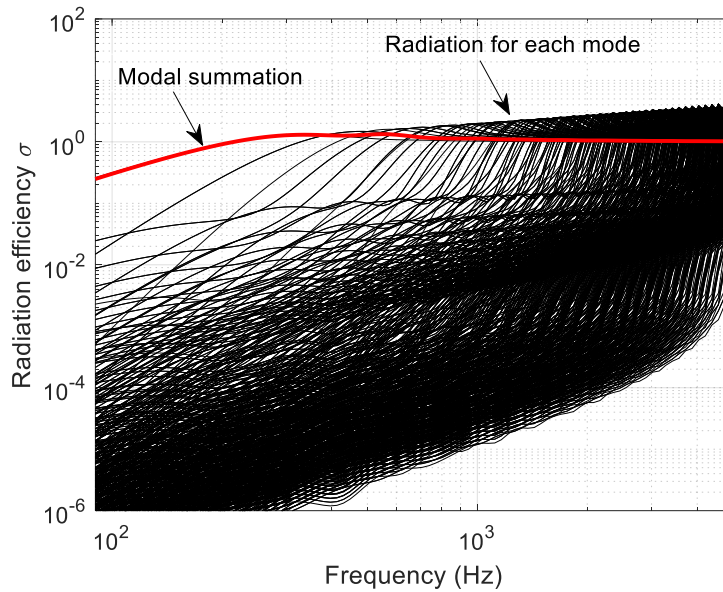
Figure 7.16. Radiation efficiency of global modes obtained by modal summation.

Each local mode subsystem consists of many strips. All the strips in one subsystem can contribute to the overall radiation efficiency. Because of they have different widths, their individual radiation efficiencies are different. Figure 7.17 shows the radiation efficiencies of the strips on the two sides of the extrusion obtained by using the modal summation approach assuming they are simply supported and by using the 2.5D model from Chapter 6. In both methods the equivalent widths derived in section 7.3 are used and they are assumed simply supported. In the 2.5D models the strips are infinite long and a wide wavenumber range with small wavenumber spacing were used in order to capture all the significant waves in the strips. In the modal summation approach the strips are 20 m long. The first six natural frequencies in the width direction and 600 natural frequencies in the length direction (3600 natural frequencies in total) were chosen to calculate the radiation efficiencies of the strips. From Figure 7.17, the modal summation approach and the 2.5D calculation can give very close results in terms of their radiation efficiencies.
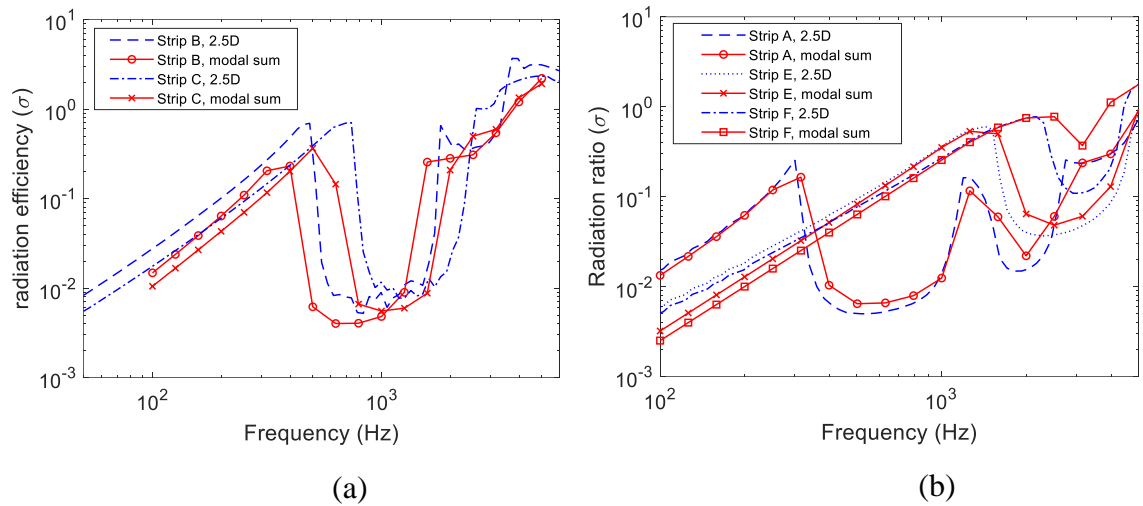
Figure 7.17. Radiation efficiencies of the strips obtained by the modal summation approach and by the 2.5D FE/BE models. (a) strips on the top plate, (b) strips on the bottom plate, indicated in Figure 7.3.

In Xie et al.'s SEA model [54] the radiation efficiency of the top plate subsystem is the average of the radiation efficiencies of all the strips on the top plate assuming that the average vibration of each strip is equal and that the vibration of each strip is uncorrelated with the others, and the same for the bottom plate. The averaged radiation efficiency is expressed as

$$\overline{\sigma} = \frac{1}{S}\sum_i S_i \sigma_i \tag{7.21}$$

where σ_i is the radiation efficiency of each strip, S_i is the area of each strip and S is the total surface area of the top or the bottom plate. Xie et at. [54] assumed that the average vibration of each strip is equal. However, in reality each strip vibrates differently, for instance Figure 7.18 shows the vibration levels of the three different length strips on the receiving side (panel is indicated in Figure 6.16 and Figure 7.3 and the results is calculated by the 2.5D FE model) with a mechanical excitation on the other side. Below 400 Hz and above 2500 Hz, the vibration levels of strip A is higher than the other two groups. Strip E is higher between 400 Hz and 800 Hz and strip F is higher from 1600 Hz to 2500 Hz.
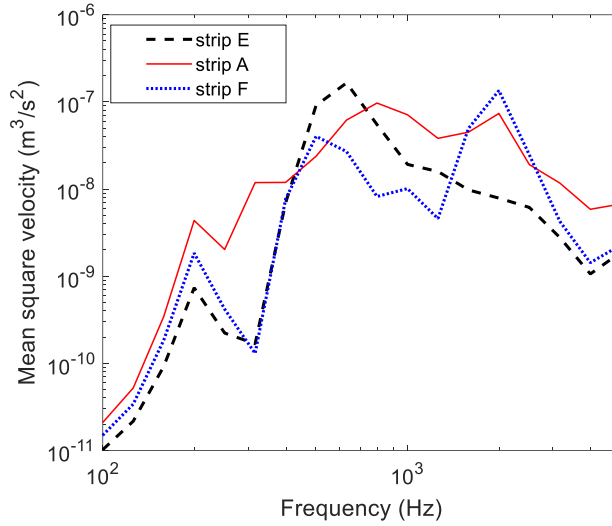
Figure 7.18. Vibration levels of the trips on the receiving side, indicated in Figure 6.16 and Figure 7.3, results calculated by the 2.5D FE model.

The difference in vibration levels will make their contributions to the total radiation efficiency of the plate differently. One alternative way to calculate the total radiation efficiency is to find a weight factor for each strip according to their area and vibration levels. The weighted radiation efficiency is expressed as

$$\overline{\sigma} = \sum_i \frac{S_i \left\langle \overline{v_i^2} \right\rangle \sigma_i}{S \left\langle \overline{v^2} \right\rangle} \tag{7.22}$$

where $\left\langle \overline{v_i^2} \right\rangle$ is the mean square velocity of the strips and $\left\langle \overline{v^2} \right\rangle$ is the mean square velocity of the whole plate on each side. To obtain the weight factors, the excitation should be shifted to different points to get the averaged vibration levels in order to omit the effect introduced by the excitation location. On the top plate (indicated in Figure 6.16) the two strip groups have approximate width and their individual radiation efficiencies are similar (Figure 7.17(a)), therefore the averaged radiation efficiency is used, see Figure 7.19(a). On the bottom plate, the three strip groups have different width and their individual radiation efficiencies are different (Figure 7.17(b)), both the averaged and the weighted radiation efficiencies are calculated and used in the SEA model to compare their difference in prediction. The radiation efficiencies on the two sides of the extrusion are shown in Figure 7.19(b). It is found that the averaged and weighted radiation efficiencies are similar, which indicates that the assumption that the average vibration of each strip is equal in [54] is reasonable.
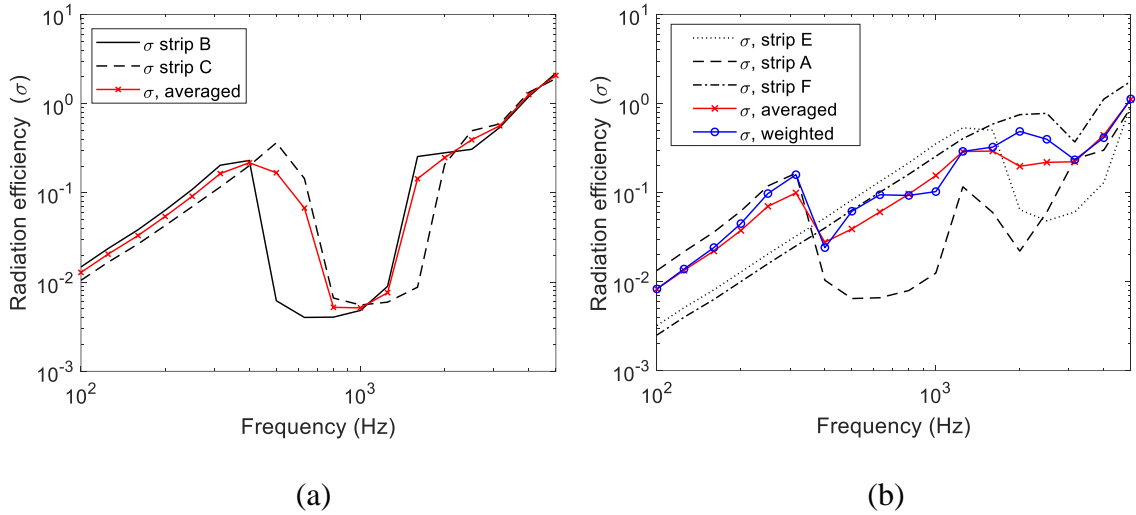
Figure 7.19. (a) Radiation efficiency of the top plate subsystem by modal summation, (b) radiation efficiency of the bottom plate by modal summation, indicated in Figure 6.16 and Figure 7.3.

Once the radiation efficiencies of global and local modes have been determined, the coupling loss factors from the extruded panel to the cavities can be calculated. The coupling loss factors from the cavities to the global and local modes can be obtained based on the consistency relationship [82].

$$n_i \eta_{ij} = n_j \eta_{ji} \tag{7.23}$$

7.5.3   CLFs between global mode and local mode subsystems

The coupling between global and local modes of the extruded panel will be discussed in this section. Relevant research on the coupling loss factors between global and local modes is lacking apart from Xie et al. [54]. Based on the previous studies on wave propagation in beam-plate systems [110, 111], the beams will generate long wavelength waves. When the long wavelength waves propagate along the stiff beams, they will transmit power to the attached plates which will generate short waves in these attached plates. If the difference in their wavelengths is large, the plates principally introduce damping and represent a locally reacting impedance to the beam behaviour [110, 111]. Xie et al. [54] estimated that the wavelengths of the local waves in the strips are around one fifth of those of the global waves in the extrusion. This can also be seen from the two lines that represent the free bending waves in the global modes and in the strips in Figure 6.3. It shows that the wavenumbers in the strips are around five times of those for the global waves. The extrusion could therefore

be analogous to a beam-plate system. The global modes are equivalent to the beam and the local modes are equivalent to the strips.

If a local mode subsystem is coupled with the global modes, the power balance equation for the local mode systems assuming no input power given to them can be expressed as

$$-\omega E_g \eta_{gl} + \omega E_l (\eta_{lg} + \eta_l) = 0 \tag{7.24}$$

where the first term represents the power transmitted to the local system and the second term represents both the power dissipated by the damping and that reflected back to the global modes. E_g and E_l are the stored energy of the global and local subsystems, η_{gl} and η_{lg} are the coupling loss factors from global to local and from local to global subsystems respectively. η_l is the damping loss factor of the local modes.

From references [110, 111], the approach can be simplified by assuming that the local modes do not affect the global behaviour. Then the influence from the local modes on the global modes can be neglected. The power input to the local modes is therefore equal to the power dissipated by the local modes themselves.

$$W_{g,l} = \omega E_g \eta_{gl} = \omega E_l \eta_l \tag{7.25}$$

which yields the coupling loss factor from the global to local modes, given by

$$\eta_{gl} = \frac{W_{g,l}}{\omega E_g} \tag{7.26}$$

Xie [60] derived the coupling loss factor from the energy (E_g) in the extruded panel and the power ($W_{g,l}$) transmitted from the beams to the plates. $W_{g,l}$ was derived analytically from a simply supported beam model. Assuming waves in the extruded panel cause it to vibrate with a normal velocity v_1 and v_2 at the two ends (v_1 and v_2 are assuming to have same amplitude but different phase), forces F_1 and F_2 are generated at the two ends of the strips, see Figure 7.20.
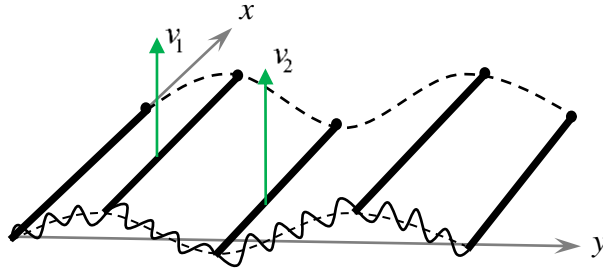
Figure 7.20. Power input from global modes to local modes [60].

The power input to a strip can be estimated by

$$W_{in} = \frac{1}{2} Re(F_1^* v_1 + F_2^* v_2) \tag{7.27}$$

where W_{in} is equal to $W_{g,l}$ in Equation (7.25). The details of the derivation of the velocity and force at the two ends of the strips are given in reference [60]. Also, for a highly damped beam that the interference from the two ends are negligible, Equation (7.27) is expressed by

$$W_{in} = \frac{1}{2} Re(Z_0)(|v_1|^2 + |v_2|^2) \tag{7.28}$$

where $Z_0 = \frac{1}{2} m c_B (1 + i)$ is the characteristic impedance of a semi-infinite beam. m is the mass per unit length and c_B is the phase velocity of bending waves. The total stored energy per unit length of the tranveling waves in the global modes is calculated by [60]

$$E_g = \frac{1}{2} m_g |v_1|^2 = \frac{1}{2} m_g |v_2|^2 \tag{7.29}$$

where m_g is the equivalent mass per unit area of the whole panel. As explained before, v_1 and v_2 are assumed to have the same amplitude but different phase. Having obtained the power and the total energy, the coupling loss factor can be obtained from Equation (7.26).It can also be obtained approximately by [54]

$$\eta_{gl} = \frac{W_{g,l}}{\omega E_g} \approx \frac{2p \, Re\{Z_0\}}{m_g D \omega} \approx \frac{m_l p}{m_g k_l D} \tag{7.30}$$

where k_l is the wavenumber of the strips and p/D means the number of strips per unit width of the plate. The coupling loss factor η_{lg} is calculated based on the consistency relation in Equation (7.23).

7.5.4 CLFs between local mode subsystems

The local mode subsystems consist of many strips. Generally, the most commonly used joints in extruded panels are shown in Figure 7.21. Approximated equations were provided to predict the transmission coefficients through such joints are provided by Craik [82].

Cross joint   'T' joint   Corner joint
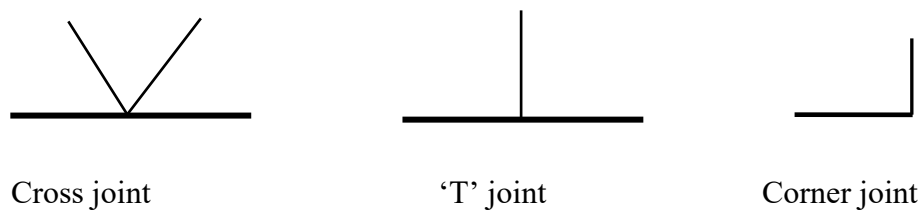
Figure 7.21. Commonly used joints in extruded panels.

According to Craik [82], the angle between the strips does not affect the transmission coefficient very much. A wave propagating through a corner is equivalent to a wave propagating through two plates with a joint between them. If the joint is assumed to be simply supported, there is an analytical equation to calculate the transmission coefficient of bending waves between two plates with different properties (the joint is assumed to be symmetric about the neutral axes of the two plates). Consider a wave incident at angle θ on a straight line junction between two plates, see Figure 7.22, the transmission coefficient is expressed as
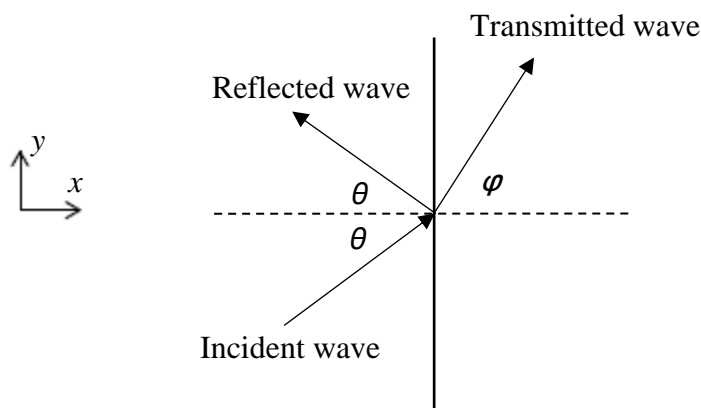
Figure 7.22. Reflection and transmission of bending waves at a line junction between two plates.

$$\tau_{12}(\theta) = \frac{2\psi\sqrt{\chi^2 - s^2}\sqrt{1 - s^2}}{\psi^2 + \psi(\sqrt{\chi^2 + s^2}\sqrt{1 + s^2} - \sqrt{\chi^2 - s^2}\sqrt{1 - s^2}) + \chi^2} \quad (7.31)$$

where $\chi = \frac{k_2}{k_1}$ and $\psi = \frac{D_2 k_2^2}{D_1 k_1^2}$, in which k_i and D_i are the structural wavenumber and bending stiffness of the plates i respectively. For diffuse incidence, the transmission coefficient is given by

$$\tau_d = \int_{-\pi/2}^{\pi/2} \tau_{12}(\theta) \cos\theta \, d\theta \quad (7.32)$$

According to Craik, the transmission coefficient through different joint types can be modelled by using the following equations together with the parameters presented in Table 7.6. The energy reduction $R = 10\log_{10}(1/\tau_{12})$ by joints is (for $\chi \geq 1$) [82]

$$\begin{cases} R_{12} = 20\log_{10}[(\chi/A)^{0.5} + (A/\chi)^{0.5}] + B + C/\chi + D\log_{10}(1 + 1/\chi^4) \\ R_{21} = 20\log_{10}[(\chi/A)^{0.5} + (A/\chi)^{0.5}] + B + C\chi + D\log_{10}(1 + \chi^4) \end{cases} \quad (7.33)$$

Table 7.6. Parameters for calculating random incidence transmission loss in dB for different joints [82].

Joints	A	B	C	D
$\vee$	ψ	-2.0053	0.2535	1.56
$\perp$	ψ	4.0153	0.2535	1.56
$\lrcorner$	$\psi/2$	0.2353	0.2353	1.56

The transmission coefficient through the joint can therefore be obtained from the energy reduction. For two aluminium plates joined together, the transmission coefficient calculated by using Equation (7.32) is $\tau_{12} = 0.336$ for two identical thickness plates and $\tau_{12} = 0.133$ for two plates with thicknesses $h_1 = 0.003$ m, $h_2 = 0.006$ m. The approximate values given by Equation (7.33) are identical, which shows the two methods are nearly equivalent. In the current extrusion the top plate and middle stiffeners are of the same material and thickness, so the transmission coefficient for a cross joint is $\tau_{cross} = 0.084$ and for a 'T' joint $\tau_{Tee} = 0.149$. The bottom plate has a layer of rubber, which increases its mass density. The transmission coefficient through a 'T' joint from the middle stiffeners to the bottom plate is

$\tau_{Tee} = 0.148$ and from the bottom plate to the middle stiffeners is $\tau'_{Tee} = 0.138$. The transmission coefficient through a cross joint from the middle stiffeners to the bottom plate is $\tau_{cross} = 0.084$ and in the return direction it is $\tau'_{cross} = 0.074$ .The transmission coefficient through a corner joint from the middle stiffeners to the bottom plate is $\tau_{corner} = 0.351$ and in the return direction is $\tau'_{corner} = 0.300$.

Once the transmission coefficients between strips are determined, the coupling loss factor between two strips is calculated by using [82]

$$\eta_{12} = \frac{Lk_1\tau_{12}}{\pi\omega n_1(f)} \tag{7.34}$$

where τ_{12} can be the transmission coefficient through a 'T' joint, a cross joint or a corner joint. Then the coupling loss factors between local modes can be derived for the extrusion according to the naming convention in Figure 7.23.
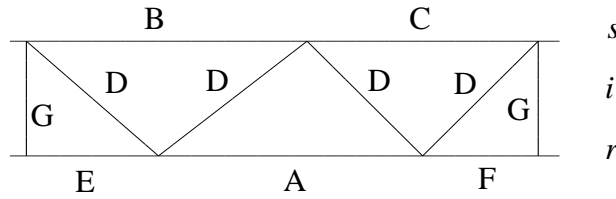
Figure 7.23. A unit of the extrusion. *s* indicates the excitation side, *i* for the intermediate layer and *r* means the receiving side.

The power flow from the local modes on the source room side to the intermediate local modes of the extrusion consists of the contributions of all the strips on the source room side. So

$$W_{si} = \omega m_B \left\langle \overline{v_B^2} \right\rangle \eta_{BG} + 3\omega m_B \left\langle \overline{v_B^2} \right\rangle \eta_{BD} + 3\omega m_C \left\langle \overline{v_C^2} \right\rangle \eta_{CD}$$
$$+ \omega m_C \left\langle \overline{v_C^2} \right\rangle \eta_{CG} \tag{7.35}$$

where W_{si} is the transmitted power from the source room side to the intermediate local modes, m_i is the mass of the strip and $\left\langle \overline{v_i^2} \right\rangle$ is its mean-square velocity, η_{ij} is the transmission coefficient from strip i to strip j. The mean-square velocity of the strips may be

different because the excitation may locate locally to a particular position. To derive a more general coupling loss factor from the local modes on the source room side to the intermediate local modes, it can be assumed that in the SEA model the strips in each subsystem have the same mean square velocity, which yields

$$W_{si} = m_s \left\langle \overline{v_s^2} \right\rangle \omega \eta_{si} \tag{7.36}$$

where $\left\langle \overline{v_s^2} \right\rangle$ is the mean square velocity of the plate on the source room side, η_{si} is the coefficient coupling loss factor from subsystem s to subsystem i. The transmitted power from the intermediate local modes to the receiving room side can be derived analogously. If the influence from the ends is ignored and a cross joint is used to model the transmission from strips B and C to strips D and G, the coupling loss factor between local modes from the source room side to the middle stiffeners is

$$\eta_{si} = \frac{m_B \eta_{BG} + 3m_B \eta_{BD} + 3m_C \eta_{CD} + m_C \eta_{CG}}{m_s}$$
$$= \frac{4 \dfrac{L k_s \tau_{cross}}{\pi \omega} \left(\dfrac{l_B}{n_B(f)} + \dfrac{l_C}{n_C(f)} \right)}{l_B + l_C} \tag{7.37}$$

Similarly, the power flow from the intermediate local modes to the local modes on the receiving room side can be calculated by

$$\eta_{ir} = \frac{m_G \eta_{GE} + 2m_D \eta_{DE} + 4m_D \eta_{DA} + 2m_D \eta_{DF} + m_G \eta_{GF}}{m_i}$$
$$= \frac{2 \dfrac{L k_i \tau_{corner}}{\pi \omega} \left(\dfrac{l_G}{n_G(f)} \right) + 8 \dfrac{L k_i \tau_{cross}}{\pi \omega} \left(\dfrac{l_D}{n_D(f)} \right)}{2l_G + 4l_D} \tag{7.38}$$

k_s and k_i are the wavenumbers of the strips on the source room side and the intermediate strips respectively. L is the length of joint and l is the width of the strips. In the reverse direction, the coupling loss factors can be obtained by using the consistency relationship in Equation (7.23) between subsystems.

7.6 Using the SEA model to predict sound transmission through extruded panels

By combining the results from the previous sections, an SEA model was created to predict the sound transmission through and radiation from the extruded panel. The SEA model is used to represent two reverberant chambers connected by the currently considered train floor. The volumes and dissipation loss factors of the source room and the receiving room are arbitrary because they will not affect the prediction. Here the source room is 126 m^3 and connected to the top plate of the extruded plate and the receiving room is 348 m^3 and connected to the bottom plate. The volumes of the source room and the receiving room are chosen based on the ISVR reverberant chambers used in the measurement in [105]. The train floor area is 20 m^2. The dissipation loss factors are calculated from the measured reverberation time (T_R) in the source room and the receiving room [105] by using $\eta_{1(6)} = 2.2/(fT_R)$.

Xie et al. [54] give the experimental result of the damping loss factor of the global modes of the extrusion as $\eta_2 \approx 0.045$ for all frequencies. In the 2.5D FE/BE model, the local subsystems 3 and 4 were given a damping loss factor of 0.005 and the bottom plate which is rubber covered (local subsystems 5) has a damping loss factor of 0.02 for all frequencies. These values are used in the SEA model.

The SEA model may have different coupling relationships (i.e. subsystems only have modal energy once they have cut on) depending on the cut on frequencies of the three local mode subsystems. The three local mode subsystems have different cut on frequencies, which satisfy

$$f_5 < f_3 < f_4 \tag{7.39}$$

where f_3, f_4, and f_5 are the cut on frequencies of local mode subsystems 3, 4, and 5 (defined in Figure 7.1 and Figure 7.2). When the frequency is below f_5, only the global modes connect the two rooms. In the frequency region $f_5 < f < f_3$, the global modes are coupled to the local modes on the receiving room side. Both the local modes and global modes will radiate sound to the receiving room. When $f_3 < f < f_4$, the local modes on both sides are cut on. When $f > f_4$, the extrusion is fully excited, and local modes are dominant in sound

radiation. A schematic representation of the SEA model at different frequencies is shown in Figure 7.24.
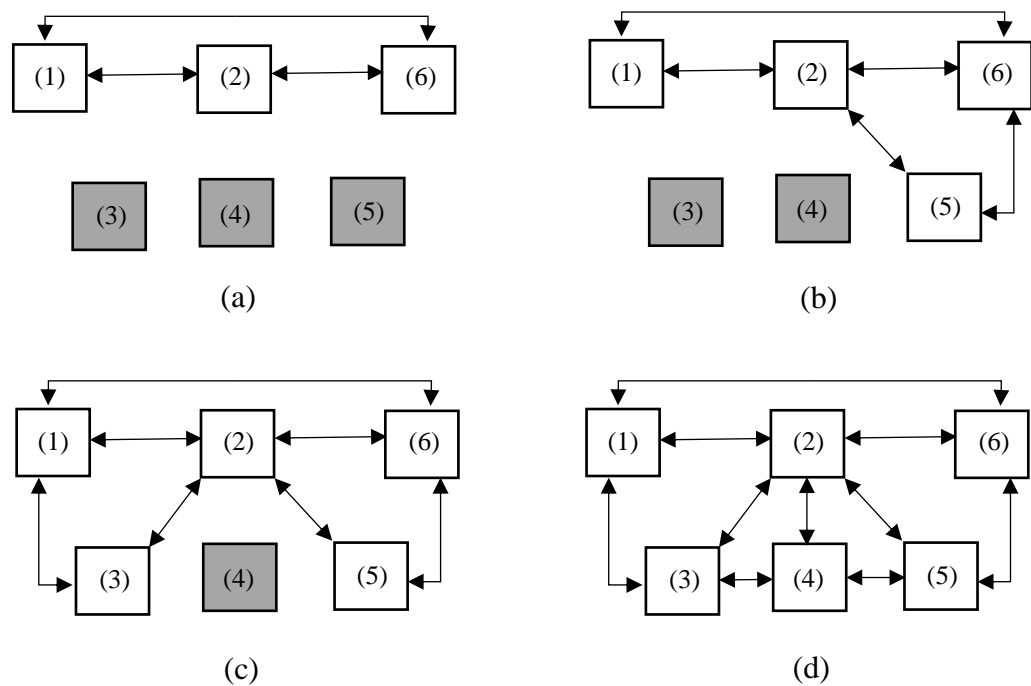
Figure 7.24. SEA model for different frequency regions. (a) $f < f_5$, (b) $f_5 < f < f_3$, (c) $f_3 < f < f_4$, (d) $f > f_4$. Grey colour means the subsystem is not included.

7.7   Results from the SEA model

The SEA model created in Section 7.6 is used to predict the sound transmission loss through the extruded panel discussed in this work, as well as its sound radiation efficiency. The SEA model has a reputation to solve high frequency problems. To achieve good accuracy, various assumptions need to be hold. For instance, behaviour dominated by resonances, reverberant, lightly damped structures, many modes in the excitation bandwidth, 'weak' coupling (the interaction of two subsystems is not affected by the presence of a third one). The first natural frequency of the 20 m long extrusion is 186 Hz. In the 200 Hz one-third octave band, there are seven modes and in the 250 Hz band, there are six. The local modes cut on at 322 Hz, more than 130 modes exist from the 315 Hz band above. By assuming they are weakly coupled, the current SEA model can be applicable above 200 Hz.

7.7.1   Sound transmission loss

In simulating the sound transmission loss though the extruded panel, sound power is given to the source room, and the SEA model is used to predict the sound pressure in the receiving room. The sound transmission loss is obtained from the difference between the sound pressure levels in the two rooms. The mean sound pressure in the source room and receiver can be calculated by $\langle \overline{p_1{}^2} \rangle = \rho c_0^2 E_1 / V_1$ and $\langle \overline{p_6{}^2} \rangle = \rho c_0^2 E_6 / V_6$, where E_1, E_6 are the energy in the source and receiving room and V_1, V_6 are the volumes of the source room and receiving room respectively. The sound reduction is calculated by [51]

$$R = L_{p1} - L_{p6} + 10 \log_{10} \left(\frac{S}{A_6} \right) \tag{7.40}$$

where L_{p1} is the sound pressure level in the source room and L_{p6} is the value in the receiving room. S is the surface area of the panel, A_6 is the total absorption area in the receiving room, expressed as $A_6 = 55.26 V_6 / (c_0 T_{60,r})$, with $T_{60,r}$ is the reverberation time in the receiving room. The sound transmission loss of the extruded panel calculated by using the SEA model is given in Figure 7.25. It is compared with the sound transmission loss obtained by Xie et al.'s SEA model [54] and the measured data from reference [64, 105]. Xie et al.'s SEA model and the current SEA model do not have significant differences below 1000 Hz in terms of the prediction. Above 1000 Hz, the sound transmission loss obtained by the current SEA model agrees well with the measurement. It can give better prediction than Xie et al.'s SEA model at high frequency. The use of the averaged and weighted radiation efficiency on the receiving side does not cause obvious difference in prediction of sound transmission loss. The disagreement below 1000 Hz needs further investigation.
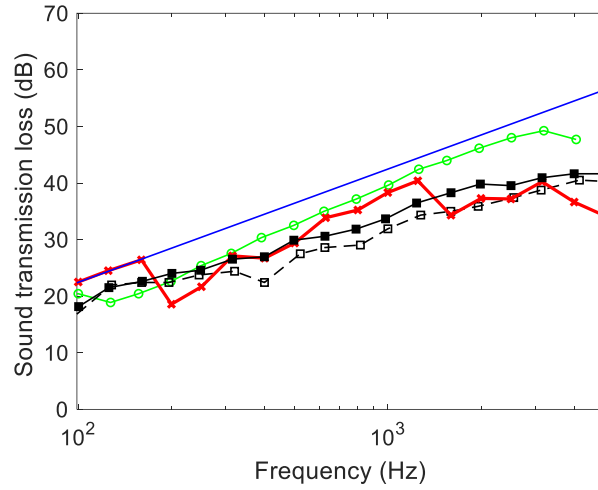
Figure 7.25. Sound transmission loss of extrusion. —○—: Xie et al.'s SEA model [54], —✳—: the current SEA model; —■—: measured in [56]; – ▫ –: measured in [64, 105]; ——: mass law.

7.7.2 Sound radiation efficiency

In simulating the radiation efficiency of the extruded panel in the SEA model, a mechanical force is applied to the stiffeners or strips on the top plate of the extruded panel. The excitation side and the receiving side are indicated in Figure 6.16. When the force is applied to the stiffener, it directly excites the global vibration while when it is applied to the strips, it excites both the global and local vibration. The input power is given by

$$P_{\text{in}} = F_{rms}^2 \, \text{Re}(Y) \tag{7.41}$$

where F_{rms} is the root mean square force; 0.707 N is set for the root mean square force in the SEA model as a force with unit amplitude is used in the 2.5D FE model. Y is the driving point mobility at the excitation position. It is calculated (for either a strip or the global motion of the whole panel) by using modal summation assuming simply supported boundaries [60]

$$Y(x_0, y_0) = \frac{4i\omega}{\mu ab} \sum_{m,n=1}^{\infty} \frac{\sin^2(m\pi x_0/a) \sin^2(n\pi y_0/b)}{\omega_{m,n}^2(1 + i\eta) - \omega^2} \tag{7.42}$$

The force location is at (x_0, y_0), μ is the mass per unit area of the strip or the whole panel. a and b are the corresponding dimensions. For strips, their equivalent widths are used. m and n are indices of the natural modes, η is the damping loss factor and $\omega_{m,n}$ is the $(m, n)^{th}$ natural frequency.

If the force is applied to a stiffener, the driving point mobility is calculated based on modal summation over global modes. The input power calculated by using Equation (7.41) is given to the global mode subsystem. If the force is applied to a strip, both the global driving point mobility and the local driving point mobility should be calculated by using Equation (7.42) and it is assumed that local modes in other strips do not contribute. In this case the input power should be divided between both the global mode subsystem and the local mode subsystem on the excitation side according to their mobilities.

Figure 7.26(a) shows an example of the driving point mobility obtained from Eq. (7.42) when a force is applied to the stiffener connecting strips B and C in Figure 7.3. It is compared with the results obtained from the 2.5D FE model which is considered as a validation. The analytically calculated driving point mobility is close with the value obtained from the 2.5D FE model. Figure 7.26(b) shows an example of the global and local driving point mobility when a force is applied on a point on strip B (the location is the same as position F_6 in Figure 6.16). From Figure 7.26(b), the first natural frequencies of the global and local modes are predicted well. At high frequency, the local driving point mobility is dominant and the calculated local driving point mobility agrees well with the 2.5D FE predicted values. Below the first natural frequency of the global modes (186 Hz), using the equivalent width of the strip in Equation (7.42) overestimates the driving point mobility for local modes, indicated by the local driving point mobility overtaking the total one in Figure 7.26(b). In this frequency region there is no modes therefore the SEA model is not valid. However, the input power is calculated based on the driving point mobility of the global and local subsystems and given to the SEA model. A consequence is that the power that is input to the local subsystem is higher than the actual value. Even though below its first natural frequencies, the local modes on the excitation side is not included in the SEA model, it will overestimate the contribution from the local modes as the energy below the first natural frequency is stored in the local modes subsystem but does not exchange with other subsystems. This might lead to an underestimation of the radiation efficiency below the first natural frequency of the global modes.
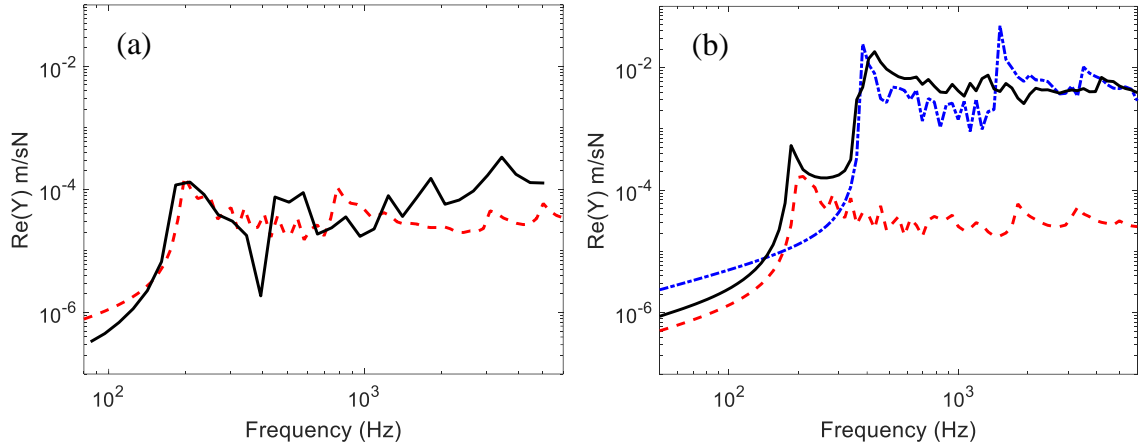
Figure 7.26. (a) The driving point mobility when a force is applied to the stiffener, - - -: by modal summation; ——: by 2.5D FE model, (b) the global and local driving point mobility when a force is applied to strip B, - - -: global driving mobility by modal summation; -----: local driving mobility by modal summation with equivalent width; ——: total mobility, by 2.5D FE model.

The radiation efficiency for the panel includes the contributions from the global and local modes. For radiation from one side, it is given by [54]

$$\sigma = \frac{\overline{W}_g + \overline{W}_l}{\rho c S \left\langle \overline{v^2} \right\rangle} = \frac{\rho c S \left\langle \overline{v_g^2} \right\rangle \sigma_g + \rho c S \left\langle \overline{v_l^2} \right\rangle \sigma_l}{\rho c S \left\langle \overline{v_g^2} \right\rangle + \rho c S \left\langle \overline{v_l^2} \right\rangle} = \frac{\left\langle \overline{v_g^2} \right\rangle \sigma_g + \left\langle \overline{v_l^2} \right\rangle \sigma_l}{\left\langle \overline{v_g^2} \right\rangle + \left\langle \overline{v_l^2} \right\rangle} \qquad (7.43)$$

where v_g is the velocity due to global modes, v_l is the velocity due to local modes, σ_g is the radiation efficiency of global modes and σ_l is the radiation efficiency of local modes. S is the area of the extruded panel. $\left\langle \overline{v_g^2} \right\rangle$ and $\left\langle \overline{v_l^2} \right\rangle$ are the time and spatially averaged mean square velocities of the global and local modes (the overbar inside the bracket means the time average and the bracket means the spatial average), obtained from

$$\left\langle \overline{v_l^2} \right\rangle = \frac{E_i}{m_i} \qquad (7.44)$$

where E_i is the stored energy in each subsystem and m_i is the total mass of the subsystem.

As it has been proved that the 2.5D method is able to predict the radiation efficiency of the extruded panel with good quality in Chapter 6, the sound radiation efficiency predicted by

the SEA model with assistance from the 2.5D FE model is compared with the calculations by using the 2.5D model in the WANDS software. In the 2.5D model, the extruded panel is treated as baffled. Figure 7.27 shows the SEA predicted radiation efficiency of the extruded panel when the mechanical excitation is applied on a strip (at position F_4 in Figure 6.16). The use of the averaged and weighted radiation efficiency on the receiving side does not cause obvious differences in the radiation efficiency on the excitation side, thus the radiation efficiency on the excitation side predicted by using the averaged one is shown. Figure 7.28 shows the SEA predicted radiation efficiency of the extruded panel when the mechanical excitation is applied on another strip (at position F_6 in Figure 6.16).

It can be seen that the SEA model can predict the radiation efficiencies of the extrusion well. On the excitation side, the SEA slightly underestimates the results at low frequency. This is because the local mobility is overestimated below the first natural frequency, see Figure 7.26. this will increase the contribution of the strips and underestimate the total radiation efficiency of the extrusion at low frequency. On the receiving side, the SEA predicted results agree well with the values obtained from the 2.5D models in WANDS software. The use of the averaged and weighted radiation efficiency for the local modal subsystem causes minor difference above 1600 Hz. Both are acceptable for prediction.
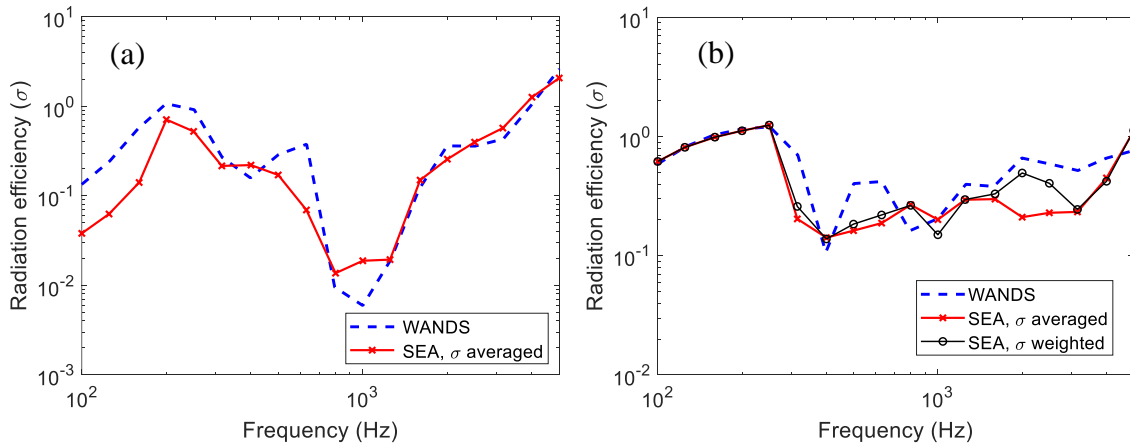
Figure 7.27. The radiation efficiency predicted by the SEA with assistant from the 2.5D model compared with with results obtained from the 2.5D model created in WANDS software for unit excitation at position F_4 in Figure 6.16, (a) results on excitation side, (b) results on receiving side.
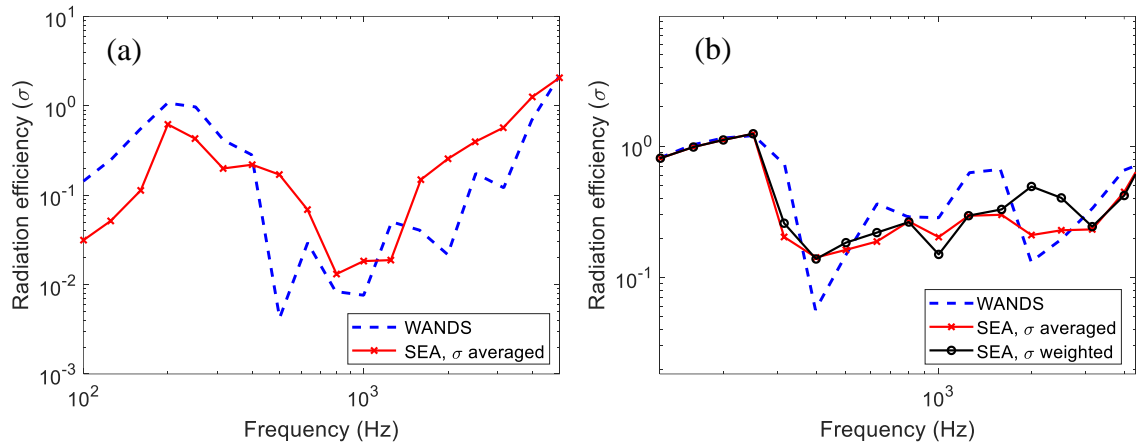
Figure 7.28. The radiation efficiency predicted by the SEA with assistant from the 2.5D model compared with with results obtained from the 2.5D model created in WANDS software for unit excitation at position F_6 in Figure 6.16, (a) results on excitation side, (b) results on receiving side.

Figure 7.29 shows the SEA predicted radiation efficiency of the extruded panel when the mechanical excitation is applied to a stiffener (the same location as F_2 in the WANDS model, see Figure 6.16). The SEA model can also give acceptable prediction of radiation efficiency of the extruded panel when the mechanical excitation is applied to the stiffeners.
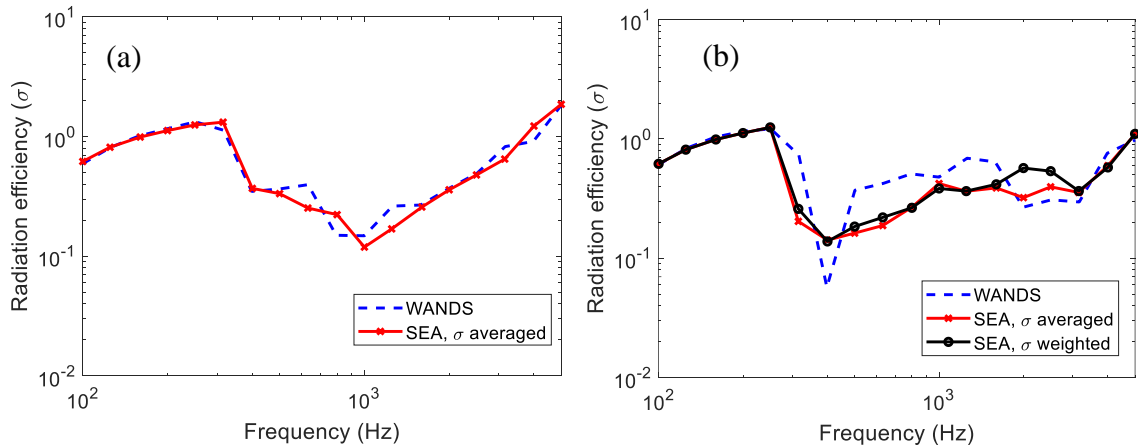
Figure 7.29. The radiation efficiency predicted by the SEA with assistant from the 2.5D model compared with with results obtained from the 2.5D model created in WANDS software for excitation on stiffener, (a) results on excitation side, (b) results on receiving side. (the same location as F_2, see Figure 6.16).

To compare with the measurements [64] and Xie et al.'s SEA model [54], the two sides of the extrusion are combined. The overall radiation efficiency of the extrusion is calculated by

combining the sound power and the averaged mean square velocity on the two sides. Figure 7.30 indicates the comparison of sound radiation efficiency when the force is at a stiffener. In the measurements the excitations were at locations P3 and P4, see reference [64, 105] and Figure 6.17. some differences appear on the measured data. However, in the SEA model shifting the excitation from P3 to P4 or the other way around does not make a noticeable difference to the results. From Figure 7.30, it can be seen that Xie et al.'s SEA and the current SEA model can predict the radiation efficiency with acceptable accuracy above 250 Hz. At low frequency, the two SEA models overestimate the radiation efficiency. This is possible because the SEA parameters were determined based on a simply supported extrusion while in the measurements the extrusion is free. The difference in the boundary conditions may has caused the disagreement below the first natural frequency of the extrusion.

Figure 7.31 indicates the comparison when the excitation is at a strip. P1 and P2 were located at the same strip in the measurements [64, 105]. The SEA model gives similar predictions when exciting at the two locations. Above 1000 Hz, the two SEA models give very similar results. At low frequency, Xie et al.'s SEA model gives a relatively flat prediction while the current SEA model captures the main trend of the radiation efficiency compared with the measurements.
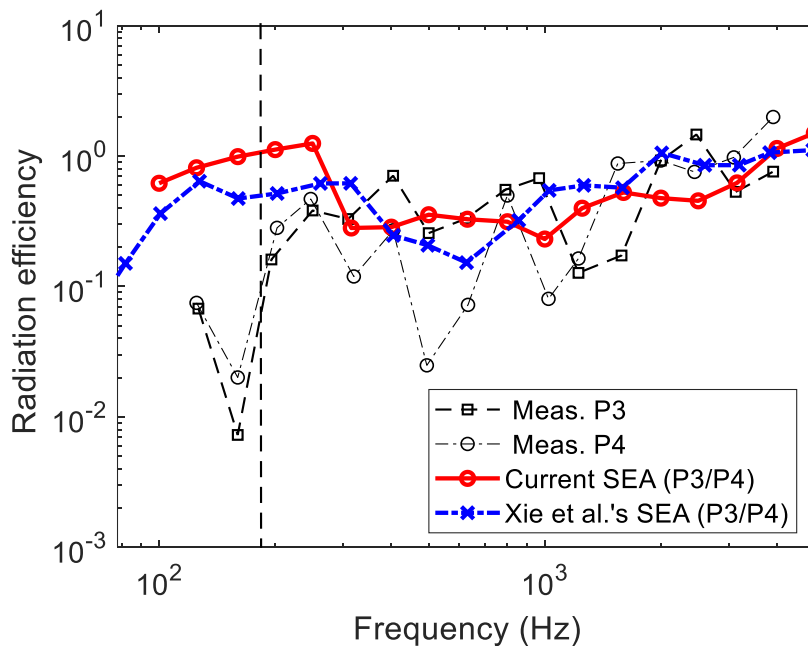
Figure 7.30. Prediction of radiation efficiency compared with measurements [64, 105] and Xie et al.'s SEA model [54]. Force at a stiffener, indicated in Figure 6.17.
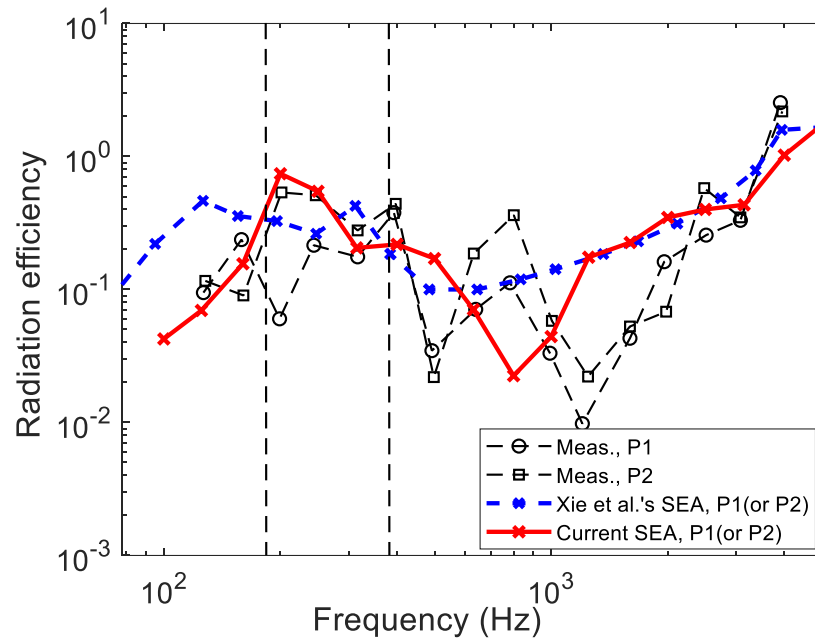
Figure 7.31. Prediction of radiation efficiency compared with measurements [64, 105] and Xie et al.'s SEA model [54]. Force at a strip, indicated in Figure 6.17.

The SEA model can give good prediction of radiation efficiency of the extruded panel, but one thing should be noticed is that above the cut on frequency of the local modes, the contribution from the strips become significant. The contribution of each strip to the overall radiation efficiency of the local mode subsystems depends not only on their individual radiation efficiencies and areas, but also their individual vibration levels. An alternative approach would be to divide the local modes subsystems into groups for each type of strip or even into one subsystem per strip. That would make the model bigger but may give more reliable results. One question would be about the modal density/overlap of such a system

7.8   Summary

An SEA model is created to study the vibroacoustic behaviour of extruded panels, including the radiation efficiency and the sound transmission loss. In the SEA model, the extrusion was separated into four subsystems according to Xie et al. [54], one for global modes and three for local modes. The 2.5D FE/BE model was used to help to determine the essential parameters for the SEA model, for instance, the modal densities of the global and local subsystems, their radiation efficiencies, the coupling loss factors and the transmission coefficients through local subsystems. An equivalent width for each strip was found based on the cut on frequencies obtained from the 2.5D FE/BE model. Simply supported boundary

conditions with the equivalent widths obtained from the 2.5D FE model can be used to predict their modal densities and radiation efficiency well.

The SEA model can give predictions of sound transmission loss that match measured results with acceptable accuracy. It was also used to predict the sound radiation efficiency when a mechanical force is applied either to a stiffener or a strip. For both cases, the SEA model with the parameters determined from the 2.5D FE model can predict the sound radiation efficiency on the excitation and receiving sides with good quality and high efficiency.

Chapter 8   Modelling of interior airborne noise

8.1   Framework for predicting airborne noise

Based on the various developments from this thesis, this chapter provides an overall framework to predict the airborne noise inside a railway vehicle. This framework is illustrated in the flowchart in Figure 8.1. It is applied here as a case study to a specific metro vehicle for which measured data are available to illustrate the procedures. Although the aerodynamic noise has been considered in Chapter 5, it does not contribute significantly to a metro vehicle as they generally run at low speeds. Therefore, this is neglected and the approach is explained assuming that the most significant source is rolling noise. The sound power incident on the train floor and on the sides are treated separately following the procedures introduced in Chapters 3 and 4 respectively. Using these estimates of the sound power incident on the train external surfaces, the sound power transmitted into the train cabin is obtained by multiplying it with the transmission coefficients of the train walls. These transmission coefficients could be obtained using the methods developed in Chapter 6 and 7 but for this particular case study measured values are used. A separate SEA model is then used for the interior noise taking these transmitted powers as input. This SEA model is only used to represent the interior acoustic space, unlike that in reference [27] which also includes the exterior noise sources and sound transmission. This assumes a one-way coupling of the train walls in the SEA model. According to the measurements, the sound transmission loss of the train body is more than 20 dB above 100 Hz except the gangway region. The power transmitted back to the outside will therefore be negligible and the one-way coupling assumption is reasonable.
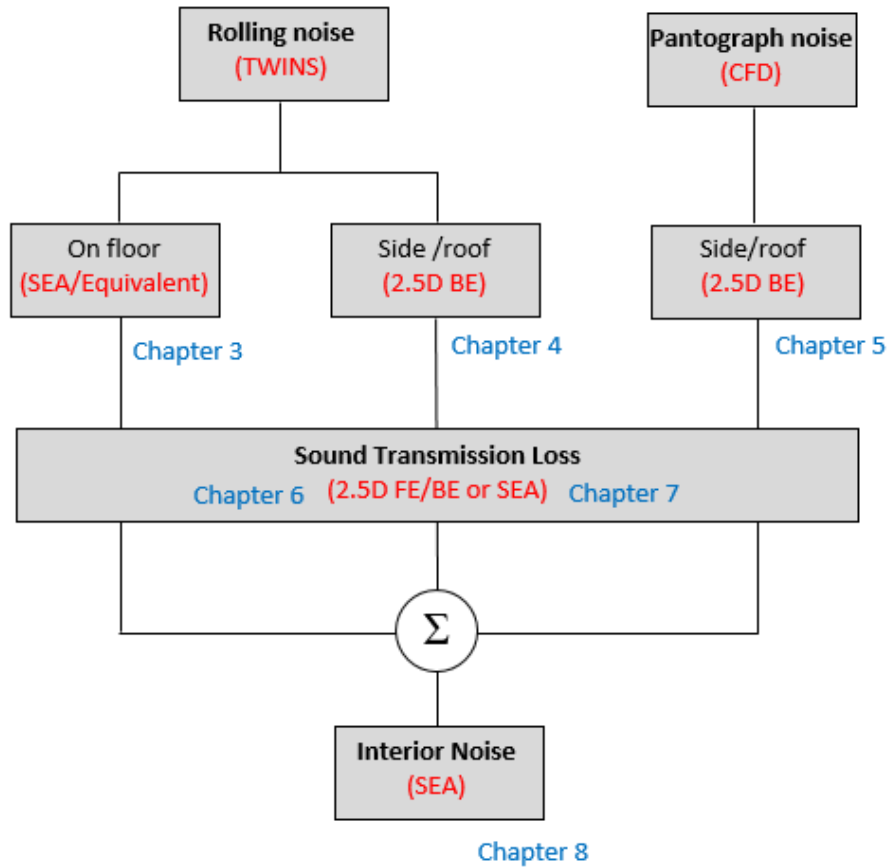
Figure 8.1. The framework to predict airborne noise in a railway vehicle, 'Equivalent' in the floor box means the equivalent source model from [16].

The general framework outlined above is applied to predict the noise inside a metro train. It was running at 50 km/h during the tests. Figure 8.2 shows an overall view of the field measurements on this metro train. Microphones were located at various positions outside and inside a trailer passenger carriage[3]. The carriage being measured had four doors and five windows on each side, and various pieces of equipment mounted below the floor. Rolling noise was assumed to be the main noise source as other equipment was switched off where possible. The sound pressure was measured below the train floor, on the train external sides and inside the train. The sound power of the rolling noise for this train was calculated by using the TWINS model with discretely supported sleepers and validated against measurements of noise at the trackside. More details about the measurements and rolling noise calculation for this train can be found in **Appendix B**.

---

[3] The measurements were carried out within the EU project RUN2Rail by Vibratec and Polytechnic University of Valencia (UPV) in collaboration with Metro de Madrid.

Figure 8.2. Overview of field measurement on a running train (photo: Polytechnic University of Valencia (UPV)).

The SEA model for interior noise modelling is introduced first, followed by the calculation of the essential input parameters required for the SEA model. The sound pressure distribution in the train cabin and the experimental validation are shown and discussed at the end of the chapter.

8.2   SEA model for the internal space

An SEA model is used in this Chapter to represent the internal acoustic space. The SEA method is based on a diffuse field assumption. To check whether the interior of the train can be considered as a diffuse field, the modal overlap factor (average number of modes within the modal half-power bandwidth) is calculated by [112]

$$M = \frac{2.2}{T_{60}} \times \frac{4\pi V f^2}{c_0^3} \tag{8.1}$$

where T_{60} is the reverberation time in the train cabin and V is the whole volume of the train internal space. It is 93.74 m^3 according to the measurements in **Appendix B.4**. The modal overlap goes above 3 from the 160 Hz one-third octave band. Above this frequency, the train cabin can be considered as a diffuse sound field.

In the numerical framework, the interior volume is divided into several segments to create an SEA model. To allow a more straightforward calculation of the input power, the subdivision is based on the configuration of the doors and windows, see Figure 8.3. Nine subsystems were created for the interior and another two subsystems were created for the

gangway at the two ends, thus giving an eleven-subsystem SEA model. The final SEA subsystems are illustrated in Figure 8.4. The lengths and volumes of each subsystem are listed in Table 8.1.
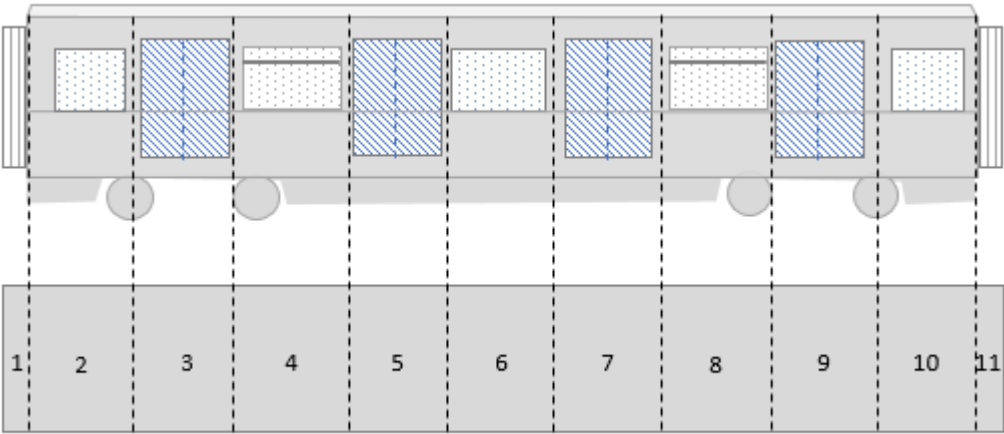
Figure 8.3. The division of the interior space.
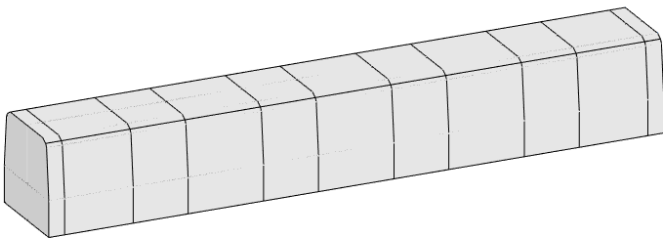
Figure 8.4. 11 subsystem SEA model for train interior noise.

Table 8.1. Length and volume of each subsystem.

Subsystem	1	2	3	4	5	6	7	8	9	10	11
Length (m)	0.46	2	1.6	2.2	1.6	2.2	1.6	2.2	1.6	2	0.46
Volume (m^3)	2.576	11.2	8.96	12.32	8.96	12.32	8.96	12.32	8.96	11.2	2.576

It is also required that in an SEA model in each subsystem the modal overlap should be greater than 1. Again, the modal overlap in each subsystem is also calculated. Subsystems 1 and 11 have the minimum volumes, the modal overlap in these two subsystems is greater than 1 above the 630 Hz band. For the other subsystems the modal overlap is above 1 from the 250 Hz band.

To use the SEA method, another criterion, more than five modes in each subsystem in each one-third octave band, is required. The number of modes in a volume below frequency f is calculated by [112]

$$N_i = \frac{4\pi}{3}V_i\left(\frac{f}{c_0}\right)^3 + \frac{\pi}{4}S_i\left(\frac{f}{c_0}\right)^2 + \frac{L_i}{8}\left(\frac{f}{c_0}\right)^1 \tag{8.2}$$

where V_i is the volume, S_i is the total surface area and L_i the total edge length of each subsystem. The number of modes in each frequency band is the difference between the number of modes at the upper and lower band limit of frequency. Most subsystems have more than five modes above from the 160 Hz band. Subsystems 1 and 11 have the smallest volumes and they do not satisfy the criteria until the 250 Hz band. Considering the modal overlap factor and modes number in each subsystem, the SEA model is applicable above 250 Hz (including the 250 Hz band).

The energy balance for each subsystem is explained in Chapter 3. It is expressed in matrix form

$$[\mathbf{P}] = \omega[\mathbf{\eta}][\mathbf{E}] \tag{8.3}$$

where the power input from the outside area of the train to the internal SEA subsystems can be written in a vector form $[\mathbf{P}] = [P_{\text{in},1} \quad \cdots \quad P_{\text{in},N}]^T$; this will be discussed later in sections 8.3~8.5 in this chapter. $[\mathbf{E}] = [E_1 \quad \cdots \quad E_N]^T$ is the vector of the energies stored in the system. Assuming there is no coupling between two unconnected subsystems, the loss factor matrix is given by

$$[\mathbf{\eta}] = \begin{bmatrix} \eta_1 + \eta_{12} & -\eta_{21} & \cdots \\ -\eta_{12} & \eta_2 + \eta_{21} + \eta_{23} & -\eta_{32} & \cdots \\ \vdots & \vdots & & \cdots \end{bmatrix} \tag{8.4}$$

where η_i is the dissipation loss factor and η_{ij} is the coupling loss factor. The expressions for them are given in Chapter 3. The values of the parameters such as the dissipation and coupling loss factors are based on the particular design of train that is studied. In the absence of partitions between adjacent subsystems, the transmission coefficient can be set to 1 [73]. To calculate the dissipation loss factors, the absorption coefficients of the surfaces in each subsystem are required. In this work, the average absorption coefficient in the train is determined from the measured reverberation time, using the Sabine formula $\overline{\alpha} =$

$55.26V/(c_0 T_{60} S)$ [51], (with V, the total volume of the train cabin; T_{60} the reverberation time; S the total internal surface area). By doing so, the same absorption coefficient, obtained by treating the whole interior as a single volume, is used for every subsystem. The reverberation time was measured by UPV [87] and the measurements are explained in **Appendix B.4**. This and the average absorption coefficients are shown in Figure 8.5. Then the dissipation loss factors and the coupling loss factors are calculated straightforwardly following Equations (3.11) and (3.12).
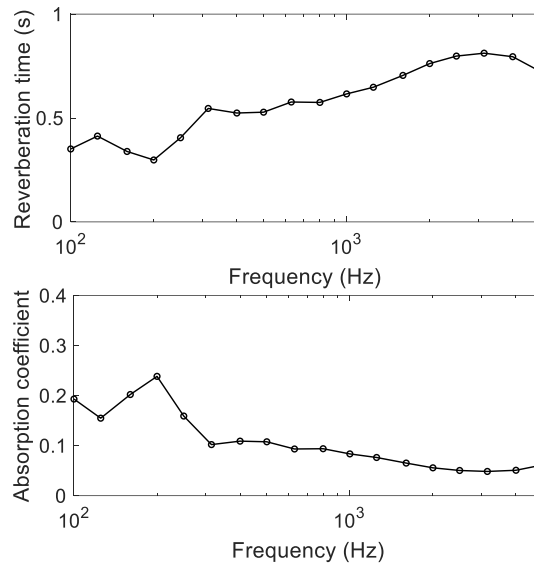
Figure 8.5. Reverberation time and absorption coefficient of the interior cabin. Measured by UPV.

By inversion of the loss factor matrix in Equation (8.3), the stored energy in each subsystem in the train cabin is obtained. The sound pressure levels in each subsystem are calculated as:

$$L_{p,i} = 10\log_{10}\left(\frac{\rho c_0^2 E_i}{V_i} \bigg/ {p_{ref}}^2\right) \tag{8.5}$$

where p_{ref} is the reference sound pressure, 2.0×10^{-5} Pa.

8.3 Calculation of the sound incident on the metro train floor

As discussed in Chapter 3, in this environment the total sound power incident on the underside of the train can be expressed as the sum of a direct and a reverberant component [24]

$$W_f = W_{dir} + W_{rev} \tag{8.6}$$

The direct and the reverberant components of sound power incident on the train floor can be calculated by following the procedure developed in Chapter 3. The configuration of the train floor studied here is shown in Figure 8.6, which indicates the division into subsystems used for the SEA model of the underfloor space. To make it simpler, the gap between the equipment in subsystems 3 and 4 is ignored, see Figure 3.21. The geometrical parameters used to create the SEA model of the underfloor space are given in Table 8.2.
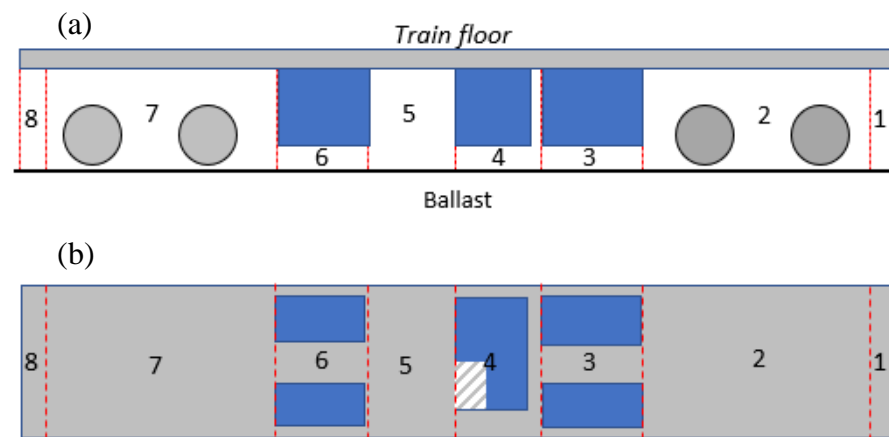
Figure 8.6. Subdivision of the space below the vehicle. (a) Side view, (b) top view.

Table 8.2. Geometry information of each subsystem for the SEA model beneath the train.

Subsystem	1	2	3	4	5	6	7	8
Length (m)	0.46	4.97	1.91	1.67	1.20	2.24	5.06	0.46
Side area (m^2)	0.49	4.74	0.74	0.67	0.48	0.89	4.84	0.49
Volume (m^3)	1.55	17.00	3.60	1.77	4.03	4.04	17.01	1.55
Interface area* (m^2)	3.36	1.88	1.06	1.06	1.88	1.88	3.36	

*Interface area refers to the connecting area between two adjacent subsystems.

After the sound power incident on the train floor has been calculated, in order to calculate the power input to the interior SEA model, they are reallocated to 11 components according to the subdivision of the interior SEA model in Figure 8.3 and the floor area in each subsystem indicated in Figure 8.4.

8.4 Calculation of the sound incident on the metro train side/roof

As discussed in Chapter 4, the sound power incident on the train side and roof can be calculated by using the 2.5D BE method. The corresponding 2.5D BE models are illustrated in Figure 4.26. The train being studied in this work had fairings along the sides of the train below the floor except in the bogie area, which can be seen in **Appendix B**. As a compromise, fairings are not included in the 2.5D model used to calculate the wheel contribution but they are included for the models representing the rail and sleeper contributions.

The sound pressure on the train external surfaces due to the track was calculated based on a unit force applied to the rail. That due to the wheel was based on monopoles and dipoles with a unit source strength. The results were then adjusted using the sound power obtained from the TWINS model. The total sound pressure (overall) on the train external surfaces due to rolling noise is shown again in Figure 8.7 based on the contribution of the two bogies beneath this carriage and the closest bogie beneath the adjacent carriage on either side (four bogies were considered).
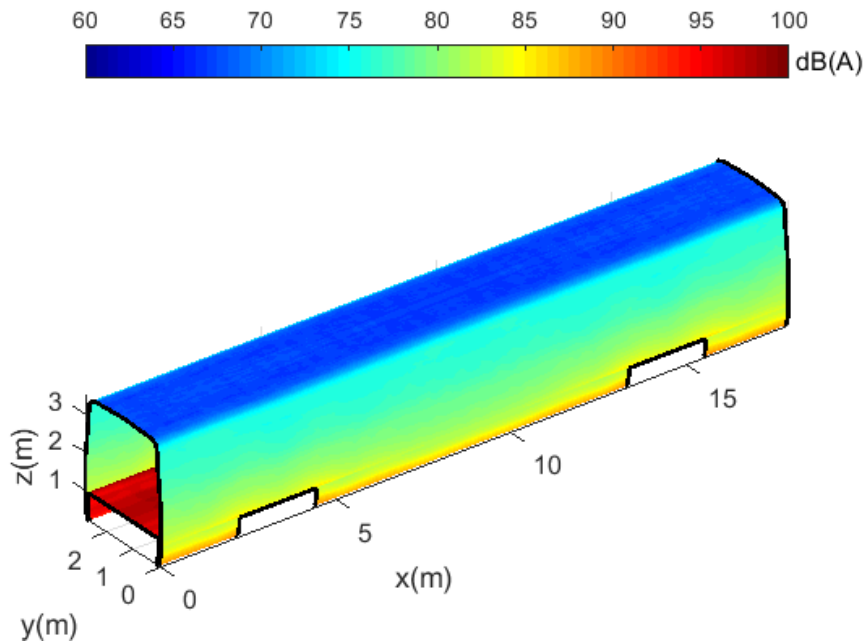
Figure 8.7. Sound pressure levels on the train external source due to four bogies.

The power incident on the side surfaces of the train is estimated from the corresponding sound pressure. The external sound field is not diffuse in practice except in a tunnel, but it is difficult to identify the incident angles associated with the sound field. Therefore, in this

work it is simply assumed that a diffuse incident field exists outside the train. For a diffuse sound field, the sound can be incident from any direction with equal probability. The total incident sound power per unit area is found by integrating all possible incident directions over a hemisphere, which will introduce a factor of 1/2. In this work, it is therefore assumed that the sound power on the train external surfaces caused by a diffuse incident field is half of that by a normal incident one (assuming the sound from different incident angles is identical). The power incident on the train external surfaces is then calculated by

$$W_s = \frac{1}{2} \int_S \frac{p_{tot,rms}^2}{4\rho_0 c_0} ds \tag{8.7}$$

where $p_{tot,rms}$ is the rms sound pressure incident on the train external surfaces due to rolling noise. The factor 1/4 is included in the integral because the sound pressure on the train external surfaces is doubled on a rigid surface whereas the incident power relates only to the incoming sound waves. The factor 1/2 outside the integral allows for a diffuse incident field assumption.

8.5 The sound power transmitted to the metro train cabin

During the measurement campaign [87] the sound transmission losses of the train floor and wall structures were measured by UPV and Vibratec by adopting portable sound sources inside the vehicle and a sound intensity probe to scan the outer surfaces. The incident intensity on the panels is deduced from the mean acoustic pressure level inside the coach using a diffuse field assumption. The transmitted intensity is measured by scanning the outer skin of the coach with the intensity probe. In the transmission coefficient measurement, the intensity on sections of the train floor, the doors, the side walls (aluminium part), the windows (glass part) and the gangway were measured individually, see Figure 8.8. The transmitted power (the power input to the SEA model) is then calculated from the sound powers incident on the exterior of these surfaces, multiplied by their individual measured transmission coefficients[4].

---

[4] The values of the transmission coefficients are confidential to the train manufacturer.
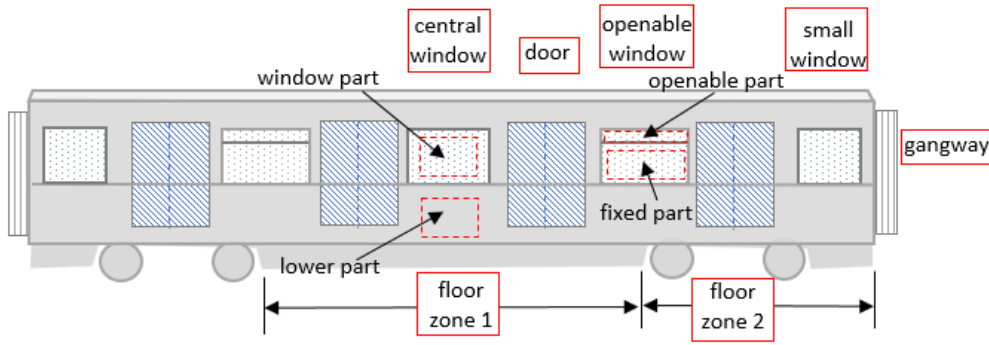
Figure 8.8. Definition of the panels.

The input power (per subsystem) to the interior SEA model then obtained as

$$P_{in,i} = W_{f,i}\tau_{f,i} + W_{s,i}\tau_{s,i} \tag{8.8}$$

where W_f and W_s are the incident power on the external train floor and sides, τ_f and τ_s are their corresponding transmission coefficients. The subscript i indicates the surface area involved in the ith subsystem. Different panels in Figure 8.8 have different coefficients, so the incident sound power and the transmission coefficients for different panels are dealt with separately and they are added together when calculating the input power for each subsystem.

The incident sound powers on the train sides, floor and gangway area are illustrated in Figure 8.9(a). The sound power transmitted through the three components are compared in Figure 8.9(b). The largest sound power is the one incident on the floor. The sound powers incident on the sides and gangway are similar to each other (the gangway area is small, but it has direct sound) and they are much lower than that on the floor. The power transmitted through the gangway is significant which is due to its higher sound transmission coefficient.
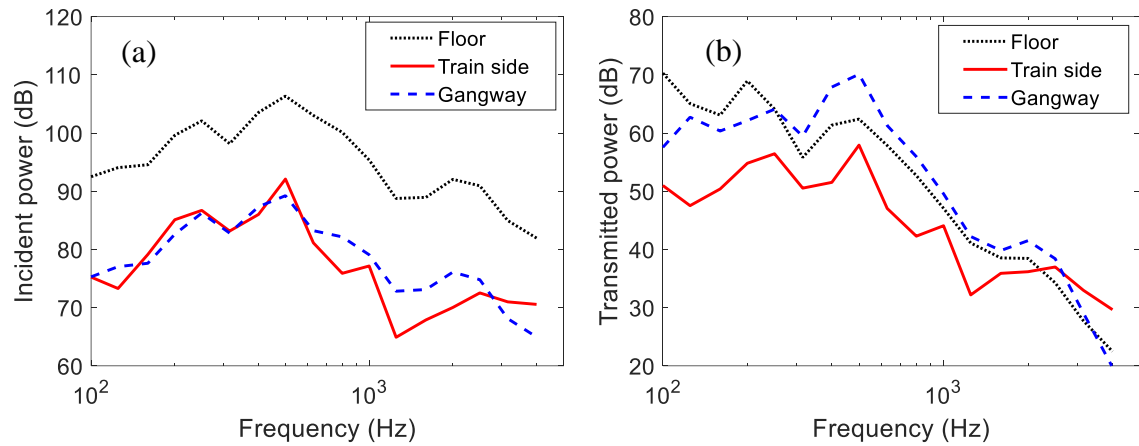
Figure 8.9. (a) Incident sound power, (b) transmitted sound power. Sound power levels in dB re 10^{-12} W.

8.6   Sound distribution in the cabin

The averaged sound pressure level inside the train is then calculated by using the SEA model introduced in Section 8.2. The sound distribution in the train cabin is illustrated for four example one-third frequency bands in Figure 8.10. The sound pressure levels at the ends of the carriage are higher than those in the middle. This can be explained by the fact that the bogies are located at the ends of the carriage, and also that the gangway has a lower sound transmission loss than other panels.
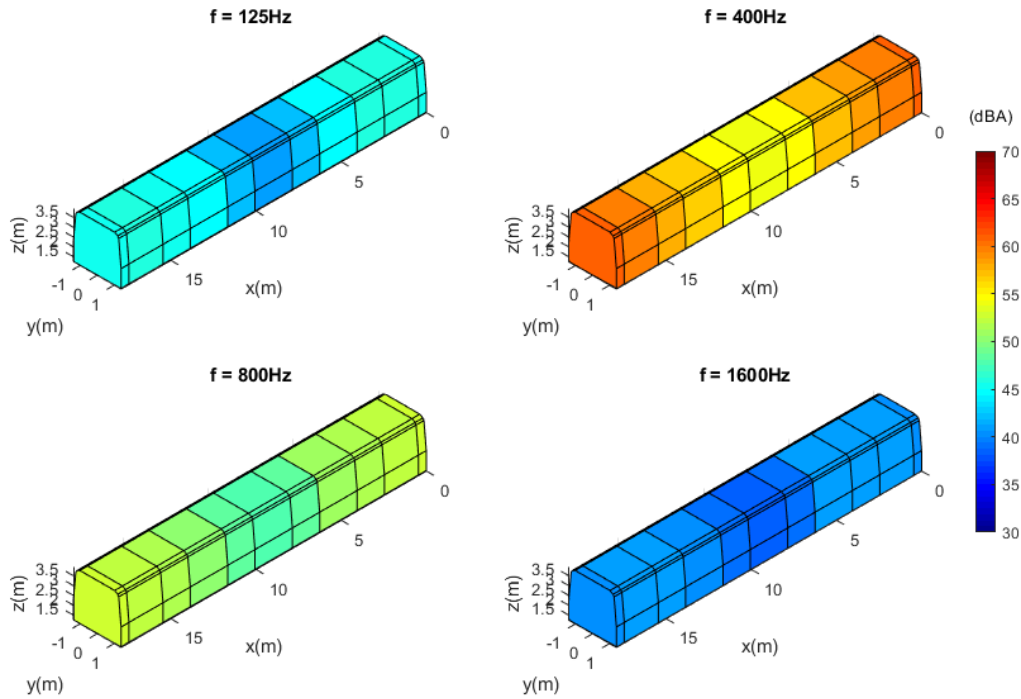
Figure 8.10. A-weighted sound pressure distribution in the train cabin in four example one-third octave frequency bands.

Sound pressure levels in each subsystem in the cabin are plotted in Figure 8.11 for different one-third octave frequency bands (actual values for all interior SPL are not shown for confidentiality reasons). The decay rates of sound along the carriage are various in different frequency bands. The sound pressure levels decay more quickly below 1000 Hz than above this frequency. For example, in the 125 Hz band, the sound decays by about 5 dB from the end to the middle of the carriage whereas between 400 Hz and 800 Hz the decay is about 8 dB. Above 1000 Hz the decay is only about 2 dB. The low decay of sound inside the train cabin at high frequency can be explained by the low absorption coefficients in the cabin at these frequencies and also the low decay rate of the vibration of the rail. The low decay rates of the rail vibration result in a more evenly distributed incident sound power on the train external surfaces, while at the same time, the low absorption coefficients in the train cabin lead to a more reverberant sound field, which results in the low decay of sound pressure levels along the train axis in the cabin at high frequency.
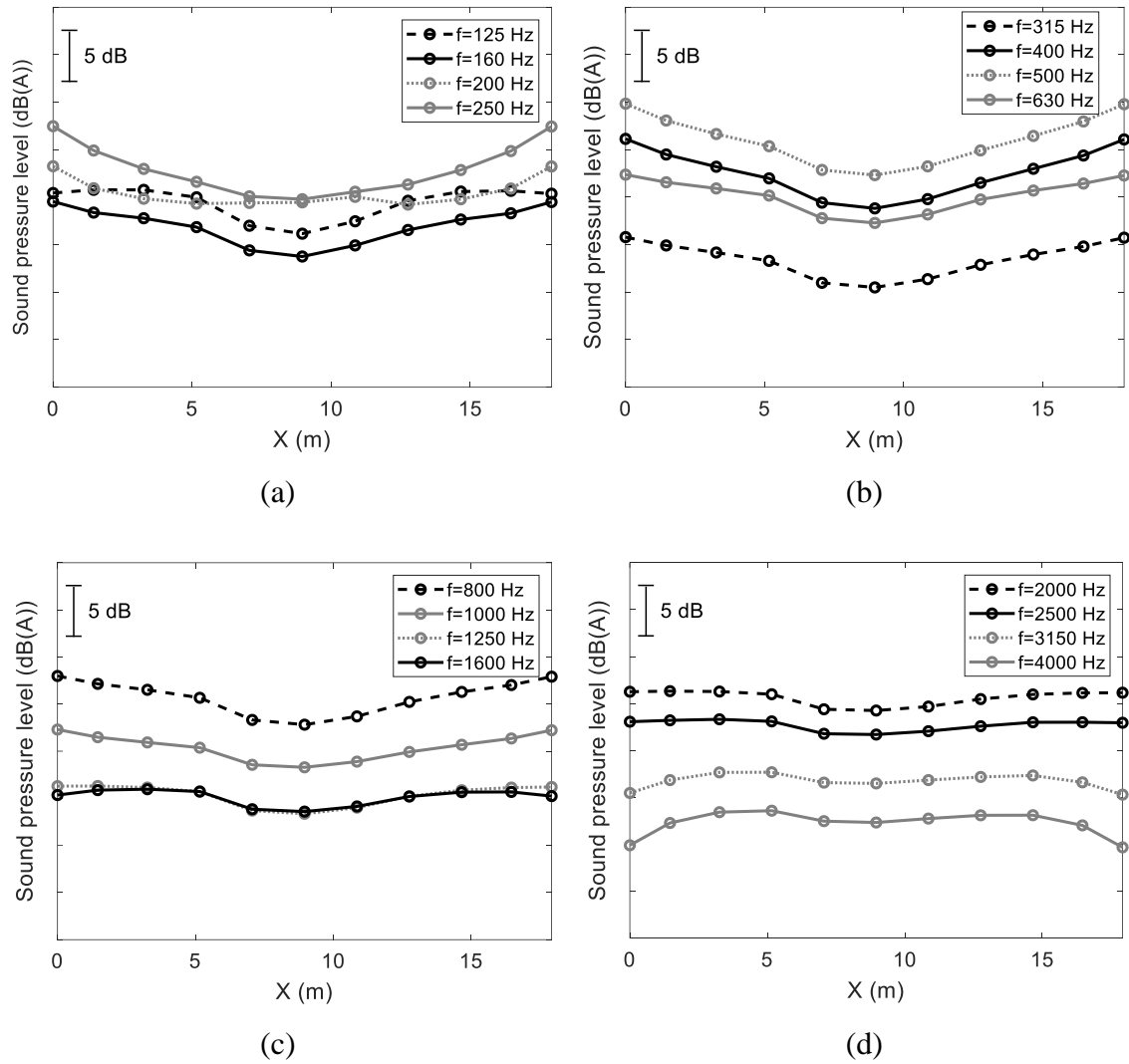
Figure 8.11. Sound pressure level distribution along the cabin axis.

The sound spectra and the contributions of the three noise components, the wheel, the rail and the sleepers, to the total sound pressure at two positions inside the train cabin are illustrated in Figure 8.12. In terms of sound pressure levels, it is concluded that the (A-weighted) sound pressure levels at low and high frequency are relatively low compared with those in mid frequency range. In terms of contributions, it is found that the different sources have similar relative contributions at the two positions. The sound radiation from the sleepers contributes the most to the interior noise below 315 Hz; the rail becomes dominant between 400 Hz and 2000 Hz; the power from the wheel is significant above 2500 Hz. Because of the presence of the equipment mounted beneath the train, there is no direct sound from the wheel to the middle region of the train floor. The direct sound from the rail is mainly incident on the bottom surfaces of the equipment in the middle region. The sleepers could be generally considered as a local source located in the bogie region. Consequently, the sound power incident on the train floor in the middle region is mainly from the reverberant sound

beneath the train floor. As seen above in Figure 8.11, the interior sound pressure levels in the middle region of the carriage are lower than those at the ends of the carriage because they are further from the source location.

(a)　　　　　　　　　　　　　　　　(b)
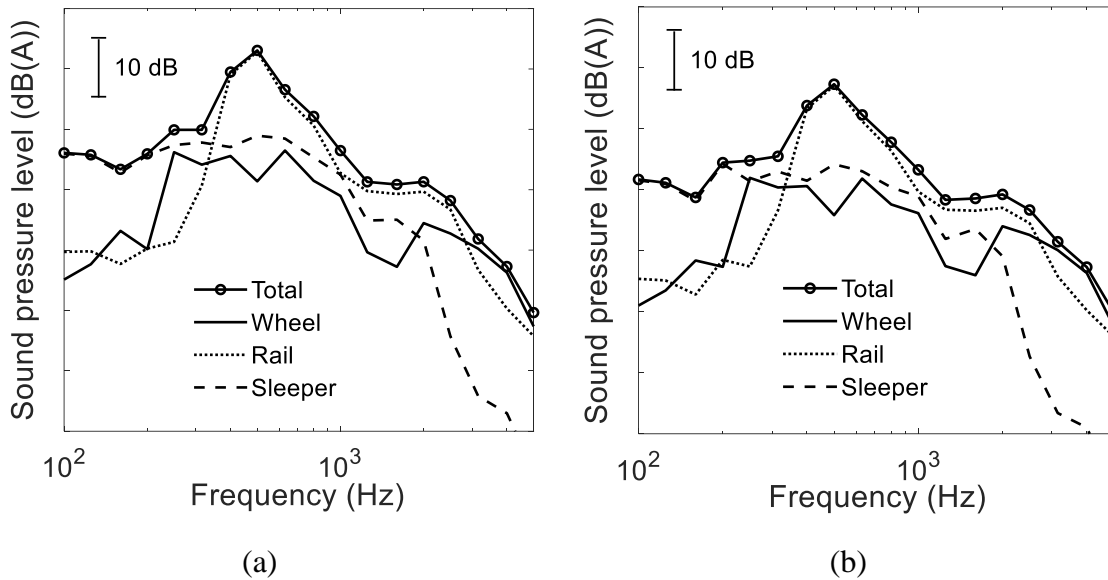
Figure 8.12. Sound pressure level showing contributions from wheels, rails and sleepers, (a) end of the carriage, (b) middle of the carriage.

8.7　Effect of increasing the number of subsystems in the SEA model

To investigate the validity of the subdivision of the SEA model, the train cabin is divided to 44 systems. Each subsystem from the previous SEA model (see Figure 8.4) is divided into four smaller ones by dividing them in the vertical and lateral axes, see Figure 8.13.
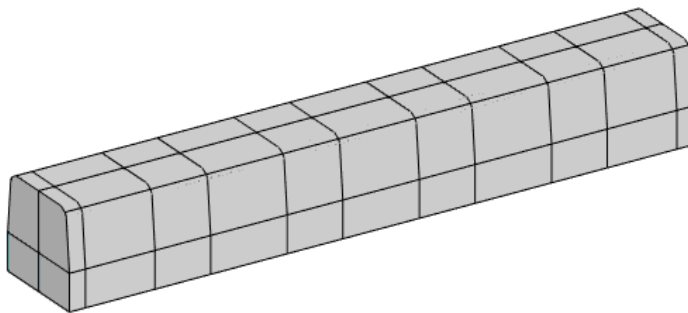
Figure 8.13. 44 subsystems SEA model.

Now to meet the requirements for using the SEA method, most of the 44 subsystems have more than five modes from the 250 Hz band except the subsystems at the two ends for the gangway region which satisfy the criterion from the 400 Hz band. The modal overlap in most subsystems is greater than 1 from the 630 Hz band. The 44 subsystem SEA model is therefore applicable from the 630 Hz band and above. The power input to each system is separated into four according to the corresponding exterior surfaces from the previous case. Figure 8.14 gives the sound distribution in the subsystems in example frequency bands (125 Hz, 400 Hz, 800 Hz and 1600 Hz). In each case the two subsystems in the upper layer are identical to each other, and the same is true for the two in the lower layer. The sound pressure levels along the train cabin from the upper layer and the lower layer are plotted in Figure 8.15. At the end of the carriage, the sound pressure level from the lower subsystems (close to the train floor) is higher than that from the upper subsystems. In the middle of the carriage, there is no noticeable difference between the two layers in terms of sound pressure level. The sound pressure levels obtained from the average of the mean-square pressures is also shown in Figure 8.15, indicated by the red curve with cross marks.
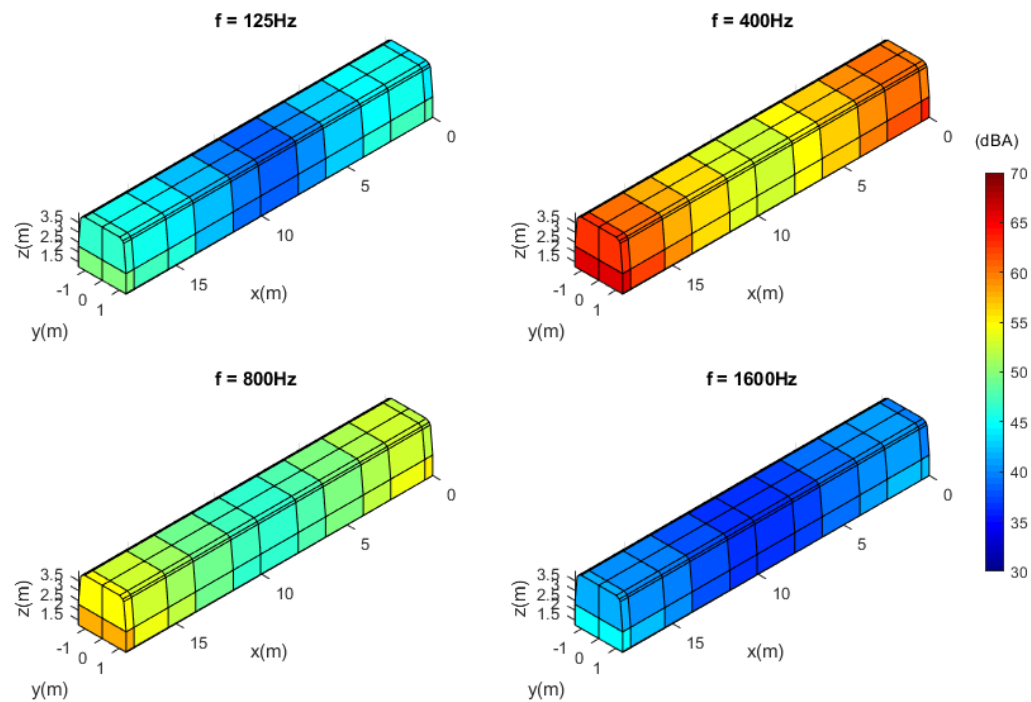
Figure 8.14. Sound pressure level distribution along the cabin axis from the 44 subsystems SEA.
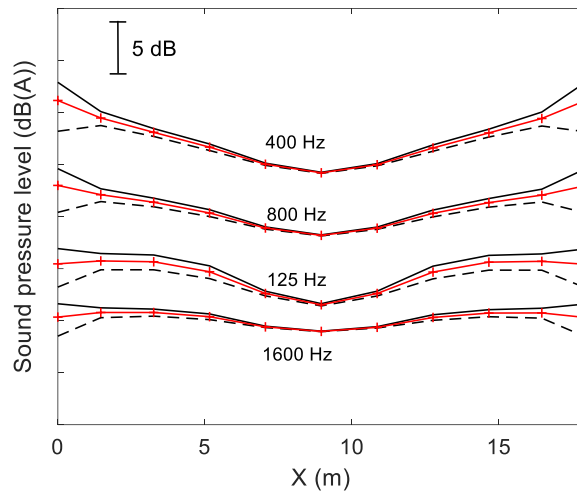
Figure 8.15. Sound pressure levels along the train cabin from the 44 subsystem SEA model. ——: from the lower subsystems; – – –: from the upper subsystems; —✳—: average results.

The predictions of the sound distribution along the train axis from the 44 subsystem SEA model (averaged results) are compared with the previous predictions from the 11 subsystem SEA model in Figure 8.16. The carriage and the sound source are symmetric about the train's centre vertical plane. The sound incident from its left side and that from its right side are identical, thus dividing the cabin into more subsystems will not improve the predictions significantly. The sound pressure levels predicted by the 44 subsystem SEA model are similar to the previous ones. For simplicity and because the measurements were only made at a single height which is near the middle, the previous 11 subsystem SEA model is used to compare with the measured data and to investigate the influence of dissipation loss factors on interior noise in the rest of this Chapter.
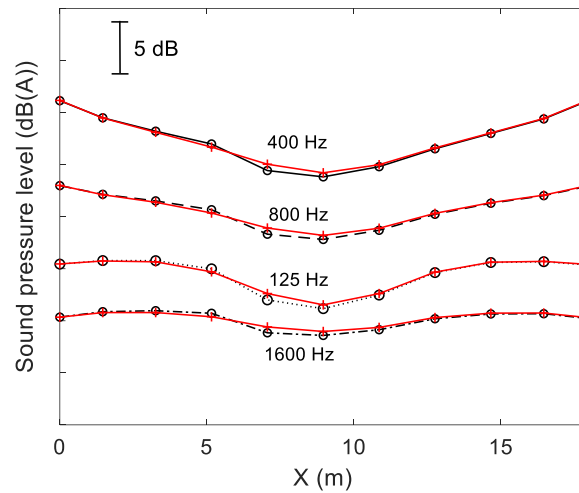
Figure 8.16. Comparison of the sound pressure level distribution along the cabin axis between the two SEA models. Lines marked with circle are from the previous SEA, Lines marked with cross are from the 44 subsystem SEA, ⋯●⋯: 125 Hz band; ━●━: 400 Hz band; ‑ ● ‑: 800 Hz band; ‑·●·‑: 1600 Hz band.

8.8　Experimental validation

Figure 8.17 shows the measurements of sound pressure inside the vehicle and Figure 8.18 shows the interior microphone positions. More details can be found in **Appendix B.5**. Five positions were measured on the centre line of the carriage at 1.5 m above the floor. Along the train axis direction, Point 2002 is in the middle of the two adjacent carriages, Point 2004 is right above the trailer bogie and Point 2006 is in the middle of the carriage. Point 2003 is between Points 2002 and 2004 and Point 2005 is between 2004 and 2006. The vehicle was running at 50 km/h during the tests.
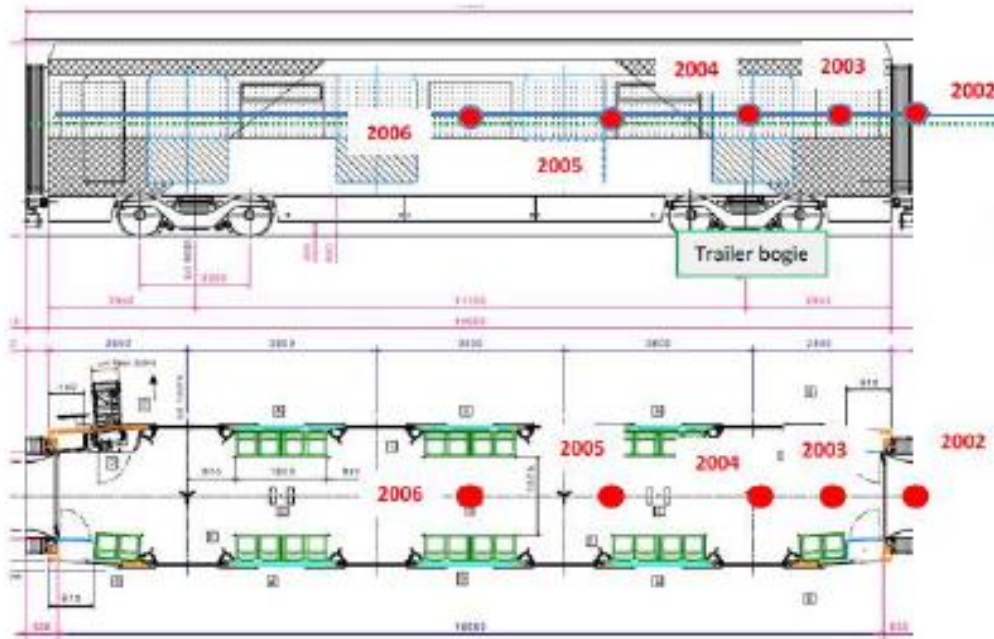
Figure 8.17. Experimental set up for interior noise measuring [87].

Figure 8.18. Measurement of interior noise. (a) Microphones 2002, 2003, (b) microphones 2004, 2005, and 2006. Photos: Polytechnic University of Valencia.

Here it should be noted that only the airborne noise inside the vehicle is considered in this work. From [87] the measurements indicated that the structure-borne noise is only important at low frequency and it decreases with increasing frequency, see Figure 8.19. Above 500 Hz, the structure-borne noise decreases rapidly to negligible levels. The comparison of the airborne and structure-borne noise associated with this vehicle shows that ignoring the structure-borne noise will only slightly affect the accuracy below 160 Hz.
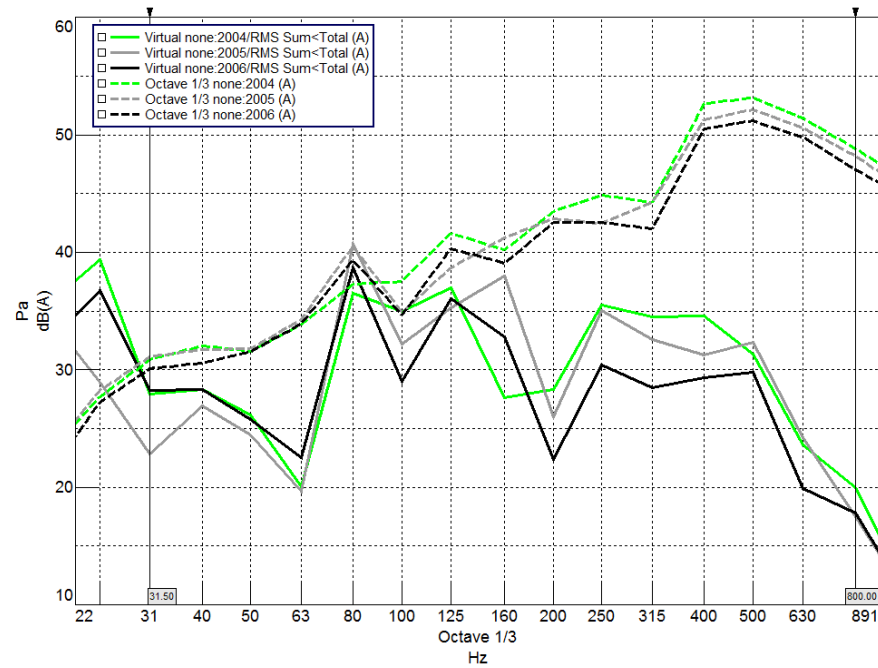
Figure 8.19. Structure-borne contribution to total interior noise for microphones 2004-2006 (based on experimental data, solid lines indicate structure-borne noise in the train cabin, dashed lines indicate total noise in the train cabin) [87].

The predictions of the noise inside the vehicle obtained by using the SEA model are compared with the measurements in Figure 8.20. The predictions capture the main trend of the sound spectrum in comparison with the measurements below 2 kHz. Their overall sound pressure levels and the relative errors are listed in Table 8.3. The difference in terms of overall sound pressure levels is around 2~3 dB. There is a peak in the measured sound pressure levels in the 3150 Hz band in some locations, especially position 2004. This is not present in the measured sound pressure levels beneath the train and on the train side surfaces. It is therefore believed that this is due to other interior noise sources.
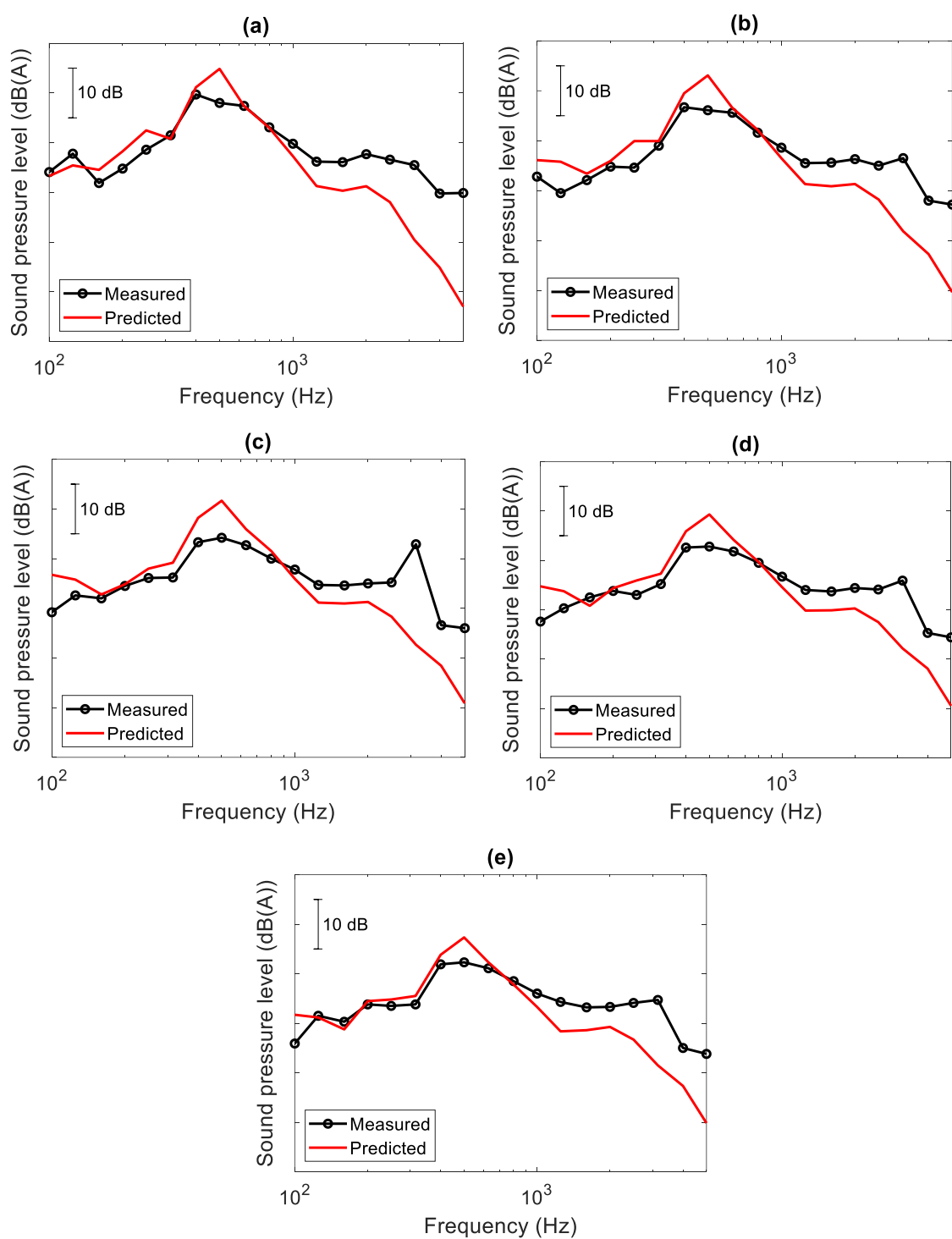
Figure 8.20. Comparison between predictions and measurements in terms of sound pressure levels in the train, (a) point 2002, (b) point 2003, (c) point 2004, (d) point 2005, (e) point 2006.

Table 8.3. Difference in overall sound pressure levels inside the train (dB(A)).

	Point 2002	Point 2003	Point 2004	Point 2005	Point 2006
Prediction−Measurement (dB(A))	2.1	2.8	3.2	2.9	1.9

Figure 8.21 shows the comparison of sound pressure distribution along the train cabin between the predictions and the measurements. Sound pressure distribution in three one-third octave frequency bands, 160 Hz (low frequency), 800 Hz (mid frequency), 1600 Hz (high frequency), and the overall sound pressure distribution are shown as examples. There are some differences in sound pressure levels but the predictions and the measurements have similar trends.
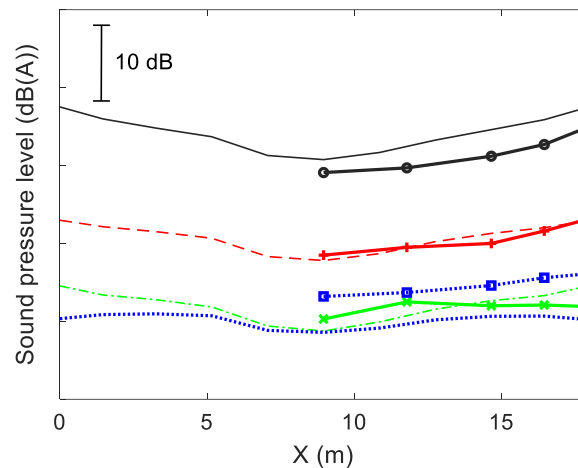
Figure 8.21. Comparison of sound decay along the train between predictions and measurements. −·−·: 160 Hz, SEA; − − −: 800 Hz, SEA; ·········: 1600 Hz, SEA; ⸺: Overall, SEA, ⸺✕⸺: 160 Hz, measured; ⸺+⸺: 800 Hz, measured; ···■···: 1600 Hz, measured; ⸺●⸺: Overall, measured.

From Figure 8.20 and Figure 8.21, it can be seen that the predicted spectra are similar to the measured ones at low frequency. Some errors appear in the 500 Hz band. This comes from the rail noise (see Figure 8.12) which has been calibrated by exterior SPL measurements but the sound incident on the surfaces may be different (e.g. it may have a different directivity to what has been assumed). The over-prediction of sound pressure in the 500 Hz band has also been found in Figure 3.24 and Figure 4.28. It seems the error in the exterior pressure has propagated to the interior. Besides, some differences appear at high frequency. Apart from the possibility that additional exterior and interior noise sources were present that have not been allowed for, there are other assumptions in the SEA model that might cause the discrepancies. For instance, the sound incident on the train external surfaces is calculated based on the assumption of a diffuse incident field. An average absorption coefficient was calculated from the measured reverberation time, while in reality different surfaces have different absorption. Also, the measured STL is likely to be inaccurate at high frequencies.

8.9   Influence of dissipation loss factor on the interior noise

8.9.1   Doubling/halving loss factors

The absorption inside the train cabin is important for the interior noise and it could be modified to control the noise. To test how the change of the absorption will affect the interior noise distribution, the original dissipation loss factors inside the train cabin are halved or doubled in the model. The sound distribution inside the train with different dissipation loss factors η_i is illustrated in Figure 8.22 for four example frequency bands.

Figure 8.22. Sound level spatial distribution for different absorption, (a) 125 Hz, (b) 400 Hz, (c) 800 Hz, (d) 1600 Hz.

It is found that the sound spatial distribution as well as the overall level is sensitive to the absorption in the train cabin, especially the sound pressure level in the middle. When the dissipation loss factors in each subsystem are halved or doubled, the sound pressure levels are not just increased or decreased by 3 dB. Instead, the change of sound pressure levels is less than 3 dB at the ends of the carriage and greater than 3 dB in the middle. When the loss factor is halved, the spatial decay of the sound along the carriage is lower while it is higher for a doubled loss factor. This is because the power input to the cabin is mainly in the bogie regions and the ends of the carriage. For a low loss factor, a more reverberant sound field is generated in the cabin leading to a more even spatial distribution. Conversely, for a high interior loss factor, the sound decays more rapidly along the carriage.

8.9.2 Effect of people

The running tests were for an empty train. In a more realistic situation, the additional absorption of passengers should be considered. The information on absorption of passengers is rather limited. Adelman-Larsen et al. [113] measured the absorption of a standing audience in a rock concert hall with a density of about 2.7 people per square metre. They are shown in Figure 8.23, along with coefficients for a seated audience in a classical concert hall with a density of about 2 person/m^2 from Meyer et al. [114]. The absorption coefficients are defined as per floor area. The absorption coefficients are greater than 1 in some frequency ranges. This can be attributed to the fact that an audience is not a simple two-dimensional surface. Therefore, the effective absorption area of an audience is larger than the area they cover on the floor. The data shows that the absorption coefficients of the audience are close to the absorption coefficients of the train at low frequency. But they are six to eight times higher than the absorption of the train in the mid-high frequency bands.
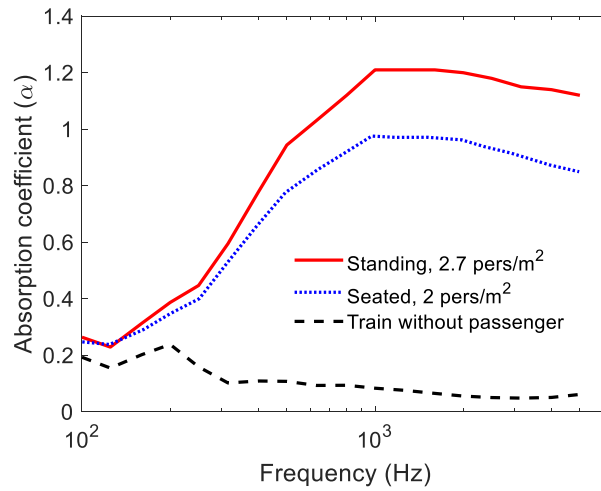
Figure 8.23. Absorption coefficients (per floor area) for passengers based on data for audience. Standing people with a density of about 2.7 people/m^2 from [113] and seated people with a density of 2 people/m^2 from [114]. Absorption of the train, measured by UPV [87].

It can be assumed that similar results can be applied to the interior of a train. The seated audience in a classical concert with a density of 2 people/m^2 corresponds to about 95 passengers seated in the train cabin considered in this work (the metro train was 2.8 m wide by 17 m long). Compared with classical concerts, audiences at rock concerts are usually standing and more densely packed, similar to passengers standing in a metro train. It is assumed that the passenger density in a fully loaded metro train is like that in a rock concert, about 2.7 people/m^2. It corresponds to a fully loaded metro train with 128 standing passengers in each carriage according to the train floor area. In practice, there will be complex diffraction effects between and around passengers and a reduction in the effective acoustic volume inside the train cabin, which are ignored in this work.

From Figure 8.17, the metro vehicle in the test had about 30 seats. It is first assumed that 24 people are seated in that vehicle. Based on the density of 2 people/m^2 an area of 12 m^2 is associated with the absorption of the seated passengers. Alternatively, 24 people standing in the train cabin are considered, which for standing people with a density of 2.7 people/m^2 will be associated with an area of 8.9 m^2. It is found that the two situations are very similar in terms of interior noise. The sound distribution along the train for the two situations are shown in Figure 8.24. Either 24 people seated or standing in the train will not decrease the sound in the train significantly at low frequency, for example, in the middle of the carriage there is a reduction of about 0.7 dB in the 125 Hz band and 1.0 dB in the 400 Hz band. However, the

decreases at high frequency are more noticeable, sound pressure levels in the middle of the carriage decreased by 2.0 dB in the 800 Hz band and by 2.6 dB in the 1600 Hz band.

An extreme situation, peak time in traffic, is also considered. It is assumed that the metro train is fully loaded with 128 standing people. With the dissipation loss factor of the floor modified to account for the presence of fully loaded passengers, the sound distribution in the train cabin along the axis is shown in Figure 8.24. The passengers do not make a significant difference to the sound distribution in the cabin at low frequency as well because the absorption is not increased much. However, at high frequency the presence of passengers increases the absorption inside the train, leading to a less reverberant sound field. As a consequence, the sound pressure level in the middle of the carriage decreased by 7.1 dB for the standing case in the 400 Hz band, by 9.6 dB in the 800 Hz band, and by 10.2 dB in the 1600 Hz band.

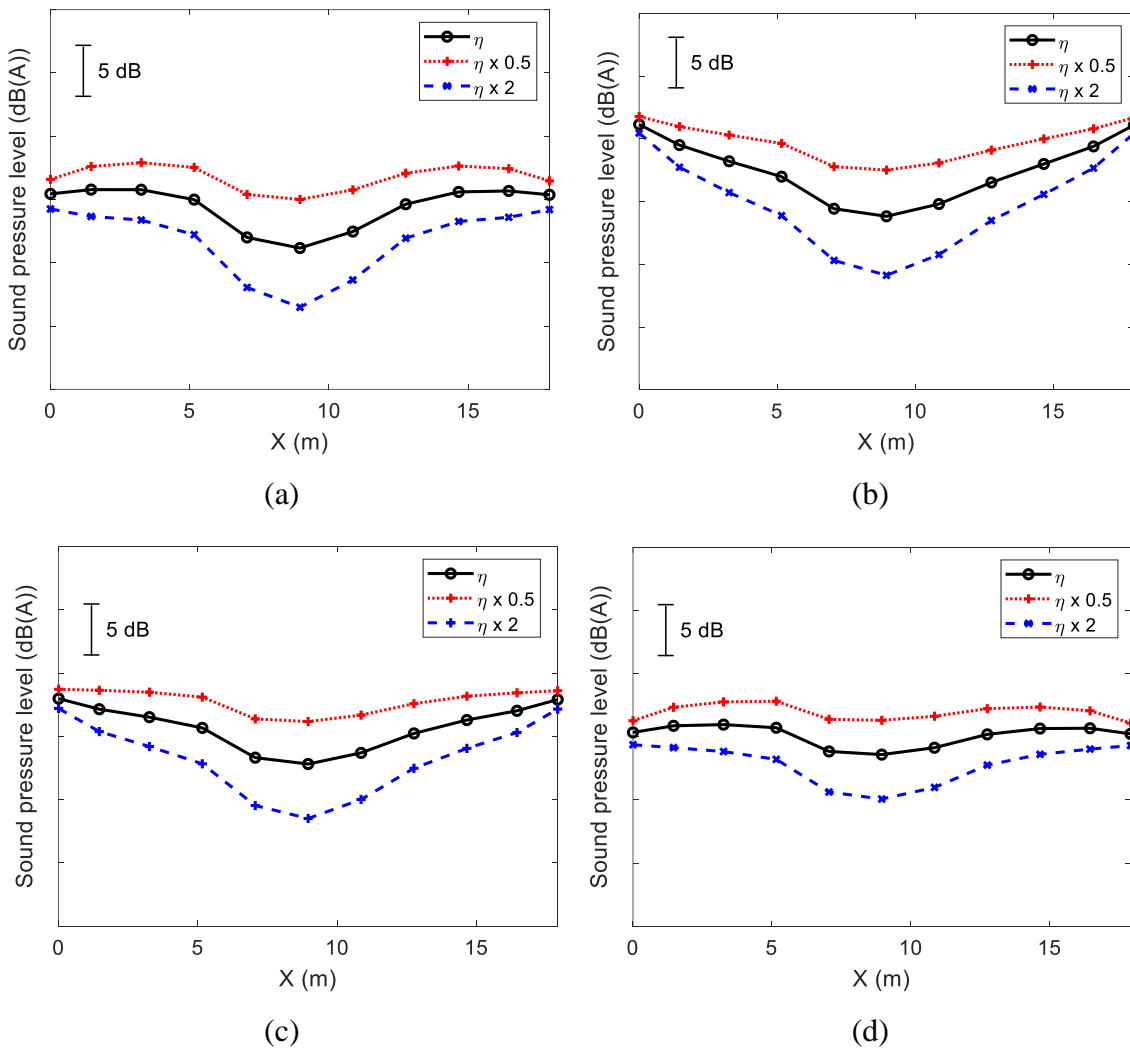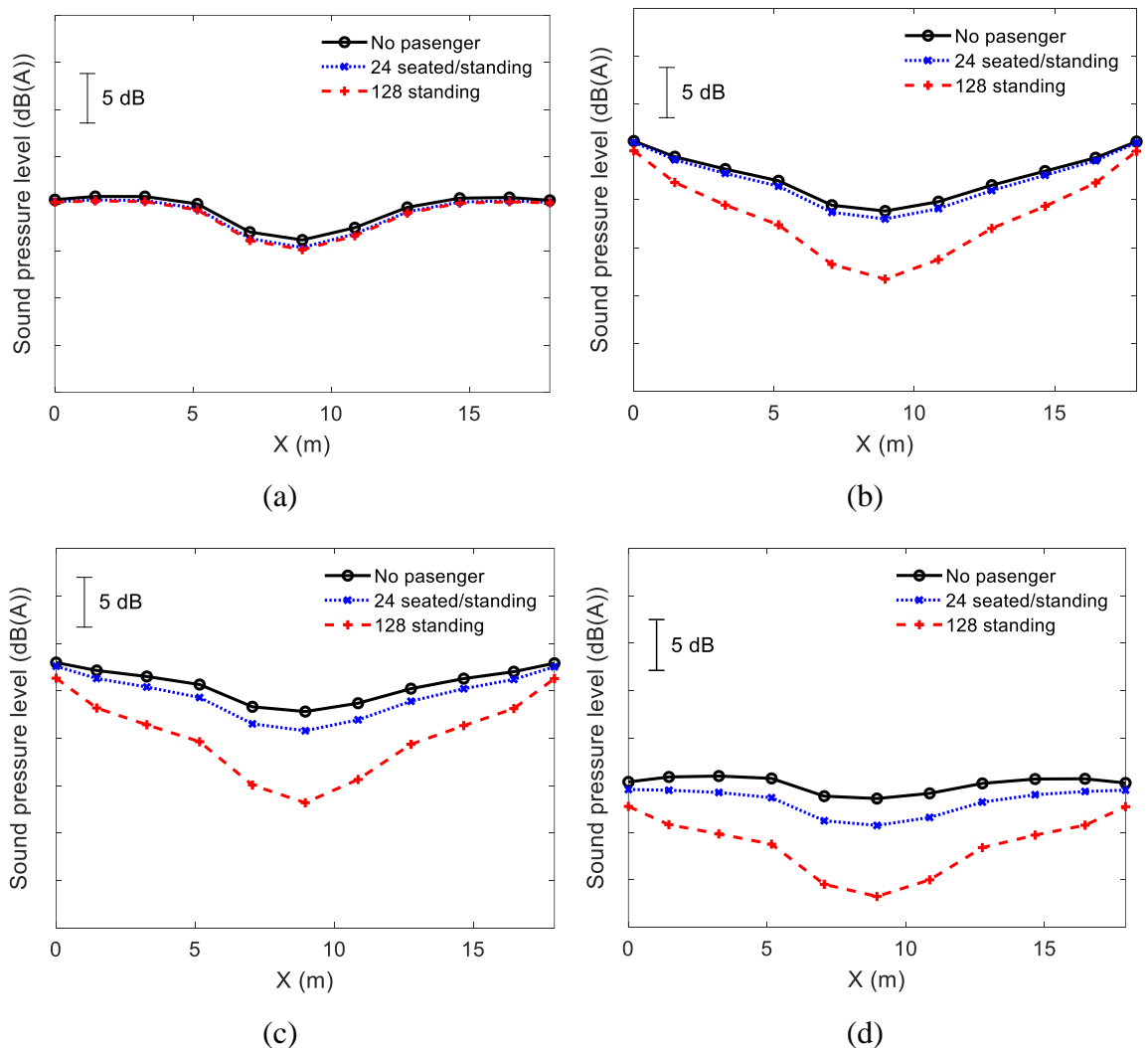
Figure 8.24. Sound level spatial distribution under different passenger load, (a) 125 Hz, (b) 400 Hz, (c) 800 Hz, (d) 1600 Hz.

The sound spectra in the train cabin at two locations are calculated and shown in Figure 8.25. It can be seen again that the passengers do not make a significant difference to the sound pressure level in the cabin at low frequency but lead to a considerable reduction of noise at high frequency. Also, the presence of the passengers provides a larger influence in the middle of the cabin than at the end. The overall sound pressure level at the end of the carriage decreases by 0.9 dB(A) for the 24 people seated/standing case and decreased by 2~3 dB(A) for the fully loaded case. In the middle of the carriage, the overall sound pressure level drops by 2.5 dB(A) for the 24 people seated/standing case and by 6~7 dB(A) for the fully loaded case.

(a) (b)
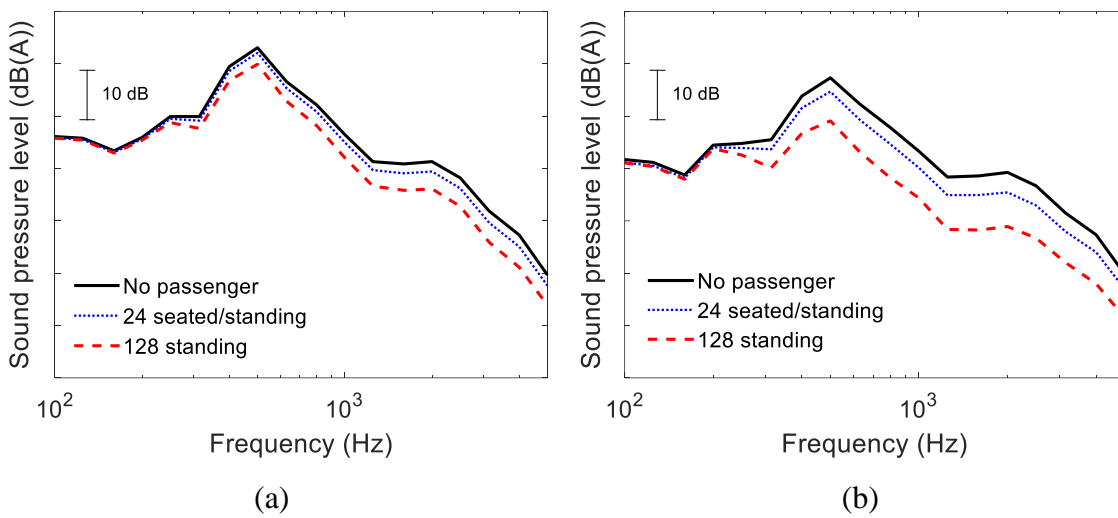
Figure 8.25. Sound pressure level at the (a) end of the carriage, (b) middle of the carriage.

8.10   Summary

In this chapter, a framework is described that can be used to predict the airborne noise inside a railway vehicle due to rolling noise. The interior noise is predicted by using an SEA model, the dissipation loss factors are determined by the measured reverberation time. The input power is calculated by combining the measured transmission loss of the train wall structures with the sound power incident on the train floor and sides. The latter is determined by using a combination of an equivalent noise source model and SEA for the under-floor area (Chapter 3), while the power incident on the sides is calculated by using a wavenumber domain boundary element method (Chapter 4). In the present chapter measured transmission losses have been used but the theoretical approaches described in Chapters 6 and 7 could also be used. Pantograph noise as considered in Chapter 5 could also be included using similar methodologies but is not relevant for the low speed considered in the case study.

The calculation procedure is applied to a metro train and the results show that the power incident on the floor is about 15-20 dB higher than that on the train sides and gangway. The sound power incident on the train sides and on the gangway are similar in level. For the case studied a large proportion of the power is transmitted into the train cabin from the gangway region, due to its lower sound transmission loss. The interior noise distribution shows that the ends of the cabin are noisier than the middle (6~7 dB(A) difference).

Existing field measurements of the sound below the vehicle, on the train side surfaces and inside the train cabin were used to validate the predictions from the models developed in this work. The comparisons show that the approach can give reasonable predictions of the interior noise.

Chapter 9   Conclusions and recommendations

The work presented in this thesis aims to create a comprehensive approach to combine the advantages of various existing methods to model the exterior noise sources, airborne transmission paths and the interior noise associated with running railway vehicles. The most important conclusions and several recommendations for future work are outlined in this chapter.

9.1   Conclusions

Rolling noise and aerodynamic noise are assumed to be the most significant noise sources associated with railway vehicles. To predict the noise inside a railway vehicle, rolling noise and the aerodynamic noise from the pantograph are considered in this work. The noise transmission through the train wall structures are investigated by using both the 2.5D FE/BE method and the SEA method with some essential parameters determined with assistance from the 2.5D FE calculation. The interior noise is predicted by using another SEA model.

The acoustical behaviour beneath the train floor has been thoroughly studied. It has both direct and reverberant sound parts because of the presence of the ballast and the equipment mounted on the train floor and the reflection and scattering of them. The sound pressure level due to the reverberant part is higher than that caused by the direct sound but the sound powers incident on the train floor from the two components are nearly the same. Measurements were carried out on a static 1:5 scale train model using an omindirectional source which showed good agreement with the sound pressure decay under the vehicle; differences are less than 1 dB on average.

Noise can also diffract from the edge of the fairings to the side surfaces of the train. A 2.5D BE approach has been developed to calculate the noise transmission from the wheel, rail and sleepers to the sound pressure on the external surfaces of a train. The sound level reduces with increasing height. The noise on the train roof due to the wheel and rail is less significant and is estimated to be around 30 dB lower than the noise impinging on the floor. Laboratory measurements have been carried out to validate the 2.5D BE models. The comparisons with the laboratory tests showed that the predicted sound pressure levels from the 2.5D model and the measured ones had a similar decay trend along the train axis direction and the average difference of the sound pressure levels between measurement and prediction was less than 3 dB.

Field measurements obtained in a recent EU project RUN2Rail (measured by UPV) have also been used to validate the predictive models for noise below the vehicle and for noise incident on the train sides. In terms of the noise beneath the vehicle, the sound pressure spectrum measured below the train floor was in reasonable agreement with the predictions, with overall sound pressure levels differing by less than 3 dB. In terms of noise incident on the train sides, the field measurements of sound pressure on a stationary train have shown that the predicted sound pressure distribution with the train height on the train sides was close to measured values. In the field measurement on a running train, the predictions and the measurements agreed well in terms of sound pressure spectrum and the overall sound pressure levels had less than 3 dB difference.

The noise from the components of the pantograph had previously been calculated by using computational fluid dynamics methods and a database of the parameters that can be used to predict the noise from these components had previously been built at the ISVR. They are employed in this work and the sound power of the pantograph has been calculated by using the component-based approach and that database. The 2.5D BE method has been used to model the noise propagation from the pantograph to the train external surfaces. The sound pressure level distribution on the train external surfaces from the 2.5D model shows that the pantograph noise is very high in a region that is quite localised directly below the pantograph. With increasing distance from the pantograph, the sound pressure level decreases rapidly due to the pantograph radiation directivity and geometric spreading. The simulation on the 1:5 scale train model shows that the difference between the sound pressure level on the train roof and sides is about 20 dB in the plane of the pantograph. The levels gradually converge with increasing distance and there is about 10 dB difference at the end of the vehicle (1 m away from the pantograph in the 1:5 scale model). The wind causes influence on the sound pressure levels but works differently in the upstream and downstream directions. The sound pressure amplitude in the upstream direction is enhanced while in the downstream direction it is attenuated. Moreover, the wind gradient in the boundary layer changes the direction of the sound, thus making the sound rays bend away from the train surfaces in the upstream direction and towards the train surfaces in the downstream direction. Therefore, a quiet shadow area is formed in the upstream direction. The amplification/attenuation of the sound pressure amplitude caused by the wind can be modelled by using an equivalent sound speed in the 2.5D model.

The noise transmission through the train wall structures (a segment of an extruded panel is considered as example) is investigated by using the 2.5D FE/BE method and the SEA approach. The simulations of sound radiation show that, below the cut on frequency of the local modes, the global radiation is dominant, while above this cut on frequency, the local modes will dominate the vibration levels and radiation efficiency. The location of the force, in particular whether it is on a stiffener or a plate strip, will affect the radiation efficiency of the extrusion. An SEA model has been created to predict the sound transmission loss and radiation efficiency of the extrusion with parameters determined from the 2.5D FE model. It has been found that the use of an equivalent width for the strips will predict their modal densities reasonably well near their cut on frequencies but underestimates them at high frequencies. With some essential parameters determined from the 2.5D FE model, the SEA model can predict the sound transmission loss and the radiation efficiency of the extrusion with good quality at most frequencies. Compared with existing measurements, the radiation efficiencies of the extrusion obtained by the current SEA model have some errors between 800 ~ 1250 Hz bands when exciting the strips. The reason for that is unknown and it needs further investigation.

Interior noise has been modelled by using an SEA model of the interior acoustic space with the excitation due to the noise sources outside the train. The calculation procedure has been applied to a metro vehicle and the results show that the sound power incident on the floor is about 15-20 dB higher than that on the train sides and gangway. The sound power incident on the train sides and on the gangway were similar in levels. In that case the highest levels of the sound power of rolling noise were transmitted into the train cabin from the gangway region, due to its lower sound transmission loss. The interior noise distribution from the simulation showed that the ends of the cabin were noisier than the middle. The added absorption due to passengers was also considered based on published data from concert audiences. If the absorption due to passengers was added, a less reverberant sound field was generated and the sound pressure decayed faster from the end of the cabin to its middle. Predictions of sound in that metro train were compared with field measurements from the RUN2Rail project. The differences were about 3 dB.

These comparisons in terms of laboratory tests and field measurements show that these models are relatively accurate and reliable. Besides, they are also computationally efficient. These approaches can help to get a better understanding of noise sources, noise transmission

paths and also interior noise. They can be used in a straightfoward way to predict the noise insde a railway vehicle.

9.2   Recommendations for future work

Through this framework, the noise inside a railway vehicle has been predicted. The following recommendations are given for further work to extend and improve the methods presented in this thesis.

First, the modelling of rail vibration in Chapter 3 and 4 is based on a Timoshenko beam supported on an elastic foundation while in reality it is discretely supported by sleepers. By using a Timoshenko beam model, the cross-section deformation of the rail was not considered. Besides, the continuous foundation will not model the rail-sleeper interaction precisely when the rail pad stiffness is high. The noise radiation from the rail can be calculated by using the 2.5D FE/BE coupled approach which will take into account the cross-section deformation of the rail. The sleepers are discrete. In modelling the sleepers in the 2.5D model, some empirical scaling factors were used. This can be considered more precisely. The sleepers can be modelled by periodic structures. The vibration of the sleepers can be obtained by using periodic square windows to truncate the vibration of the rail. By doing so, no scaling factors are required. In the 2.5D model, the wheel is considered by a single point source which might affect the prediction at high frequency. It can be improved by either using more point sources or finding other methods to model the wheel, for example, the wave number domain method in a cylindrical coordinate system.

The 2.5D FE/BE model for noise transmission through train wall structures cannot model any geometrical discontinities, for example the influences caused by the equipment on the train floor and the windows on the train sides. When using the SEA model in the current work, the averaged radiation efficiency of the strips was used to determine the coupling loss factors, while in a real situation each strip may dominate the vibration levels and the radiated sound power around their individual natural frequencies. The vibration of the strips could be further studied to understand how they contribute to the whole radiation. In Chapter 7, the extruded panel was modelled by four subsystems. It will be useful to create another SEA model to consider each strip in a separate subsystem. Also it worth creating other SEA models which have an intermediate number of subsystems. By doing so their predictions can be compared and better accuracy may be achieved.

An SEA model has been used to predict the interior noise and it showed reasonable agreement. An alternative way is to use a 2.5D FE/BE model to predict the interior noise. This will make good use of the 2.5D BE model for exterior noise prediction and there is no need to apply the inverse Fourier transform to calculate the sound spatial distribution on the train external surfaces.

The content of this thesis mainly focuses on the prediction of the airborne noise, the structure borne noise is not included. In Chapters 6 and 7 the structure-borne noise transmission through the train wall structures has been investigated. To include the structure-borne noise in the train cabin, further work is needed to calculate the mechanical force excitation that comes from the wheel/rail interaction, being transmitted through the bogie system and finally excites the train floor. The contributions from the two parts can be investigated in further work.

Noise control strategies could be used to control the interior noise, but in this thesis only the interior absorption is considered. It is interesting to find out efficient measures, for example advanced passive noise control strategies on the noise sources and transmission paths to mitigate the interior noise, including new designed wheels and embedded rails, porous absorbing material on the track, noise barriers, applying advanced material on the train external surfaces to enhance the reflection of incident sound, applying acoustic black holes on the train body to reallocate its vibration, etc.

In further work, the methodology provided for rolling noise can be extended to other noise sources, such as fans, motors, compressors, etc. The methodology provided for the aerodynamic noise sources and applied to the pantograph can be extended to other sources such as the bogie region. The method proposed for modelling the effect of flow on aerodynamic noise can be extended to rolling noise (and other sources). The angles of incident sound waves on the train wall can be further studied by using the ray tracing method and maybe validated by measurements.

Appendices

Appendix A   TWINS model for rolling noise

The following is a summary based on [2]. Rolling noise is generated by wheel and rail vibration. The vibration of rails and wheels is induced by the dynamic contact force, which is caused by the roughness on the wheel and rail running surfces. This is shown in the schematic diagram in Figure A.1. The axis system with origin at the centre of wheel/rail contact zone is shown in Figure A.2.
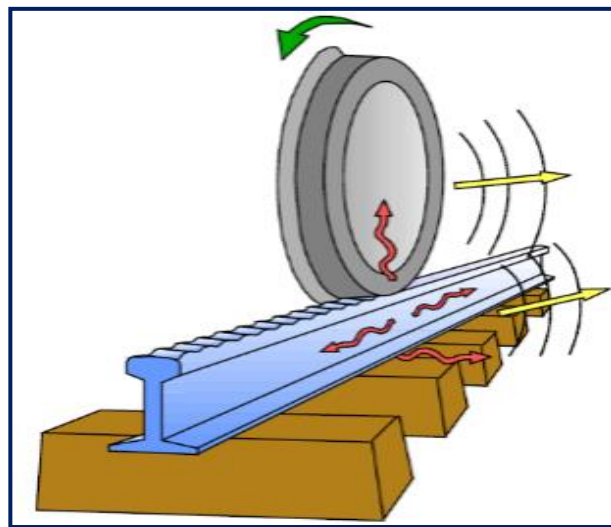
Figure A.1. The schematic diagram of rolling noise [2].
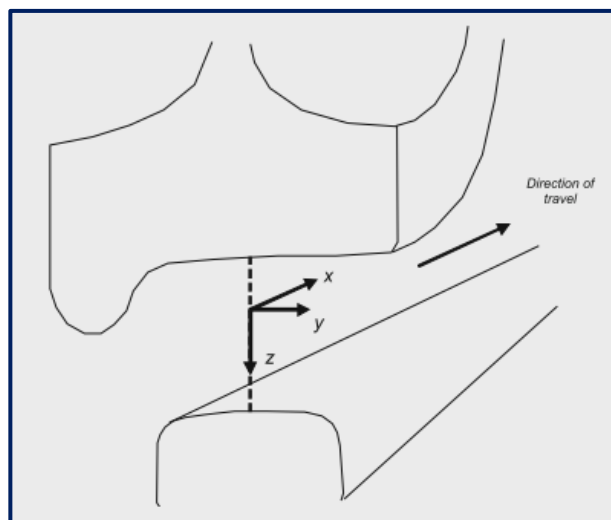
Figure A.2. Axis system with origin at the centre of wheel/rail contact zone [2].

Appendices

Thompson [2] studied the vibration behaviour of the wheel and the rail, and used a contact spring to couple the responses of the wheel and the rail. The wheel/rail system, shown in Figure A.3, can be represented by two dynamic systems connected at a point and excited by a relative displacement between them. A third system, the contact spring, is connected in paralle with the others. The motion of the wheel along the rail is ignored and replaced by a moving excitation in which the roughness strip is pulled through the gap between the wheel and the rail.
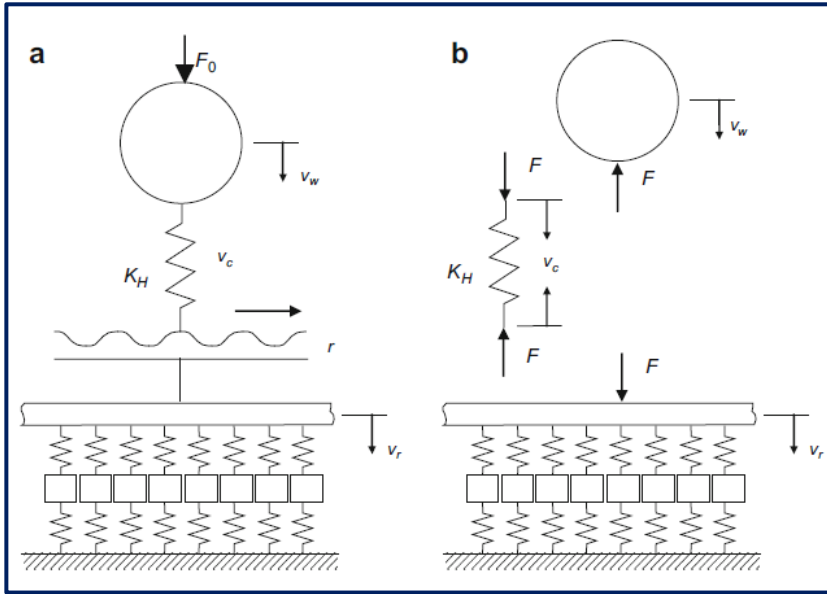
Figure A.3. Schematic diagram of the wheel/rail system, (a) excitation by roughness r, (b) dynamic forces acting in vertical direction [2].

The roughness is acting in vertical direction, but the wheel and rail are coupled not only in vertical direction but also in other directions. In practice, up to six coordinates, including three displacements and three rotations can be included. Assuming the rail is excited by a harmonic force at circular frequency ω and complex amplitude $[F]$ ($[F]$ is the excitation vector up to six forces). The mobility of the rail, $\{Y_r\}$ is calculated besed on the Timoshenko beam model and the mobility of the wheel, $\{Y_w\}$ is calculated based on the finite element model, in which modal analysis is used modal summation including the effect of rotation. The vibrational velocity amplitude of the rail ($\{v_r\}$) and the wheel ($\{v_W\}$) in the multi-degree-of-freedom coupling system are satisfied for

$$\{v_r\} = [Y_r]\{F\} \qquad (A.1)$$

$$\{v_w\} = -[Y_w]\{F\} \tag{A.2}$$

where all the variables are taking the matrix form and have up to six components. The contact zone can also be represented by a mobility matrix, $[Y_c]$, which meets the relation

$$\{v_c\} = [Y_c]\{F\} = \frac{i\omega\{F\}}{\{K_H\}} \tag{A.3}$$

where $\{K_H\}$ is the linearized contact stiffness. Roughness only acts in the vertical direction. Introducing roughness with amplitude r at angular frequency ω, the rail velocity amplitude is then expressed as

$$\{v_r\} = \begin{Bmatrix} 0 \\ i\omega r \\ 0 \end{Bmatrix} + \{v_w\} - \{v_c\} \tag{A.4}$$

Then the interaction force vector can be expressed by

$$\{F\} = [Y_r + Y_w + Y_c]^{-1} \begin{Bmatrix} 0 \\ i\omega r \\ 0 \end{Bmatrix} \tag{A.5}$$

So, the velocity amplitude of the rail and the wheel at the contact point can be obtained:

$$\{v_r\} = [Y_r][Y_r + Y_w + Y_c]^{-1} \begin{Bmatrix} 0 \\ i\omega r \\ 0 \end{Bmatrix} \tag{A.6}$$

$$\{v_w\} = [Y_w][Y_r + Y_w + Y_c]^{-1} \begin{Bmatrix} 0 \\ i\omega r \\ 0 \end{Bmatrix} \tag{A.7}$$

For any vibrating strucures, the sound power radiated by an object at a particular frequency can be written as

$$W = \rho_0 c_0 S \left\langle \overline{v^2} \right\rangle \sigma \tag{A.8}$$

Appendices

where S is the surface area of the vibrating structure, ρ_0 is the density of air and c_0 is the sound speed, which take the values 1.2 kg/m^3 and 343m/s. $\langle \overline{v^2} \rangle$ is the squared velocity normal to the surface in the frequency band of interest, which is averaged both over time and over the surface area. σ is the radiation ratio, determined by the size and shape of the vibrating structure, and also the way it vibrates. For the wheel and rail case, more details about the radiation ratio can be found out in [2].

The sound radiation from wheel/rail interaction are bluit in TWINS model (Track-Wheel Interaction Noise Software), which has become an established method for rolling noise prediction.The flowchart of calculating rolling noise in TWINS model is given in Figure A.4.
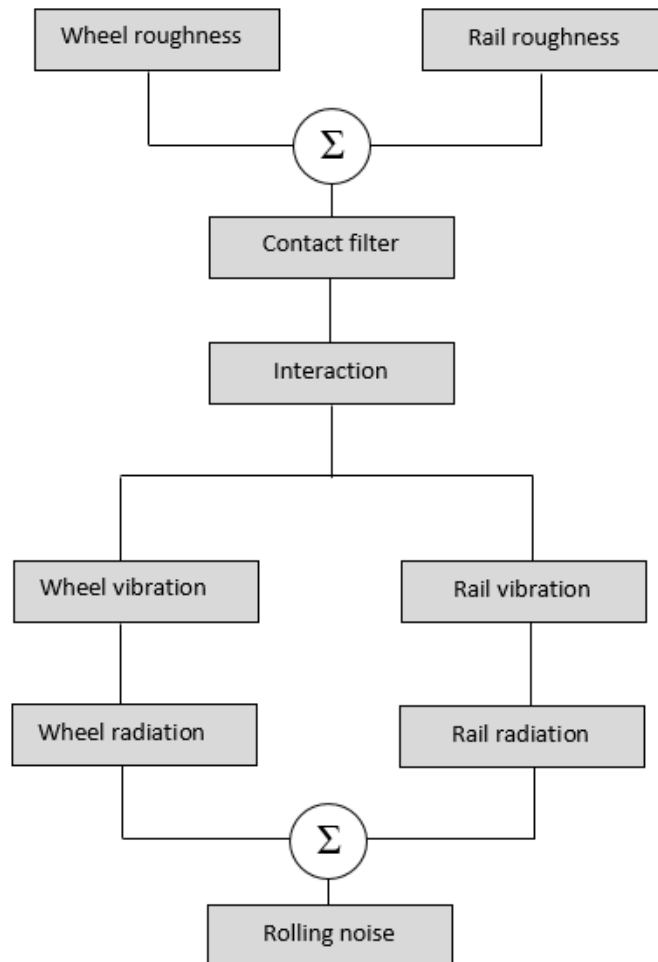
Figure A.4. The flowchart of the TWINS model [2].

Appendix B   Field measurements on a metro train in the RUN2Rail project

Field measurements were carried out as part of the EU/Shift2Rail project RUN2Rail by Vibratec and Polytechnic University of Valencia in collaboration with Metro de Madrid. A summary is given here based on information given in [87].

B.1.   Rolling noise measurements and model

Figure B.1 shows the microphone locations for the pass-by noise measurements. Three pass-by noise microphones were set aside the rail. Microphone M1 is 4 m away from the rail on the left side and the height is 1.4 m above the ground. M2 is 4 m away from the same rail but the height is 2 m above the ground. M3 is 7.5 m from the centreline of the track with a height 1.2 m above the ground.
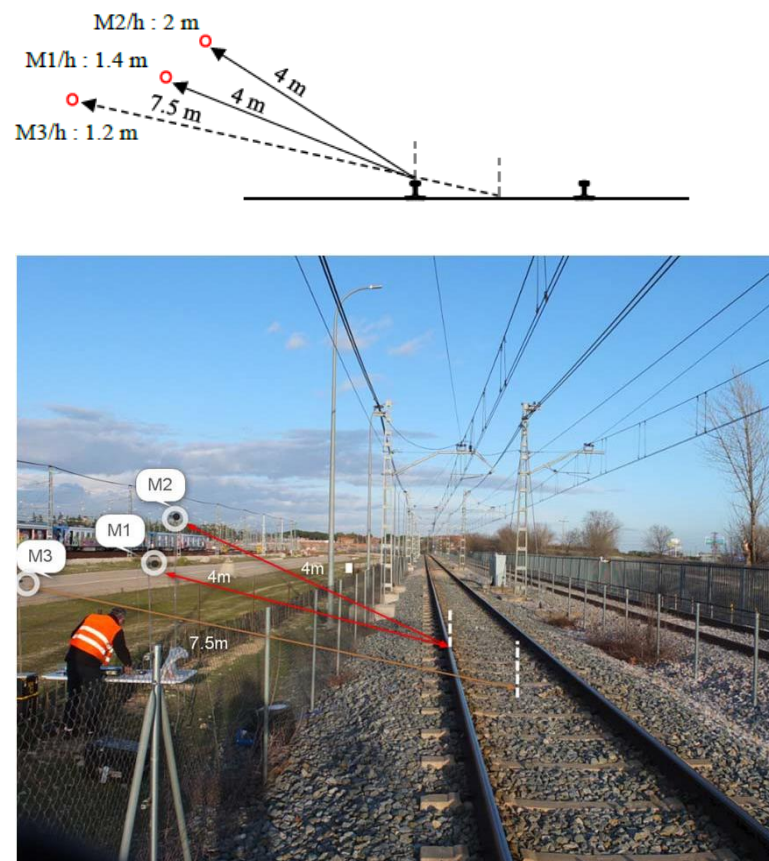
Figure B.1. Pass-by noise microphones: M1 and M2 at 4 meters from the rail head, M3 at 7.5 meters from the centreline of the track.

The sound power associated to rolling noise in this case is calculated by using the TWINS [10] model (see also Appendix A). This requires wheel and track data and calculates the

sound power radiated by wheels, rail and sleepers. The parameters for the track model corresponding to this measurement are listed in Table B.1. The parameters used for the wheel are listed in Table B.2. The natural frequencies of the most important modes are listed in Table B.3,

Table B.1 Parameters used to represent the railway track in the test.

	Vertical	Lateral
Rail bending stiffness (Nm^2)	4.86×10^6	0.88×10^6
Rail shear coefficient	0.5	0.5
Rail loss factor	0.02	0.02
Mass per length (kg/m)	54	
Pad stiffness (N/m)	800×10^6	100×10^6
Pad loss factor	0.2	0.2
Sleeper mass (half, kg)	150	
Distance between sleepers (m)	1.0	
Ballast stiffness	100×10^6	35×10^6
Ballast loss factor	1.0	2.0

Table B.2. Parameters used to represent the wheel in the test.

Wheelset mass	Radius	Density	Elastic modulus	Minimum damping ratio
1100 kg	0.43 m	7850 kg/m^3	210 GPa	0.002

Table B.3. Natural frequencies in Hz of wheel for zero-nodal-circle, one-nodal-circle, and radial modes.

	(n,0)		(n,1)		(n,R)		(n,2)	(n,C)
n	ANSYS	measured	ANSYS	measured	ANSYS	measured	ANSYS	ANSYS
0	256	351	1600		3120		4231	541
1	168	270	1830		1241		4292	3448
2	402	405	2322	2380	1816	1885	4482	4766
3	1086	1084	2914	2875	2478	2581	4870	6511
4	1955	1961	3604		3273	3166	5432	
5	2928	2939	4397	4378	4125	4548	6154	
6	3957	3975	5001	4984	5297	5401	7008	
7	5015	5042			5925	6324		
8	6086	6125						

In the current measurements, the sleeper spacing is large (1 m), and the rail pads have a high value of stiffness. Consequently, significant differences are found between the rail response measured above a sleeper and at mid-span. The effect of the discrete support provided by the sleepers is therefore considered. The commonly used continuously supported model and

the discretely supported model [2] used in the current case are shown in Figure B.2. The response in the discretely supported model is determined from the superposition of the response of the rail to the contact force and the response to the reaction forces at each support point. In the TWINS model used, the effect of the ground on the rail and sleeper radiation has been taken into account based on the work of Zhang et al. [20, 115].
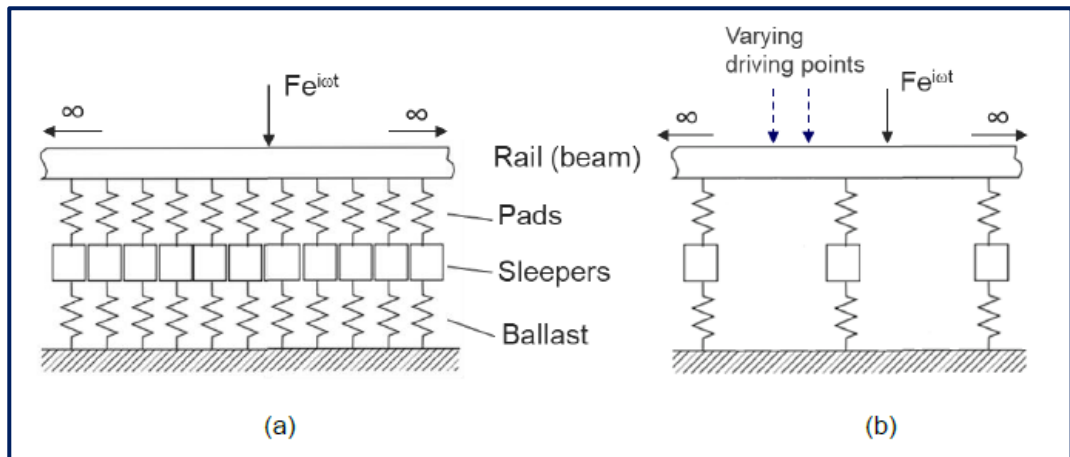
Figure B.2. Models for track vibration: (a) continuously supported; (b) discretely supported [2].

To calculate the track vibration and noise, the roughness spectrum is required. Figure B.3 shows the one-third octave band spectra of wheel and rail roughness which are used as input to the TWINS model. These are the averaged levels of the measured data described in [116].
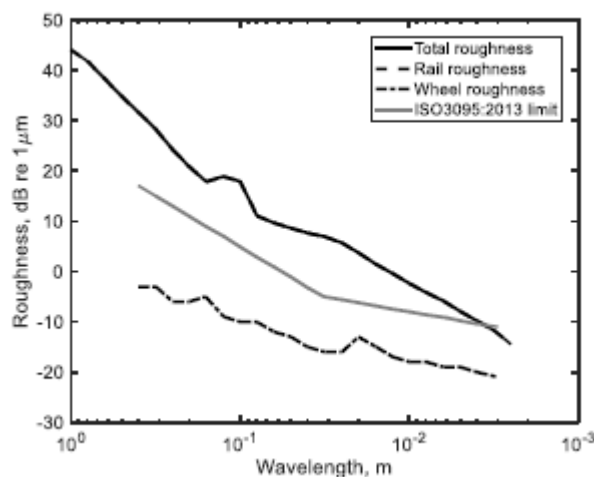
Figure B.3. Wheel and rail roughness spectra based on measured data [116].

To improve the predicted noise spectra, a correction based on the differences between the measured and predicted vibration spectra was applied to the noise calculations for the track, but no correction was applied to the wheel component. To verify the validity of the prediction

of the sound power by using the TWINS calculation software with measured roughness and measured vibration of the rail, track-side microphones M1, M2, and M3 were set to measure the sound pressure levels when the train is passing by, see Figure B.1. The comparison of sound pressure levels between the predictions and the measurements are shown in Figure B.4. In Figure B.4(a), the results at receivers M1 and M2 are averaged by averaging the mean square pressure of sound at the two receivers. It is concluded from Figure B.4 that the TWINS calculation software with discrete supported rail model is reliable to give good quality prediction of the rolling noise.
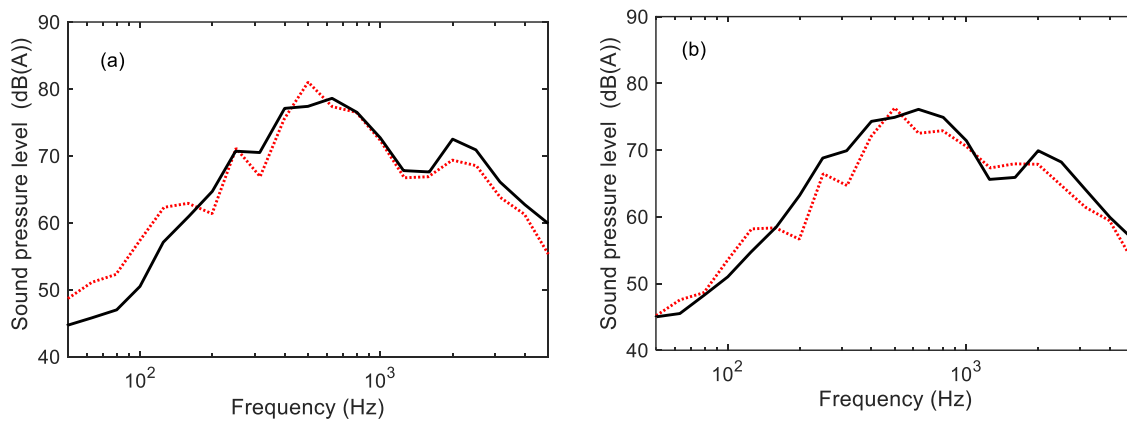
Figure B.4. Comparisons between measured and predicted noise levels after correction. (a) Averaged over receivers M1 and M2; (b) Receiver M3. ⎯, Measurement; …, TWINS prediction with discrete supports. dB re $2.0×10^{-5}$ Pa.

The predicted sound power of rolling noise from the TWINS model is then plotted in Figure B.5. It is found from Figure B.5 that the contribution from the sleepers are dominant below 200 Hz and it is negligible above 2000 Hz. The contribution from the rail becomes important in the middle frequency range from 315 Hz to 2500 Hz. Wheel sound power is not the most significant sources at most of the frequency range except the 250 Hz bands.
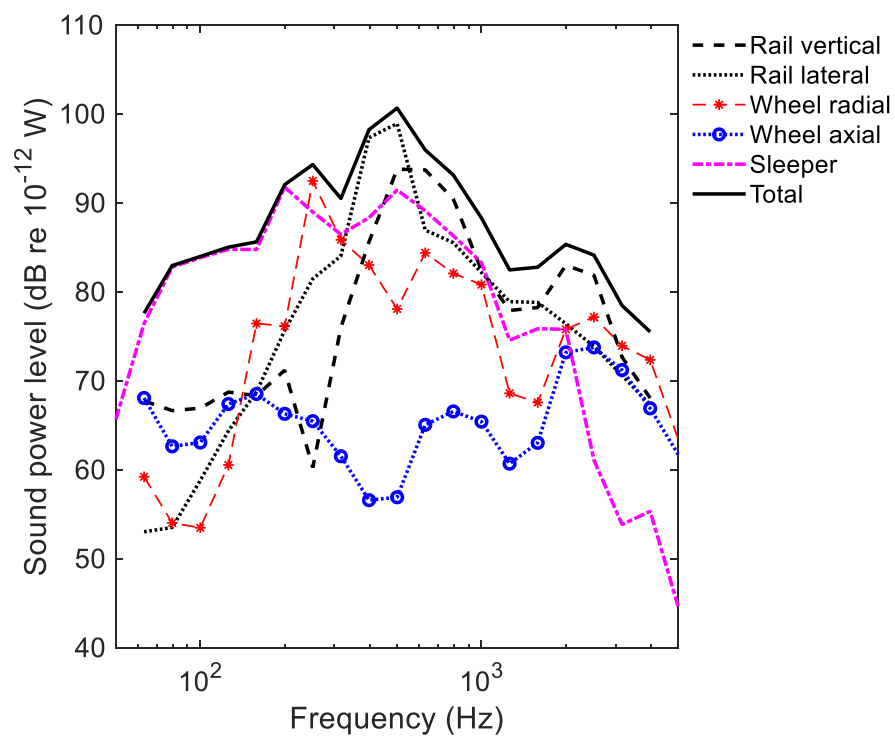
Figure B.5. Sound power spectrum for one wheel and associated track vibration showing components from the wheel, rail and sleeper for the field test situation at 50 km/h.

B.2. Acoustic measurements beneath the vehicle and on external walls on a stationary metro train.

The results of the experimental measurements carried out beneath the vehicle and on exterior walls are shown in this section. For the first case, two microphone heights $h = 0.17$ m and $h = 0.32$ m were considered over the surface of the sleepers (see scheme in Figure B.6). The microphone positions are listed in Figure B.7. Microphone position 1 was at distance of 2 m from the source. The rest of microphone positions (2, 3, 4, …, 8) had a relative separation of 1 m. For each position, two measurements were carried out.

(a)

(b)

Figure B.6. Acoustic measurements beneath the vehicle.
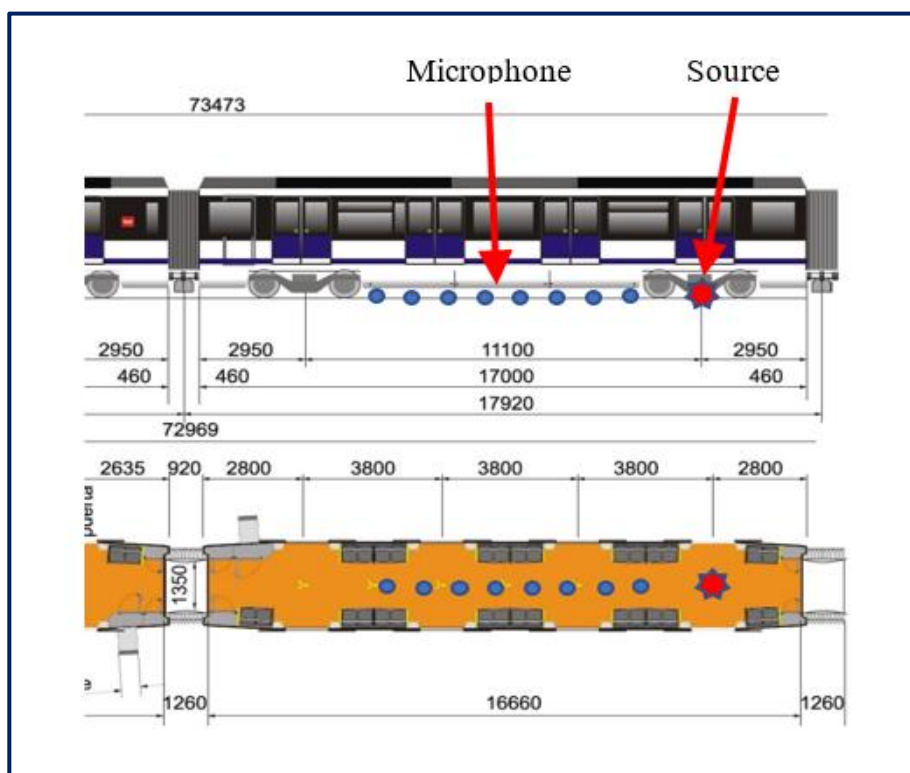
Figure B.7. Acoustic measurements beneath the vehicle.

Regarding the measurements on the exterior walls, see Figure B.8, the source was located in the central part of the bogie, close to the rail. The five microphone positions were located at a lateral distance of 0.3 m from the centre of the coach doors and right above the source. The relative vertical separation between microphone positions was 0.5 m, see Figures B.8 and B.9.

Figure B.8. Acoustic measurements on exterior walls.
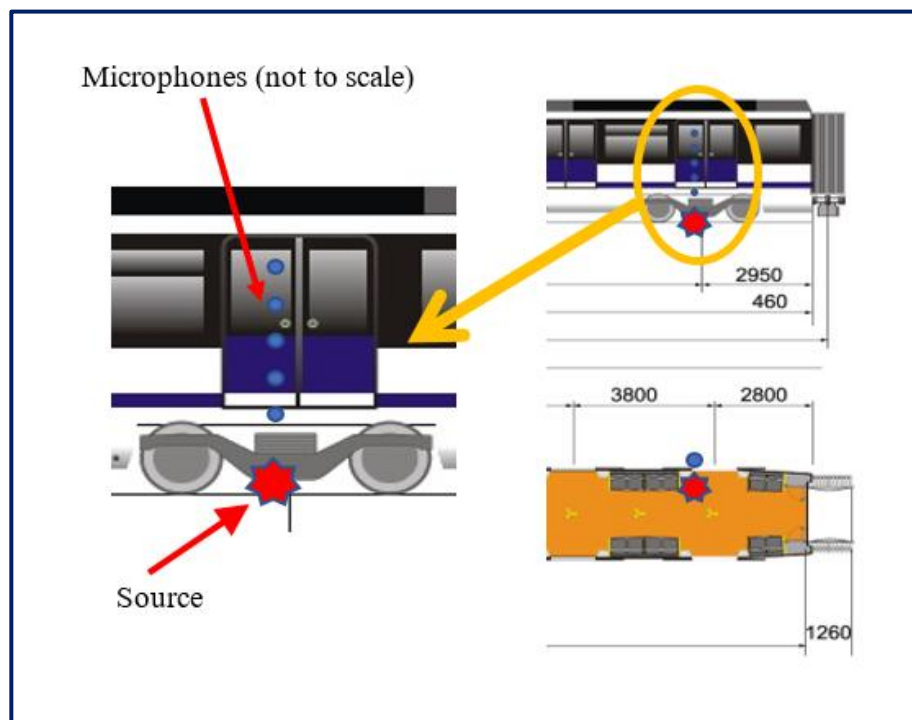
Figure B.9. Acoustic measurements on exterior walls.

B.3.   **Acoustic measurements beneath the vehicle and on external walls on a running metro train.**

During the running measurements at 50 km/h, six microphones were located below the floor, as shown in Figure B.10. Point 1002 is measured below the adjacent vehicle which had a motor bogie but it was switched off during the tests. Points 1002, 1007 and 1008 are located in the bogie area; Points 1012 and 1013 are in the middle region below the vehicle and point 1003 is in the gangway area. Their locations are listed in Table B.4.
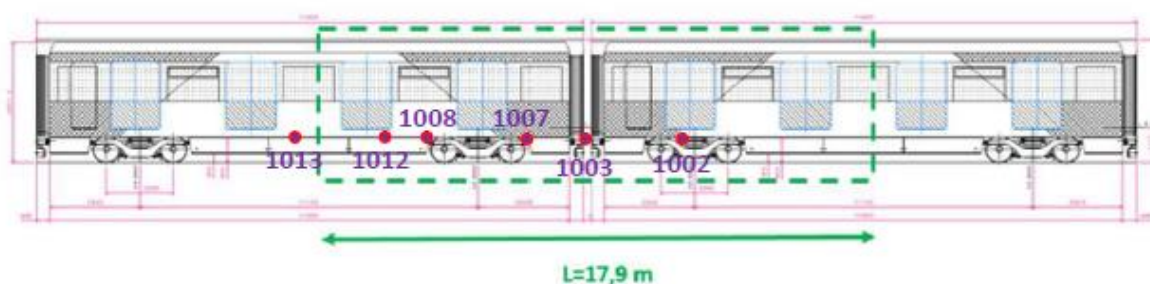
Figure B.10. Microphone locations below the floor.

For the field measurements of the sound pressure on the external train surfaces in running operation, four microphones were located above the bogie area, as shown in Figure B.11. Microphones 1006, 1009, 1011 are 0.7 m above the bottom edge of the sidewall and microphone 1010 is 1.5 m above it. In addition, two microphones were located in the gangway area at different heights, numbered as points 1004 and 1005. Their locations are listed in Table B.4.

Figure B.11. Microphone locations on the side of the train.

Table B.4. Microphone positions for external pressure measuring.

Microphone	X (m)	Y	Z
1002	-5	car centre	on the car body
1003	-3.4	left gangway wall	on the gangway floor
1004	-3.4	left gangway wall	As 1009 and 1011
1005	-3.4	left gangway wall	As 1010
1006	-1.95	left car body skin	See Figure B.11
1007	-1.6	car centre	on the car floor
1008	+1.6	car centre	on the car floor
1009	+0.25	left car body skin	See Figure B.11
1010	+0.25	left car body skin	See Figure B.11
1011	+1.75	left car body skin	See Figure B.11
1012	+3.45	0.8 from the left car skin	on the car floor
1013	+3.95	car centre	on the car floor

B.4.   Measurements of transmission loss of vehicle panels.

The measurements of transmission loss were performed in a workshop. Two artificial sources (B&K Omni-power sources 4292-L connected to B&K power amplifier Type 2734 or equivalent) were placed inside the coach in order to create a diffuse field. The transmitted intensity is measured by scanning the outer skin of the coach with an intensity probe (type B&K 3599). Two different intensity probe spacers are used: 12 mm (limit: 5 kHz) and 50 mm (limit: 1.25 kHz). Measurements were carried out during night-time, since the background noise in the workshop was low during this period. Measurements were repeated twice for each panel to insure repeatability.

Transmission loss measurements of vehicle panels are shown in figures B.12 and B.13. The sound reduction index R_d of a panel characterizes its acoustic transmission loss. It is defined by the ratio between the transmitted intensity $I_{transmitted}$ and the incident intensity $I_{incident}$, in a diffuse sound field:

$$R_d = -10 \, \log_{10} \left(\frac{I_{transmitted}}{I_{incident}} \right) = L_{I,incident} - L_{I,transmitted} \qquad (B.1)$$

L_I indicates the intensity levels in dB.

The incident intensity on the panels is deduced from the mean acoustic pressure level inside the coach using a diffuse field assumption. The average sound pressure level $L_{p,diffuse}$ is estimated using 3 microphones. Expressed in decibels (with the references: 10^{-12} W/m² for the intensity and 2.10^{-5} Pa for the pressure), the relation is:

$$L_{I,incident} = L_{p,diffuse} - 6 \text{ dB} \qquad (B.2)$$

Thus, inserting Equation (B.2) to Equation (B.1) gives:

$$R_d = \left(L_{p,diffuse} - 6 \, dB \right) - L_{I,transmitted} \qquad (B.3)$$

Finally, the sound reduction index R_d per panel is directly available in one-third octave bands up to 5000 Hz. The values of the sound reduction index are not shown due to confidentiality reasons.
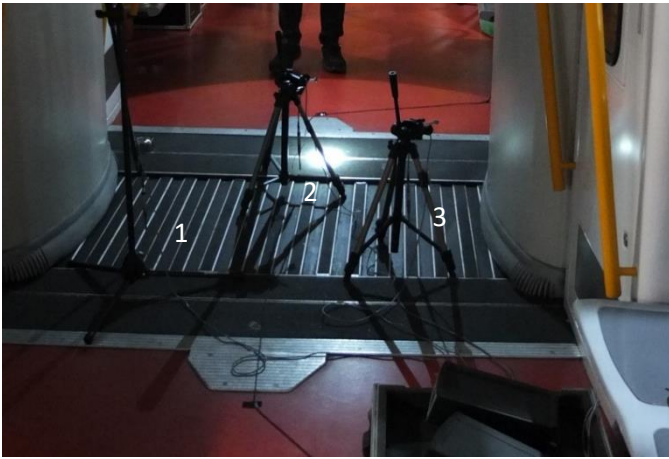
Figure B.12. Three microphones to determine the incident intensity $L_{I,incident}$, here measurement of the gangway floor panel.
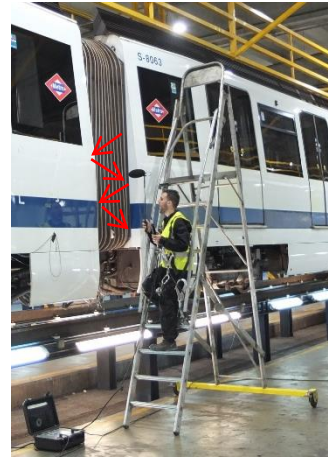
Figure B.13. Scanning of the gangway lateral panel to determine the transmitted intensity $L_{I,transmitted}$.

Figure B.14 shows the location of the investigated panels. These are listed in Table B.5. For some panels the sound reduction index Rd had to be estimated for certain frequencies due to measurement difficulties (low transmitted intensity).
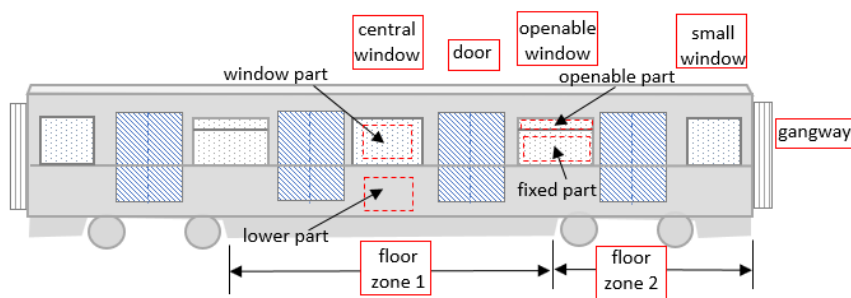
Figure B.14. Definition of the panels (view from the left side, equipped bogie on the right).

Table B.5. Panels for measurement of global sound reduction index.

Panels
Windows
Central window - window part (glass)
Central window - lower part (aluminium)
Openable window - fixed part
Openable window - openable part
Openable window - total
Small window - window part (glass)
Small window - lower part (aluminium)
Doors
F panel (left door part) - with joints
B panel (right door part) - no joints
B panel (right door part) - with joints
F + B - total
Gangway
Gangway - lateral
Gangway - floor
Floor
Floor - zone 1
Floor - zone 2

Appendices

B.5.　　Measurements of internal absorption.

The internal absorption of the coach was assessed through measurements of the reverberation time. This was measured according to standard ISO 3382-2:2008 [117]. 28 measurements were carried out, considering 7 combinations of microphone and source positions, with 4 measurements associated with each combination. In this particular case, the notation used for microphones was "Position 1" and "Position 2", while for source location the corresponding nomenclature was "Source 1", "Source 2" and "Source 3". Finally, combinations P1S1, P1S2, P2S1, P2S2, P3S1, P3S2 and P3S3 were taken into account. Additional details can be found in Figure B.15.
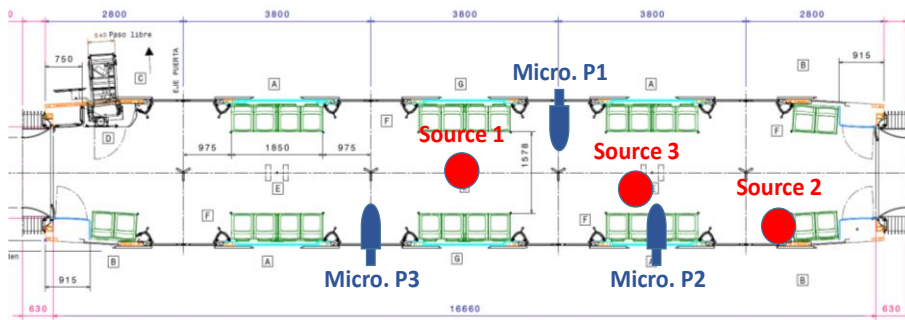
Figure B.15. Coach scheme with source and microphone positions used for reverberation time measurements.

Several conditions had to be fulfilled during the measurements. In all cases, a minimum distance of 2 m between microphone positions was kept. Also, the minimum distance between microphones and reflective surfaces was 1 m (see Figure B.16 for illustration purposes). To compute the minimum separation between microphones and sources, Equation (1) of ISO 3382-2:2008 was considered,

$$d_{min} = 2\sqrt{\frac{V}{cT_{60}}}$$
(B.4)

To calculate the volume, the following dimensions of the coach were used: length = 18 m, width = 2.48 m and height = 2.1 m, which yields $V = 93.74$ m³. For a temperature of 19ºC, the speed of sound is given by $c = 342.6$ m/s. Finally, a low value $T_{60} = 0.3$ s was assumed to compute an overestimated $d_{min} = 1.91$ m.

Figure B.16. Reverberation time measurement at different sources and microphone locations.

Figure B.17 shows the average results in one-third octave bands. Note that, as mentioned previously, for a given curve associated with a microphone and source position, four measurements have been averaged. The final mean value is also depicted (which implies the average of 28 reverberation time measurements).
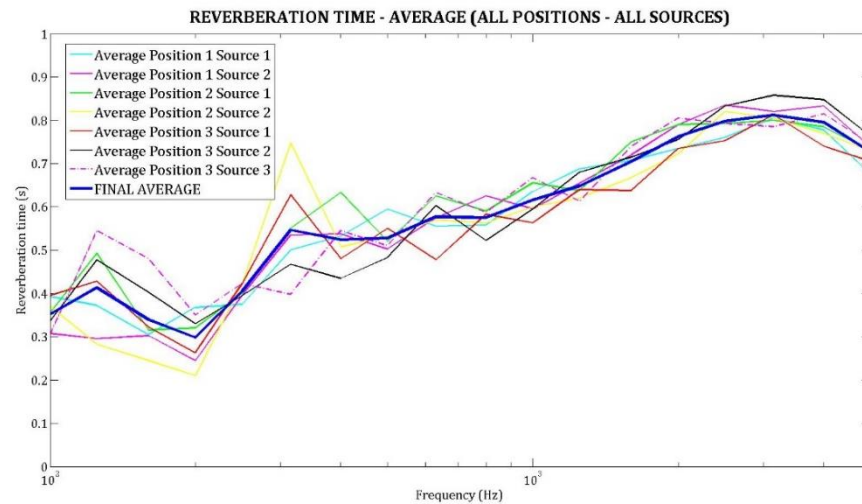
Figure B.17. Reverberation time in one-third octave bands

The absorption coefficient α was computed through Sabine's equation,

$$T_{60} = 0.1611 \frac{V}{S\alpha} \tag{B.5}$$

where the surface area $S = 164.88$ m^2 was computed neglecting front and rear coach ends. The corresponding values of the absorption coefficient are shown in Figure B.18.
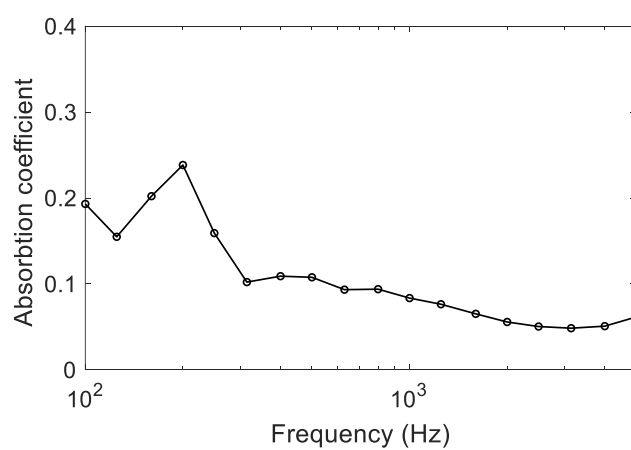
Figure B.18. Absorption coefficient in one-third octave bands.

B.6. Measurements of interior noise.

The measurement positions used for the interior noise in the metro train are shown in Figure B.19. The vehicle was runing at 50 km/h. Five positions were measured on the centre line of the carriage at 1.5 m above the floor. Along the train axis direction, Point 2002 was in the middle of the two adjacent carriages, Point 2004 was right above the trailer bogie and Point 2006 was in the middle of the carriage. Point 2003 was between Points 2002 and 2004 and Point 2005 was between 2004 and 2006.
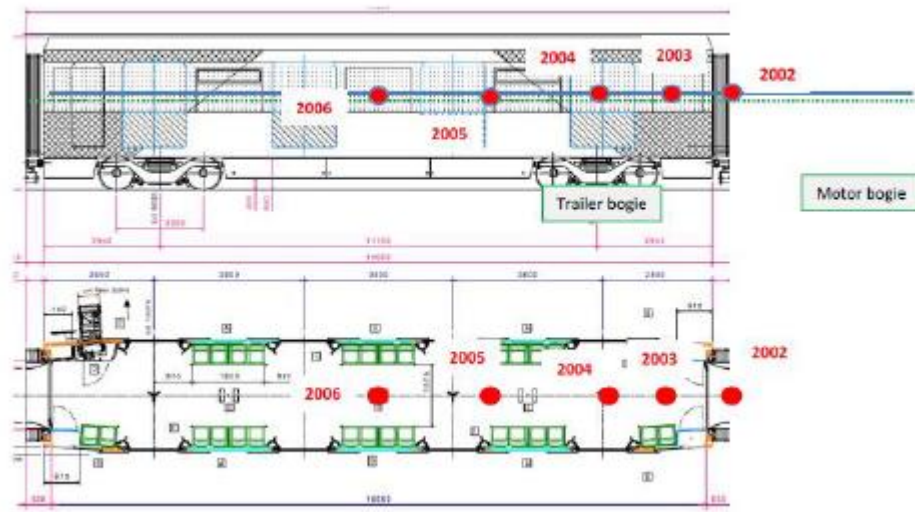
Figure B.19. Interior microphone positions.

The interior microphones set up in the measurements and the locations are shown in Figure B.20 and Table B.6.

Figure B.20. Measurement of interior noise. (a) microphones 2002, 2003, (b) microphones 2004, 2005, and 2006.

Table B.6. Interior microphone locations.

Microphones	Locations
2002	Inter circulation
2003	Between 2002 and 2004
2004	Above Trailer bogie
2005	Between 2004 and 2006
2006	Centre of the car

References

[1]. J. Zhang, X. B. Xiao, X. Z. Sheng, R. Fu, D. Yao, X. S. Jin, Characteristics of interior noise of a Chinese high-speed train under a variety of conditions, Journal of Zhejiang University-SCIENCE A. 18(8) (2017) 617-630.

[2]. D. Thompson, Railway noise and vibration: mechanisms, modelling and means of control, Elsevier, 2008.

[3]. C. Talotte, Aerodynamic noise: a critical survey, Journal of Sound and Vibration, 231(3) (2000) 549-562.

[4]. P. Bouvet, M. Rissmann, Industrial methodologies for the prediction of interior noise inside railway vehicles: airborne and structure bone transmission, 13th International Workshop on Railway noise, Ghent, Belgium. 2019.

[5]. U. Orrenius, Y.Y. Pang, B. Stegeman, S. Finnveden, Acoustic modeling of extruded profiles for railway cars, in Novem Saint Raphael, 2005.

[6]. A. Martens, J. Wedemann, N. Meunier, A. Leclere, A.G. Bahn Deutsche, D.B. Systemtechnik, High speed train noise-sound source localization at fast passing trains. Deutsche Bahn AG, Sociedad Espanola de Acoustica, SEA, 2009.

[7]. D. Thompson, E. Latorre Iglesias, X. Liu, J. Zhu, Recent developments in the prediction and control of aerodynamic noise from high-speed trains. International Journal of Rail Transportation, 3(3) (2015) 119-150.

[8]. R.H. Lyon, R.G. DeJong, M. Heckl, Theory and application of statistical energy analysis. Acoustical Society of America, 1995.

[9]. C.M. Nilsson, Waveguide finite elements applied on a car tyre. PhD thesis, Farkost och flyg, 2004.

[10]. D. Thompson, B. Hemsworth, N. Vincent, Experimental validation of the TWINS prediction program for rolling noise, part 1: description of the model and method, Journal of Sound and Vibration. 193(1) (1996) 123-135.

[11]. D. Thompson, C. Jones, Sound radiation from a vibrating railway wheel. Journal of Sound and Vibration, 253(2) (2002) 401-419.

[12]. D. Thompson, P. Fodiman, H. Mahé, Experimental validation of the TWINS prediction program for rolling noise, part 2: results. Journal of Sound and Vibration, 193(1) (1996) 137-147.

[13]. D. Thompson, Experimental analysis of wave propagation in railway tracks. Journal of Sound and Vibration, 203(5) (1997) 867-888.

[14]. C.J.C. Jones, D. Thompson, R.J. Diehl, The use of decay rates to analyse the performance of railway track in rolling noise generation. Journal of Sound and Vibration, 293(3-5) (2006) 485-495.

[15]. D. Thompson, C.J.C. Jones, N. Turner, Investigation into the validity of two-dimensional models for sound radiation from waves in rails. The Journal of the Acoustical Society of America, 113(4) (2003) 1965-1974.

[16]. T. Kitagawa, D. Thompson, The horizontal directivity of noise radiated by a rail and implications for the use of microphone arrays, Journal of Sound and Vibration. 329(2) (2010) 202-220.

[17]. N.M. Nilsson, C.J.C. Jones, D. Thompson, J. Ryue, A waveguide finite element and boundary element approach to calculating the sound radiated by railway and tram rails, Journal of Sound and Vibration. 321(3-5) (2009) 813-836.

[18]. J. Ryue, S. Jang, D.J. Thompson, A wavenumber domain numerical analysis of rail noise including the surface impedance of the ground, Journal of Sound and Vibration. 432 (2018) 173-191.

[19]. X. Zhang, G. Squicciarini, D.J. Thompson, Sound radiation of a railway rail in close proximity to the ground, Journal of Sound and Vibration. 362 (2016) 111-124.20.

Reference

[20]. X. Zhang, D.J. Thompson, Q. Li, D. Kostovasilis, M.G. Toward, G. Squicciarini, J. Ryue, A model of a discretely supported railway track based on a 2.5 D finite element approach. Journal of Sound and Vibration. 438 (2019) 153-174.

[21]. X. Sheng, T. Zhong, Y. Li, Vibration and sound radiation of slab high-speed railway tracks subject to a moving harmonic load, Journal of Sound and Vibration. 395 (2017) 160-186.

[22]. X. Zhang, H. Jeong, D. Thompson, G. Squicciarini, The noise radiated by ballasted and slab tracks, Applied Acoustics. 151 (2019) 193-205.

[23]. L. Li, D. Thompson, Y. Xie, Q. Zhu, Y. Luo, Z. Lei, Influence of rail fastener stiffness on railway vehicle interior noise. Applied Acoustics. 145 (2019) 69-81.

[24]. C.J.C. Jones, D.J. Thompson, T.P. Waters, Application of numerical models to a system of train-and track-mounted acoustic shields, International Journal of Acoustics and Vibration, 6 (4) (2001) 185-192.

[25]. W. Dai, X. Zheng, L. Luo, Z. Hao, Y. Qiu, Prediction of high-speed train full-spectrum interior noise using statistical vibration and acoustic energy flow, Applied Acoustics, 145 (2019) 205-219.

[26]. X. Zheng, Z. Hao, X. Wang, J. Mao, A full-spectrum analysis of high-speed train interior noise under multi-physical-field coupling excitations, Mechanical Systems and Signal Processing, 75 (2016) 525-543.

[27]. J. Zhang, X. Xiao, X. Sheng, C. Zhang, R. Wang, X. Jin, SEA and contribution analysis for interior noise of a high-speed train, Applied Acoustics, 112 (2016) 1158-170.

[28]. M.B. Mauclaire, Noise generated by high speed trains: new information acquired by SNCF in the field of acoustics, owing to the high speed test programme, International Conference on Noise Control. 1990.

[29]. M.A. Pallas, K.P. Schmitz, B. Barsikow, P. Fodiman, G. Holzl, DEUFRAKO: localized sound sources on the high-speed vehicles ICE, TGV-A and TR 07. 1994.

[30]. H. Tsuda, M. Kimata, H. Sawada, Prediction of the Shinkansen noise. in INTER-NOISE and NOISE-CON Congress and Conference Proceedings. Institute of Noise Control Engineering, 1994.

[31]. K. Nagakura, Y. Moritoh, Y. Zenda, Y. Shimizu, Aerodynamic noise of maglev cars. In Inter-Noise and Noise-Con Congress and Conference Proceedings, Institute of Noise Control Engineering, 6 (1994) 157-162.

[32]. N. Curle, The influence of solid boundaries upon aerodynamic sound. Proceedings of the Royal Society of London. Series A. Mathematical and Physical Sciences, 231(1187) (1955) 505-514.

[33]. M.J. Lighthill, On sound generated aerodynamically I. General theory. Proceedings of the Royal Society of London. Series A. Mathematical and Physical Sciences, 211(1107) (1952) 564-587.

[34]. M.E. Goldstein, Aeroacoustics. New York, McGraw-Hill International Book Co., 1976.

[35]. M. Ikeda, M. Suzuki, and K. Yoshida, Study on optimization of panhead shape possessing low noise and stable aerodynamic characteristics. Quarterly Report of RTRI, 47(2) (2006) 72-77..

[36]. T. Kurita, Y. Wakabayashi, H. Yamada, M. Horiuchi, Reduction of wayside noise from Shinkansen high-speed trains. Journal of Mechanical Systems for Transportation and Logistics, 4(1) (2011) 1-12.

[37]. T. Sueki, M. Ikeda, T. Takaishi, Aerodynamic noise reduction using porous materials and their application to high-speed pantographs. Quarterly Report of RTRI, 50(1) (2009) 26-31.

[38]. T. Mitsumoji, T. Sueki, N. Yamazaki, Y. Sato, M. Ikeda, R. Takinami, H. Gejima, K. Fukagata, Aerodynamic noise reduction of a pantograph panhead by applying a

flow control method, in Noise and Vibration Mitigation for Rail Transportation Systems. Springer. (2015) 515-522.

[39]. F. R. Grosche, G. Meier, Research at DLR Göttingen on bluff body aerodynamics, drag reduction by wake ventilation and active flow control. Journal of Wind Engineering and Industrial Aerodynamics, 89(14-15) (2001) 1201-1218.

[40]. E.L. Iglesias, D. Thompson, M. Smith, Experimental study of the aerodynamic noise radiated by cylinders with different cross-sections and yaw angles. Journal of Sound and Vibration, 361 (2016) 108-129.

[41]. J.E. Ffowcs Williams, D.L. Hawkings, Sound generation by turbulence and surfaces in arbitrary motion. Philosophical Transactions of the Royal Society of London. Series A, Mathematical and Physical Sciences, 264(1151) (1969) 321-342.

[42]. J. Smagorinsky, General circulation experiments with the primitive equations: I. The basic experiment. Monthly weather review, 91(3) (1963) 99-164.

[43]. D.C. Wilcox, Turbulence modeling for CFD. DCW industries La Canada, CA. Vol. 2. 1998.

[44]. S. Lei, Z. Chengchun, W. Jing, R. Luquan, Numerical analysis of aerodynamic noise of a high-speed pantograph. in Digital Manufacturing and Automation (ICDMA), Fourth International Conference on. IEEE. 2013.

[45]. X.W. Liu, Z.W. Hu, D.J. Thompson, V. Jurdic, Reduction of aerodynamic noise from square bars by introducing spanwise waviness. Journal of Sound and Vibration, 435 (2018) 323-349.

[46]. M. Smith, L. Chow. Prediction method for aerodynamic noise from aircraft landing gear. in 4th AIAA/CEAS Aeroacoustics Conference. 1998.

[47]. W. Behr, T. Lölgen, W. Baldauf, L. Willenbrink, R. Blaschko, K. Jager, J. Kremlacek, Low noise pantograph ASP recent developments. in internoise 2000. Proceedings of the 29th international congress on noise control engineering, held 27-31 August 2000.

[48]. E L. Iglesias, D. Thompson, M. Smith, Component-based model for aerodynamic noise of high-speed trains, in Noise and Vibration Mitigation for Rail Transportation Systems. Springer. (2015) 481-488.

[49]. E.L. Iglesias, D. Thompson, M. Smith, Component-based model to predict aerodynamic noise from high-speed train pantographs. Journal of Sound and Vibration, 394 (2017) 280-305.

[50]. X. Liu, Aerodynamic noise from components of a train pantograph and its reduction. PhD Thesis, the University of Southampton, 2017.

[51]. F. Fahy, D. Thompson, Fundamentals of sound and vibration, second edition, CRC Press, 2016.

[52]. V. Hongisto, Sound insulation of double panels-comparison of existing prediction models. Acta acustica united with acustica, 92(1) (2006) 61-78.

[53]. Y Zhang, X. Xiao, D. Thompson, G. Squicciarini, Z. Wen, Z. Li, Y. Wu, Sound transmission loss of windows on high speed trains. in Journal of Physics: Conference Series. IOP Publishing. 2016.

[54]. G. Xie, D.J. Thompson, C.J.C. Jones, A modelling approach for the vibroacoustic behaviour of aluminium extrusions used in railway vehicles, Journal of Sound and Vibration. 293(3-5) (2006) 921-932.

[55]. C. Nilsson, C. Jones. A coupled waveguide finite and boundary element method for calculating the sound transmission through complex panel structures. in IX International Conference on Recent Advances in Structural Dynamics. Institute of Sound and Vibration Research, University of Southampton, UK. 2006.

[56]. C.M. Nilsson, A.N. Thite, C.J.C. Jones, D.J. Thompson, Estimation of sound transmission through extruded panels using a coupled waveguide finite element-boundary element method, Notes on Numerical Fluid Mechanics & Multidisciplinary Design, 99 (2008) 306-312.

Reference

[57]. P. Geissler, D. Neumann. Modelling extruded profiles for railway coaches using SEA. in Proceedings of the 1999 ASME Design engineering technical conferences, September. 1999.

[58]. S. Bruhl, P. Faulhaber, M. Grunewald. AutoSEA2 studies on generic light weight structures. in Proc. of the first international AutoSEA users conference, San Diego, CA. 2000.

[59]. G. Maidanik, Response of ribbed panels to reverberant acoustic fields. the Journal of the Acoustical Society of America, 34(6) (1962) 809-826.

[60]. G. Xie, The vibroacoustic behaviour of aluminium extrusions used in railway vehicles. PhD Thesis, the University of Southampton, 2004.

[61]. S.K. Datta, A.H. Shah, R.L. Bratton, T. Chakraborty, Wave propagation in laminated composite plates. The Journal of the Acoustical Society of America, 83(6) (1988) 2020-2026.

[62]. L. Gavrić, Finite element computation of dispersion properties of thin-walled waveguides. Journal of Sound and Vibration, 173(1) (1994) 113-124.

[63]. U. Orrenius, S. Finnveden, Calculation of wave propagation in rib-stiffened plate structures. Journal of Sound and Vibration, 198(2) (1996) 203-224.

[64]. H. Kim, J. Ryue, D.J. Thompson, A.D. Müller, Prediction of radiation ratio and sound transmission of complex extruded panel using wavenumber domain finite element and boundary element methods. MOVIC2016 & RASD2016, Journal of Physics: Conference Series 744 (2016) 012144.

[65]. H. Kim, J. Ryue, D.J. Thompson, A.D. Müller, Application of a wavenumber domain numerical method to the prediction of the radiation efficiency and sound transmission of complex extruded panels. Journal of Sound and Vibration, 449 (2019) 98-120.

[66]. Y. Zhang, D. Thompson, G. Squicciarini, J. Ryue, X. Xiao, Z. Wen, Sound transmission loss properties of truss core extruded panels. Applied Acoustics, 131 (2018) 134-153.

[67]. Y. Liu, J.C. Catalan, External mean flow influence on sound transmission through finite clamped double-wall sandwich panels. Journal of Sound and Vibration, 405 (2017) 269-286.

[68]. Y. Liu, C. Daudin, Analytical modelling of sound transmission through finite clamped double-wall sandwich panels lined with poroelastic materials. Composite Structures, 172 (2017) 359-373.

[69]. B.K. Kim, J.G. Ih, On the reconstruction of the vibro-acoustic field over the surface enclosing an interior space using the boundary element method. The Journal of the Acoustical Society of America, 100(5) (1996) 3003-3016.

[70]. P. Shorter, B. Gardner, P. Bremner, A hybrid method for full spectrum noise and vibration prediction. Journal of Computational Acoustics, 11(02) (2003) 323-338.

[71]. S. Preis, Prediction of Light Rail Vehicle Noise in running condition using SEA. in INTER-NOISE and NOISE-CON Congress and Conference Proceedings. Institute of Noise Control Engineering. 2016.

[72]. M. Sadri, J. Brunskog, D. Younesian, Application of a Bayesian algorithm for the Statistical Energy model updating of a railway coach. Applied Acoustics, 112 (2016) 84-107.

[73]. J. Forssén, S. Tober, A.C. Corakci, A. Frid, W. Kropp, Modelling the interior sound field of a railway vehicle using statistical energy analysis. Applied Acoustics, 73(4) (2012) 307-311.

[74]. T. Kohrs, K.R. Kirchner, D. Fast, A. Vallesspin, J. Sapena, A.G. Garcia, O. Martner. Sound propagation and distribution around typical tran carbody structures. in InConference Proceedings, Euronoise. 2018.

[75]. X. Deng, Y. Zhao, H. Zhang, P. Lin, Study on Sound Absorption Seats in High Speed Trains, in Noise and Vibration Mitigation for Rail Transportation Systems. Springer. (2018) 473-482.

[76]. F. Fahy, A note on the subdivision of a volume of air in a vehicle enclosure into sea subsystems. Journal of Sound Vibration, 271 (2004) 1170-1174.

[77]. H. Jang, C. Hopkins, Prediction of sound transmission in long spaces using ray tracing and experimental Statistical Energy Analysis. Applied Acoustics, 130 (2018) 15-33.

[78]. U. Orrenius, H. Liu, A. Wareing, S. Finnveden, V. Cotoni, Wave modelling in predictive vibro-acoustics: Applications to rail vehicles and aircraft. Wave Motion, 51(4) (2014) 635-649.

[79]. A. Bistagnino, A. Vallespín, J. Sapena, Prediction of Acoustical Wall Pressure Levels of Rolling Stock Vehicles, in Noise and Vibration Mitigation for Rail Transportation Systems. Springer, (2015) 675-682.

[80]. ISO 3095: Acoustics-railway applications-measurement of noise emitted by railbound vehicles. International Standards Organization, Geneva, 2013.

[81]. T.X. Wu, D.J. Thompson, Vibration analysis of railway track with multiple wheels on the rail. Journal of Sound and Vibration, 239(1) (2001) 69-97.

[82]. R.J.M. Craik, Sound transmission through buildings : using statistical energy analysis. Aldershot: England Gower Publishing Limited. 1996.

[83]. R. Broadbent, D. Thompson, C. Jones, The acoustic properties of railway ballast. Proceedings of Euronoise, Edinburgh, UK, 2009.

[84]. B. Lawrence, Scale model facility for railway vibration and noise. MEng Acoustical Engineering individual project, University of Southampton, 2013.

[85]. L. Ratkevicius, Models of Shielding of Sound Sources on Railway Vehicles. MSc Acoustical Engineering research project, University of Southampton, 2017.

[86]. X. Zhang, D. Thompson, H. Jeong, G. Squicciarini, The effects of ballast on the sound radiation from railway track. Journal of Sound and Vibration, 399 (2017) 137-150.

[87]. P. Bouvet, M. Rissmann, D. Thompson, X. Liu, H. Li, G. Squicciarini, G. Xie, Validation of complete virtual test method for structure-borne and airborne noise transmission. RUN2Rail Deliverable 4.3, August 2019 (www.run2rail.eu).

[88]. D. Duhamel, Efficient calculation of the three-dimensional sound pressure field around a noise barrier. Journal of sound and vibration, 197(5) (1996) 547-571.

[89]. T. Wu, Boundary element acoustics: fundamentals and computer codes. Wit Pr/Computational Mechanics, 2000.

[90]. M. Delany, E. Bazley, Acoustical properties of fibrous absorbent materials. Applied acoustics, 3(2) (1970) 105-116.

[91]. X. Zhang, D. Thompson, E. Quaranta, G. Squicciarini, An engineering model for the prediction of the sound radiation from a railway track, Journal of Sound and Vibration. 461 (2019) 114921.

[92]. J. W. Strutt (Lord Rayleigh), The theory of sound, Dover, 1945.

[93]. X. Zhang, Modelling of track sound radiation, PhD thesis, the University of Southampton, UK, 2016.

[94]. H.A. Schenck, Improved integral formulation for acoustic radiation problems. The journal of the acoustical society of America, 44(1) (1968) 41-58.

[95]. F.J. Fahy, P. Gardonio, Sound and structural vibration: radiation, transmission and response. Elsevier, 2007.

[96]. T. Lölgen, Wind tunnel noise measurements on full-scale pantograph models. The Journal of the Acoustical Society of America, (1999) 105:1136.

[97]. M.M. Zdravkovich, Flow around circular cylinders: Volume 2: Applications. Oxford university press. Vol. 2. 1997.

[98]. C. Baker, T. Johnson, D. Flynn, H. Hemida, A. Quinn, D. Soper, M. Sterling, Train aerodynamics: fundamentals and applications, Butterworth-Heinemann, Oxford, 2019.

Reference

[99]. C. Bailly, G. Comte-Bellot, Wall-Bounded Turbulent Flows in Turbulence. Springer. 2015.

[100]. G. Gabard, Sound Propagation in Uniform Flows. Aeroacoustics lecture notes, University of Southampton. 2017.

[101]. A.D. Pierce, R.T. Beyer, Acoustics: An introduction to its physical principles and applications. Acoustical Society of America, 1990.

[102]. D. Blokhintzev, The propagation of sound in an inhomogeneous and moving medium I. The Journal of the Acoustical Society of America, 18(2) (1946) 322-328.

[103]. D. Blokhintzev, The Propagation of Sound in an Inhomogeneous and Moving Medium II. The Journal of the Acoustical Society of America, 18(2) (1946) 329-334.

[104]. C.M. Nilsson, C.J.C. Jones, WANDS 2 theory manual. ISVR Technical Memorandum no 975, University of Southampton, 2007. (https://www.southampton.ac.uk/engineering/research/groups/dynamics/rail/wavenumber_finite_and_boundary_elements_with_application_to_railways.page)

[105]. A.D. Müller, Acoustical investigation of an extruded aluminium railway vehicle floor panel. MSc Thesis, University of Southampton, 2004.

[106]. D.J. Thompson, N.S. Ferguson, J.W. Yoo, J. Rohlfing, Structural waveguide behaviour of a beam-plate system. Journal of Sound and Vibration, 318(1-2) (2008) 206-226.

[107]. S. P. Timoshenko, S. Woinowsky-Krieger, Theory of plates and shells. McGraw-hill, 1959.

[108]. A.W. Leissa, Vibration of plates. Ohio State Univ Columbus, 1969.

[109]. M. Heckl, Structure-Borne-Sound. In: Bianchi G. (eds) Noise Generation and Control in Mechanical Engineering. International Centre for Mechanical Sciences (Courses and Lectures), vol 276. Springer, Vienna, 1982

[110]. M. Heckl, Wave Propagation on Beam-Plate Systems. The Journal of the Acoustical Society of America, 33(5) (1961) 640-651.

[111]. G.L. Lamb, Input Impedance of a Beam Coupled to a Plate. The Journal of the Acoustical Society of America, 33(5) (1961) 628-633.

[112]. D. Thompson and F. Fazi., Absorption and reverberation, Architectural and Building Acoustics lecture notes, University of Southampton, 2017.

[113]. N.W. Adelman-Larsen, E.R. Thompson, A.C. Gade, Suitable reverberation times for halls for rock and pop music. J Acoust Soc Am, 127(1) (2010) 247-55.

[114]. E. Meyer, D. Kunstmann, H. Kuttruff, Über einige Messungen zur Schallabsorption von Publikum. Acta Acustica united with Acustica, 14(2) (1964) 119-124.

[115]. X. Zhang, D.J. Thompson, G. Squicciarini, Sound radiation from railway sleepers. Journal of Sound and Vibration, 369 (2016) 178-194.

[116]. D. Thompson, X. Liu, H. Li, G. Xie, P. Bouvet, M. Rissmann, L. Baeza, F. Denia, J. Giner, J. Carballeira, J. Martínez, M.L. Trifiletti, Complete virtual test method for structure-borne and airborne noise transmission, RUN2Rail Deliverable 4.2. March 2019 (www.run2rail.eu).

[117]. ISO 3382-2:2008: Acoustics. Measurement of room acoustic parameters. Part 2. Reverberation time in ordinary rooms. International Standards Organization, Geneva, 2008.